

**THE UTILITY OF COMPLEX SOIL REFLECTANCE
IMAGE PROPERTIES FOR SOIL MAPPING**

Thesis

**Submitted in fulfillment of the requirement for the degree of
Doctor of Philosophy**

at the

**Department of Environmental and Geographical Sciences
Faculty of Science and Engineering
The Manchester Metropolitan University**

by

Abdulrahman Al-Hussaini

December 1999

DECLARATION

No part of this work has been submitted for the award of a qualification at this or any other institution. All published reference has been fully referenced.

A. Al-Hussaini

ABSTRACT

This investigation is concerned with the application of complex quantitative analysis to remotely sensed data for mapping soils. The major aim of this thesis is to examine, by means of illustrative examples, the utility of complex image metrics in the detection, differentiation, and partitioning of satellite images of soil landscapes. Satellite images have been widely used for soil mapping. In order to realise the maximum potential of satellite imagery, improvements are needed both in visual presentation of such images, and in their automatic classification, in order to reveal the complex properties of soil landscape.

A Landsat TM image of the Al-Ahsa area of Saudi Arabia was used in the investigation. It presents an ideal region for remote sensing studies due to the absence of vegetation cover and the existence of different type of landforms in a region of low topography. Three techniques for modelling complex elements of images were used and evaluated; Fast Fourier Transform (FFT), Artificial Neural Network Analysis (ANN), Fractal and Multifractal Analysis.

The FFT technique developed in this thesis isolates spatial frequency components in specific wavebands. The inverse FFT images are enhanced to (i) display optimised zoning of the image, and (ii) to display specific features. This technique partitions images into major zones that are different zones from the standard soil maps. The ANN technique developed is a non-linear measure of image texture. It shows difference within an image. The texture model is trained on areas selected on the basis of the existing soil map. Substitution analysis of training areas allows an assessment of image zones and boundaries. The texture image is displayed by linear contrast stretch. Zonation does not correspond with published maps or with FFT zonation. The fractal method is based on the local fractal dimension that is used as a texture measure based on a moving pre-set size filter over the entire image. The resulting images do not give zones but shows clear patterns of complexity such as spatial transitions. It is possible to derive areas of similar patterns of transition in complexity.

There are implications of these results for soil mapping at the theoretical and practical levels. The implications of the theoretical level are about the existences of soil units defined following the classical approach. In the practical level, the classical approach would be abandoned. There is at present nowhere near the same support of the ideas to complement the traditional mapping approach and raise awareness that soils are inherently complex. The study has important implications for classical theory and practice of soil mapping.

ACKNOWLEDGEMENTS

I would like to extend gratitude to my Director of Studies Dr Jim Petch for his time valuable advise, constructive criticism and encouragement throughout the duration of this study. Moreover, for his kind endeavour and patience, my sincere thanks are extended to him for going through my draft writings innumerable times.

The author also wishes to thank the following for their help and support throughout the period of preparation and work on this study:

All the staff of the Department of Environmental and Geographical Sciences and technicians during my stay in the department for support and use of facilities.

-To my friend in the department Dr Mustapha Heddi for his constructive arguments, valuable suggestions

-To Mr Muhammad Islam for his help and time to set-up the style format of Microsoft Word Processing for my thesis layout.

-Saudi Cultural Attaché in London for his support and encouragement.

-My university in Saudi Arabia, especially colleagues in the Department of Geography for their financial and moral support.

-To my friend Dr Muhammad Al-Jabr for his encouragement to complete my higher education and to introduce me to Jim.

-To the staff of the Saudi Centre of Remote Sensing for producing and providing Landsat-TM data imagery for this study.

-To my brother Muhammad for his help to send the necessary materials and in different ways.

-To my cousin Muhammad for his time and using his 4 × 4 car to visit and to show me the study area location.

-Lastly and most importantly my parents who were very supportive and my family especially my wife deserves special thanks for her understanding, patience and unquestioning support, particularly in difficult moments.

TABLE OF CONTENTS

<u>DECLARATION</u>	ii
<u>ABSTRACT</u>	iii
<u>ACKNOWLEDGEMENTS</u>	iv
<u>TABLE OF CONTENTS</u>	v
<u>LIST OF FIGURES</u>	x
<u>LIST OF TABLES</u>	xvii
<u>LIST OF TABLES</u>	xvii
<u>CHAPTER 1</u>	1
<u>INTRODUCTION</u>	1
<u>1.1 Introduction</u>	1
<u>1.2 Classical approach of Soil Classification and mapping</u>	3
<u>1.3 Structural approach to soil classification and mapping</u>	7
<u>1.4 Purpose of study</u>	8
<u>CHAPTER 2</u>	10
<u>THE GEOLOGICAL AND PHYSIOGRAPHICAL FEATURES OF THE STUDY</u>	
<u>AREA AND SOILS RESOURCES</u>	10
<u>2.1 Introduction</u>	10
<u>2.2 Geological History and formations</u>	14
<u>2.3 Geological Formations and Topographical features of the Al-Ahsa</u>	16
<u>region</u>	16

2.3.1 Geological Structures	16
2.3.2 Neogene formation	18
2.3.3 Unconsolidated sedimentary materials.....	19
2.3.3 Silt and gravel	19
2.3.4 Sabkha deposits	19
2.3.5 Aeolian sands.....	20
2.4 Soil and landform units.....	20
2.4.1 Alluvial plain	20
2.4.2 Gypseous pediplain with sand cover	24
2.4.3 Sand sheet and dunes.....	24
2.4.4 Sabkha	25
2.4.5 Sand dunes.....	25
2.5 A brief review of soil reflectance factors.....	26
2.5.1 Soil texture, water content, and surface roughness effects.....	27
2.5.2 Tone and Colour	32
2.5.3 Mineral content.....	32
2.5.4 Organic matter content	35
2.5.5 Pattern.....	37
2.6 Conclusion	38
<u>CHAPTER 3</u>	40
<u>RESEARCH DESIGN AND DATA PROCESSING STRATEGY</u>	40
3.1 Introduction.....	40
3.2 Spectral Analysis Technique.....	41
3.3 The Artificial Neural Network Technique.....	46
3.4 Multifractal Analysis	51
3.5 Data Processing Strategies.....	55
3.5.1 Test Segments.....	55
3.5.2 Data sources.....	55
3.5.3 Image Processing.....	56
3.6 Summary	60
<u>CHAPTER 4</u>	62
<u>SPECTRAL ANALYSIS</u>	62
4.1 Introduction.....	62
4.2 Spatial spectra as a property of images.....	62
4.2.1 Spatial filtering	62
4.2.2 Fourier analysis	66

4.2.2.1	<i>Introduction</i>	66
4.2.2.2	<i>Computation of the discrete Fourier Transform</i>	67
4.2.2.3	<i>Fourier transform applications in remote sensing</i>	68
4.3	Data processing for spectral analysis	71
4.3.1	Strategic investigative procedures	71
4.3.2	Pseudo-colour images	75
4.3.3	Enhancement Techniques	76
4.3.3.1	<i>Linear contrast stretch</i>	77
4.3.3.2	<i>Histogram Equalisation</i>	78
4.3.3.3	<i>Square root contrast stretch</i>	78
4.3.3.4	<i>Infrequency</i>	78
4.3.4	Unsupervised classifier	79
4.4	Results and Discussions	83
4.4.1	Introduction	83
4.4.2	Image statistics	86
4.4.3	Assessment of output images	94
4.4.4	Analysis of images for soil Landscape identification	97
4.4.4.1	<i>Test segment I</i>	97
4.4.4.2	<i>Test Segment II</i>	108
4.4.4.3	<i>Test Segment III</i>	117
4.6	Summary	125
 <u>CHAPTER 5</u>		127
 <u>ARTIFICIAL NEURAL NETWORK MODELLING</u>		127
5.1	Introduction	127
5.2	Multilayer Perceptrons (MLP)	128
5.2.1	Introduction	128
5.2.2	Training Multilayer Perceptrons	129
5.2.3	The Back Propagation Algorithm	131
5.2.4	Over-fitting and Generalisation	133
5.2.5	Other Neural Networks	135
5.2.5.1	<i>Radial Basis Function Networks</i>	135
5.2.5.2	<i>Kohonen Networks</i>	137
5.3	ANN in Image Processing	138
5.4	Experimental Strategies	140
5.4.1	Convolution filter model	140
5.4.2	Training Set Strategy	141
5.5	Results and Discussions	142
5.5.1	Introduction	142
5.5.2	Image Statistics	143
5.5.3	Assessment of output images	156
5.5.4	Analysis of images for soil landscape identification	166

<u>5.5.4.1 Test segment I</u>	167
<u>5.5.4.2 Test segment II</u>	167
<u>5.5.4.3 Test segment III</u>	169
<u>5.6 Summary</u>	169
<u>CHAPTER 6</u>	171
<u>MULTIFRACTAL ANALYSIS</u>	171
<u>6.1 Introduction</u>	171
<u>6.2 Fractal analysis</u>	172
<u>6.2.1 Background</u>	172
<u>6.2.2 Fractal Theory</u>	175
<u>6.2.3 Fractal Surface Measurement Methods</u>	177
<u>6.2.3.1 Isarithm Method</u>	177
<u>6.2.3.2 Variogram Method</u>	178
<u>6.2.3.3 Triangular Prism Method</u>	178
<u>6.3 Applications of Monofractal</u>	179
<u>6.4 Multifractal Approach</u>	180
<u>6.5 Application to image analysis</u>	182
<u>6.6 Image processing</u>	183
<u>6.7 Results and Discussions</u>	185
<u>6.7.1 Introduction</u>	185
<u>6.7.2 Image statistics</u>	186
<u>6.7.3 Assessment of output images</u>	192
<u>6.7.4 Analysis of multifractal images for soil landscape identification</u> 194	
<u>6.7.4.1 Test Segment I</u>	194
<u>6.7.4.2 Test Segment II</u>	216
<u>6.7.4.3 Test Segment III</u>	216
<u>6.7.5 Analysis of fractal images for soil landscape identification</u>	216
<u>6.8 Summary</u>	225
<u>CHAPTER 7</u>	226
<u>DISCUSSION AND CONCLUSIONS</u>	226
<u>7.1 Introduction</u>	226
<u>7.2 The Interpretation of maps in terms of complex elements</u>	227
<u>7.2.1 Theoretical Considerations</u>	227
<u>7.2.2 Empirical Results</u>	231
<u>7.3 Discussion</u>	234
<u>7.4 Conclusion</u>	238
<u>7.5 Further Work</u>	240

References and Bibliography 242

LIST OF FIGURES

<u>Figure 2.1: Map showing the location of Al-Ahsa region.</u>	11
<u>Figure 2.2: Schematic Hydrogeological Cross Section of the Arabian Sedimentary Basin (after Al-Jabr, 1989).</u>	13
<u>Figure 2.3: General geological map of the Arabian Peninsula (after Al-Sayari and Zott, 1978).</u>	15
<u>Figure 2.4: Surface geological formation (see text for description key after Al-Jabr, 1989).</u>	17
<u>Figure 2.5: General soil map and the locations of test segments (after MAW, 1986). ...</u>	21
<u>Figure 2.6: General landform map (after MAW, 1995).</u>	22
<u>Figure 2.7: Field photographs showing (a) flat sabkha, and (b) sand sheet and dunes of test segment I.</u>	23
<u>Figure 2.8: Spectral reflectance curves for bare soil (after Belward and Valenzulea, 1991).</u>	29
<u>Figure 2.9: Spectral reflectance curves for silty loam at various contents (after Hoffer, 1978).</u>	31
<u>Figure 2.10: Reflectance of three soil types; namely (a) organic-dominated, (b) minimally altered, (c) iron-dominated (after Stoner and Baumgradner, 1981).</u>	33
<u>Figure 2.11 Relationship between organic matter content and reflectance (after Hoffer, 1978).</u>	36
<u>Figure 3.1: A filtered inverse image of Band 7 showing an artefact features when the low frequency blocked out.</u>	43
<u>Figure 3.2 Diagrams representing PCT, infrequency histogram, and unsupervised fuzzy k-means cluster.</u>	45
<u>Figure 3.3. Neural Network Structure for 3 × 3 window of pixels values.</u>	48
<u>Figure 3.4 Scatter plot of Band 7 against Band 4.</u>	59
<u>Figure 4.1. The three basic types of spatial filters (above), frequency filters display in 3 D representing (a) low-pass, (b) high-pass, and (c) band-pass (below) (after Schowengerdt, 1983 and Sonka <i>et al.</i>, 1994).</u>	64

<u>Figure 4.2. Image formation in the spatial and Fourier domains (after Schowengerdt, 1983).</u>	65
<u>Figure 4.3. A colour composite of Landsat imagery of the study area (Bands 7, 4, and 1, size 1024 × 1024 pixels).</u>	72
<u>Figure 4.4. Fourier transformed filters (a) original magnitude, (b) kernel band-pass, (c) first band-pass, (d) second band-pass, (e) third band-pass, (f) fourth band-pass, (g) fifth band-pass.</u>	74
<u>Figure 4.5. Illustration of differences of (a) conventional classification, (b) fuzzy k-means classification (after Jensen, 1996).</u>	82
<u>Figure 4.6. Images of Landsat Band 7 representing (a) segment I, (b) segment II, (c) segment III.</u>	84
<u>Figure 4.7. Images (a) to (g) represent the original image and the filtered inverse FFT images of segment I.</u>	85
<u>Figure 4.8. Histogram of the original TM raw data (segment I, Band 7).</u>	87
<u>Figure 4.9. Histogram of the kernel filtered image (segment I, Band 7).</u>	88
<u>Figure 4.10. Histogram of the first band-pass filtered image (segment I, Band 7).</u>	89
<u>Figure 4.11. Histogram of the second band-pass filtered image (segment I, Band 7).</u>	90
<u>Figure 4.12. Histogram of the third band-pass filtered image (segment I, Band 7).</u>	91
<u>Figure 4.13. Histogram of the fourth band-pass filtered image (segment I, Band 7).</u>	92
<u>Figure 4.14. Histogram of the fifth band-pass filtered image (segment I, Band 7).</u>	93
<u>Figure 4.15. PCT images of Band 7, (a) original, (b) kernel, (c) First band-pass, (d) second band-pass, (e) third band-pass, (f) fourth band-pass, (g) fifth band-pass (Segment I).</u>	98
<u>Figure 4.16. Infrequency images of Band 7, (a) original, (b) kernel, (c) First band-pass, (d) second band-pass, (e) third band-pass, (f) fourth band-pass, (g) fifth band-pass (Segment I).</u>	101
<u>Figure 4.17. Unsupervised fuzzy <i>k</i>-means images of Band 7, (a) original, (b) kernel, (c) First band-pass, (d) second band-pass, (e) third band-pass, (f) fourth band-pass, (g) fifth band-pass (Segment I).</u>	104

<u>Figure 4.18. PCT images of Band 4, (a) original, (b) kernel, (c) First band-pass, (d) second band-pass, (e) third band-pass, (f) fourth band-pass, (g) fifth band-pass (Segment I).</u>	105
<u>Figure 4.19. Infrequency images of Band 4, (a) original, (b) kernel, (c) First band-pass, (d) second band-pass, (e) third band-pass, (f) fourth band-pass, (g) fifth band-pass (Segment I).</u>	106
<u>Figure 4.20. Unsupervised fuzzy k-means images of Band 4, (a) original, (b) kernel, (c) First band-pass, (d) second band-pass, (e) third band-pass, (f) fourth band-pass, (g) fifth band-pass (Segment I).</u>	107
<u>Figure 4.21. PCT images of Band 7, (a) original, (b) kernel, (c) First band-pass, (d) second band-pass, (e) third band-pass, (f) fourth band-pass, (g) fifth band-pass (Segment II).</u>	109
<u>Figure 4.22. Infrequency images of Band 7, (a) original, (b) kernel, (c) First band-pass, (d) second band-pass, (e) third band-pass, (f) fourth band-pass, (g) fifth band-pass (Segment II).</u>	111
<u>Figure 4.23. Unsupervised fuzzy k-means images of Band 7, (a) original, (b) kernel, (c) First band-pass, (d) second band-pass, (e) third band-pass, (f) fourth band-pass, (g) fifth band-pass (Segment II).</u>	113
<u>Figure 4.24. PCT images of Band 4, (a) original, (b) kernel, (c) First band-pass, (d) second band-pass, (e) third band-pass, (f) fourth band-pass, (g) fifth band-pass (Segment II).</u>	114
<u>Figure 4.25. Infrequency images of Band 4, (a) original, (b) kernel, (c) First band-pass, (d) second band-pass, (e) third band-pass, (f) fourth band-pass, (g) fifth band-pass (Segment II).</u>	115
<u>Figure 4.26. Unsupervised fuzzy k-means images of Band 4, (a) original, (b) kernel, (c) First band-pass, (d) second band-pass, (e) third band-pass, (f) fourth band-pass, (g) fifth band-pass (Segment II).</u>	116
<u>Figure 4.27. PCT images of Band 7, (a) original, (b) kernel, (c) First band-pass, (d) second band-pass, (e) third band-pass, (f) fourth band-pass, (g) fifth band-pass (Segment III).</u>	118

<u>Figure 4.28. Infrequency images of Band 7, (a) original, (b) kernel, (c) First band-pass, (d) second band-pass, (e) third band-pass, (f) fourth band-pass, (g) fifth band-pass (Segment III).</u>	119
<u>Figure 4.29. Unsupervised fuzzy k-means images of Band 7, (a) original, (b) kernel, (c) First band-pass, (d) second band-pass, (e) third band-pass, (f) fourth band-pass, (g) fifth band-pass (Segment III).</u>	120
<u>Figure 4.30. PCT images of Band 4, (a) original, (b) kernel, (c) First band-pass, (d) second band-pass, (e) third band-pass, (f) fourth band-pass, (g) fifth band-pass (Segment III).</u>	121
<u>Figure 4.31. Infrequency images of Band 4, (a) original, (b) kernel, (c) First band-pass, (d) second band-pass, (e) third band-pass, (f) fourth band-pass, (g) fifth band-pass (Segment III).</u>	122
<u>Figure 4.32. Unsupervised fuzzy k-means images of Band 4, (a) original, (b) kernel, (c) First band-pass, (d) second band-pass, (e) third band-pass, (f) fourth band-pass, (g) fifth band-pass (Segment III).</u>	123
<u>Figure 5.1 Histogram of the second output of the ABCD image (Band 7, segment I).</u>	147
<u>Figure 5.2 Histogram of the second output of the ABC image (Band 7, segment I).</u>	148
<u>Figure 5.3 Histogram of the second output of the ABD image (Band 7, segment I).</u>	149
<u>Figure 5.4 Histogram of the second output of the ACD image (Band 7, segment I).</u>	150
<u>Figure 5.5 Histogram of the second output of the BCD image (Band 7, segment I).</u>	151
<u>Figure 5.6 Histogram of the second output of the AABCD image (Band 7, segment I).</u>	152
<u>Figure 5.7 Histogram of the second output of the ABBCD image (Band 7, segment I).</u>	153
<u>Figure 5.8 Histogram of the second output of the ABCCD image (Band 7, segment I).</u>	154
<u>Figure 5.9 Histogram of the second output of the ABCDD image (Band 7, segment I).</u>	155
<u>Figure 5.10. Illustration diagram of the three segments showing the four zones A, B, C, D.</u>	157

<u>Figure 5.11 Images (a) to (r) represent the ANN outputs of the training scheme (Band 7, segment I).</u>	160
<u>Figure 5.12 Images (a) to (r) represent the ANN outputs of the training scheme (Band 4, segment I).</u>	161
<u>Figure 5.13 Images (a) to (r) represent the ANN outputs of the training scheme (Band 7, segment II).</u>	162
<u>Figure 5.14 Images (a) to (r) represent the ANN outputs of the training scheme (Band 4, segment II).</u>	163
<u>Figure 5.15 Images (a) to (r) represent the ANN outputs of the training scheme (Band 7, segment III).</u>	164
<u>Figure 5.16 Images (a) to (r) represent the ANN outputs of the training scheme (Band 4, segment III).</u>	165
<u>Figure 6.1 Histogram of the <i>MAX</i> pointwise Hoelder exponent image (Band 7, segment I).</u>	189
<u>Figure 6.2 Histogram of the <i>ISO</i> pointwise Hoelder exponent image (Band 7, segment I).</u>	190
<u>Figure 6.3 Histogram of the <i>SUM</i> pointwise Hoelder exponent image (Band 7, segment I).</u>	191
<u>Figure 6.4 Images a to f represent different Hoelder exponent images for Band 4 and 7 (segment I).</u>	195
<u>Figure 6.5 Images a to f represent different Hoelder exponent images for Band 4 and 7 (segment II).</u>	196
<u>Figure 6.6 Images a to f represent different Hoelder exponent images for Band 4 and 7 (segment III).</u>	197
<u>Figure 6.7 Images (a) to (f) represent <i>MAX</i> Hoelder exponent of multifractal segmentation of different parameters set-up for Band 7 (segment I).</u>	198
<u>Figure 6.8 Images (a) to (f) represent <i>ISO</i> Hoelder exponent of multifractal segmentation of different parameters set-up for Band 7 (segment I).</u>	199
<u>Figure 6.9 Images (a) to (f) represent <i>SUM</i> Hoelder exponent of multifractal segmentation of different parameters set-up for Band 7 (segment I).</u>	200

Figure 6.10 Images (a) to (f) represent *MAX* Hoelder exponent of multifractal segmentation of different parameters set-up for Band 4 (segment I)..... 201

Figure 6.11 Images (a) to (f) represent *ISO* Hoelder exponent of multifractal segmentation of different parameters set-up for Band 4 (segment I)..... 202

Figure 6.12 Images (a) to (f) represent *SUM* Hoelder exponent of multifractal segmentation of different parameters set-up for Band 4 (segment I)..... 203

Figure 6.13 Images (a) to (f) represent *MAX* Hoelder exponent of multifractal segmentation of different parameters set-up for Band 7 (segment II). 204

Figure 6.14 Images (a) to (f) represent *ISO* Hoelder exponent of multifractal segmentation of different parameters set-up for Band 7 (segment II). 205

Figure 6.15 Images (a) to (f) represent *SUM* Hoelder exponent of multifractal segmentation of different parameters set-up for Band 7 (segment II). 206

Figure 6.16 Images (a) to (f) represent *MAX* Hoelder exponent of multifractal segmentation of different parameters set-up for Band 4 (segment II). 207

Figure 6.17 Images (a) to (f) represent *ISO* Hoelder exponent of multifractal segmentation of different parameters set-up for Band 4 (segment II). 208

Figure 6.18 Images (a) to (f) represent *SUM* Hoelder exponent of multifractal segmentation of different parameters set-up for Band 4 (segment II). 209

Figure 6.19 Images (a) to (f) represent *MAX* Hoelder exponent of multifractal segmentation of different parameters set-up for Band 7 (segment III). 210

Figure 6.20 Images (a) to (f) represent *ISO* Hoelder exponent of multifractal segmentation of different parameters set-up for Band 7 (segment III). 211

Figure 6.21 Images (a) to (f) represent *SUM* Hoelder exponent of multifractal segmentation of different parameters set-up for Band 7 (segment III). 212

Figure 6.22 Images (a) to (f) represent *MAX* Hoelder exponent of multifractal segmentation of different parameters set-up for Band 4 (segment III). 213

Figure 6.23 Images (a) to (f) represent *ISO* Hoelder exponent of multifractal segmentation of different parameters set-up for Band 4 (segment III). 214

Figure 6.24 Images (a) to (f) represent *SUM* Hoelder exponent of multifractal segmentation of different parameters set-up for Band 4 (segment III). 215

Figure 6.25 Images (a) to (e) represent fractal dimensions images of different parameters set-up for Band 7 (segment I)..... 218

Figure 6.26 Images (a) to (e) represent fractal dimensions images of different parameters set-up for Band 4 (segment I)..... 219

Figure 6.27 Images (a) to (e) represent fractal dimensions images of different parameters set-up for Band 7 (segment II)..... 220

Figure 6.28 Images (a) to (e) represent fractal dimensions images of different parameters set-up for Band 4 (segment II)..... 221

Figure 6.29 Images (a) to (e) represent fractal dimensions images of different parameters set-up for Band 7 (segment III). 222

Figure 6.30 Images (a) to (e) represent fractal dimensions images of different parameters set-up for Band 4 (segment III). 223

LIST OF TABLES

<u>Table 2.1: Particle size classes most widely adopted internationally (after White, 1997).</u>	27
<u>Table 2.2: Summary of landform unit, soil type, and reflectance properties.</u>	38
<u>Table 3.1: Characteristics of Landsat TM system (adapted from Jensen, 1996).</u>	58
<u>Table 4.1: Masking filters.</u>	73
<u>Table 4.2: An Example of Pseudo-Colour Table.</u>	76
<u>Table 4.4. Summary of the features identification of the inverse filtered images</u>	124
<u>Table 5.1. Image statistics of segment I.</u>	144
<u>Table 5.2. Image statistics of segment II.</u>	145
<u>Table 5.3. Image Statistics of segment III.</u>	146
<u>Table 5.4. Summary of the features identification of the ANN images.</u>	168
<u>Table 6.1: Multifractal segmentation parameters.</u>	184
<u>Table 6.2: Image statistics of Hoelder exponent images for the three segments.</u>	188
<u>Table 6.3. Summary of the features identification of the fractal images.</u>	224
<u>Table 7.1: Summary of major identifying features for the three techniques.</u>	231
<u>Table 7.2: The relation of the three complex metrics to mapped units.</u>	234

CHAPTER 1

INTRODUCTION

1.1 Introduction

This thesis is concerned with the problem of mapping the complex properties of soil. That is not the complexity of patterns of soil properties but the intrinsic property of complexity itself. In contrast with almost all mapping studies of soil this thesis address the problem of mapping metrics of complexity rather than complex patterns of simple metrics. It avoids, therefore, the simplifying assumptions of identifying soil units, the first level of application of any traditional metric system. In this thesis soil units are used only as a comparison of metrics of complexity with conventional mapping procedures. The significance of this is first, it allows a test of conventional mapping methods. But, secondly, it provides a more objective means of testing what field scientists have established, the existence of real units in a very complex world.

The problem of mapping complexity is central to the whole problem of soil resource mapping. In this, there are two issues, of complexity and of adequately mapping large areas. These problems are related of course but not totally. Soils are intrinsically and extremely complex even at microscopic scale and this complexity is apparent at all small scales. For mapping, however, the usefulness of the exercise is only at scales,

which involve large areas. Soil resource mapping is a regional issue. At such scales complexity is inherent if only because the problem scale is so much smaller than the mapping scale. Soils are mapped in the field at 1: 5000 to 1: 10000 scales or by remote sensing at 1:5000 to 1: 25000, but they are interpreted and the subject of planning at the 1: 50,000 to 1: 1,000,000 scale. Complexity is the norm in this situation.

The problems of studying soil resources are adequately mapping large areas and characterising and displaying complex phenomena. Such study is made possible only because of the availability of remotely sensed digital images of the earth's surface. Although there are a number of field studies which have dealt with soil complexity, these are, if only because of cost of sampling and analysis, of limited extent (Webster and Oliver, 1990). They range from studies of individual fields or problems of the order of 100 m to studies of soil properties over centimetres. In all such studies soils are sampled at discrete locations or soil properties interpolated. Only images provide empirically derived continuous measures of soil properties, which allow us properly to study complexity.

The application of remotely sensed data in the field of soil cartography began in the thirties with the utilisation of low-level aerial photography. Aerial photography has been used as useful supplement to field survey for delineating soil boundaries. The methodology developed during World War II and continues to be developed today using satellite images (Mather, 1987; Townshend, 1981; Brady and Weil, 1999). The early

applications of Landsat data were based on the interpretation of colour and grey tone differences between terrain features and were limited mainly to small scale mapping of large geographical areas. Such interpretations were confirmed by field checking because soil characteristics can only be substantiated in the field (Mulders, 1987; White, 1977).

Landsat satellite data are routinely available as single images covering over 30,000 square kilometres. Data is of reflectance of solar radiation in up to six visible and infrared wavebands at 30-meter resolution. The relations between Landsat reflectance measures and soil properties are well established (Mulders, 1987; Barret and Curtis, 1990). Satellite remote sensing is now widely used in conjunction with field survey and classical soil series modelling for compiling soil maps (Burrough, 1986; Mather, 1987).

1.2 Classical approach of Soil Classification and mapping

The soil is at the interface between the atmosphere and the lithosphere, which is the mantle of rocks making up the crust of the earth (White, 1987). Because of complexity of soil constituents and of the physical, chemical, and biological forces to which it is exposed, there is little merit in attempting to give a particular definition of soil (Rowell, 1994; White, 1987; Wild, 1993). What is clear is that there is an extraordinary range of soil types in the landscape. This due to the great diversity of, 1) parent material, 2) climate, 3) vegetation, 4) organisms and topography, and 5) time (Brady and Weil 1999; White 1987).

The classical approach to soil mapping is to apply a predetermined system of classification to an area. Such systems are developed on an empirical base to provide a rational and complete expression of the relation of soil to soil forming factors. In general the process of classification can be described (White, 1987) as 1) identification of the full range of fluctuation in the population, 2) creation of classes within the population according to similarity between individuals, 3) and prediction of the likely adaptation of a confused individual to a class.

The purpose of soil classification, like any other classification, is to group soils with similar properties so that the name of the group is useful in transporting information about members. Although the members may differ in other respects, the soil group should give information that applies to all members of the same group (Brady and Weil 1999; Rowell, 1994; White, 1987; Wild, 1993), and distinguishes them from members of other groups. White (1987) considers that soil classification is more difficult and contentious than the classification of other natural populations, because of the lack of distinguishable heredity characteristics of individuals within one generation that are transmitted from one generation to another.

Many soil classification systems have been developed. Each has aimed to develop its own system in order to assess specific soil resources, but for international understanding more general classification systems are required. The two commonly used soil classification systems have been recommended by FAO (FAO/UNESCO Soil Map of

the World) and USDA (US Department of Agriculture). In addition, there are national classification systems such as the Soil classification for England and Wales, Canadian Soil classification, and Australian Soil Classification. The discussion of these systems is beyond the scope of this research.

Soil survey primarily involves collecting information about soils in the field. This information will usually be complemented by laboratory measurements on samples from the field. The effort put into survey and the methods used depend on the human and financial resources available, the purpose of the survey, and the limitation of any classes to be created.

The output map of soil survey may be a classification, and a map showing the distribution of different soil classes at a scale consistent with sampling on the ground (Rowell, 1994; White, 1987). The information needs for soil survey depend on its declared approaches, for which they generally viewed as much wider than simply the mapping of soil units (Townshend, 1981; Courtney and Trudgill, 1984).

Reliability of soil information is a critical factor for developing robust and coherent analysis of soil mapping systems and evaluating landscape and land-cover more efficiently. In addition, an accurate soil map is one of the key data layers in integrating soil data with remote sensing and GIS data (Adams *et al.*, 1995; Brady and Weil, 1999; Burgess and Webster, 1980). In using such technologies, soil properties have to be

inferred from aerial photography and satellite data. Although these techniques provide a way to extrapolate from ground-based observations; the conventional methods are not substituted. On the other hand, the available soil map derived by conventional soil survey may not provide the desired accuracy for several reasons, one of which is the subjectivity of the mapping methods (Burrough, 1989; Campbell, 1996; Brady and Weil, 1999).

There are mainly two basic approaches to soil remote sensing. One, following the classical approach, is to produce a high quality image that can be used by soil scientists to make important decision about the available soil types, their distribution and boundaries. Since soil has a complex nature, it is often not possible to assign soil to predefined classes. Therefore, the operator skill of image analysis together with deduction plays an important role in image interpretation. Most remote sensing techniques are capable of detecting superficial phenomena, and offer a synoptic view of the landscape. However, in the study of soils, which are three-dimensional natural bodies, fieldwork is always a necessary complement to check the allocation of units and designation of boundaries.

The second approach is the structural approach, which is described in the following section.

1.3 Structural approach to soil classification and mapping

In the sixties the application of remote sensing to soil mapping received a new stimulus with development of a structural approach to soil cartography (Burrough, 1989; Brady and Weil, 1999; Fisher, 1987). With this approach, the object of soil cartography is not to map the distribution of definite, predefined classification groups of soil types, but to map groups derived from measurement of soil parameters in geographical space with their heterogeneity and structure (Burrough, 1989; Odeh *et al.*, 1992; Townshend, 1981). Combinations of soil components with detailed characteristics of point measures and their pattern and structure are used to characterise soil types. In addition, soil boundaries and soil map units are not necessarily discrete and homogeneous but can be regarded as continuous and heterogeneous (Fryberger *et al.*, 1983; Fryberger *et al.*, 1984; Odeh *et al.*, 1992). Units of such maps are characterised not by the dominant soil but by combinations of soil properties with details of the content, complexity, genesis and relative area of each component. For mapping soil cover types and compilation of such soil maps remote sensing is ideal.

In the structural approach mathematical and statistical algorithms are used for dividing the image into areas of different spectral responses, which are assumed to be related to soil properties. There is potential for extending this approach, which is based on the development in mathematical and statistical techniques for analysing and modelling large complex data sets. Soil phenomena have been modelled using geostatistical (kriging) methods, artificial neural net models, and some limited work has been

undertaken on fractal as well as multifractal properties and structures. Advanced geostatistical methods involving analysis of the semivariogram and kriging have been applied to soils with considerable success (Burrough, 1989; Webster and Oliver, 1990; Odeh *et al.*, 1992) but only over limited areas. As suggested by several researchers, the utility of both kriging and fuzzy *k*-means are optimums for soil mapping. For instance, the kriging method can be utilised in order to create a detailed spectral soil map beyond the limitation of sizes of pixels by interpolating unsampled locations. Fuzzy *k*-means clustering analysis can then be used for classifying the final kriged map (Burrough, 1997). In the fractal method, Zeng *et al.* (1996) demonstrated considerable potential for understanding soil behaviour by quantifying soil structure using and computing fractal parameters of soil density, and the utility of fractal lacunarity together with fractal dimension for quantifying small scale soil structure over data generated with x-ray computed topography. Also, Culling (1986) has used fractal dimension to measure the spatial variation of soil-pH values on a small transect of soil. Such models may be able to form the basis for a structural approach to soil classification and mapping which allows the soil scientist to measure and model complex spatial properties and patterns.

1.4 Purpose of study

This investigation is concerned with the application of complex quantitative analysis to remotely sensed data for mapping soils. It uses a set of techniques for measuring complex properties of image data, which were available in commercial software packages. These are:

- Fast Fourier Analysis for the isolation and mapping of spatial frequency spectra bands of images.
- Artificial Neural Network Models of image texture modelling.
- Fractal and Multifractal Analysis of local and whole image properties.

The first aim was to apply each technique to the classification and segmentation of a satellite image, which represented a set of soil landscapes relatively unaffected by vegetation.

In the application of each technique, the objectives were:

- To develop the procedures by which a soil map could be obtained,
- To explore the controls on the procedures and the relations of image outputs to these controls,
- To develop an appropriate means of visualisation.

A further aim was to evaluate the usefulness of the three techniques for soil mapping. In this evaluation there were two objectives:

- Comparison of the performance of the three techniques in mapping soil landscapes.
- Comparison of the three techniques singly and in combination with conventional soil mapping.

CHAPTER 2

THE GEOLOGICAL AND PHYSIOGRAPHICAL FEATURES OF THE STUDY AREA AND SOILS RESOURCES

2.1 Introduction

This chapter deals briefly with main physical factors and their influence on soil formation. The brief description of the landform units is also covered in this chapter together with a consideration from first principles of the soil reflective responses, which might be expected in the soils of the study region.

Soil is formed as a result of the interaction of many factors, the most important of which are parent material, climate, organisms, relief, and time (Brady and Weil, 1999). These soil-forming factors control the nature and rate of soil formation. To these must be added the effects of human activity which in the case of the Al-Ahsa oasis are significant, see figure 2.1 (Al-Jabr, 1989). In areas away from the oasis the general absence of vegetation means that the soil landscape at the regional scale reflects closely parent material and relief and process of erosion and deposition.

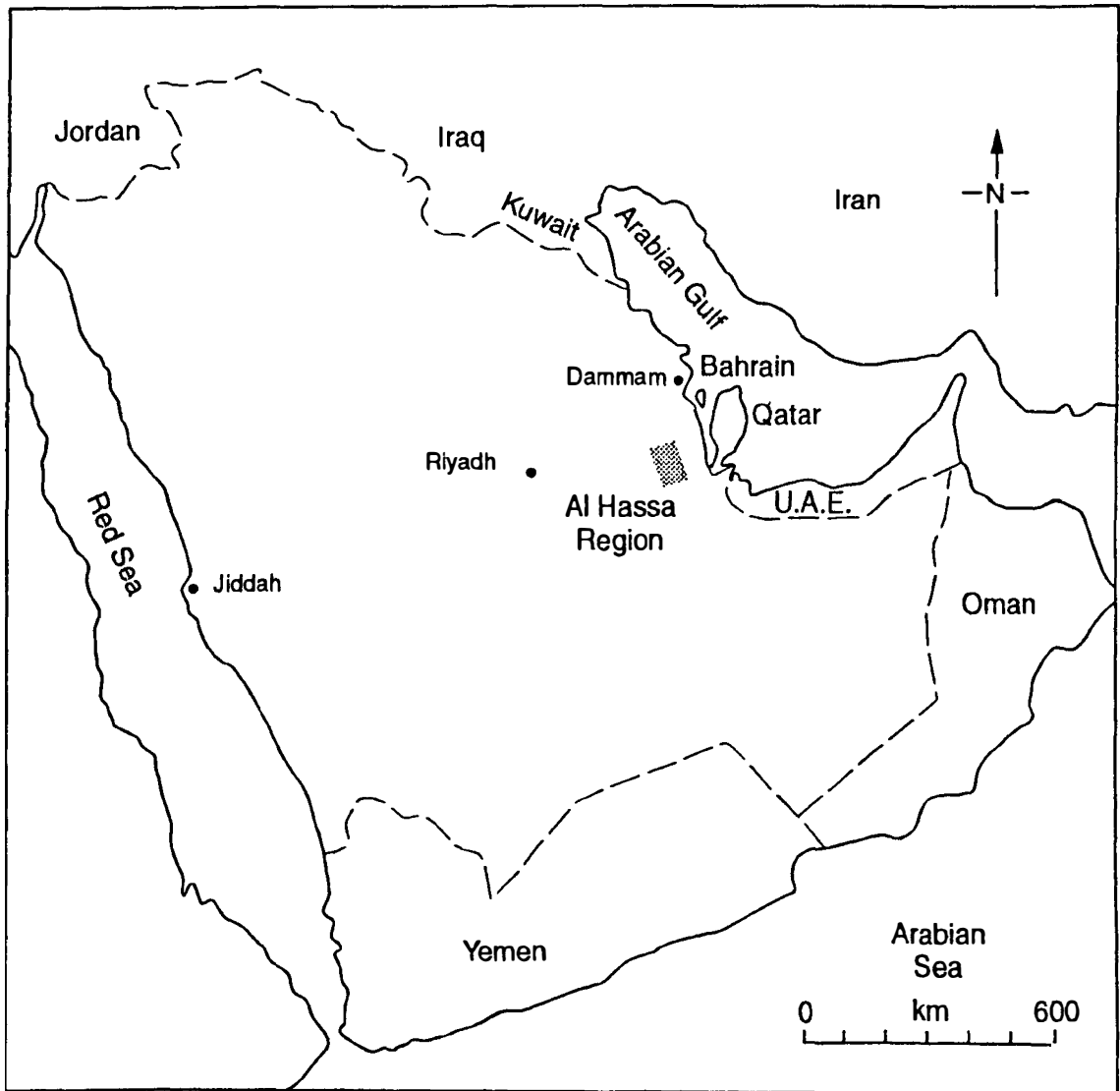


Figure 2.1 Map showing the location of Al-Hassa region

Soil may form by the weathering of consolidated rock or unconsolidated superficial deposits, which have been transported by water, wind or gravity (see Figure 2.2). These deposits originate from denudation of consolidated rock. Generally, weathering proceeds by physical disruption of the rock structure which exposes the constituent minerals to chemical alteration. Forces of expansion and contraction induced by diurnal temperature variations cause rock shattering and exfoliation, which are found in desert soil surfaces (Al-Barrak, 1993; El-Khatib, 1980).

Even water in arid and semi-arid areas is a dominant agent in weathering, not only because it initiates solution and hydrolysis, but also because it sustains plant life on rock surfaces. In arid and semi-arid areas lichens play a special part in the weathering because they produce chelating agents which trap the elements of the decomposing rock in organo-metallic complexes. Generally speaking, the growth, death and decay of plants and other organisms markedly enhance the solvent action of rainwater by the addition of carbon dioxide from respiration. Plant roots also contribute to the physical disintegration of rock (Al-Barrak, 1993; El-Khatib, 1980).

Water carrying suspended rock fragments has a scouring action on surfaces. The suspended material can vary in size from the finest grains to the gravel, and pebbles moved along and constantly abraded by running water in drainage paths. Particles carried by wind also have a sandblasting effect, and the combination of wind and water to form

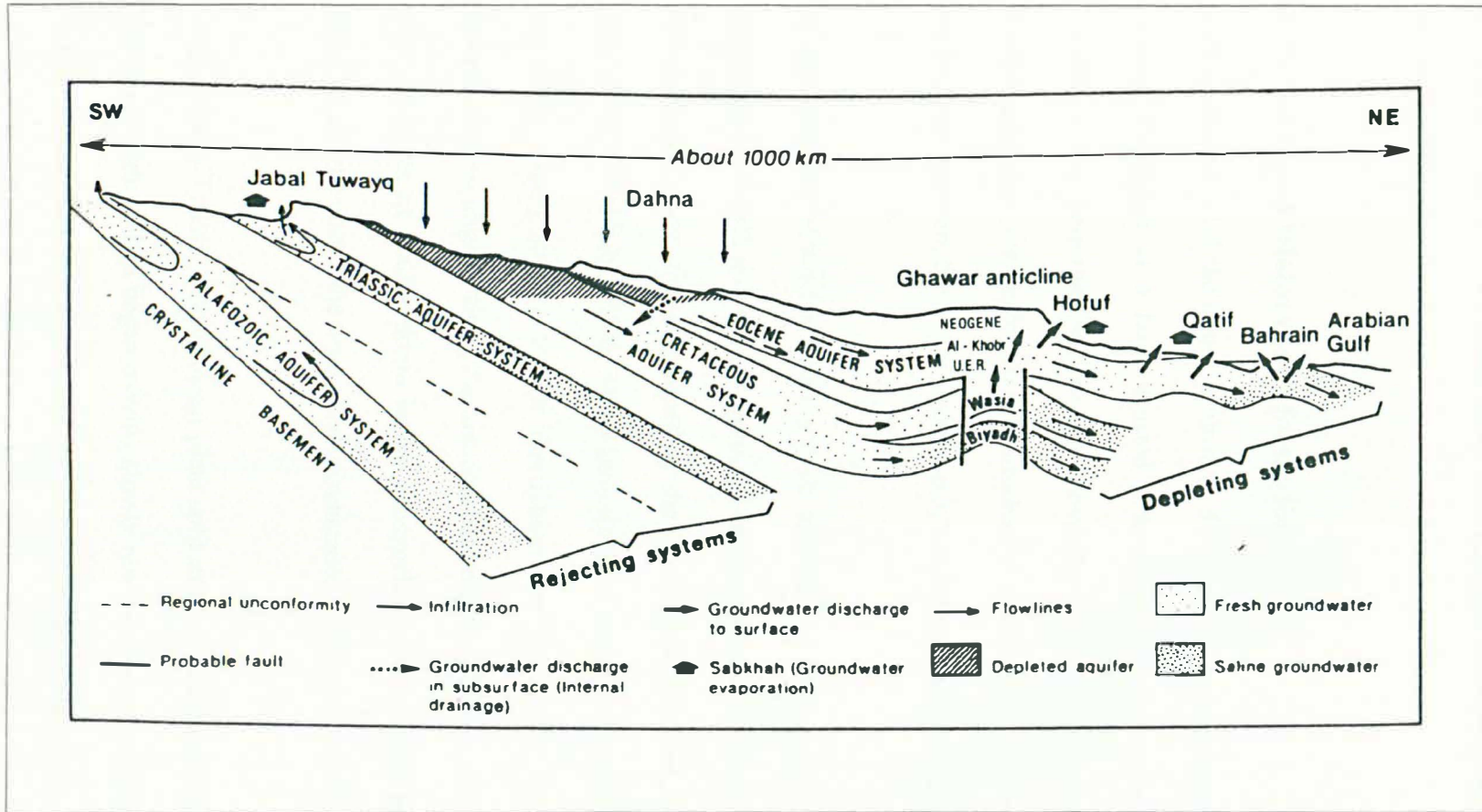


Figure 2.2: Schematic Hydrological cross section of the Arabian sedimentary basin (after Al-Jabr, 1989).

waves produces powerful forces along shorelines and along exposed rock surfaces (Al-Barrak, 1993).

2.2 Geological History and formations

At the regional level the major control on differences in soil properties is geology. The Arabian Peninsula is a huge crusted plate composed of ancient sedimentary and volcanic rocks, deformed and metamorphosed and injected by plutonic intrusions. In Precambrian time, the peninsula was attached to Africa as part of the Nubian Shield. In the late Precambrian, the surface was deeply eroded and peniplaned (see Figure 2.3).

At the beginning of the Cambrian, a great sedimentary basin or geosyncline (the Tethys) had developed north and east of Arabia. Turkey, northern Iraq, and south-western Iran now occupy the area that developed by the Great Basin (Al-Jabr, 1989; Al-Sayari and Zott, 1978; El-Khatib, 1980). Many thousands of meters of sediment accumulated in this deep, slowly-sinking trough throughout the Palaeozoic, Mesozoic, and early Cenozoic times, aligned along the junction between the Arabian and Iranian plates. The thick sequence of marine strata in the geosyncline was buckled into great folds and sliced by overthrusts at the time of late Cretaceous (Al-Barrak, 1993; Al-Jabr, 1989).

In the middle Tertiary, the Arabian plate split away from the African shield along the Red Sea trough. It then began moving slowly north-eastward, impinging on the edge of the great Asian plate in Iran and sliding beneath the latter plate. This separation of

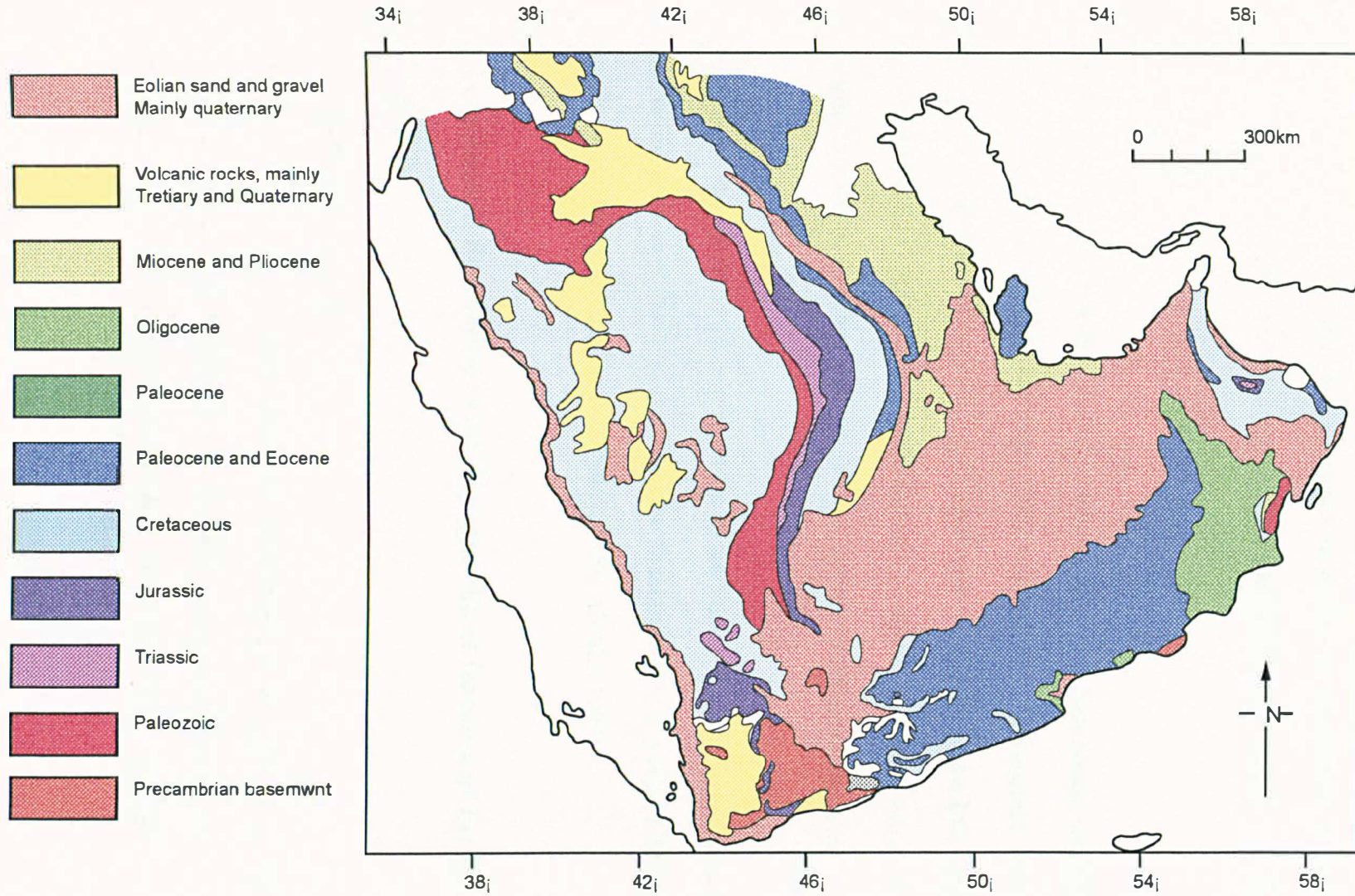


Figure 2.3 General geological map of the Arabian peninsula (after Al-Sayari and Zotl, 1978)

Arabia from Africa was accompanied by extensive volcanism along the western edge of the peninsula. The Arabian plate remained relatively stable, and its cover of shelf sediment was barely disturbed throughout the Palaeozoic and Mesozoic, and during the Tertiary orogeny.

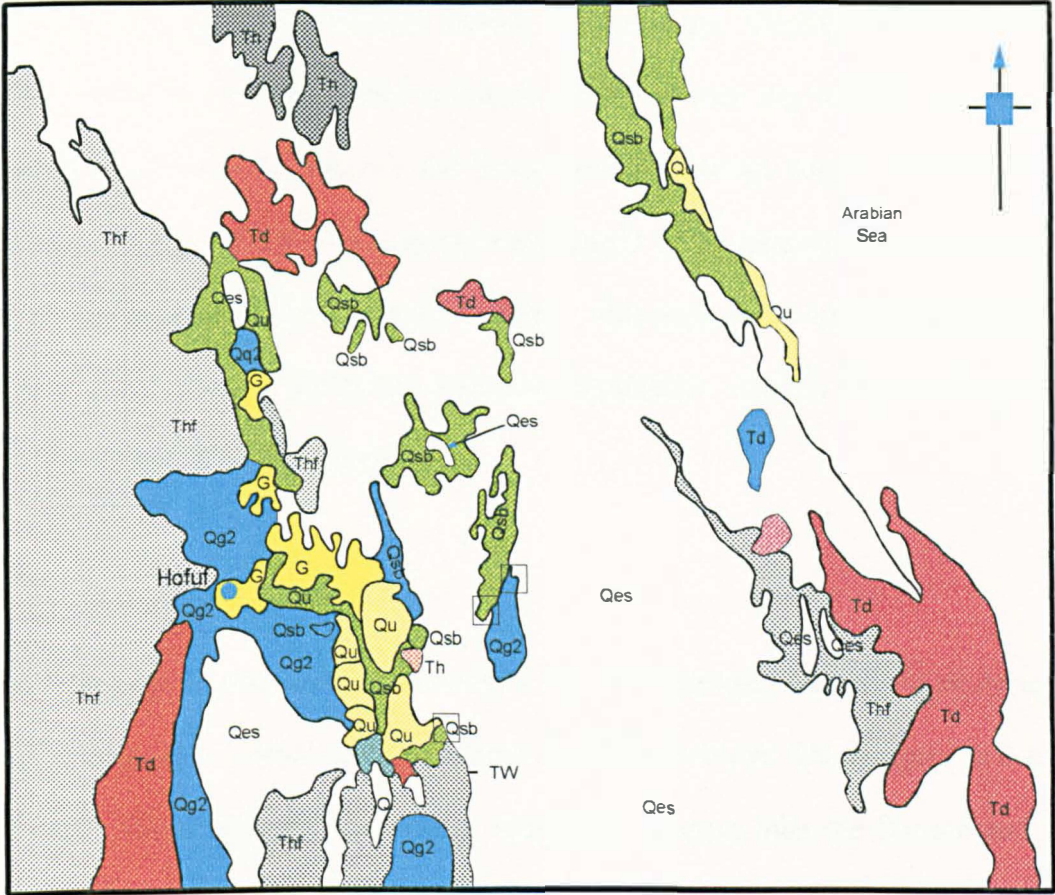
Eastern part of Saudi Arabia is underlain mainly by marine limestones, sandstones and shales deposited since Palaeozoic times. Occasional periods of emergence are indicated by gaps and unconformities. To the north and north-west as far as the Iraq frontier, the border of this area is the outcrop of the boundary between the upper-most Cretaceous (Aruma Formation) and basal Tertiary (base of Umm er Radhuma formation).

The general dip of the strata is from strata to the east in a gentle, continuous manner, interrupted in the eastern part of bordering the Arabian Gulf by a series of folds oriented mainly in a north-south direction (Al-Barrak, 1993; Al-Jabr, 1989).

2.3 Geological Formations and Topographical features of the Al-Ahsa region

2.3.1 Geological Structures

Figure 2.4 shows the geological formations of the region with respect to its relationship to topography, soils, and hydrology. The Al-Ahsa region is underlain mainly by marine limestone, sandstone, and shale deposited since Palaeozoic times. Gaps and



- Eolian Sand
- Sabkha Deposits
- Silt and Gravel
- Gravel
- Hofuf, Dam, and Hadrukh Formations

1: 500,000

Figure 2.4: Surface Geological formations (see text for description key after Al-Jabr 1989)

unconformities indicate occasional periods of emergence. Geologically a part of the Arabian Shelf, the Mesozoic and Cenozoic series of strata dip towards the east. The outcrops consist only of Tertiary and Quaternary sedimentary rocks. The morphogeny and hydrogeology of this area is strongly influenced by the Ghawar structure developed out by Cretaceous and lower Tertiary tectonics. This north-south-trending anticline west of Al-Ahsa is 20 to 40 kilometers wide and contains the world's largest oil field (Al-Sayari and Zott, 1978; El-khatib, 1980).

2.3.2 Neogene formation

This formation is what mainly determines the soil characteristics of the study region, since it is the most extensive and recent set of parent materials. The Neogene is a series of mainly continental and transitional sediments, younger than the Eocene and older than the Quaternary. The most frequent lithological types are sandy limestone, marls, chalky limestones with subordinate sandstone and clay. Due to the depositional environments, both lateral and vertical changes are frequent and rapid.

The Neogene series has been subdivided from the base upwards into the following formations:

- Hadruk formation (Th). It is composed principally of white, grey and pink silty-calcareous sandstones, with sandy limestone and sandy marl.
- Dam formation (Td). It is pink marls with intercalations of red and green clays, sandstones, chalky and coquina limestons.

Hofuf formation (Thf). It is sandy cream and white marl, with subordinate tan rubbly sandy limestone and chalky limestones. In certain areas, gravel, conglomerate, and sand are present near the base.

2.3.3 Unconsolidated sedimentary materials

Several low basins are floored with thin but extensive layers of gravel representing concentrations of coarse debris from the surrounding area, residual material derived from older sediment or rock by removal of intergranular fines, and lag concentrations from earlier gravel deposits (Qg1). They may consist of mixed limestone and quartz pebbles along with quartz and other pebbles derived from the basement complex (Qg2).

2.3.3 Silt and gravel

Silt and associated fine sediments including caliche-like and gypsiferous deposits in undrained depression (Qs); gravel composed chiefly of limestone and other gravels in some areas (Qg); unconsolidated surface deposits, sand and gravel; may include unrecognized equivalents of other units of Quaternary age (Qu).

2.3.4 Sabkha deposits

Sabkhas are filled with silt, clay, and muddy sand along with gypsum and anhydrite, and frequently a salty surface covering. They underly coastal and inland playas (Qsb).

2.3.5 Aeolian sands

Large areas, particularly in the south-eastern coastal area covered by aeolian sand deposits (Qes). These include the following types of area:

- Dikakah irrregular surface of bush and grass covered sand.
- Barchan dunes and various undulating sand sheets.

2.4 Soil and landform units

Figures 2.5 and 2.6 show the distribution of soils and landforms units. These units are defined by the United States/Saudi Arabian Joint Commission for Economic Development for the Ministry of Agriculture and Water, Land Management Department (MAW, 1986, 1995).

2.4.1 Alluvial plain

The mapping unit consists of nearly level and gently sloping plains. Small intermittent streams begin and generally terminate within the alluvial plain zone. Drainage nets are not well developed. The Gypsiorthids and similar soils are on linear and convex plains. They are loamy, slightly saline to strongly saline soils (Al-Barrak, 1993; MAW, 1986, 1995).

The Calciorthids are in small depression on linear and concave plains throughout most of the alluvial plains. They are deep, loamy, calcareous, and slightly saline to strongly

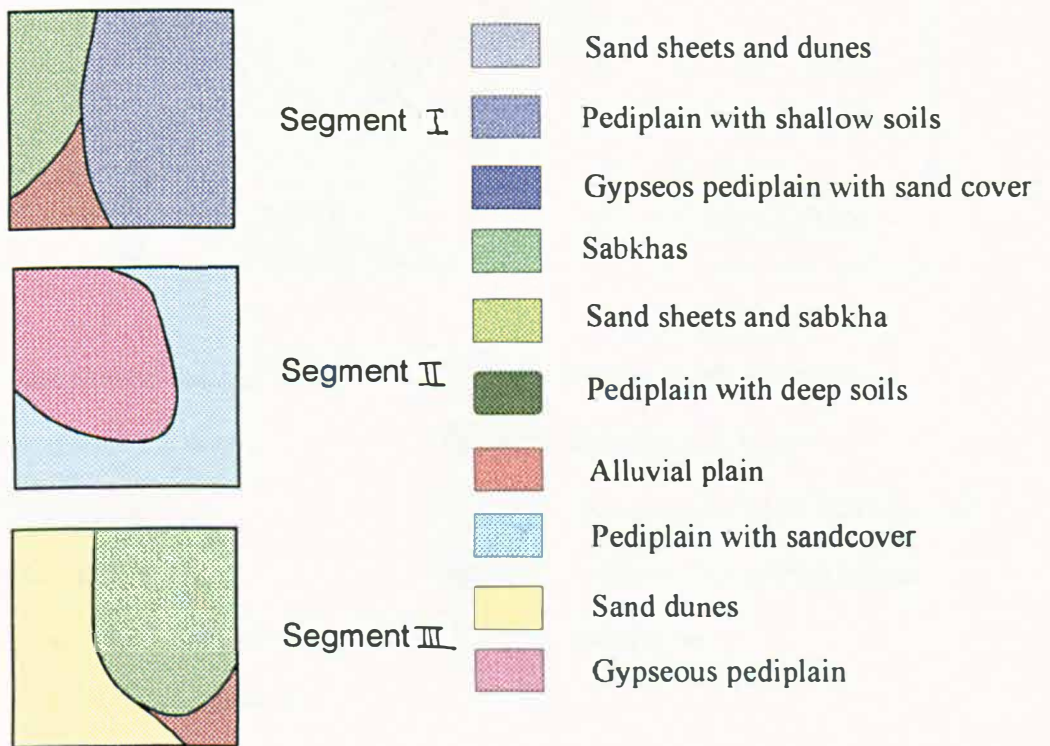
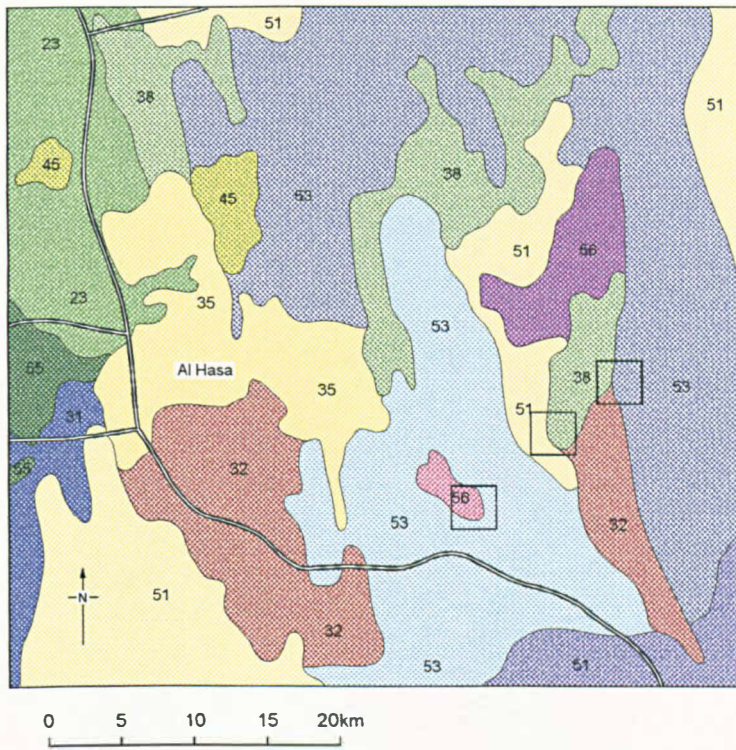


Figure 2.5 General soil map and the locations of test areas (after MAW, 1986)

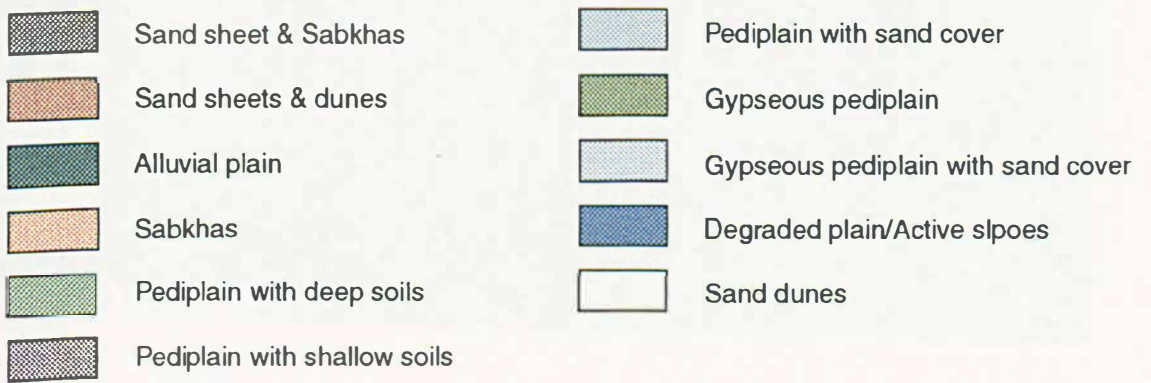
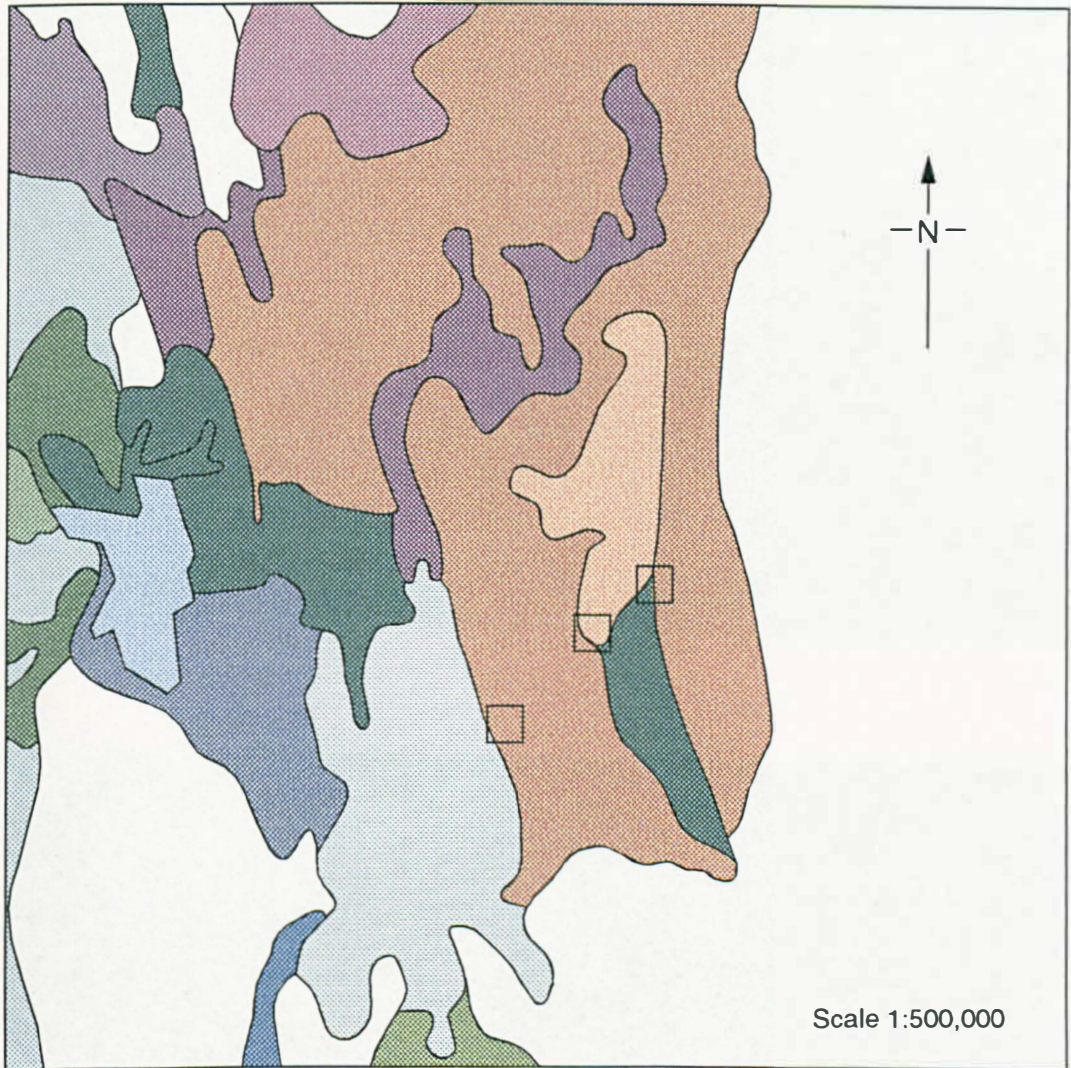


Figure 2.6 General Landform map (after MAW 1995)

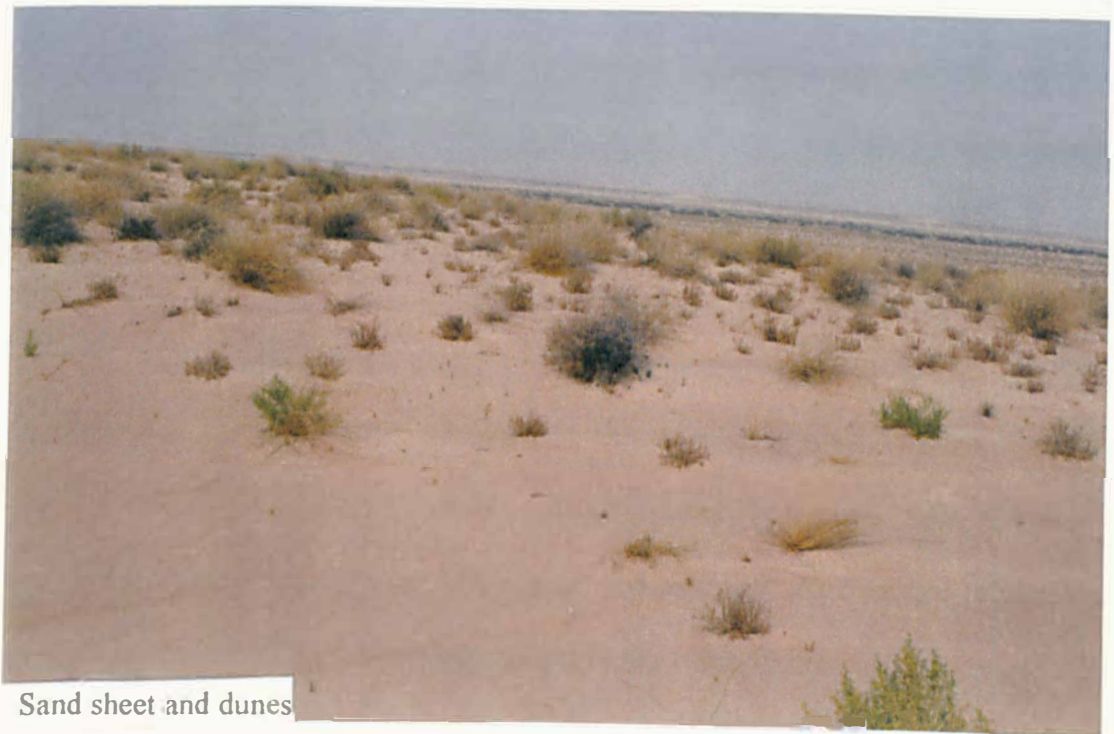


Figure 2.7: Field photograph showing the flat sabkha and the sand sheet and dunes of the study area. (Segment I).

saline soils. There are also intermixed throughout the unit with small areas of very gravel soils (Al-Barrak, 1993; El-Khatib, 1980; MAW, 1986, 1995).

2.4.2 Gypseous pediplain with sand cover

Gypseous pediplain map unit supports of two main types of soils. About 45 percent of the unit consists of shallow Gypsiferous, loamy soil underlain by gypsum pan. These soils are well drained, strongly saline and calcareous. Their permeability is slow; infiltration rate is moderately high; and available water capacity is low. These soils are classified as Gypsiorthids/Petric Gypsisols (MAW, 1986, 1995).

About 30 percent of the unit has moderately deep, loamy soils that are well-drained, strongly saline, slowly permeable and have moderate infiltration rate and low available water capacity. In addition, about 20 percent of the area is occupied by rock outcrops and very shallow soils (Al-Barrak, 1993; El-Khatib, 1980, MAW, 1986, 1995).

2.4.3 Sand sheet and dunes

The map unit of sand sheet consists of gently sloping to steep soils on dunes. The dunes are 2 to 4 meters high and are closely spaced throughout the map unit. There is no evident drainage pattern. Individual areas of this map unit are irregular in shape and range from 3,000 to 40,000 hectares in size (MAW, 1986, 1995).

About 80 percent of the unit are Torripsamments on dunes and 20 percent minor soils and areas of rock outcrop. The Torripsamments and similar soils are on dunes and their slope range from 3 to 60 percent. The steeper soils are on the lee side of the dunes. The Torripsamments are deep, sandy, and non-saline to slightly saline soils. Also, included in this map unit are small areas of nearly level and gently sloping sandy soils in interdunal areas, small areas of loamy soils, soils that have excess gypsum, and moderately saline and strongly saline soils, all of which are in interdunal depressions (El-Khatib 1980, MAW, 1986, 1995).

2.4.4 Sabkha

The Sabkha map unit consists of playas and local basins without a drainage outlet. They receive runoff from the surrounding higher lands and remain wet for most of the time, and are even ponded for short periods after any appreciable rain in the area. The soils are stratified consisting of deep, loamy, or clay, strongly saline material. They contain large crystals of gypsum that occur in thin layers. The water table is high, and the surface, when dry, has a puff or a crust of salts. The soils are classified Salorthids / Gypsic Solonchaks (MAW, 1986, 1995).

2.4.5 Sand dunes

The mapping unit of this zone consists of gently sloping to steep soils on dunes with nearly level and gently sloping soils on plains. The dunes are mostly less than 5 meters high. A drainage pattern is not evident and individual areas of this unit are irregular in

shape and range from about 6,000 to 200,000 hectares in size (El-Khatib, 1980, MAW, 1986, 1995).

This map unit is about 60 percent Torripsamments on dunes, 30 percent Gypsiorthids, and 10 percent minor soils. The Torripsamments and Gypsiorthids are intricately mixed. The Torripsamments and similar soils are on dunes, and the steeper soils are on the lee side of dunes; the soils are deep, sandy, non-saline to slightly saline soils. Permeability is rapid and the water retention difference is moderately low (MAW, 1986, 1995).

The Gypsiorthids and similar soils are on plains between dunes. They are loamy, strongly saline soils and very shallow and shallow to a layer cemented by crystalline gypsum. Also included in this map unit are nearly level and gently sloping sandy soils in small-scattered interdunal areas (MAW, 1986, 1995).

2.5 A brief review of soil reflectance factors

Arid lands are ideal for spectral remote sensing of soils due to the lack of vegetation and the favourable exposure of surface. Spectral reflectance curves from most soil materials are generally less complex in appearance than those from vegetation (Asrar, 1989; El-Baz, 1984; Swain and Davis, 1978). Figure 2.8, for example, shows typical spectral reflectance curves for clay and sandy soils. As this curve indicates, one of the most outstanding reflectance characteristics of these soils is a generally increasing level of reflectance with increasing wavelength, particularly in the visible and near-infrared

portions of the spectrum. However, the effects of variations in water holding capacity affect this trend in the moisture sensitive near infrared (Swain and Davis, 1978). Texture, moisture content, organic matter, and iron oxide control soil spectral properties.

2.5.1 Soil texture, water content, and surface roughness effects

Soil texture is perhaps the main criterion used in classifying soils. The term soil texture basically refers to the relative proportions of clay, silt, and sand particles in a mass of soil (Kahle, 1984; Asrar, 1989; Belward and Valenzuela, 1991; Barrett and Curt, 1992; Lillesand and Kiefer, 1994). Two of the most widely used systems of soil classification based on size of constituent particles are given in table 2.1.

Table 2.1: Particle size classes most widely adopted internationally (after White, 1997).

Soil Particle Size (mm)		
Soil Name	Engineering Definition	Agricultural Soil Science Definition
Gravel	2.0 - 76.2	2.0 - 76.2
Sand	0.074 - 2.0	0.05 - 2.0
Silt	0.005 - 0.74	0.002 - 0.05
Clay	Below 0.005	Below 0.002

In general, as the moisture content of soil increases, the reflectance decreases particularly in the water absorption bands. This would be attributed, of course, to fact that the incoming radiation is strongly absorbed by water in specific wavebands irrespective of the material containing the water (Hunt and Salisbury, 1970, Kahle, 1984).

The water absorption bands around 1.4 and 1.9 μm relate to the fundamental vibration frequencies of water molecules in the soil. Generally, the decreased reflectance in the water absorption bands causes a decreased reflectance in the wavelengths between the water absorption bands (Swain and Davis, 1978; Asrar, 1989; Belward and Valenzuela, 1991).

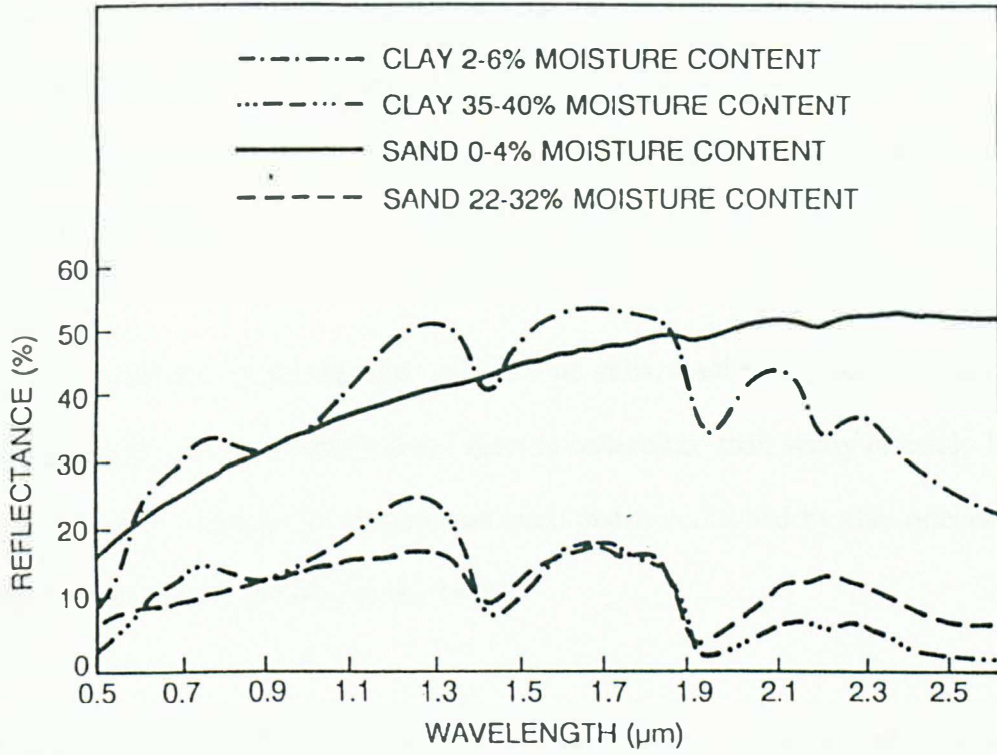


Figure 2.8: Spectral reflectance curves for bare soil (after Belward and Valenzuela, 1991).

Figure 2.9 shows the different percentage of moisture content in silty loam soil, indicating the greatest effect in the water absorption bands at 1.4 and 1.9 μm . This would be attributed to the strong relationship between soil texture and water content, for instance, the relative proportions of sand, silt, and clay do indeed affected the movement of air and water through a soil (Swain and Davis, 1978; Asrar, 1989; Belward and Valenzuela, 1991).

On the contrary, some spectral response of soils, kaolinitic ones for example, that contain finer particles exhibit lower spectral reflectance than sandy or sandy loam soils owing to the absorption of infrared radiation that is controlled by clay minerals (Kahle, 1984; Asrar, 1989; Whalley *et al.*, 1991).

In addition to the effect of water content on soil, there is also a great effect of soil texture on surface roughness. For instance, small particle size produces smooth soil surfaces, which have high levels of reflectance (Belward and Valenzuela, 1991). In short, if the particle size decreases, the soil surface becomes smoother and more incoming energy is reflected. Whalley *et al.* (1991) showed in detail that the reflectance increased with decreased particle size. Reflectance also decreased exponentially with increase in water content for sand and sandy loam soils. However, the values of reflectance of clayey soil or soils containing finer particles were less than those of sand or sandy loam soil. This was attributed to the absorption of infrared light by clayey minerals, such as Kaolinite.

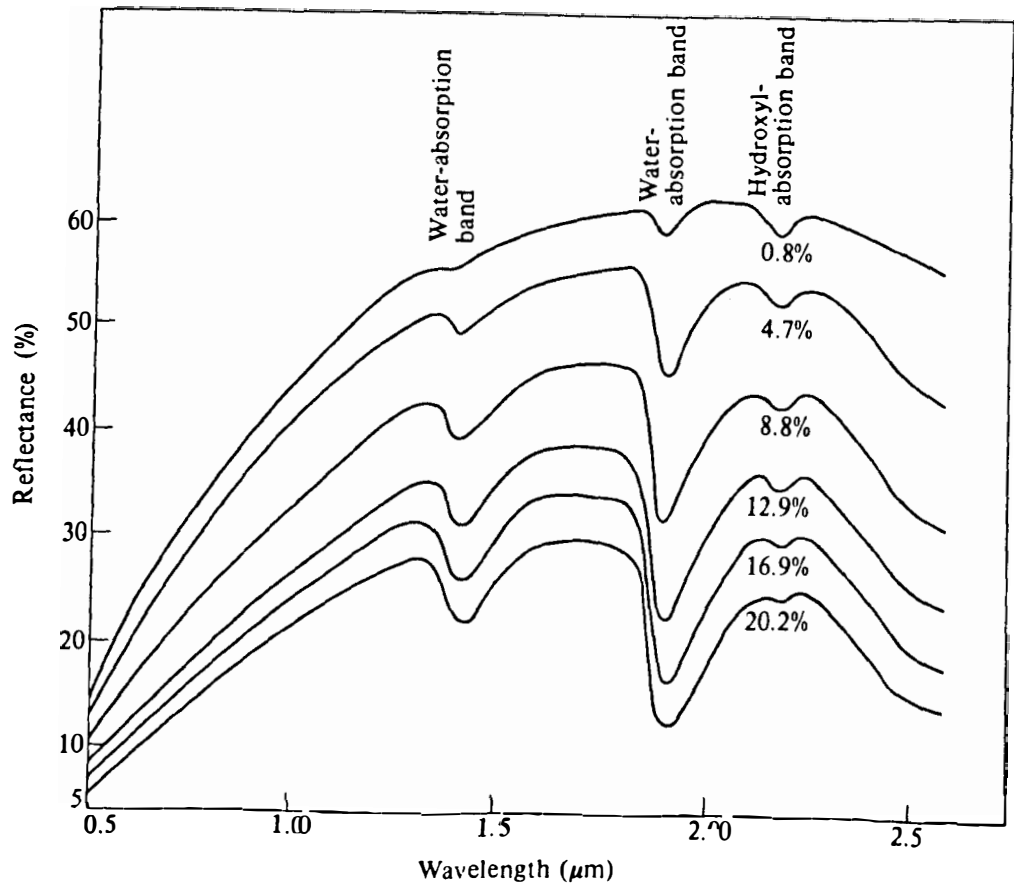


Figure 2.9. Spectral reflectance curves for silty loam soil at various moisture contents (after Hoffer, 1978).

2.5.2 Tone and Colour

Tone is an important parameter in image interpretation; it is a measure of the relative brightness or colour of an object. The relative image tones can be differentiated between the various physical ground attributes such as low and higher ground. For instance, in the drainage conditions, higher ground is generally drier with lighter tones whilst the lower ground is wetter with darker tones (Campbell, 1996).

2.5.3 Mineral content

The inorganic component of most consists primarily of crystalline minerals, with appreciable amount of non-crystalline materials (Jackson *et al.*, 1986). Soil minerals are derived from weathered rocks. These minerals are classified into primary and secondary minerals, depending on the type of weathering. Primary minerals are embodied into soils when rocks disintegrate as a result of mechanical weathering. The chemical weathering of primary minerals creates secondary minerals. The reflectance properties of soil minerals are affected by isomorphous substitution within some of these minerals and by their impurities. Isomorphous substitution occurs when different atoms occupy the same site within a crystal lattice of clay minerals. An example of this phenomenon is the mineral pyroxene. Some clay minerals, which are members of the same isomorphous series is also a factor in determining soil reflectance. Minerals in nature are rarely pure, since trace elements are often trapped in crystal lattice during crystallisation. These impurities affect the colour and other reflectance properties of minerals (Hunt and Salisbury, 1970).

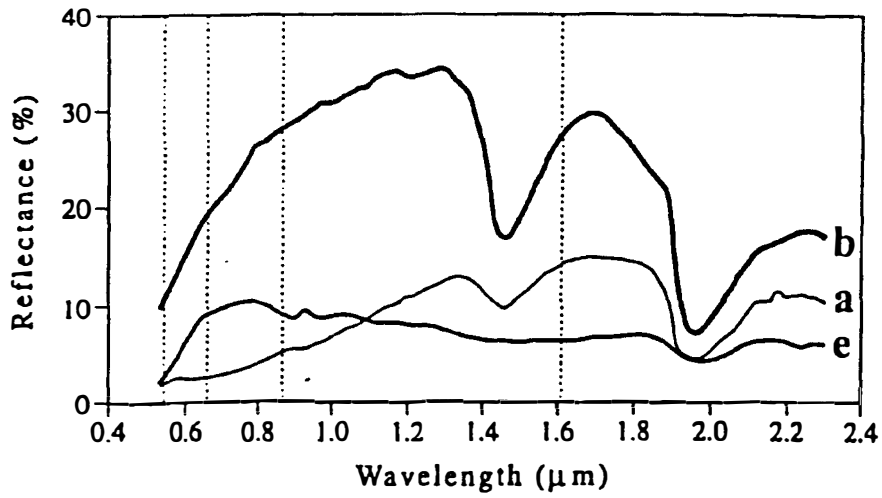


Figure 2.10: Spectral reflectance of three soil types; namely (a) organic-dominated. (b) minimally altered (c) iron-dominated (after Stoner and Baumgradenr, 1981).

The most abundant products of chemical weathering are clay minerals and oxides of iron, aluminium, silicon and titanium. The process also produces carbonates, sulphate, and phosphates. These minerals tend to be stable in soil, as long as the environmental conditions permit. Therefore, elemental composition is another factor in determining soil reflectance (Hunt and Salisbury, 1970).

Unsatisfied valences occur on the surfaces and at the edges of clay mineral particles. The exposed oxygen and hydroxyls of the silica and alumina sheets act as negatively charged sites, and these sites attract hydrogen ions. The hydroxyl groups formed at the edge of clay particles cause specific absorption features in the soil reflectance curves (Hunt and Salisbury, 1970).

One of a significant factor that influences the spectral reflectance characteristics of soil is iron oxide. This is attributed to the red colours of many soils that contain unhydrated iron oxide. However, not only the iron oxide determines redness, but also a combination of manganese dioxide as well as partially hydrated iron oxide (Hunt and Salisbury, 1971a, b, and c). Therefore, a significant decrease in reflectance is based on the amount of iron oxide in a soil. In general, lower iron oxide content is associated with greater reflectance in the visible region. Figure 2.10 shows that the iron oxide content of the soil can cause a difference in reflectance of as much as 40 percent (Hunt and Salisbury, 1971a, b, and c).

Crystalline particles of both primary and secondary minerals are often coated with non-crystalline substances in soils, which consist of organic and inorganic materials. These particle coating substances often serve as cementing agents that bind particles into aggregates. Soil reflectance is therefore affected by both particle coating and by aggregation (Irons *et al.*, 1989)

2.5.4 Organic matter content

The soil organic matter content is another property that significantly influences the reflectance characteristics of soil. Organic matter is composed of a) nonhumic substances such as carbohydrates, proteins, peptides, aminoacides, fats, waxes, resins, and pigments, and b) humic substances, being humic acids, fulvic acids, and humins. In general, the higher the percentage of organic matter contents in a soil, the lower levels of spectral reflectance will be (Figure 2.11). The most affected part of the electromagnetic spectrum is the wave bands in the visible part of the spectrum (Swain and Davis, 1978; Asrar, 1989; Belward and Valenzuela, 1991).

In colour remote sensing images, areas of high organic matter content usually appear dark. Moreover, soils that have a low amount of organic matter content tend to reflect more light and sometimes appear as light brown or grey in colour. However, soils that have developed under different climatic conditions may not show the same relationship between colour and organic matter content (Asrar, 1989; Belward and Valenzuela, 1991).

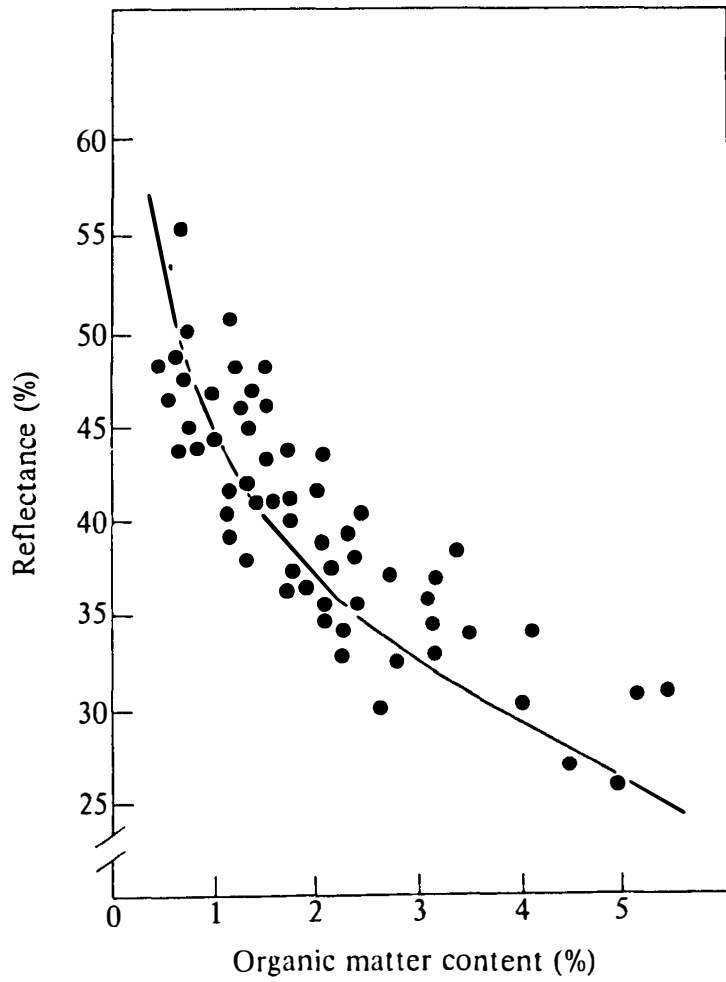


Figure 2.11: Relationship between organic matter and reflectance (after Hoffer, 1978).

In general, as would be expected, a dark soil area which exhibits no inverting between the reflective and thermal portions of the spectrum, is evidence of a relatively moist soil. Any areas that exhibit light in both the reflective and the thermal portions of the spectrum are evidence of a relatively light-coloured, dry soil. And, any area which is dark in the reflective portion but light in the thermal portion of spectrum, might be due to a high percentage of organic matter content, or be evidence of a relatively dry soil.

2.5.5 Pattern

The pattern is an important parameter in image interpretation. It refers to the spatial arrangement of objects. The pattern can be formed by different object elements, such as rock or drainage type. A specific description can be used for different types of a pattern (i.e. in drainage pattern such as linear, radial, rectangular, concentric). Pattern depends as a whole on scale, where a unit, which may form a pattern on a large scale, may have to be described under a textural term on small-scale images (Campbell, 1996).

Table 2.2: Summary of landform unit, soil type, and reflectance properties.

Landform unit	Soil type	Reflectance properties
Sabkha	Salorthid / Gypsic solochk	Low in dry and crust, medium low in dry, very low in wet
Alluvial plain	Gypsiorthid / Calciorthid	Medium, medium low in moister content
Sand sheet and dunes	Torripsammet	High in dunes, medium in interdunal
Gypseous pediplain	Gypsiorthid / Petric Gypsisls	Medium, medium high with minerals

2.6 Conclusion

It is possible to specify how particular soil properties influence the wavelengths and amounts of reflectance radiation. Reflectance from soils is a compound effect of its various constituents. Net reflectance may not easily be interpretable in terms of reflectance from soil constituents. Measured reflectance by satellite sensors introduces their effects due to radiance mixing, and non-direct reflectance. However, it has been demonstrated repeatedly (Barret and Curtis, 1992; Campbell, 1996) that soil properties and types can be distinguished by satellite remote sensing. This thesis assumes, therefore, that soil properties either simple or compound, can be distinguished by satellite remote sensing.

In the next chapter, the research methodology including selection of study sites together with data processing will be described.

CHAPTER 3

RESEARCH DESIGN AND DATA PROCESSING STRATEGY

3.1 Introduction

The principal use of remote sensing in soil studies and soil mapping is in discriminating and mapping different soil landscape units. The allocation of a soil type to a unit of land is a fundamental problem of soil mapping, for which conventional field survey is used sometimes in combination with remote sensing. Since soil types are normally determined a priori then the classification of remotely sensed images is by hard classification techniques only. If the soil types are reasonably discrete and mutually exclusive and thus separable by sharp boundaries, then such techniques can be successful. Unfortunately soil landscapes are always continuous and often have no clear boundaries. Therefore, humans visually interpret remotely sensed data by synergistically taking into account context, edges, texture, and tonal variation or colour.

Most digital image processing classification algorithms such as hard and soft classifiers or even linear mixed models, based on the use of the spectral tonal information, are used to derive image maps on the assumption of existing mappable units. With both visual and digital mapping techniques, complexity is a problem, and neither uses any measures of complexity.

However, other measures are available, which do not assume units. They measure spectral properties of complex patterns. Three methods were selected (Fast Fourier transform (FFT), Artificial neural network (ANN), and Fractal and Multifractal) from what was known of those available. In none is there any prior assumption about the existence of units. The three methods are chosen in order to explore mathematical relations and to find out more about complex structures by examining different aspects of complexity. These techniques were applied to three test areas (described in chapter 2) which have an assemblage of different soil landforms exposed in relatively small areas of eastern Saudi Arabia and an absence of vegetation cover. This chapter describes the method for establishing the working procedures and for subsequently assessing their utility for mapping soil landscapes.

This chapter is divided into two main sections. The first section describes the methodology and research design that was followed to establish the techniques. The second section describes the method of data processing undertaken in each area to assess the utility of the techniques.

3.2 Spectral Analysis Technique

Spectral analysis was based on the Fast Fourier Transform (FFT) technique. This routine of FFT when applied to an image is to transfer it from the spatial domain to frequency domain, where the frequency components can be manipulated (Mather, 1987; Jensen, 1996).

The spectral image processing technique developed in this study for the enhancement of spectral and textural features is basically an extension of the general FFT filtering procedures used in image processing (Pratt, 1978; Mather, 1987; Jensen, 1996). Image filtering using predefined operators such as compass gradient, line filtering or Laplacian masks are useful for the enhancement of general spatial or directional features (Pratt, 1978). However, if feature size is to be taken into consideration, then special convolution operators are required. Gonzalez and Waintz (1987) stated that frequency domain filtering techniques allow filtering functions to be more conveniently specified. Masks in the frequency domain act as spatial frequency filters in the spatial domain. Which is related by inverse transform from the Fourier transform.

FFT displayed as a 2D plot or image of points, which shows variance components. This is best viewed as a radial plot with distance related to frequency and angle related to angular direction of the frequency. Specific spatial frequencies correspond to rings around the centre and specific frequency bands to donut shaped areas.

Using conventional image masking techniques both a kernel and donut shaped masks can be defined to cover parts of the FFT image (the user must consider the low frequencies, in order to avoid artefact output image, see figure 3.1). These masks can then be used to retain or exclude parts of the FFT and hence to retain or exclude specific spatial frequencies. The resulting spatial frequencies are then reconstituted using the inverse FFT. The resulting images are images of the spatial frequency components of

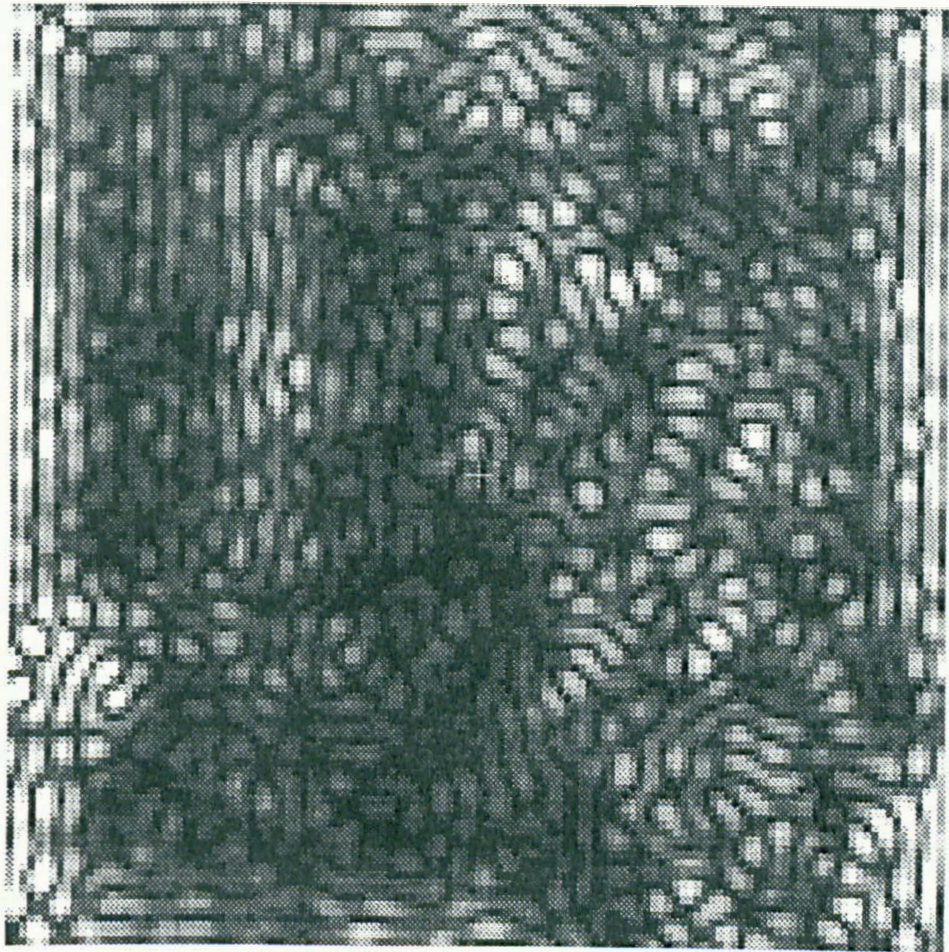


Figure 3.1 A filtered inverse FFT image of Band 7 showing an artefact features when the low frequency blocked out.

reflectance. The first research problem is to establish the location of the donut areas in the FFT and hence the spatial frequencies.

The Fast Fourier Transform analysis output produced images in which it was difficult to distinguish and to identify complex elements from raw data. It was necessary to apply conventional enhancement techniques in order to establish a displaying system for examining results. Enhancement techniques used are described in chapter 5. Since it was not possible, *a priori* to know which elements of images were important, a range of enhancement techniques were employed which exposed and emphasised different image elements. The effects of these techniques are described by figure 3.2.

- PCT: One of the method producing a hard-copy remote sensing brightness map is to output a density-sliced map to a screen or printer. Density slicing refers to the conversion of continues tone of an image into a series of discrete class interval corresponds to a specific brightness value range.
- Infrequency: Another method to produce a hard-copy, which is basically a histogram inversion. This method can produce the image in which the bright pixels represent those grey levels in the original image, which were infrequent.
- Unsupervised fuzzy k -means: It is an unsupervised soft classifier that considers each pixel in a fuzzy classification has m membership grade values. The intensity of a pixel in each band is proportional to the degree of membership of that pixel to the corresponding cluster output.

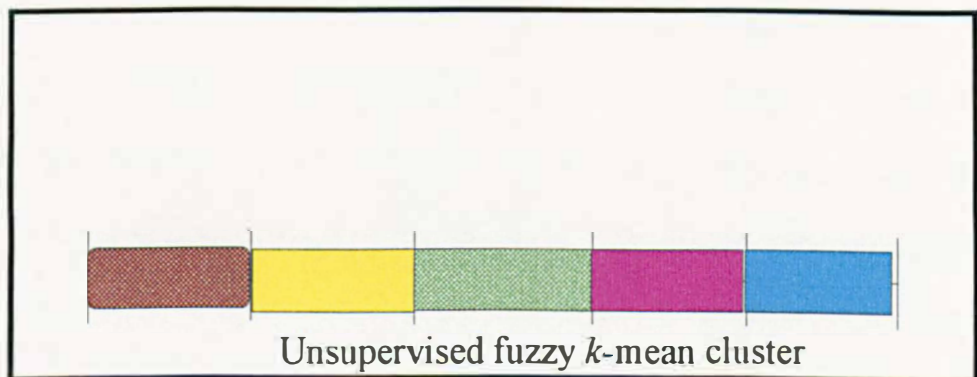
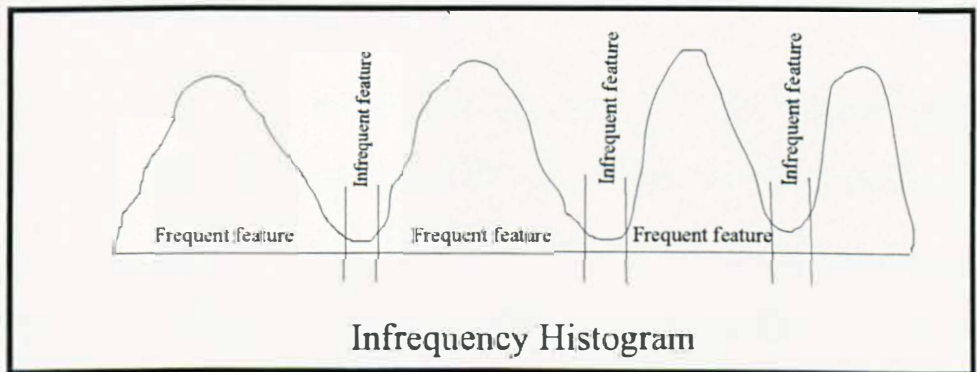
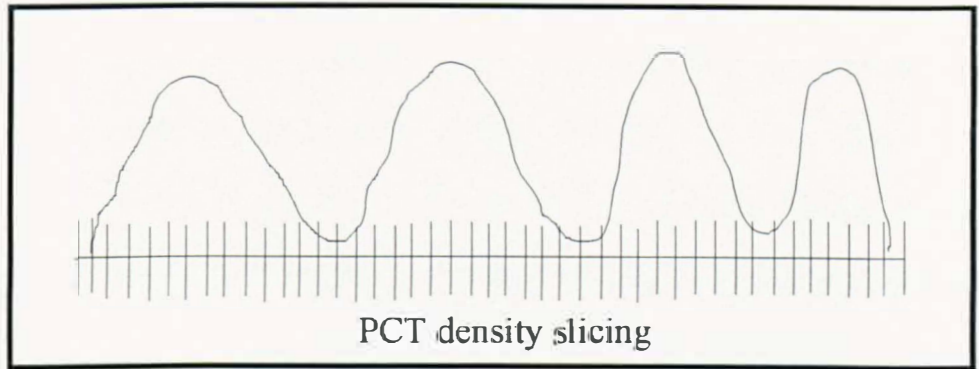


Figure 3.2: Illustration of the displaying methods (PCT, Infrequency, Unsupervised fuzzy k -means cluster).

3.3 The Artificial Neural Network Technique

Artificial Neural Network (ANN) models have been used widely for classifying land cover/land use in remotely sensed data (Campbell, 1996; Jensen, 1996, Mather *et al.*, 1998). Such models are not known to have been used for identifying complex elements of soil landscapes. ANN models have showed limited success in other areas of feature recognition in a variety of application areas (Heddi and Petch, 1998; Clark and Boyce, 1999).

Before describing the ANN technique and the approach to the research problem developed in this project the neural net model is described. The basic element of a network is the processing node. Each processing node mimics the biological neurone and performs two functions. First it sums the values of its inputs. This sum is passed through an arbitrary activation function to produce the node's output value. The processing nodes are organised into layers, each generally interconnected to the following layer. There are no interconnections within a layer, however. In addition, there is an input layer that serves as a distribution structure for data being presented to the network. No processing is done at this layer. One or more actual processing layers follow the input layer. Any layers in between the input and output layers are termed hidden layers. Figure 3.3 shows the network structure that being implemented in this investigation, which is the basic three layers neural network. The interconnections between each node have an associated weight. When a value is passed down that

interconnection, it is multiplied by the weight. These weight values contain the distributed learned information of the network.

As described in chapter 5, there are many algorithms for processing the artificial neural network analysis. One of the most widely used algorithms is the backpropagation algorithm, which was used in this investigation. Backpropagation is an iterative, gradient training procedure. The training data consists of a pair of data vectors. The input data vector is the pattern to be learned and the desired output vector is the set of output values that should be produced by the network upon recall of the input training pattern. The goal of the training is to minimise the overall error between the desired and actual outputs of the network. Backpropagation methods have been used in this study.

The ANN architecture has proven to be robust and flexible and has been used widely in image processing for image classification (recent studies e.g Mather *et al.*, 1998; Foody and Boyd, 1999; Kavzoglu and Mather, 1999). As with other classification techniques, the quality of output is controlled by the set-up training sites.

However, the interesting possibility for using these networks is that, while performing some form of feature extraction the training mechanism adapts the weight sets in such a way that elements shape of image features are recognised. This capacity for feature recognition was used here to model and map textural elements of images.

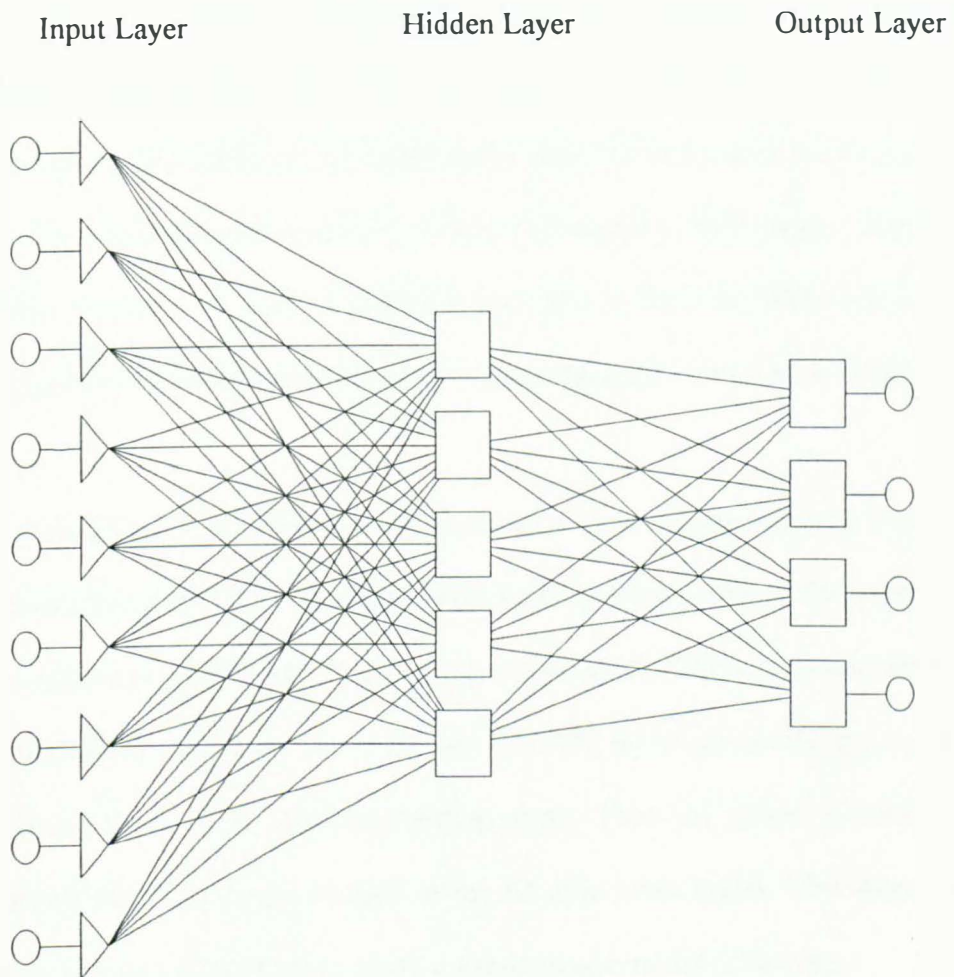


Figure 3.3 Neural network structure for 3×3 window of pixels values.

Texture is a complex element of soil images. That is texture is the aggregate of unit features that may be too small to be discerned individually on an image. When the scale of an image is reduced, the texture becomes progressively finer and ultimately disappears. Consequently, texture is important on large scales or full resolution images where it can help to differentiate between features of similar reflectance, such as smooth texture of sandy alluvial materials, which will contrast, with rough texture of coarse deposits. Texture is usually random and non-random at different scale. It has superimposed and non-homogenous elements, which have non-linear variation.

In an image the way in which texture is modelled is using the nine pixels around a pixel (i.e. relationship itself) in the inputs layer with the pixel value as the output. The ANN model expresses the relation between a pixel values and its neighbours and as such is a measure, albeit a restricted one, of texture. In ANN, the model is first generated from test data using inputs from selected training areas. Then the model is used to generate predicted values for larger images using the nine input layers. The output images are predicted values of reflectance using a whole image model of texture.

The output image pixel values show differences due to the values of the set of nine pixels around each pixel and due to the texture model/ANN model. In order to show texture effects the output image is divided by the original image. Differences in the resulting image show therefore differences in the extent to which local textures differs from the overall image texture.

Knowing this a strategy can be derived to show how within the limitations of the ANN software available, texture varies across the image. By selective inclusion and exclusion of training areas across parts of the image, the effect of different areas on the whole image texture model can be controlled. The texture patterns in the resulting image can then be examined to see how training area selection affects the texture patterns and features.

Four areas ABCD were used in each image and the following training area selection used.

- ABCD.
- ABC: taking out linear feature training D.
- ABD: taking out training C.
- BCD: taking out A.
- AABCD: adding up another training for A.
- ABBCD: adding up another training for B.
- ABCCD: adding up another training for C.
- ABCDD: adding up another training for linear feature D.

Due to the lack and drawback and limitations of the software that was used to process the neural network analysis, the training sets was tripled using the same co-ordinates, otherwise the system will not run and train the neural network structure for this particular investigation.

Experiment were carried out, using another subset, to ascertain the optimum training set-up whether moving windows or single input image and number of elements to use in the hidden layer. It was found that a 3×3 moving window was most appropriate, and the number of elements in the input layer of the network was 9 elements as images. The number of elements in the hidden layer was 5 elements, and that based on the suggestion of several researchers, that the number of hidden layers and the number of elements per layer affect the performance of neural networks. Therefore, to avoid the network from being static within a localised minima if too many number of elements has been selected, or fewer number of elements would not partition the image properly, the decision of number of elements should be half of input and output elements (Paola and Schowengerdt, 1994; Rau *et al.*, 1994; Bruzzone *et al.*, 1997). The design, structure, and implementation of experimental strategy for neural network analysis are described chapter 5.

3.4 Multifractal Analysis

Many remotely sensed images are difficult to analyze by means of classical image processing tools because they are very complex and irregular. Such shapes are obtained for instance Landsat data with the spatial distribution of surface features, such as geomorphological and geological units. The important information often lies in the texture and not in the contours (Bagnold, 1965). In these environments, classical methods of image analysis such as enhancements techniques, conventional classification, and soft and linear mixed model classification may not reasonably

distinguish complex elements (i.e. soil properties, lithological properties) in the field of satellite image processing. That is why new techniques are needed to extract the features of interest.

Remote sensing of the earth creates a problem of interrelating the characteristics of geophysical fields with those of spatial features observed at different spatial resolutions. Different sampling of irregular 3 dimensions geophysical fields may strongly change their pattern, depending on the pixel size. It is far from being an easy task to try and find some universal distribution the characteristics of which, within certain limits, would be independent of the spatial resolution cell. Therefore, the description of geophysical fields depends closely on the characteristics of the remote sensing system (Clarks, 1986; De Cola, 1989; Lam, 1990; Olsen *et al.*, 1993).

In recent years in part as a response to this problem, the use of fractal geometry in image processing has grown, especially for texture characterisation (Lam *et al.*, 1997, 1998; Quattrochi *et al.*, 1997, 1998). In particular, the fractal dimension employed as descriptor of natural object surfaces has been widely investigated. However, as pointed out by Levy-Vehel (1998), the fractal dimension does not fully characterise textures. To overcome the limitations of the single fractal dimension, fractal geometry has to be extended and multifractal parameters estimated (Levy-Vehel, 1998).

Attempts are now being made to use fractal and multifractal geometry to quantitatively describe complex elements estimated from remotely sensed images. The estimates of these complex elements then can be interpreted in terms of geophysical and geographical parameters (e.g. Levy-Vehel and Berroir, 1991, 1993; Levy-Vehel, 1998; Mather *et al.*, 1998; Emerson *et al.*, 1999; Qiu *et al.*, 1999; Heddi *et al.*, 1999).

The Multifractal technique provides a stable and reliable means of identifying features of images. It is primarily designed to compute the fractal dimension for natural surfaces using data from satellite imagery (Levy-Vehel, 1998). The underlying concept of multifractal estimation is not only to measure changes that occur gradually for the majority of land surface but also to measure minor changes within the majority of land surface that should be considered as a complexity.

Data sets from test segments I, II, and III with size 128×128 pixels were used to compute the local fractal dimensions for each cell in the matrix array. The local estimate of the fractal dimension is based on:

- Edge detection; this approach uses the initial discrete values and quantifies the local fractal dimension around each cell.
- The segmentation process; this is based on the fact that multifractal exponents respond differently to signals as step edges, lines, or corners.

The edge detection and segmentation of images can be achieved by using the multifractal technique. In order to produce a segmented image, the data sets must be enhanced by pointwise Hoelder exponent capacities. The selected exponent capacities are *MAX*, *ISO*, and *SUM* as suggested by Levy-Vehel (1998) because these exponents are suitable to extract information such as linear features, for instance, from satellite imagery. The pointwise Hoelder exponent capacities depend on the size of the kernel window similar to moving filters. Although the larger size of the kernel window will reduce time computing, the result will not be optimum in terms of presenting and identifying complex features. Therefore, the smaller the size of the kernel window, the better the results especially for complex elements. Multifractal segmentation of images can be achieved by changing parameter values. These parameters are point values of 1 or 2, where spread values are ranging from 0.1 to 0.9. The set-up parameters of multifractal segmentation of this investigation processing are presented in table 6.1 chapter 6. These parameters produce different segmentation images. This means, the larger the number of spread values the more points to trace the edges of data sets imagery, where the small number of spread values, the fewer points to trace the edges.

Then, we use the regularisation dimension. This computes the fractal dimension of images that are expressed as contour zonations, and the local fractal dimension presents individual contour line. The computation of the regular dimension of the image is based on its parameter values. Therefore, the parameter values, which show the number of contour lines to be presented in images, were set-up as 4, 8, 16, 32, 64 lines. These

numbers of lines should show the sensitivity of partitioning in identifying complex features.

3.5 Data Processing Strategies

3.5.1 Test Segments

The best available soil data for large areas is from Landsat satellite imagery of arid zones. In such areas there is little vegetation and soil properties and patterns are easily detected. The study site selected to be examined for the experimental methods of this research is the Al-Ahsa region between the Arabian Gulf and the As Summan Limestone Plateau in the eastern province, Saudi Arabia. The test segments are about 20 Kilometres east of Hofuf City, and about 30 kilometres away from the Arabian Gulf.

The general geomorphology of Alahsa area consists of (i) sand sheets and sabkhas, (ii) alluvial plain, (iii) sand sheets and dunes, (iv) sand dunes, (v) and gypseos pediplain with sand cover (see chapter 2).

3.5.2 Data sources

To perform this study, Satellite imagery is used from the Landsat 5 Thematic Mapper (TM) sensor taken on 28 May 1996 at sun time 6:22:51. The co-ordinates of the image centre are $25^{\circ} 40'$ for the latitude and $49^{\circ} 51'$ for the longitude. The TM sensor records seven bands of the region of the visible and infrared electromagnetic spectrum (see table 3.1). The subset of Landsat imagery was used to represent the selected test

segments. This subset consisted of 1024×1024 pixels, which represents about 30 km x 30 km on the ground.

Satellite TM image bands 4 and 7 were used for this investigation and the selection was based on two procedures. The statistical investigation, which was the first procedure, was based on an examination of the scatter plot of TM bands to find two bands that would contain the most information (figure 3.4). The visual inspection was based on comparison of each stretched TM band, first as grey level images, and then as colour composites of three bands. The factor governing this assessment was the ability of individual bands to distinguish between different landforms depicted on the general soil map (1:250,000) land resources map (1:500,000), topographic map (1:50,000 and 1:250,000), and geologic map (1:500,000) of the test area, bearing in mind the spectral reflectance characteristics of different soil landscape.

Using the latter procedure, it was evident that the best three band colour composite that offered the best discrimination between various soil-landscape for the three test segments was TM band 7 displayed as red; TM 4 displayed as green; and TM band 1 displayed as blue.

3.5.3 Image Processing

The EASI/PACE version 6.2 image-processing package was used for the creation of the Band-pass filters and for processing the original data as well as the transformed image

data sets. The EASI/PACE package has implemented on an IBM PC/Pentium Pro compatible. The EASI/PACE module Imageworks was used to produce and create the Band-pass filters for each data set using Graphic command parameters. The image enhancement techniques such as PCT, histogram inversion, and unsupervised fuzzy k -means-clustering algorithm were applied to the various image data sets. All of these methods were carried out by EASI/PACE 6.2 image processing package.

The ANN modelling was also carried out using EASI/PACE image processing software. The neural network NN module is a back propagation method, which was used to carry out the model design in order to (i) create the network architecture model, (ii) training, and (iii) running supervised neural network classifier (iv) producing hard copy image by using linear contrast stretch enhancement.

A Signal processing software package called Fraclab from INRA France was used to compute the fractal dimension values of bands 4 and 7. The Fraclab is designed to run on Matlab platforms to provide specialised spatial analytical functions for characterising signal processing and digital image processing such as remotely sensed data.

Band	Bandwidth (μm)	IFOV(m)	Quantization (bits)	Principal applications
1	0.45-0.52	30×30	8	Designed for water-body penetration, Coastal-water mapping, Soil and Vegetation discrimination, Forest mapping, Cultural feature identification.
2	0.52-0.60	30×30	8	Designed for green reflectance peak for vegetation discrimination and vigour assessment, Useful for cultural feature identification
3	0.63-0.69	30×30	8	Chlorophyll absorption for plant for plant species differentiation.
4	0.76-0.90	30×30	8	Useful for determining vegetation types, water bodies, spring lines and drainage network morphometry. Geobotanical studies.
5	1.55-1.75	30×30	8	Useful for vegetation moisture content and soil moisture content, snow/cloud differentiation.
6	10.4-12.5	120×120	8	Useful in thermal mapping of sediments, Lithological mapping, ground water studies, topographic mapping and extraction of subsurface anomalies, Discrimination of siliceous rocks.
7	2.08-2.35	30×30	8	Useful for discrimination of metamorphic rocks, hydrous mineral and carbonates separation, Hydrothermal alteration.

Table 3.1: Characteristics of Landsat TM system (adapted from Jensen, 1996).

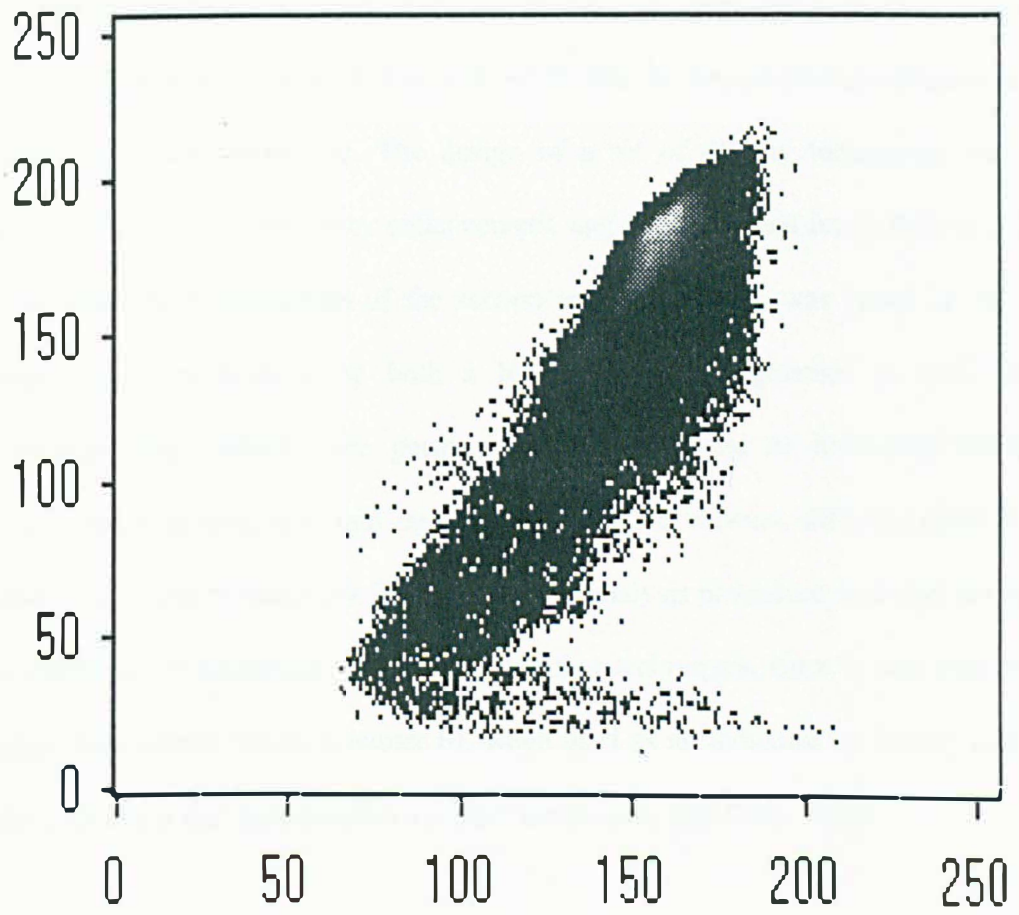


Figure 3.4 Scatter plot of Band 7 against Band 4.

3.6 Summary

Different methods of processing techniques were described in this chapter. These methods include the spectral analysis technique which is based on the spatial filtering; emphasising or de-emphasising certain frequency components of an image for investigating the best frequency components that represent the data sets, that were performed only on a single band (bands 4 and 7). This technique produced images using inverse fast Fourier transform. The design of a set of display techniques was also described (e.g. PCT, Infrequency enhancement, and Unsupervised fuzzy k -means). This was followed by a description of the second technique which was based on the feed forward neural network using both a backpropagation algorithm as well as the convolution filter, which were performed on single band or individual bands of multispectral data sets, to obtain the optimum contrast between different objects (e.g. landform units and boundaries). The multifractal analysis procedure was also discussed. This technique is potentially superior to the other techniques, since it was expected to produce the optimal results (chapter 6), when used as an indicator of feature space, or by directly using the segmentation as classified outputs (De Cola, 1989).

Each technique has been used in image processing. However, it is rare for FFT to be applied other than in signal noise extraction and it is used here to try to identify spatial spectral features. ANN is not known to have been used in earth resource analysis other than for conventional classification. Fractal and multifractal analysis similarly are not known to have been used for image segmentation for soil resource mapping.

Image processing technique, however, is not limited to the methods described briefly in this chapter. The content of this chapter is restricted to the digital image processing approach. The details of image analysis are described in chapters 4, 5, and 6.

CHAPTER 4

SPECTRAL ANALYSIS

4.1 Introduction

The spectral analysis chapter is concerned with the application of complex quantitative analysis to remotely sensed data sets as a method of measuring spatial patterns and structures. The principal objective of this part of the study is to assess if and how spectral analysis model can be used for defining patterns of the reflectance properties of soil. Also, the purpose here is to examine how far the patterns can be revealed through a set of image enhancement and visualisation procedures.

4.2 Spatial spectra as a property of images

4.2.1 Spatial filtering

Spatial filtering is a pixel by pixel transformation of an image. The transformation depends not only on the grey levels of the pixel being processed, but also on the grey levels of neighbouring pixels. Consequently, spatial filtering is an operation to alter the grey level of a pixel according to its relationship with the grey levels of other pixels (Jensen, 1997, Richards, 1994; Schowengerdt, 1983; Mather, 1987).

General spatial filters used in image processing of remotely sensed imagery are based on three basic types (i) low pass filter, (ii) high pass filter, and (iii) band pass filter. Figure 4.1 depicted the three basic types of spatial filters. Schowengerdt (1983) stated

that these basic filters might be combined to form a wide variety of more complex filters. In digital remotely sensed imagery, spatial filtering are two-dimensional functions as shown in Figure 4.1.

The effects of low pass and high pass filtering on an image and its histogram are well distinguished. Further substantial details about these filters are given in Hord (1982), Niblack (1986), and Richards (1994). Low-pass filtering smoothes the detail in an image and reduces the grey level range which is the image contrast. On the contrary, the high pass filtering enhances the detail at the expense of large area radiometry and produces an image with relatively narrow histogram centred at zero grey level (Hord, 1982; Jensen, 1997). The histogram of high pass images is virtually always symmetric about mean grey level of zero. As a result, high pass must be contrast stretched to all positive Grey levels for display. Figure 4.2 represents the application of low pass and high pass filtering of Landsat imagery.

The primary use of band pass filter is for eliminating periodic noise from an image. This type of filter can be constructed in a similar way as previous filter, although band pass filters have not had general application in image processing of remotely sensed imagery, (Jensen, 1997; Schowengerdt, 1983; Sonka *et al.*, 1994). The next section is the advanced spatial filtering, which will be described thoroughly, and is known as Fast Fourier Transform.

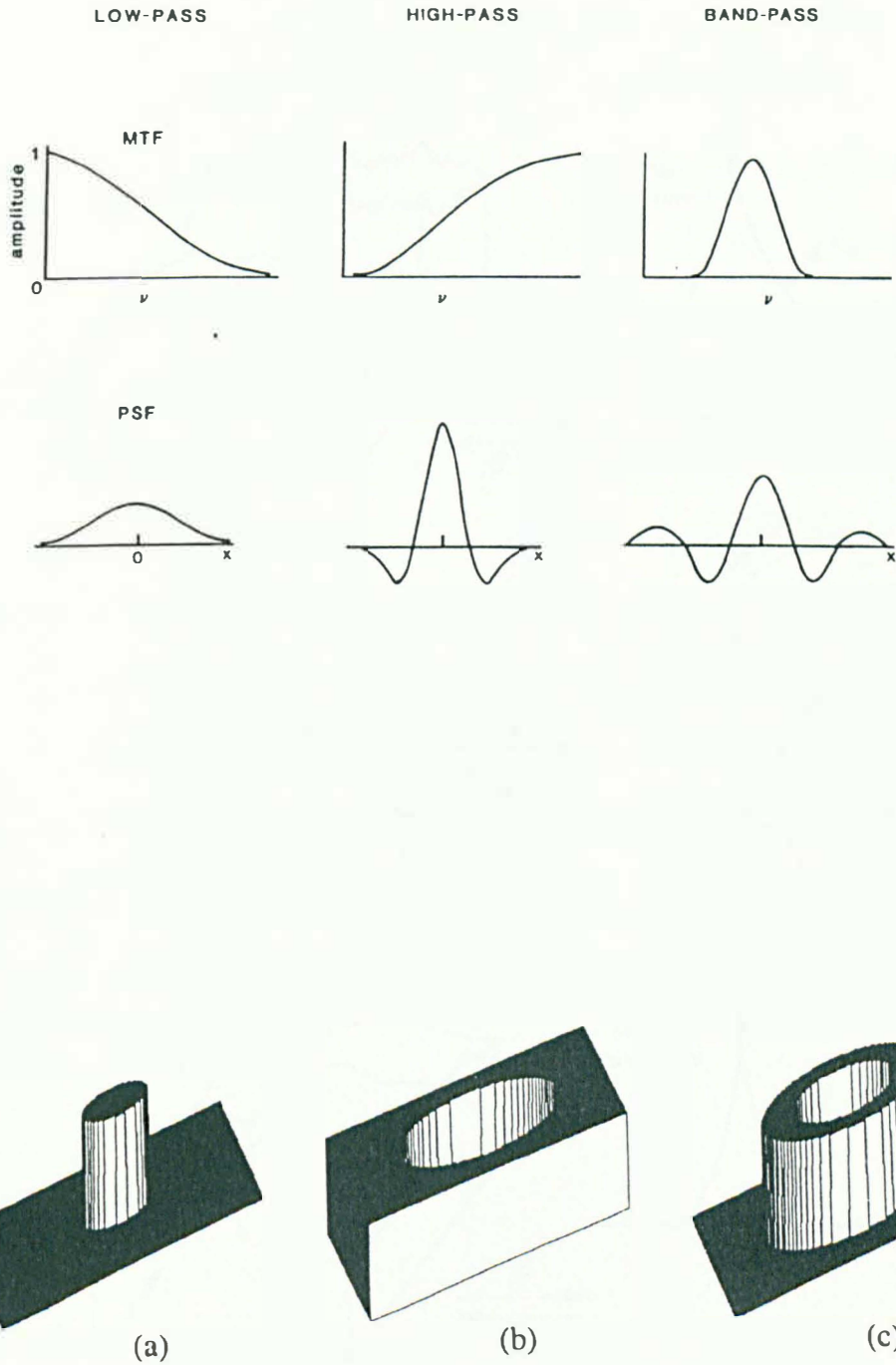


Figure 4.1: The three basic types of spatial filters (above), frequency filters displayed in 3 D representing (a) low-pass filter, (b) high-pass filter, and (c) band-pass filter (down) (after Schowengerdt, 1983 and Sonka, *et al.* 1994).

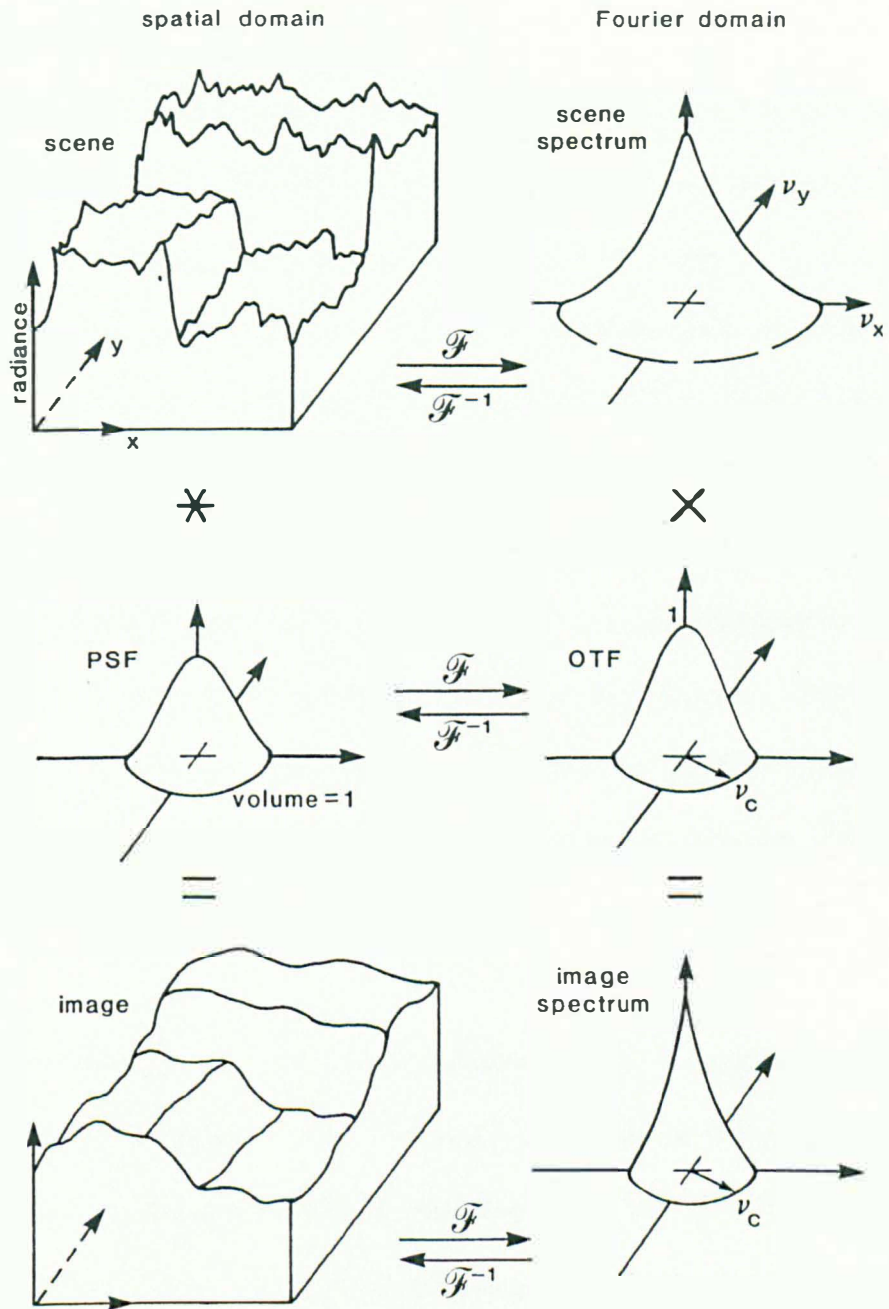


Figure 4.2: Image formation in the spatial and Fourier domains (Schowengerdt, 1983).

4.2.2 Fourier analysis

4.2.2.1 Introduction

Any image can be separated into its various spatial frequency components through application of a quantitative operation called a Fourier transform. This produces a set of sinusoidal waves that in combination represent the original series more or less exactly. The Fourier transform operates on a single band image in order to break down the image into its frequency components (Lillesand and Kiefer, 1994; Mather, 1987; Richards, 1994). The sinusoidal waves with varying amplitudes, frequencies, and directions characterise the scale components of the image (Jensen, 1996; Sonka *et al.*, 1994). The scale components are expressed as a two-dimensional space in which they are given in terms of frequency, which are cycles per basic interval. This is called the frequency domain whereas the normal row and column co-ordinate system in which images are normally expressed is termed the spatial domain (Mather, 1987; Niblack, 1986; Richards, 1994).

In Fourier transform, the grey scale values, forming a single band image, can be viewed as a three dimensional surface. The rows and columns are defining two axes and the grey scale value at each pixel giving the third dimension. Mather (1987) stated that the Fourier transform provides details of (i) the frequency of each of the scale components of the image and (ii) the proportion of information associated with each frequency component. Frequency can be characterised with respect to cycles per basic interval. Where the basic interval in the across-row direction is the number of pixels on the scan

lines, the basic interval in the down column direction is the number of scan lines (Jensen, 1997; Lillesand and Kiefer, 1994; Mather, 1987).

4.2.2.2 Computation of the discrete Fourier Transform

Fourier analysis is a mathematical technique for separating an image into its various spatial frequency components (Jensen, 1996; Watson, 1993). To utilise Fourier analysis in digital image processing of remotely sensed data, the two-dimensional discrete Fourier transform equation must be implemented, which can be defined for a square image as:

$$F(u, v) = \frac{1}{NM} \sum_{x=0}^{N-1} \sum_{y=0}^{M-1} f(x, y) e^{-2\pi i \left(\frac{ux}{N} + \frac{vy}{M} \right)}$$

Where: $F(u, v)$ = frequency spectrum of the original image $f(x, y)$

N = number of pixels in the x direction

M = number of pixels in the y direction

Because every remotely sensed image may be described as a two-dimensional discrete function, this equation may be used to compute the Fourier transform of an image (Niblack, 1986; Sonka *et al.*, 1994). Since the Fourier transform is a reversible process, the image information from the frequency domain can be converted to the spatial domain using an inverse Fourier transform of the form:

$$f(x, y) = \sum_{u=0}^{N-1} \sum_{v=0}^{M-1} F(u, v) e^{2\pi i \left(\frac{ux}{N} + \frac{vy}{M} \right)}$$

When the Fourier Transform is computed, the output will be two images. The first image is the magnitude of the Fourier transform and can be displayed as a two-dimensional image (Niblack, 1986; Sonka, *et al.* 1994). It represents the magnitude and the direction of the different frequency components in the image $f(x, y)$. The other image represents phase information in the image $f(x, y)$. Although we usually ignore the phase information when we display the Fourier transform, we cannot offset the original image without it (Jensen, 1996; Richards, 1994; Watson, 1993). Frequencies, for instance, are along two directions (x and y), the digital value component frequency = (0,0) is at $(M/2+1, M/2+1)$ where M is the image size. On a 1024×1024 image, for example, the digital value should be at (513,513). Points away from the digital value indicate higher frequencies. The transform at point $(M/2+1+x, M/2+1+y)$ corresponds to the cosine wave component which repeats every M/x pixels along x direction and every M/y pixels along y direction (Mather, 1987; Sonka *et al.*, 1994).

4.2.2.3 Fourier transform applications in remote sensing

The idea of using Fast Fourier transformation is based on the ability of utilising frequencies over satellite images whenever an image is transferred from spatial domain into frequency domain. In many remote-sensing images, most of the visually interpretable data in the Fourier transform are contained in the magnitude of the transform images (Jensen, 1996; Gonzalez and Wintz, 1987; Muller, 1988). The Fourier magnitude images are symmetric about their centre (Andres *et al.*, 1994; Hassan, 1988; Olsson and Eklunch 1994; Pratt *et al.*, 1980). Therefore, the intensity at

the centre represents the magnitude of the lowest frequency component. The frequency increases away from the centre and any bright values found in and around the centre indicate that an image is dominated by very low spatial frequencies.

Fourier techniques have been used in image analysis to identify and to eliminate noise effects to identify the components of interference, and as an aid to discovering the sources and identifying potential resolution within the imaging system (Jensen, 1996; Mather, 1987; Richards, 1994; Schott, 1997). Using fast Fourier transform, we can manipulate directly the frequency information of the image. The manipulation can be performed by multiplying the Fourier transform of the original image by a mask image, the frequency domain filter, which will block (or weaken) certain frequency components by eliminating the values of certain parts of the frequency spectrum. Then we compute the inverse Fourier transform of the manipulated frequency spectrum to obtain a filtered image in the spatial domain (Jensen, 1996; Schott, 1997).

Removal of noise from an image first requires identification of the noise either in the spatial image or in the frequency image. Once the noise pattern is identified, there are three methods for noise suppression which are based on (i) blocking (ii) smoothing, (iii) and interpolation. The blocking filter sets selected values of the blocking filter and uses a rounding algorithm based on the sine function (Bracewell, 1986) to taper values at the edges of the filter. The interpolation filter uses values just beyond the edge of the noise

and bilinearly interpolates across the noise pattern. This latter filter is the least intrusive filter and is useful for testing whether a blocking or smoothing filter is necessary.

Selection of an appropriate filter is dependent upon the type of noise present. Several geometric shapes of filters are provided for various types of noise patterns, which are based on point, full line, rectangular, periodic block, wedge, angular harmonic, and ellipse. The ellipse shape filter is used to reduce noise that clusters along either the line or pixel axis in the frequency domain.

According to Stromberg and Farr (1986), any differences between the original and the Fourier spectrum image could be used to aid in classifying features with different texture. In addition, authors described a frequency domain texture classification process that used annular band pass filters to recognise and place apart regions, which contain specific texture patterns. This method was applied to characterise geological textures in a SAR image.

Ehrhard *et al.* (1993) has modified Stromberg and Farr's method to adapt to optical implementation. The modified method constructs a large number of images from information that has been placed apart in the frequency domain by single side band-pass filters. Also this method eliminates the low pass filter required by the Stromberg method, when computing the magnitude of the filtered images. The band pass filtered magnitudes within each band pass are aggregated to create the single image for each

annular band. The statistical classifier is applied over the sets of images for the selected annular bands to identify the unique textural features within an object class. In short, it has been demonstrated that when the Fourier transforms were multiplied by a set of band-pass filters, the inverse transforms could be used as a texture metric images to successfully classify background land cover types using conventional statistical classifiers.

4.3 Data processing for spectral analysis

4.3.1 Strategic investigative procedures

The Image processing technique investigated in this study (Figure 4.3) for the enhancement of spectral and textural features is an extension of the general filtering procedures. Image filtering using predefined operators such as compass gradient, line filtering, or Laplacian masks is useful for the enhancement of general spatial or directional features (Pratt, 1978). However, if feature sizes are to be taken into consideration, then special convolution operators are required. Gonzalez and Wintz (1987) stated that frequency domain filtering techniques allow special filtering functions to be more conveniently specified. Spatial masks for the speed and simplicity of implementation can then approximate the frequency domain filtering functions.

In order to make analysis and interpretation on the transformed images, displaying technique as well as frequency components should be established. It was found that the suitable technique in terms of making interpretation is to use pseudo colour and

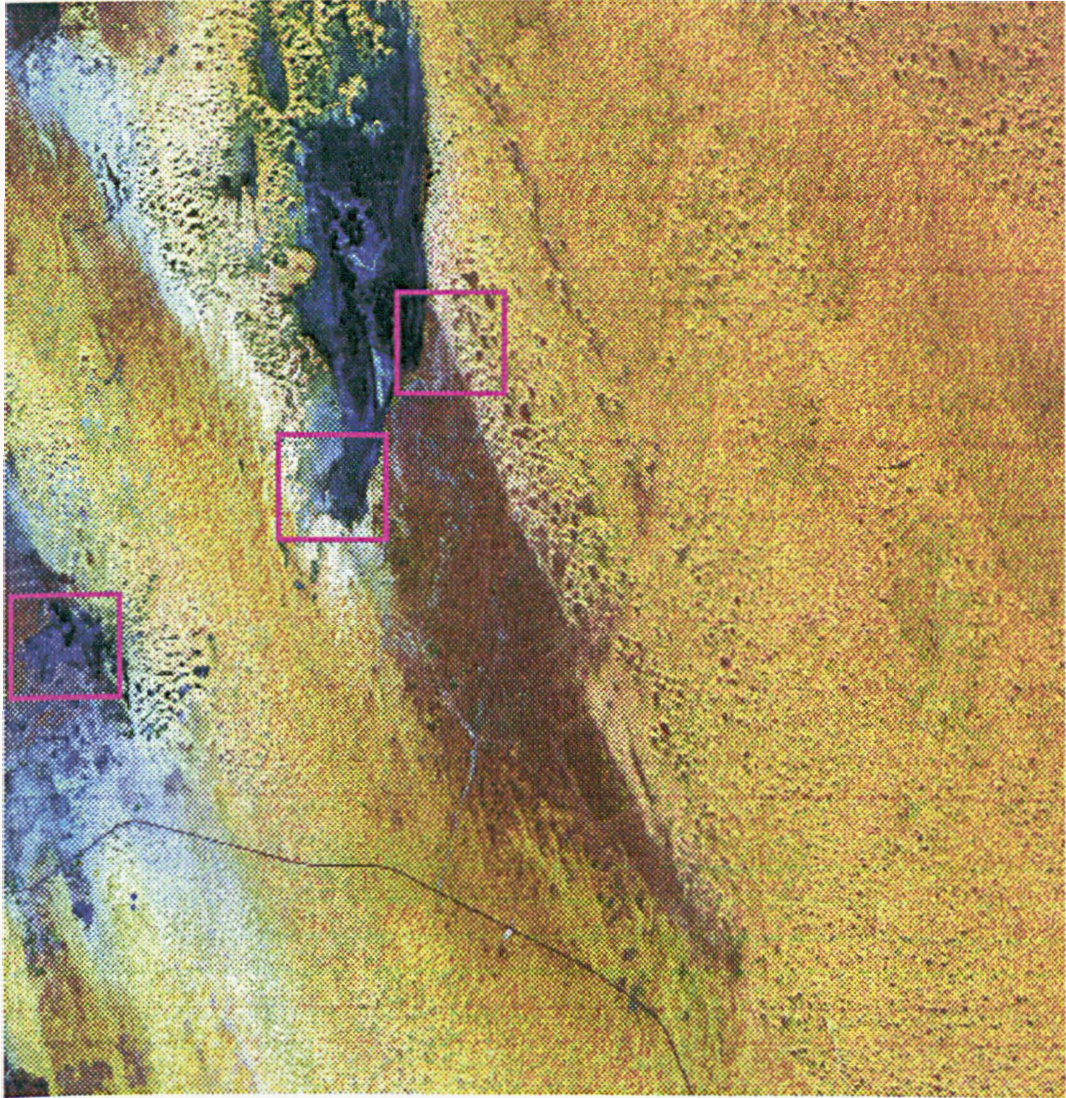


Figure 4.3: A colour composite of Landsat TM imagery of the study area (Band 7, 4, and 1, size 1024 x 1024 pixels).

infrequency techniques (described thoroughly in sections 4.3.2 & 4.3.3 for PCT and section 4.3.3.4 for infrequency)

Removal of frequency from an image first requires identification of the kernel of band-pass filter size, and this procedure (method of trial and error) can be achieved in frequency image by drawing circles from the origin of the magnitude image. Once the kernel filter is identified, the other ring filters can be drawn gradually away from the Kernel filter. The band-pass filters designed are described in table 4.1 and shown in Figure 4.4.

Table 4.1: Masking filters.

Filter	Inner radius Pixels	Outer radius Pixels
Kernel filter	40
First filter	50	60
Second filter	60	70
Third filter	70	80
Fourth filter	80	90
Fifth filter	90	100

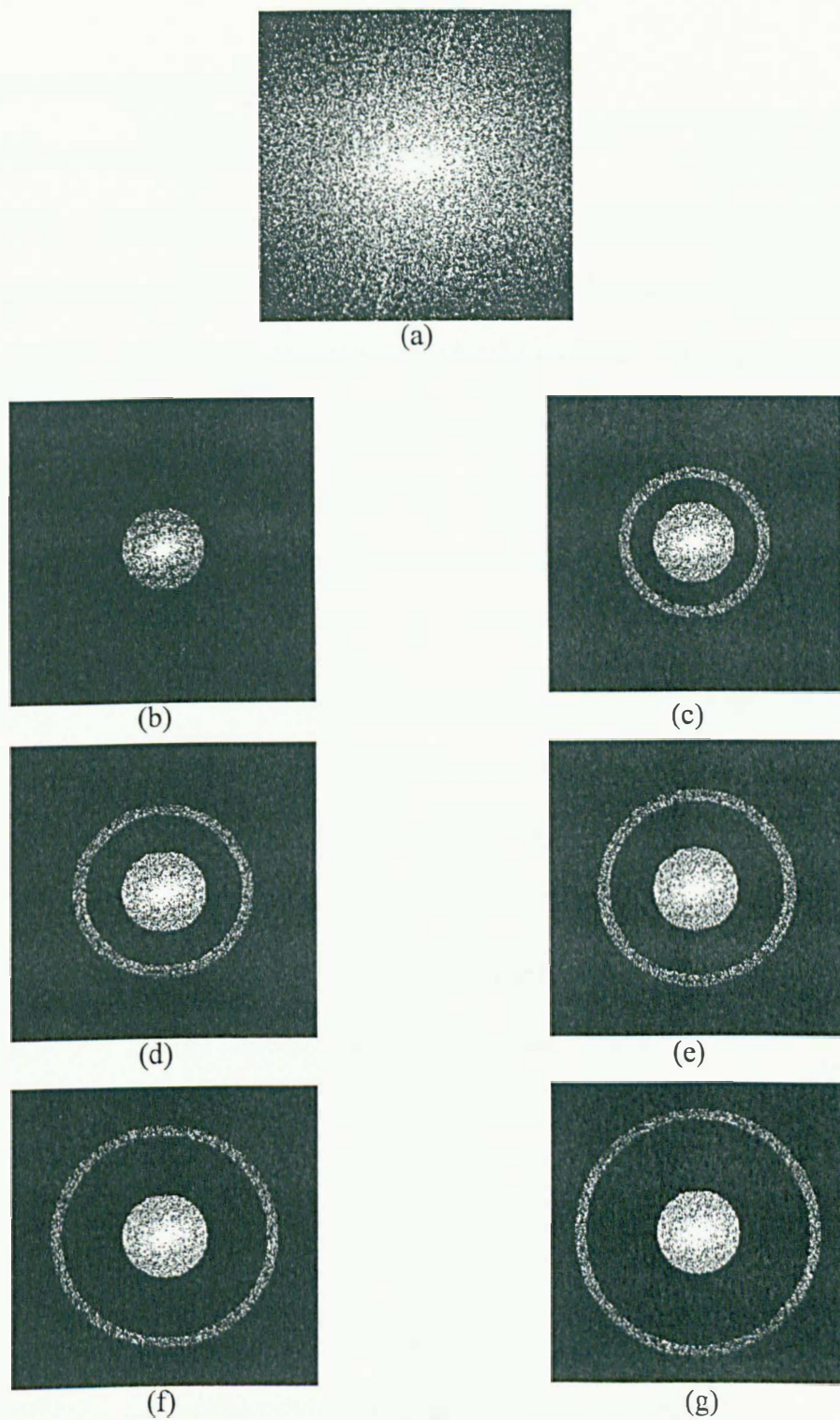


Figure 4.4: Fourier transformed filters, a) original magnitude image, b) kernel band-pass, c) first band-pass, d) second band-pass, e) third band-pass, f) fourth band-pass, g) fifth band-pass.

4.3.2 Pseudo-colour images

Most video display systems have the ability to show a single image band in 256 distinct colours on the display monitor. When this is done, we say the image band is being shown in pseudo-colour mode. This is distinct from showing a single grey scale image. Pseudo-colour mode is useful since every level in an image can be shown in a different colour, thus allowing grey levels of interest to be highlighted or allowing grey levels close in value to be readily distinguished from each other since they can be assigned very different colours (Campbell, 1996; Jensen, 1996; Mather, 1999).

Pseudo-colouring is made possible by the use of a Pseudo-Colour Table (PCT). PCTs work by mapping each input grey level from an image band to three output levels, one for each of red, green, and blue. These new output levels are passed to the colour guns thus showing the image in pseudo-colour on the display monitor. A PCT is made up of three sections: red, green, and blue, each with 256 entries. Given an input grey level x , a red section R , a green section G , and a blue section B then:

$$r = R(x)$$

$$g = G(x)$$

$$b = B(x)$$

Where r , g , b , are the output levels for the red, green, and blue colour guns. The entries in a PCT can be modified allowing different colours to be chosen.

Table 4.2: An Example of Pseudo-Colour Table.

Input Grey Level	Output Red Level	Output Green Level	Output Blue Level	Resulting Colour
0	0	0	255	Bright Blue
1	255	0	0	Bright Red
2	0	255	0	Bright Green
3	200	200	200	Light Grey
4	0	0	0	Black
5	0	0	128	Dark Blue
...
254	160	160	0	Medium Yellow
255	160	255	160	Light, Bright Green

In the example PCT in Table 4.2, we see that when pseudo-colour mode is enable for an image band, all image pixels with a grey level of 0 will displayed in bright blue, pixels with a grey level of 1 in bright red, and so on and so forth.

The predefined Pseudo-colour tables, which are available in the EASI/PACE image processing system, allow the user to quickly replace the existing PCT with a standard PCT provided by the systems, which is based on series of short colour ramps is applied to the inverse filtered FFT images.

4.3.3 Enhancement Techniques

The Landsat satellite sensors were designed to be capable of detecting a wide range of terrain brightness, from oceans or black basalt plateau, to snow or desert areas. A very

wide few individual scenes have brightness ranges that utilise the full sensitivity range of the sensor. Therefore, pixel values in Landsat scene commonly occupy a relatively small part of possible range of image values. The examination of the image histogram is a useful and necessary preliminary step for successful manipulation of image contrast. The image histogram describes the frequency of occurrence (along the vertical axis) of the grey levels (along the horizontal axis) in an image. From the previous, it can be seen that the pixel values occupy only a small area of the available range. This limited range causes the low contrast and enhancement techniques were used to stretch the data to occupy the full range of the grey levels available; this produces an image with greater range and shows greater contrast. Of the many methods available for contrast stretching the two most popular are the simple linear stretch, and the histogram equalisation stretch. (Campbell, 1996; Jensen, 1996; Mather, 1999). The following image enhancements as:

4.3.3.1 Linear contrast stretch

Performs a linear contrast stretch. The linear function maps (stretches) input grey level between the minimum and maximum values found in the selected input image, to output grey level between 0 and 255. With a 2% tail trimming of image histogram data is performed before the minimum and maximum values are determined. The contrast stretch is performed evenly across the input range of grey levels.

4.3.3.2 Histogram Equalisation

Performs histogram equalisation. The equalisation function produces an image where output grey levels are uniformly distributed between 0 and 255. The lookup table function is derived from a cumulative frequency distribution of the input image data.

4.3.3.3 Square root contrast stretch

Performs square-root contrast stretch. The square-root function maps (stretches) input grey levels between the minimum and maximum values found in the selected input image, to output grey levels between 0 and 255. With a 2% tail trimming of image histogram data is performed before the minimum and maximum values are determined. Unlike the linear function, the contrast stretch is greater at the lower end of the input data range.

4.3.3.4 Infrequency

Infrequency brightening (also termed “histogram inversion”) produces an image in which the high (bright) pixels represent those grey levels in the original image which were infrequent (i.e. accounted for a small proportion of the entire image). The lookup table function is derived from an inverted (upside down) histogram of the input image data values.

This function is useful for highlighting rare or small features in an image that may otherwise go unnoticed. The infrequency enhancement “brightens” these features so that they become more obvious. This enhancement can be useful in the detection of lineaments or edges, which owing to the thinness of their dimensions can go unnoticed.

Performs infrequency brightening or histogram inversion. The function produces an output image where infrequently occurring grey levels are assigned high grey levels in the output and vice versa. The lookup table function is derived from an inverted, upside down, histogram of the input image data.

4.3.4 Unsupervised classifier

Fuzzy set concepts were first proposed by Zadeh (1965) to produce a mathematical method for dealing with continuous data. The term fuzzy has appeared to describe undetermined values in data, which means inaccuracies in measurement or estimation, or to describe imprecise or overlapping semantics used to describe or classify data. Therefore, fuzzy set classification logic, which takes into account the heterogeneous and imprecise nature of the real world may be used in conjunction with supervised and unsupervised classification algorithms (Burrough and McDonnell, 1998; Bonham-Carter, 1994; Jones, 1997).

The IFOV (instantaneous field of view) of a sensor system normally records the reflected or emitted radiant flux from heterogeneous mixtures of biophysical materials

such as soil, water, and vegetation. Also, surface features usually grade into one another without sharp, hard boundaries. Reality is actually very indefinite and heterogeneous (Wang, 1991; Lam, 1993). In addition, conventional classification methods of remotely sensed data generally produce discrete information categories. And, it is inherently assumed that classes memberships are precisely defined, so that the attribution of a pixel to a cover category is always achievable (Swain and Davis, 1978, Curran, 1985). As a result, analysts usually use very precise classical set theory to classify remotely sensed data into discrete, homogeneous information classes, ignoring the ambiguity found in the real world. Unlike being assigned to a single class out of number of possible classes, each pixel in a fuzzy classification has number of membership grade values, each associated with how probable it is to be associated with each of the classes of interest (Figure 4.5). For this, the information may be used by the analyst to extract more definite landscape information, especially concerning the makeup of mixed pixels (Fisher and Pathirana, 1990 and 1993; Foody and Trodd, 1993; Jensen, 1996).

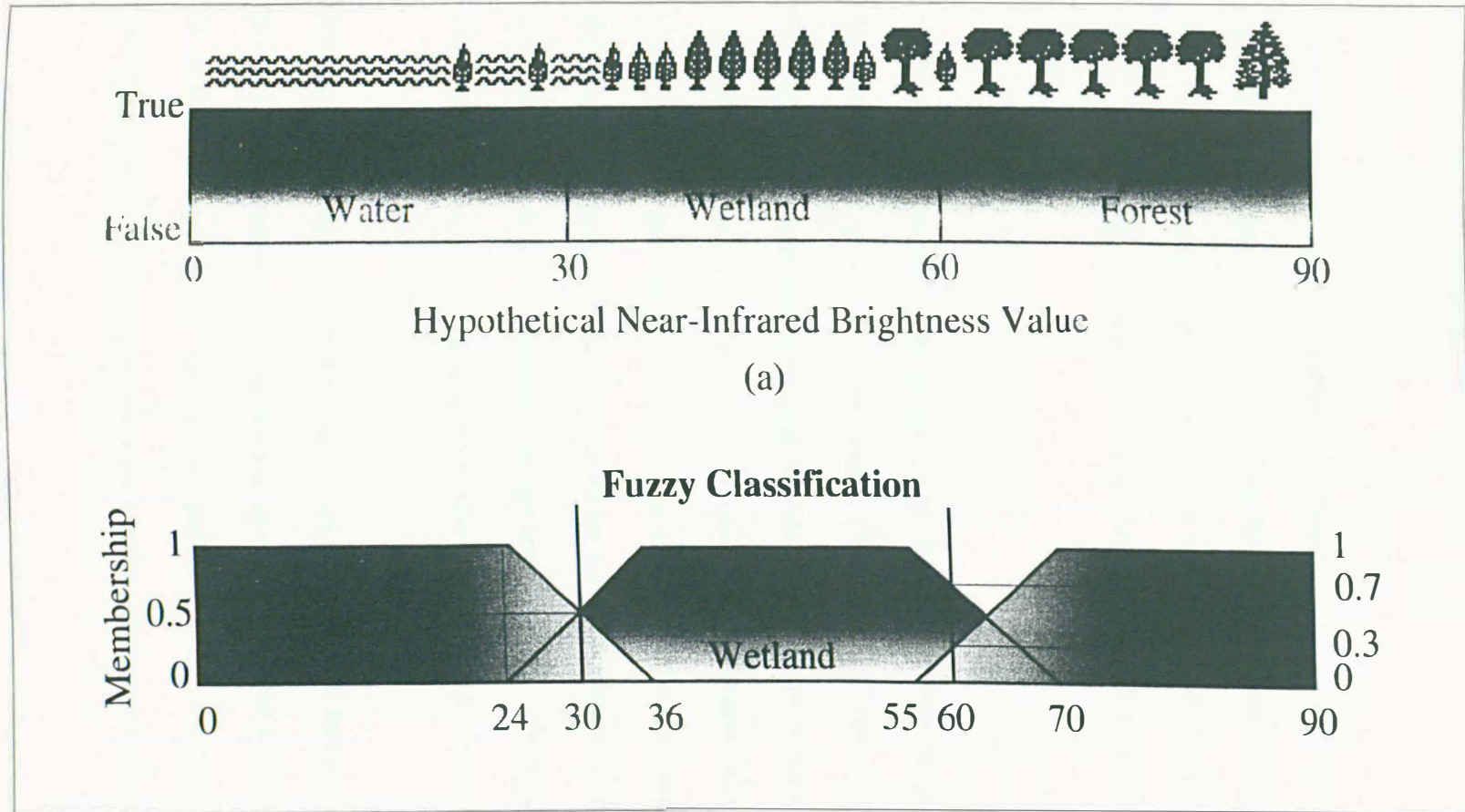
In classical set theory, the membership of a set is defined as true or false, 1 or 0. However, membership of a fuzzy set is expressed on a continuous scale from 1 for identifying full membership to 0 for identifying no membership at all. In addition, fuzzy membership values must lie in the range as mentioned above, but there are no practical controls on the choice of fuzzy membership values. Thus, the values are simply chosen to reflect the degree of membership of a set that is based on subjective

judgment and, therefore, values need not increase or decrease routinely with class number (Campbell, 1997, Maselli *et al.*, 1996, Jones, 1997).

The method of fuzzy *k*-means, which is also known as fuzzy *c*-means, is such a technique that has been used in soil science, vegetation mapping, and many other disciplines (McBratney and de Gruitjer, 1993; Odeh *et al.*, 1990; Jensen, 1996). Many authors prefer to term the method continuous classification rather than fuzzy classification. For this reason, McBratney and de Gruitjer (1992) proposed the term continuous classification to better describe the method of grouping data using the fuzzy *k*-means technique.

Fuzzy *k*-means as described by Bonham-Carter (1994), McBratney and Odeh (1997) works by an iterative procedure that usually starts with an initial random allocation of the objects to be classified to *k* clusters (Figure 4.5). After given the cluster-allocation, the centre of each cluster is calculated as the average of the attributes of the objects. In the next step, the objects are reallocated among the classes according to the relative similarity between objects and clusters. Reallocation proceeds by iteration until a stable solution is reached where similar objects are grouped in one cluster. Allocation of objects in conventional *k*-means is always to the nearest cluster, with membership function equal 1 to this cluster, and membership function equal 0 to all others, while fuzzy *k*-means membership values may range from 0 to 1.

Conventional Classification



Fuzzy Classification

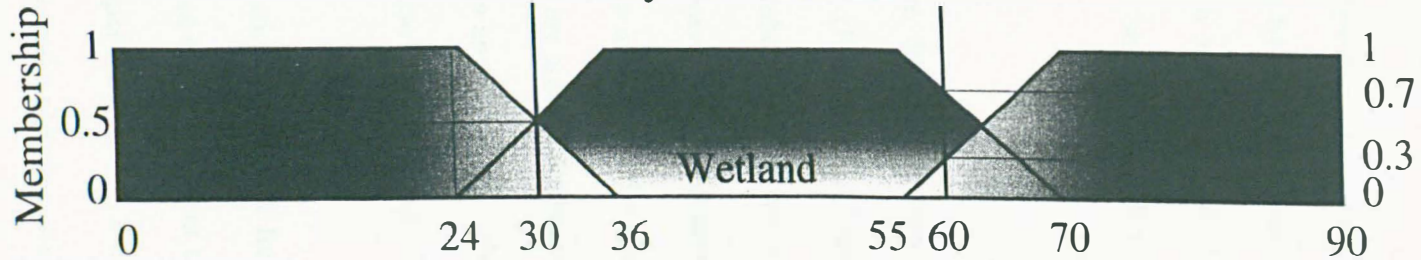


Figure 4.5: Illustration of differences of (a) conventional classification. (b) fuzzy k-means classification (after Jensen, 1996).

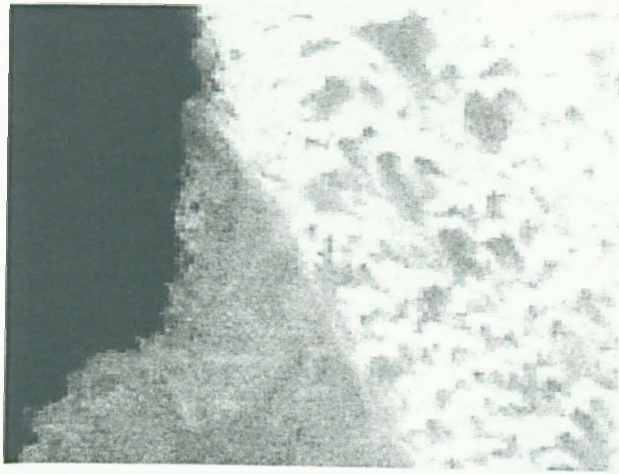
4.4 Results and Discussions

4.4.1 Introduction

The Fourier models as described earlier in section (4.2.2) were applied to band 4 and 7 of Hofuf data sets for images of size 1024 rows by 1024 columns. Three test areas were selected for this particular investigation, which are within the Hofuf image data sets (test area I, II and, III), and the size of each segment is 128 rows by 128 columns (Figure 4.6).

The results of the Fourier analysis procedure described earlier in this chapter are expressed as images of spectral components (Figure 4.7). These images show the contributions of particular spatial spectral wavebands to the reflectance image at each pixel. Higher values show that the selected waveband dominates in that area of the image more than in areas with lower values. The images can thus be considered as maps of spatial spectral dominance. Since the images are automatically rescaled by the image-processing algorithm it is not possible to assign any meaning to the actual values or to frequency distributions. Statistical parameters also have no direct meaning.

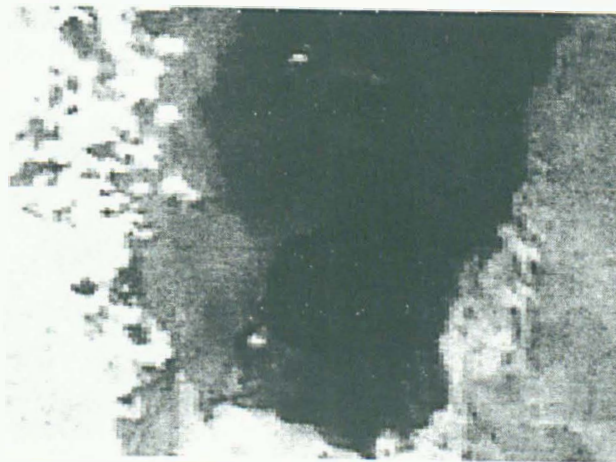
The assessment of results is based first on a consideration of the frequency distributions of image Digital Numbers and secondly on a set of enhancement techniques which are derived experimentally. These are an unsupervised fuzzy *k*-means classifier, an infrequency enhancement (histogram inversion), and a pseudo-colour look up table



a

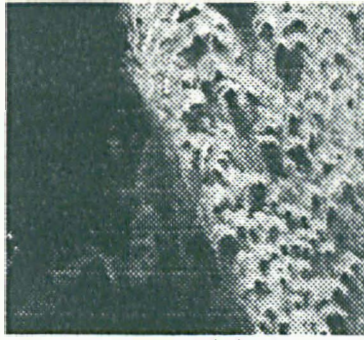


b

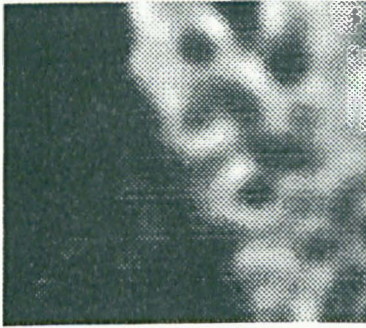


c

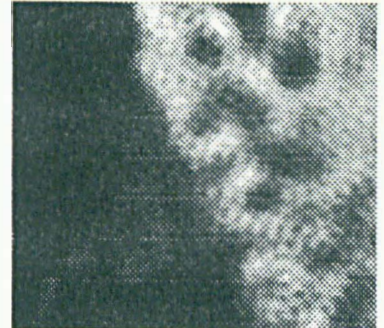
Figure 4.6: Images of Landsat-TM Band 7 representing (a) segment I, (b) segment II and (c) segment III.



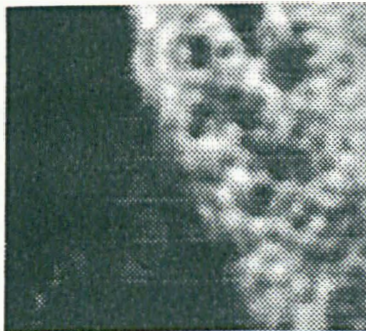
(a) Original



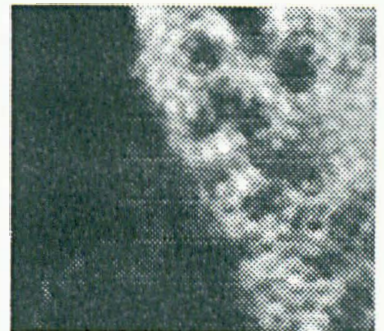
(b) Inverse kernel



(c) First inverse band-pass



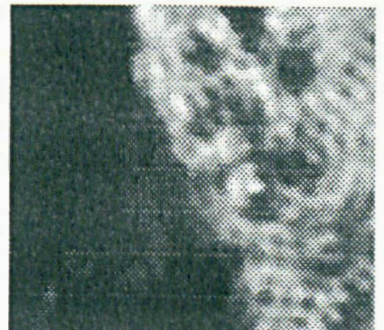
(d) Second inverse band-pass



(e) Third inverse band-pass



(f) Fourth inverse band-pass



(g) Fifth inverse band-pass

Figure 4.7: Images (a) – (g) represent the original image and the filtered inverse FFT images of segment I.

(PCT). The land resource map and soil map for the test areas are described in chapter 2. Copies of these maps are provided in the pocket appendix at the end of this thesis.

4.4.2 Image statistics

The resulting data structures for the transformed images as well as the original Landsat TM data images were compared on the basis of histograms of bands 4 and 7. Only the histograms of band 7 are considered in this discussion, due to the similarity of results.

The data structures of the transformed images were somewhat different from the original images. The histogram of Band 7 raw data shows four or five broad peaks across a dynamic range of values from 0 – 210 out of the full 0 – 255 range. The peak in the 140 – 150 DN range appears a dual peak. Other peaks are at approximately 40, 65 and 190 DN (see figure 4.8). A division of the image into five classes is supported by the subsequent fuzzy *k*-mean cluster unsupervised classification that finds five areas. The histograms of the filtered inverse FFT images show that peaks are (i) preserved, (ii) sharpened of peaks in higher part of range, (iii) some discernible relative shifts in range of heights peak. There are differences in these histograms but it is not possible to associate peaks across pass-bands but this is probably reasonable (see figures 4.9 to 4.14). Frequency histograms are not likely to be sensitive indicators of different spectral contributions, especially as the band-passes are a mixture of the low frequency kernel plus a specific higher frequency band.

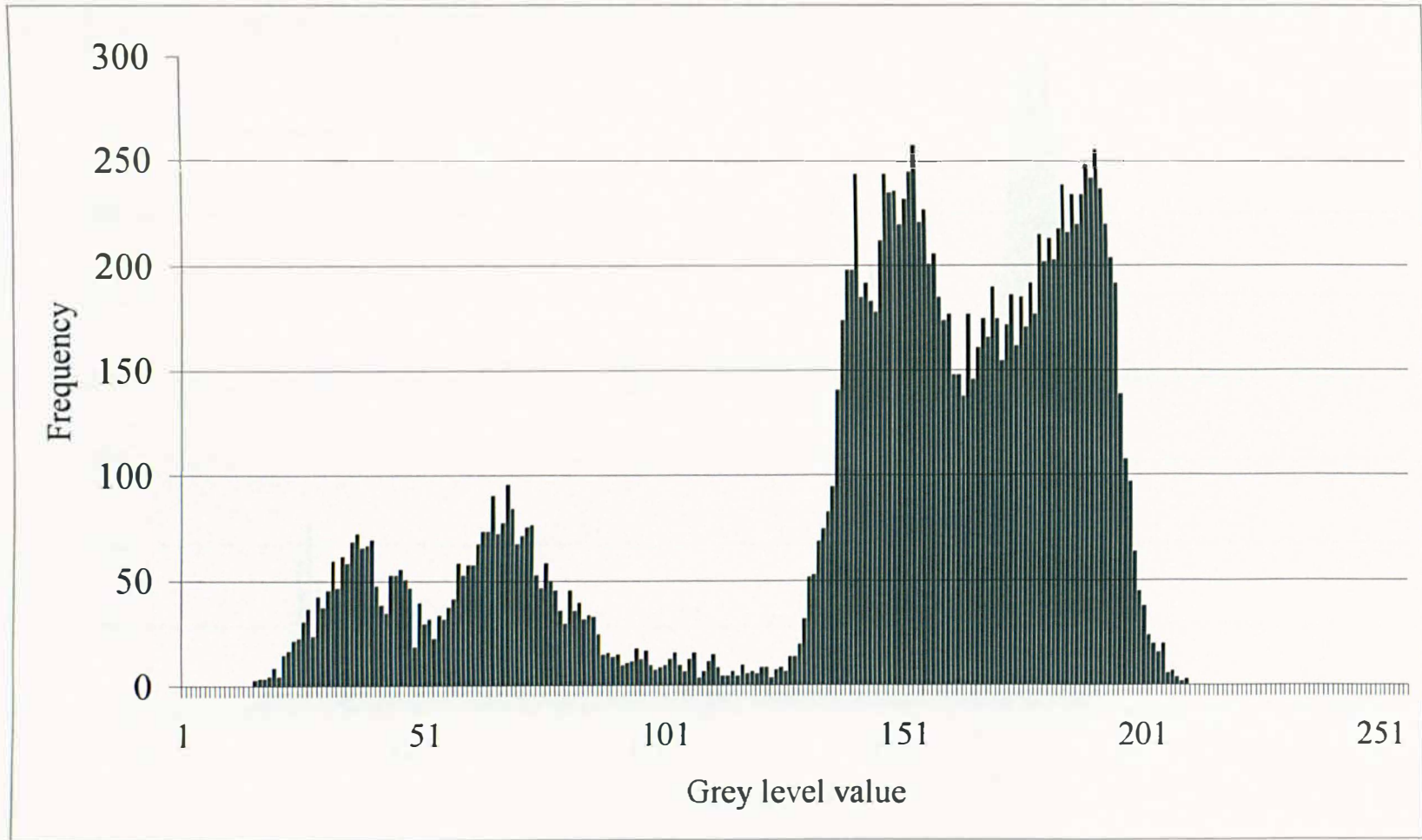


Figure 4.8: Histogram of the original TM raw data (Band 7)

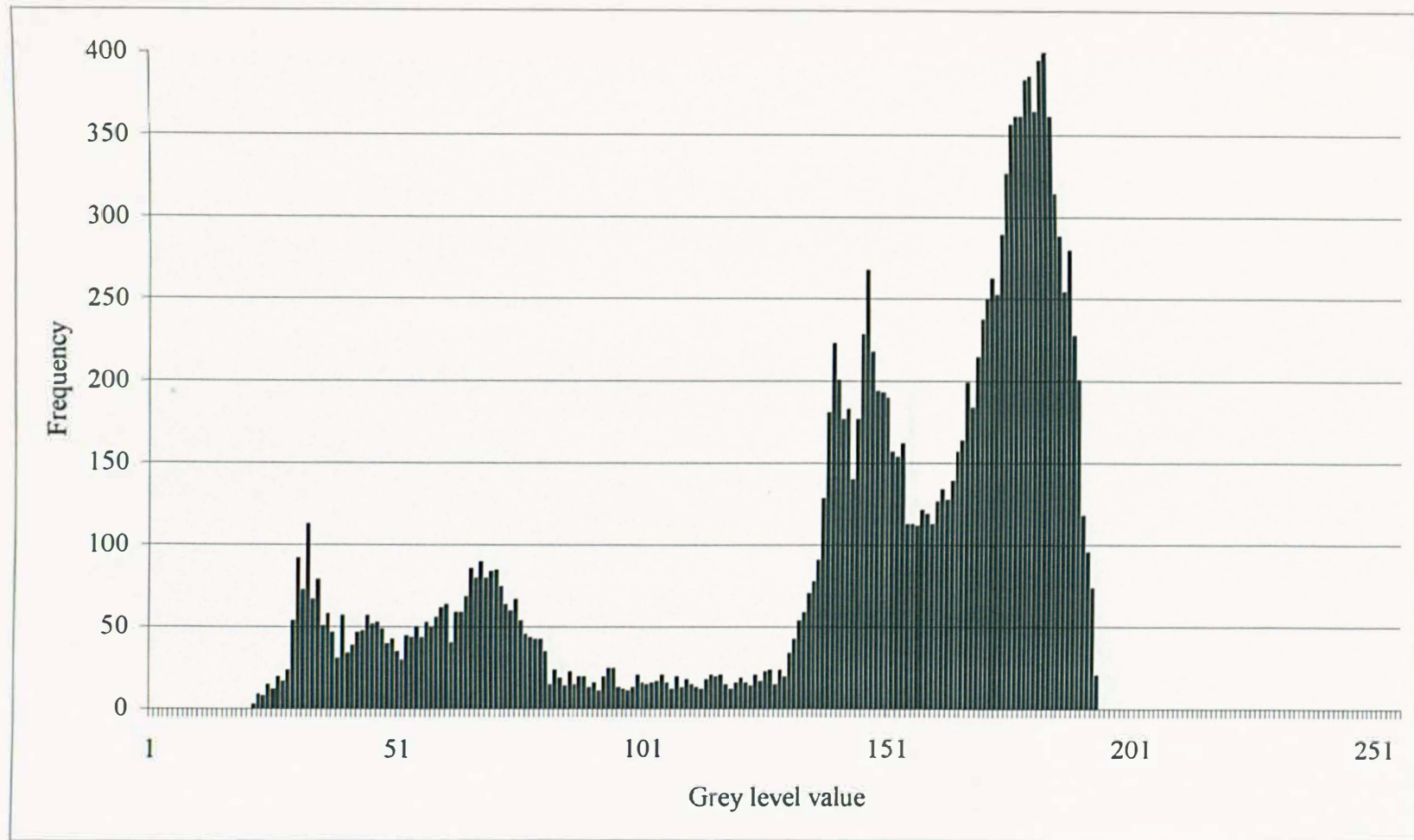


Figure 4.9: Histogram of kernel filter image (Band 7).

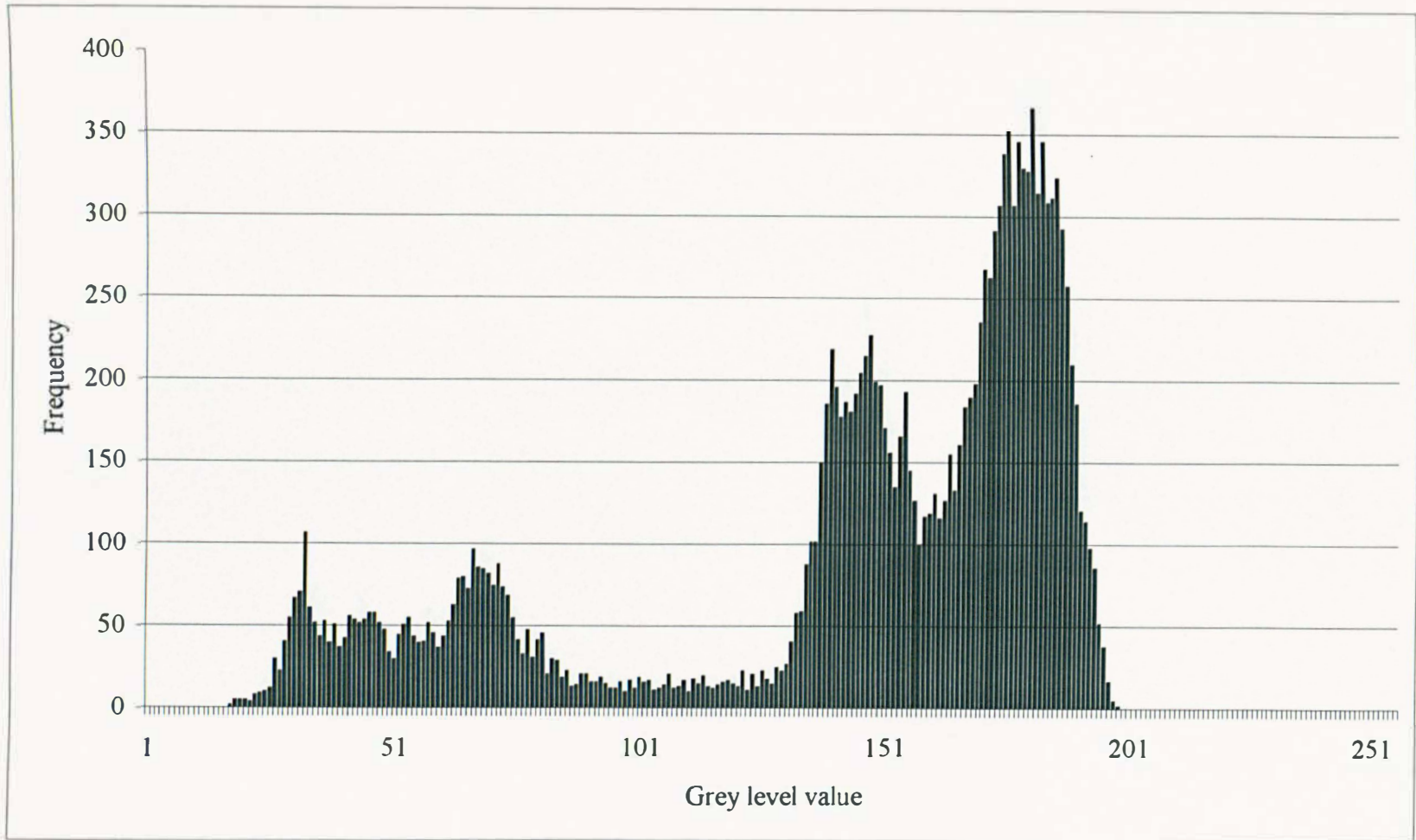


Figure 4.10: Histogram of first band-pass filtered image (Band 7).

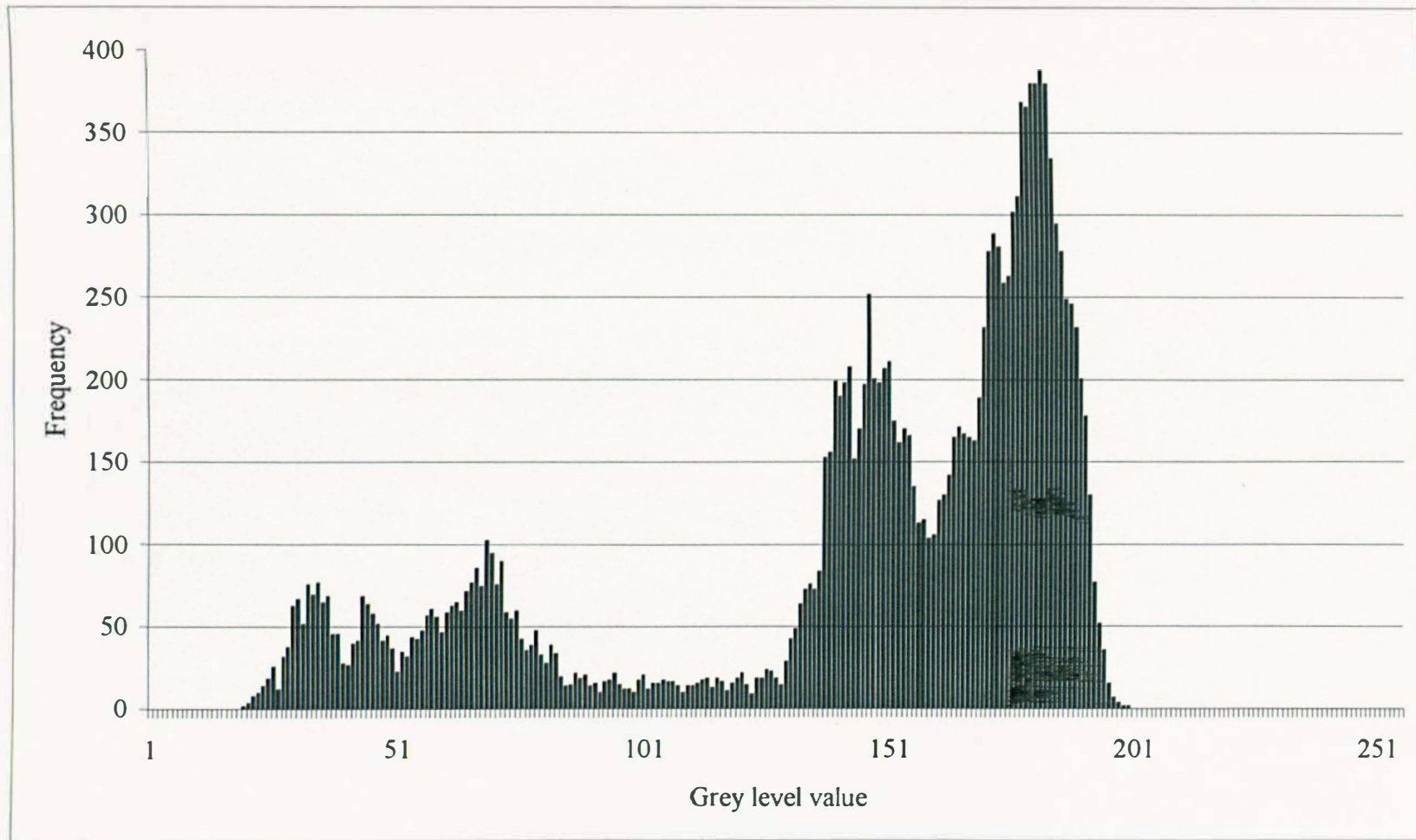


Figure 4.11: Histogram of second band-pass filtered image (Band 7).

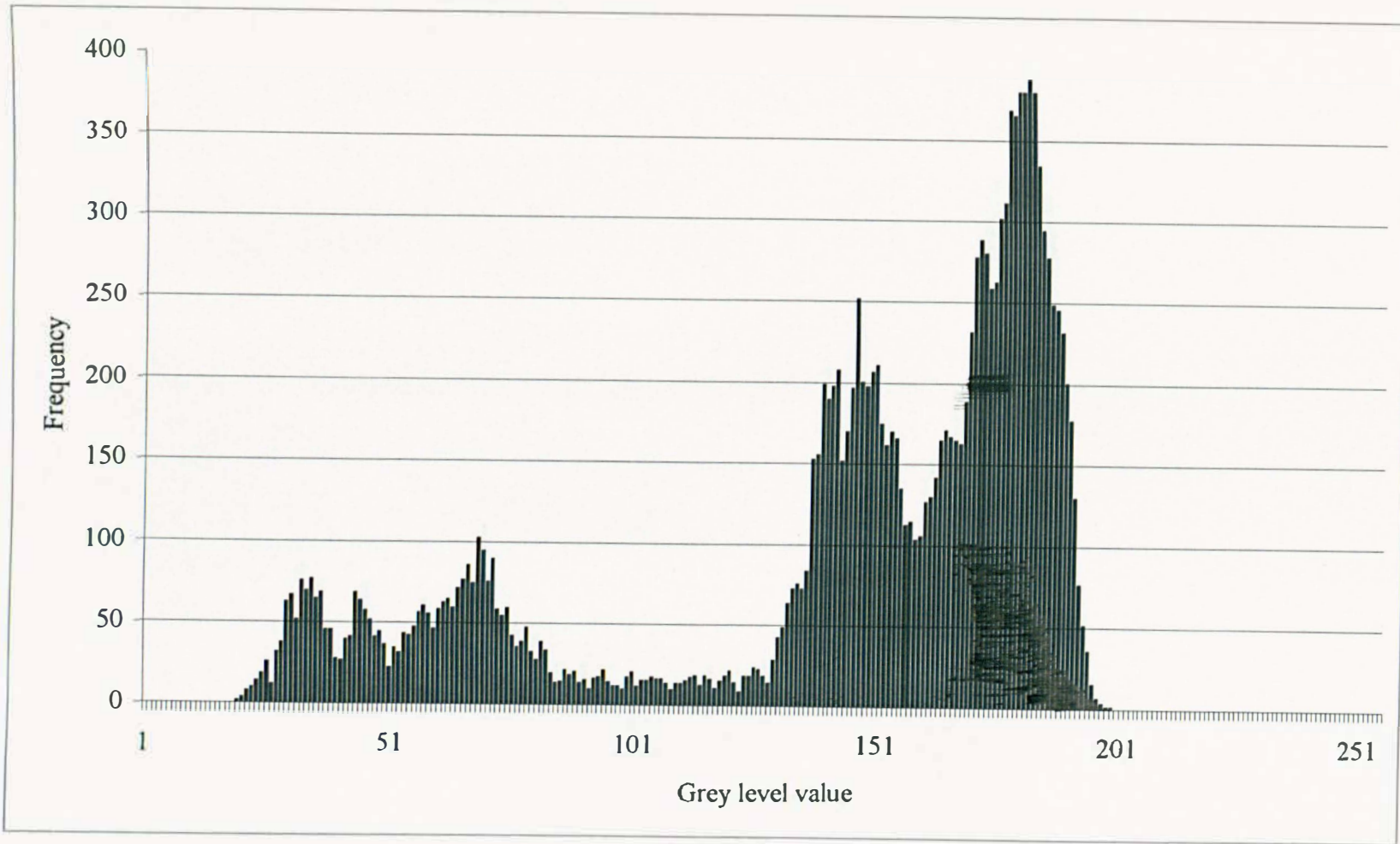


Figure 4.12: Histogram of the third band-pass filtered image (Band 7).

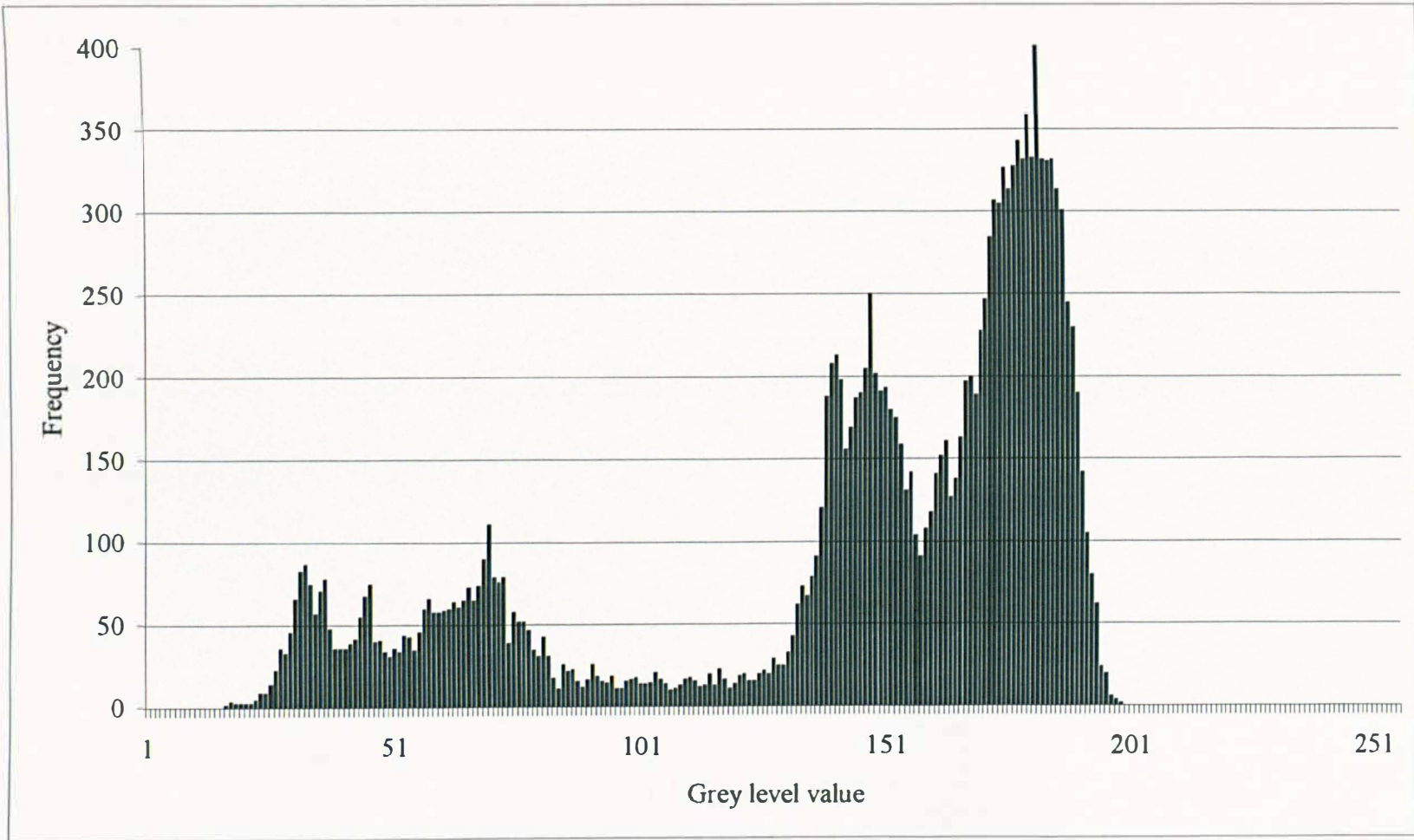


Figure 4.13: Histogram of the fourth band-pass filtered image (Band 7).

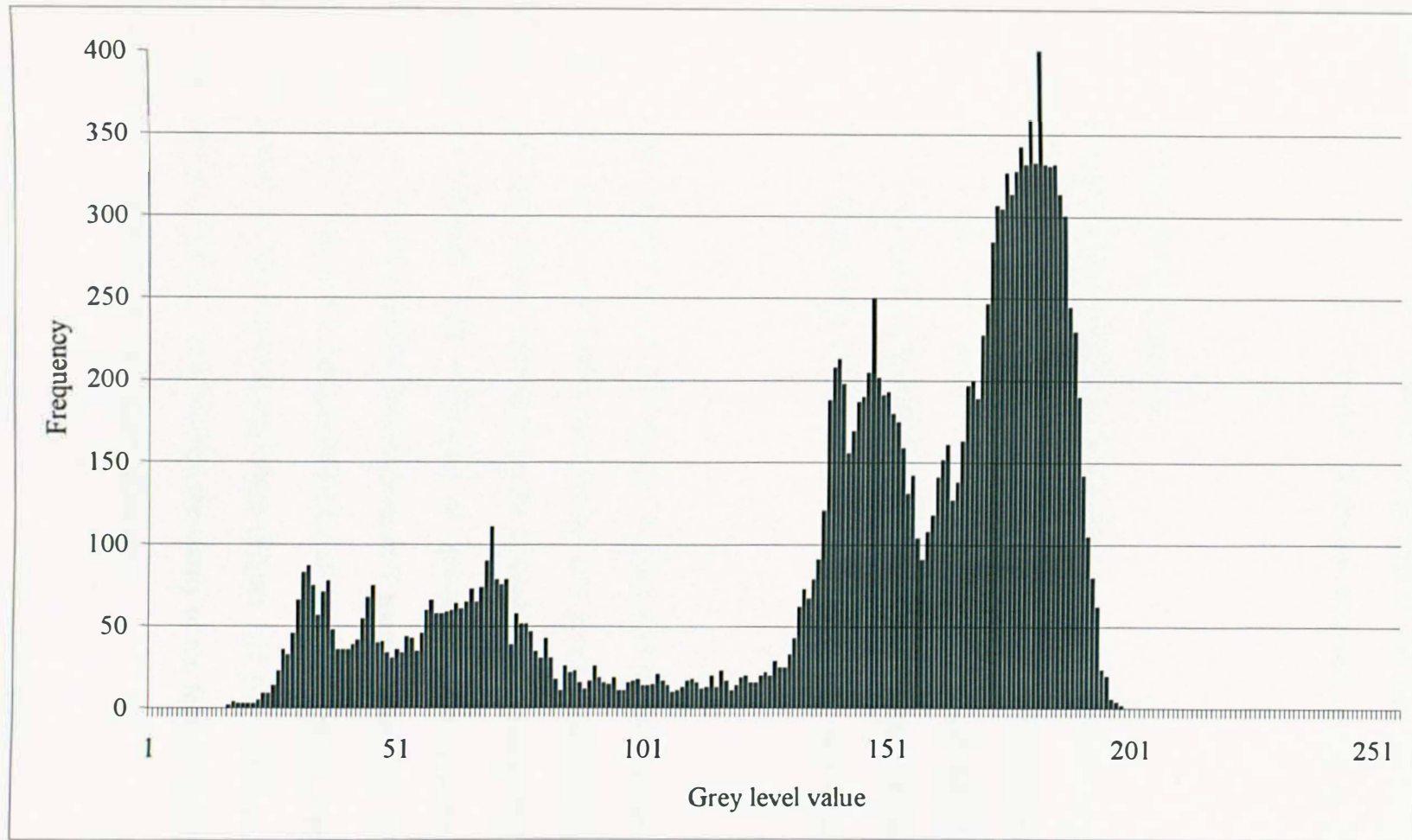


Figure 4.14: Histogram of the fifth band-pass filtered image (Band 7).

The fact that there are identifiable differences implies that there are real spatial spectral component effects within the image. These are analysed below in terms of image properties.

4.4.3 Assessment of output images

Inverse transform of filtered FFT are presented using a set of enhancement techniques (described earlier in sections 4.3.2, 4.3.3.4 and 4.3.5). The PCT image for the original band 7 (Figure 4.15a) shows that partitioning of the test areas I, II and III, lacks spatial coherence. All the images of the original raw data appear dominated by noise when the DN values are presented as PCT enhancements in which all data values have equal weight.

In contrast, the filtered inverse FFT images (Figures 4.15 (b) to (g)) presented as PCT enhancements show a reasonable partitioning into zones. The coherence gradually changes with band-passes. Starting from the filtered kernel inverse FFT images, the coherence is relatively high. Coherence of spatial elements is lower for images increasing shorter partial spectral band-passes. PCT transform revealed the presence of complex linear feature which was persistent for all band-pass images. This feature can be distinguished visually in the kernel image (Figure 4.15 (b)), however, in the other band-pass images (Figures 4.15 (c) to (g)) the clarity of the feature degrades gradually from the kernel image to the fifth band-pass image.

Band 4 shows a different spatial effect of band-pass filtering with PCT enhancement from the previous band. The major main grouping is less than in Band 7. This is noticeable and clear visually by recognising and identifying the grouping features, which is presented in red, orange, and yellow patterns. Unfortunately band 4 showed less partitioning presentation, due to the lower amount of information of spectral reflectance in the feature space. However, the degree of partitioning other features is noticeable, but in a poor scattering and arrangement of colour scheme. For instance, it is difficult to distinguish a clear and dominance feature in the original image. But, when evaluating the performance of the filtered inverse FFT images presented as PCT enhancements, the resulting images showed clear patterns. Also, the degree of coherence of patterns degrades gradually from kernel-filtered image to the last band-pass filtered image. The kernel-filtered image, for instance, shows the clearest presentation of pattern features.

There is a reasonable contrast among various features of the filtered images except in the original image. One of the most apparent features in the original image of Band 7 is not clear (Figure 4.16 (a)). Additionally, because of lack of partitioning of the image, the coherence of features is poor. However, not only do filtered inverse FFT images show a good contrast between features but also the partitioning of the patterns is clear. However, the coherence of patterns is degraded gradually from the first to the fifth filtered inverse FFT images (Figures 4.16 (b) to (g)).

In addition to the various zones of the image, there are significant linear features being delineated in the filtered images with different degrees of contrast. For instance, the images (Figures 4.16 (d) and (e)) showed clearly a thin linear feature delineated over much of their area. Although linear features are less apparent in other images such as Figures 4.16 (b) and (g), these features have a clear and persistent pattern.

The infrequent features are also clear in Band 4, with similar feature identification to Band 7. The major difference between Band 4 and Band 7 is quality and clarity of the various features. The situation is also similar when comparing the original raw data to the filtered images. These contrasts can be described in terms of coherency of features and robustness of patterns. For instance, the features of the original image are less clear than in the filtered image. The infrequent features are scattered and did not show any apparent and well developed arrangement of patterns. However, in the case of filtered images the situation is totally different in terms of representing coherent images. Even though the degree of coherency of features is different (e.g. kernel image, first band-pass and fifth band-pass filter), these features are partitioned and can be identified easily.

The spatial arrangement of features of unsupervised fuzzy k -means results are less scattered than the previous transformation, due to the forcing into classes by the system. Therefore, these features appeared as coherent patterns. But this apparent coherency changes from the original raw data to the filtered images. For instance, the original raw

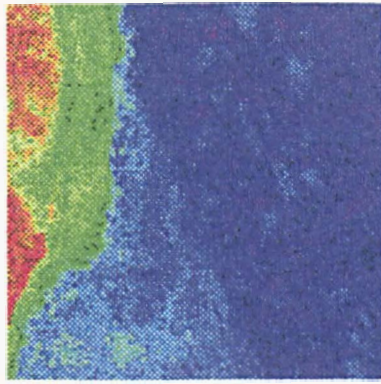
data of band 7 has more scattered patterns especially in the right part of the image, while the filtered images showed more coherent patterns, which are easily distinguished. However, the quality of pattern especially in the right part is degraded. The filtered kernel shows the clearest partitioning of features. Although the other filtered images showed clear features, they have a broken appearance compared with the kernel filtered.

In Band 4, there is a surprising feature in the original image especially in the middle part of the image. This feature, which is in blue colour, is not present in the filtered images. The quality of patterns in the original raw data showed more features than in Band 7. For instance, there are more noticeable patterns and these can be distinguished all over the image. Although the filtered images showed fewer patterns, they are clearly defined.

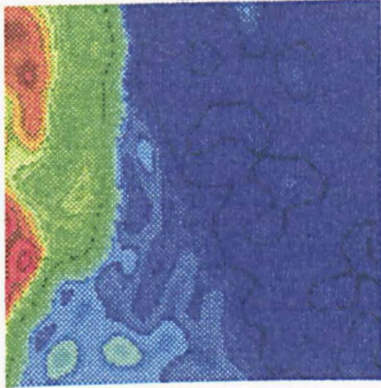
4.4.4 Analysis of images for soil Landscape identification

4.4.4.1 Test segment I

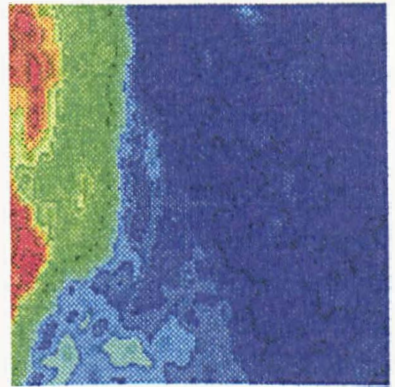
Figure 4.15 shows pseudo-colour images of TM band-7 displayed using stepped predefined pseudo colour tables, which are based on a series of short colour ramps (described earlier in section 4.3.2). The procedures were applied to the original image and the transformed band-pass images as well. Although this PCT displays reasonable discrimination between different soil units, this basic routine did not exploit fully the



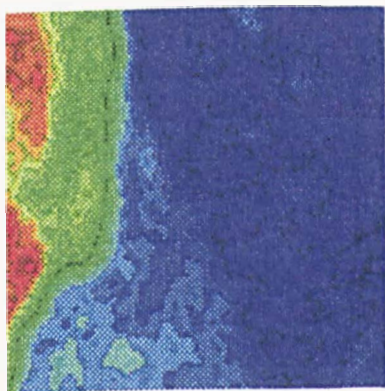
(a)



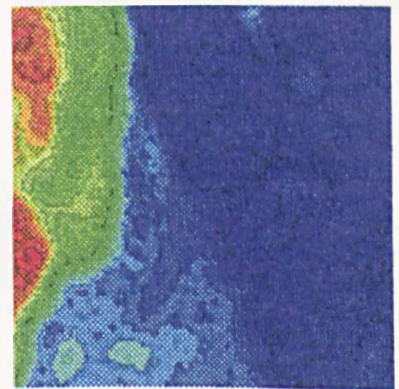
(b)



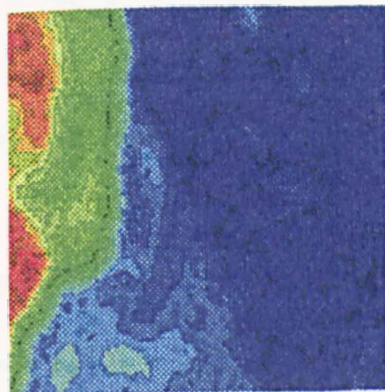
(c)



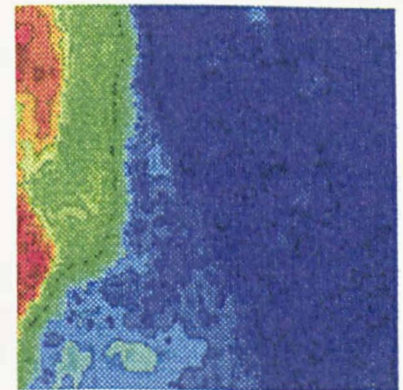
(d)



(e)



(f)



(g)

Figure 4.15:PCT images of Band 7, (a) original (b) kernel (c) First band-pass (d) second band pass (e) third band pass (f) fourth band pass (g) fifth band pass (Segment I).

RGB colour space, due to, probably, the low degree of digital brightness for this particular band (Table 4.2).

By transforming the original image figure 4.6 (a) from original mode to colour mapped mode using PCT procedure, the end product was the image shown in figure (4.15 (a) to (g)). It can be seen that the transformed images (Figure 4.15 (b) to (g)) have been divided into coherent zones. Those zones having similar colour and texture can be clearly recognised, and discriminated over the whole images. Comparing these images with soil maps (MAW, 1986, 1995), there is a close correspondence between the spectral filtered images and the mapped units. However, the images show greater detail as might be expected. The PCT original image (Figure 4.15 (a)) produced more zones than the soil maps with broken and complex patterns.

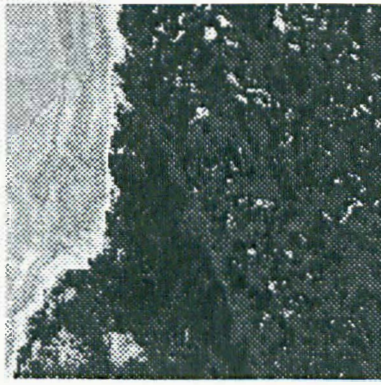
The band-pass images especially the kernel image (Figure 4.15 (b)) produced coherent zones. There was also a linear feature established by this procedure. The sabkha unit has a very low reflectance in the IR band- 7 region. It is displayed as green, yellow, and orange colours and shows a clear black linear feature within the area. These patterns can be easily discriminated by the colour zones. Within the sabkha unit, there is a distinct zone in the northwest corner appearing as a light green colour zone.

The sand sheet area is displayed in dark blue colour, with a few small green and light blue zones (Figure 4.15). The transition between sand sheet and alluvial plain areas is

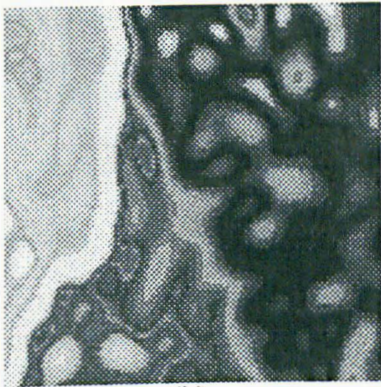
represented by a complex linear feature. In addition, there were many well-defined black linear features within this area especially in the filtered band-pass image (Figure 4.15b), which can be easily distinguished.

The alluvial plain area can be partitioned into four zones according to its appearance in these images. First one is the blue colour zone located in the north east and east of this unit, with elongated dark blue areas, and an oval green colour zone at the north part of this unit, where there may be a few dunes. Second zone is the light blue, which is displayed as a broken patterns in the original raw data (Figure 4.15 (a)), while it is coherent in the transformed images especially in the kernel band-pass image (Figure 4.15 (b)). Third zone is considered as a transitional zone, which is displayed as a moderate blue and located in-between the light blue and dark blue zones. Fourth zone is the green colour; with a two sharper green colour spots, which might be related to the appearance of dunes. In addition, the four zones were well established and can be discriminated from each other.

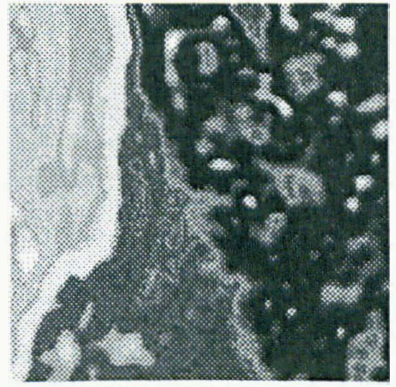
The infrequency enhancement images of band- 7 are presented in figure 4.16. The raw data and the six of band-pass images are displayed as grey scale. These images are transformed using infrequency enhancement technique to enhance the discrimination between different soil units, in other words, it highlights the infrequent features. Various zones exhibit some degree of grey scheme variation except the raw data (Figure 4.16



(a)



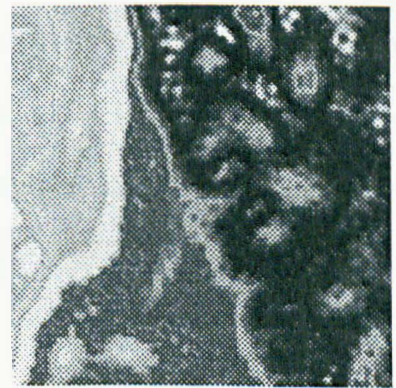
(b)



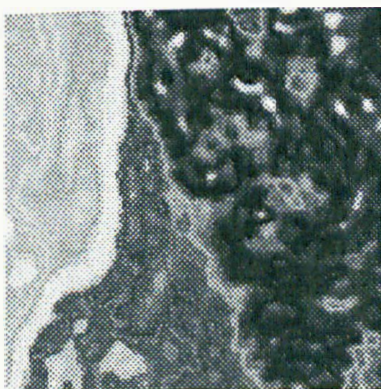
(c)



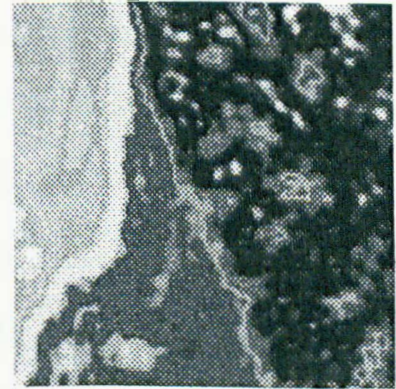
(d)



(e)



(f)



(g)

Figure 4.16: Infrequency images of Band 7, (a) original (b) kernel (c) First band-pass (d) second band pass (e) third band pass (f) fourth band pass (g) fifth band pass (Segment I).

(a)) which shows less variation, and does not show the detailed variations as produced by band-pass images (Figures 4.16 (b) to (g)).

In these images, the improvements of patterns in the spatial information are self-evident. The degree of similarity between the images and soil maps (MAW, 1986, 1995) is not fully convincing. The sabkha area, discriminated by its grey brightening, is displayed as one zone, with a few very small white zones. However, the sand sheet and alluvial plain areas, are difficult to discriminate.

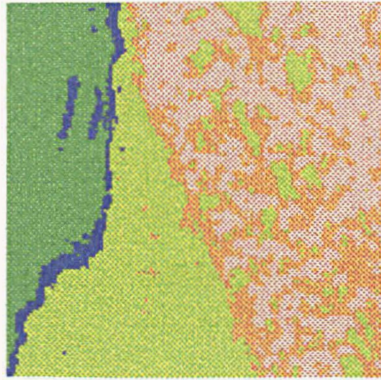
The units mapped in the soil map as three individual units (sabkha, sand sheet & dunes, and alluvial plain) can be partitioned into more zones, as might be expected. The one at north west of sabkha area can be discriminated by its light grey especially in the kernel band-pass image (Figure 4.16 (b)). The small area within the alluvial plain unit can be easily identified which might be represented as an aeolian sand dune that covers a small part of this unit.

The sand sheet area can be separated into two geomorphologic features: a) the grey and light grey, which represent dunes, b) the black area would be presented as a sand sheet area. The alluvial plain area also can be divided into two features, a grey and a light grey feature. These features can be easily identified and appeared like a coherent zone especially in the fourth band-pass image (Figure 4.16 (f)). With respect to linear

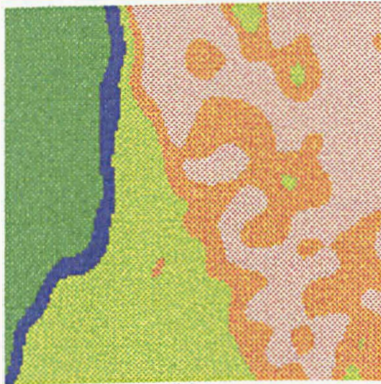
features, the band-pass filter images shown clear and robust linear features, especially in fourth and fifth band-pass images (Figure 4.16 (f) and (g)).

Figure 4.17 shows the results of unsupervised fuzzy k -means clustering that was applied to both the raw data and the band-pass images of band 7. These images show five different classes represented by different colours. Comparison of these images to soil maps (MAW, 1986, 1995) indicates a reasonable agreement for most of the areas. Greater disagreement occurs in the middle and east part of the alluvial plain and sand sheet & dunes areas, where there are mixed zones in the images, which in the map were classified as individual zones. The same thing is found in the sand sheet area but with slightly less severity especially in the raw data (Figure 4.17 (a)).

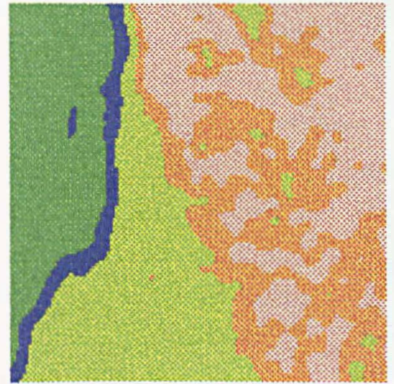
While it appears mixed and incoherent in the original image (Figure 4.17 (a)), the band-pass images (Figure 4.17 (b) to (g)) produced robust and coherent zones as well as linear features. For example, the alluvial plain appears like a uniform zone in the transformed images, with small zones coloured as yellow and blue, which may be represented as dunes. The sand sheet is produced very neatly in the band-pass images especially figure 4.17 (b), rather than the raw data, which produced scattered and broken classes.



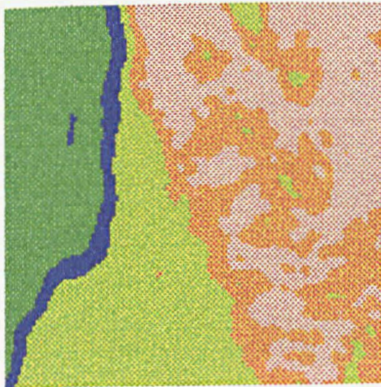
(a)



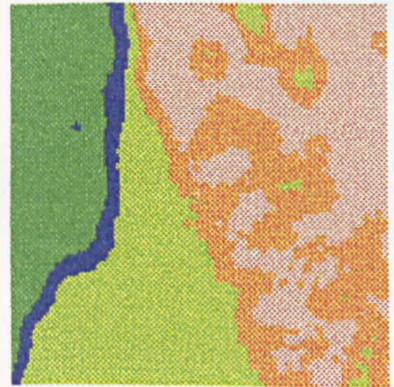
(b)



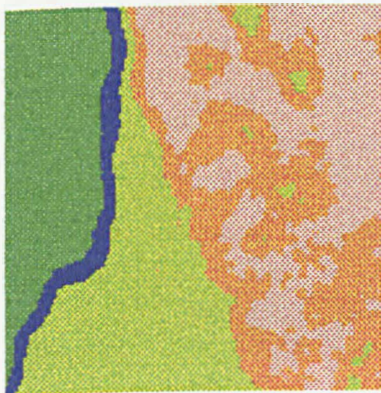
(c)



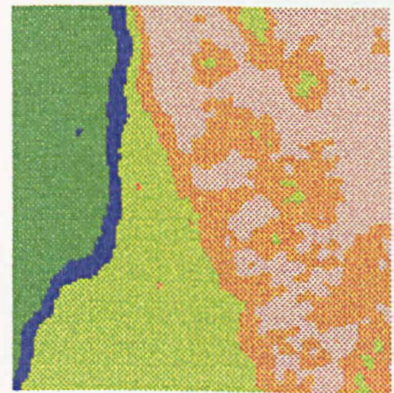
(d)



(e)



(f)



(g)

Figure 4.17: Unsupervised fuzzy k -means images of Band 7, (a) original (b) kernel (c) First band-pass (d) second band pass (e) third band pass (f) fourth band pass (g) fifth band pass (Segment I).

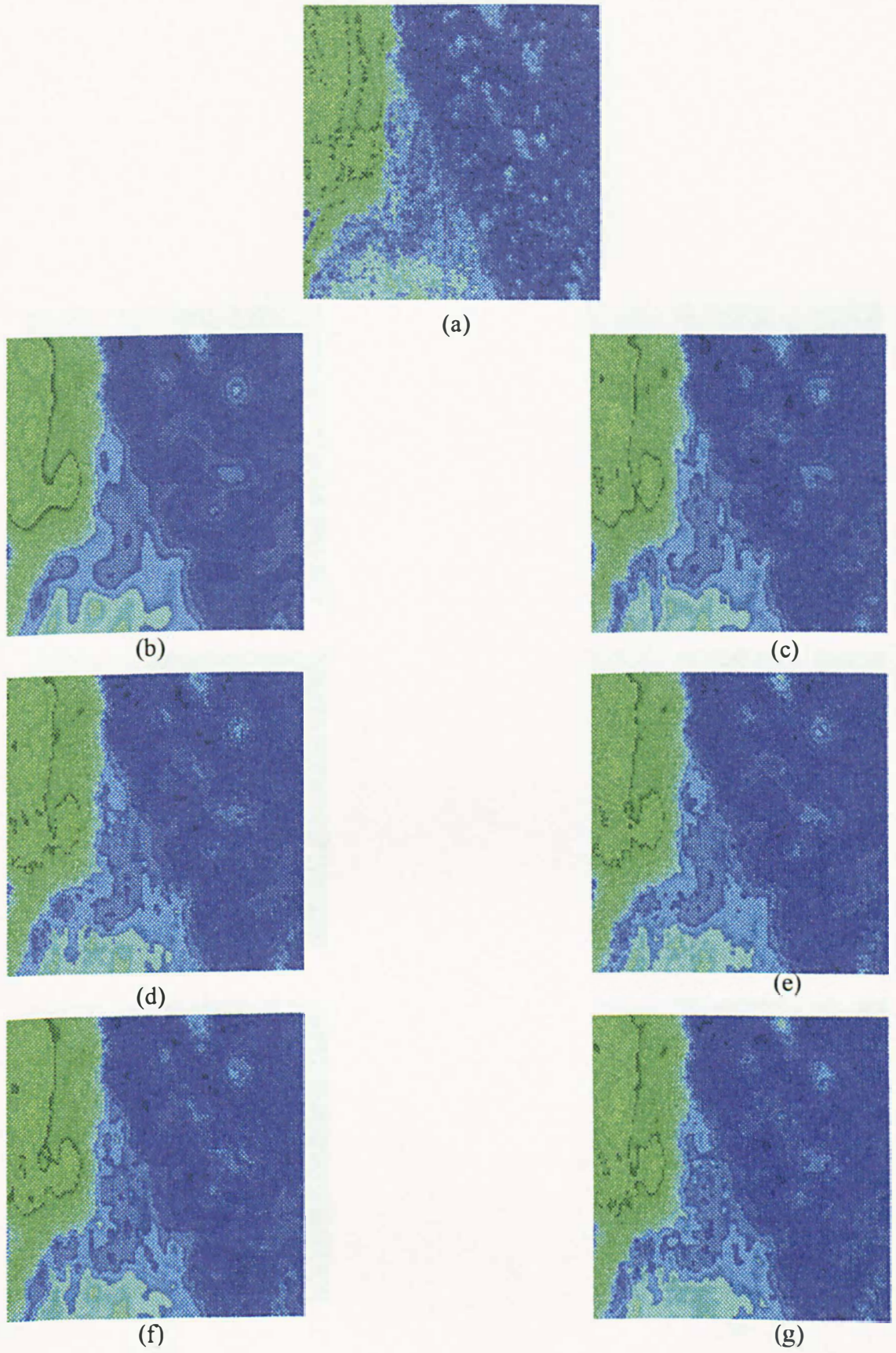
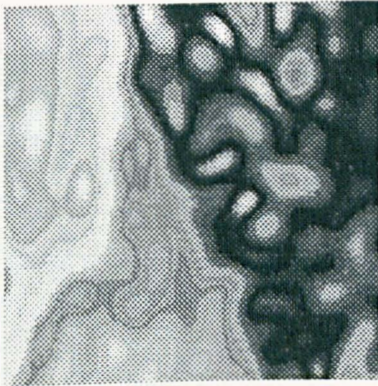


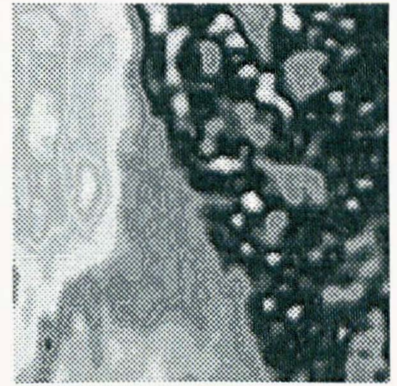
Figure 4.18: PCT images of Band 4, (a) original (b) kernel (c) First band-pass (d) second band pass (e) third band pass (f) fourth band pass (g) fifth band pass (Segment I).



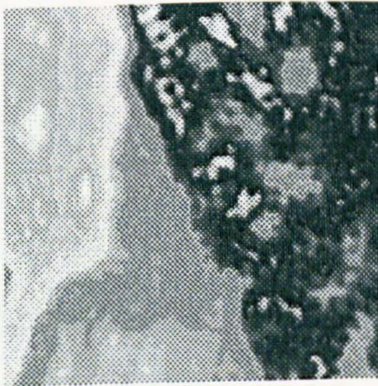
(a)



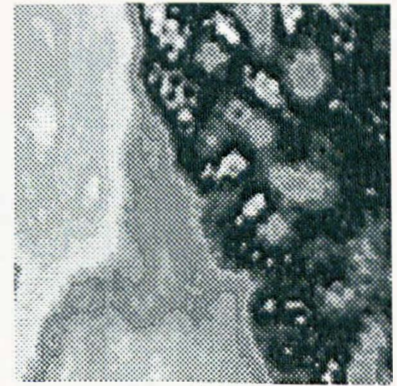
(b)



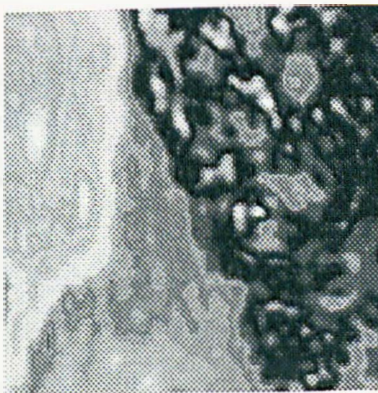
(c)



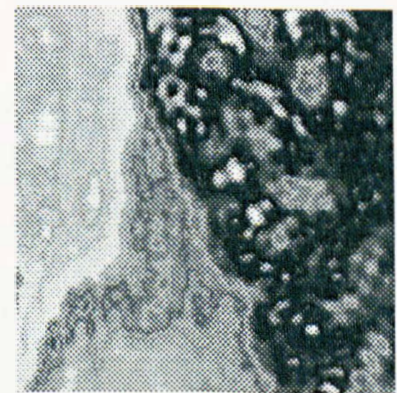
(d)



(e)

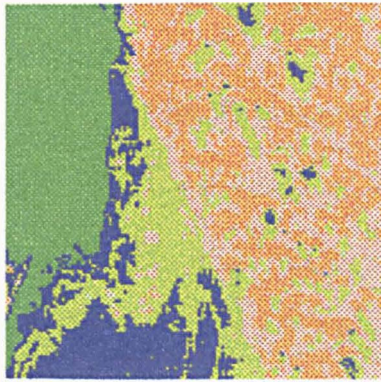


(f)

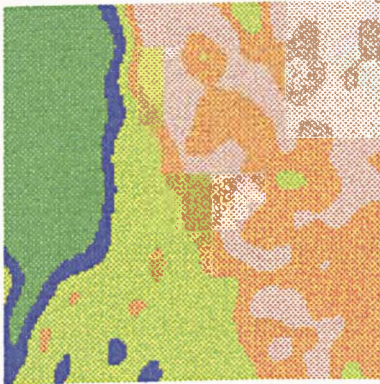


(g)

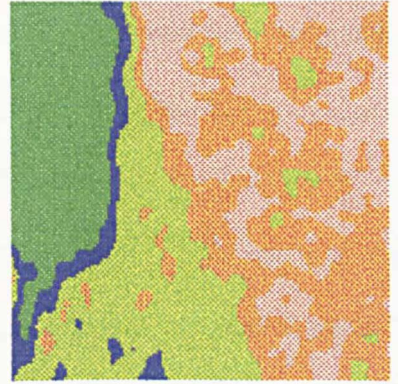
Figure 4.19: Infrequency images of Band 4, (a) original (b) kernel (c) First band-pass (d) second band pass (e) third band pass (f) fourth band pass (g) fifth band pass (Segment I).



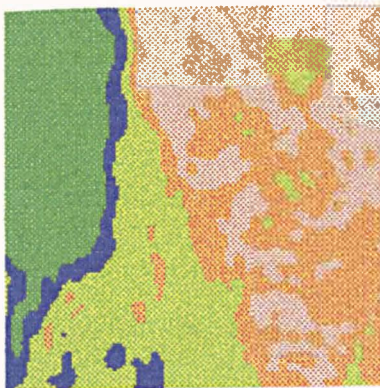
(a)



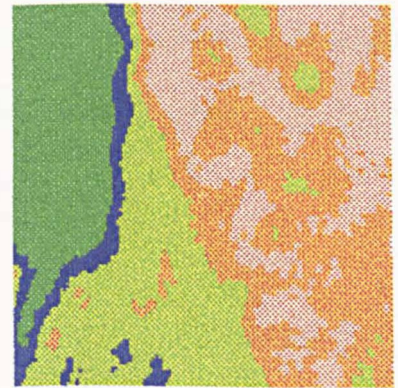
(b)



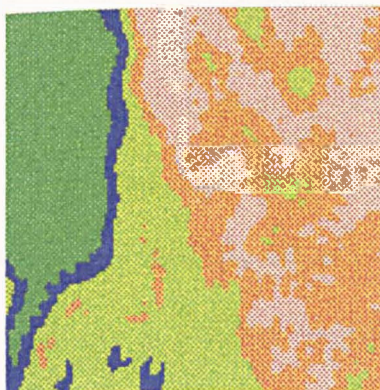
(c)



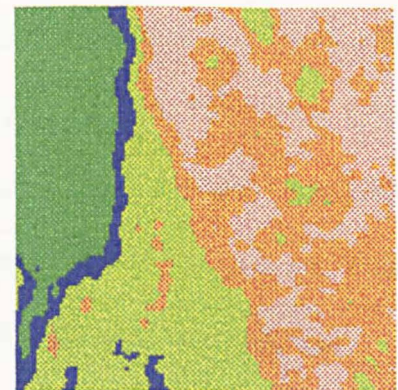
(d)



(e)



(f)



(g)

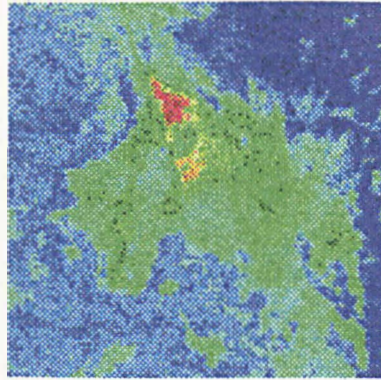
Figure 4.20: Unsupervised fuzzy k -means images of Band 4, (a) original (b) kernel (c) First band-pass (d) second band pass (e) third band pass (f) fourth band pass (g) fifth band pass (Segment I).

In terms of linear feature, the original image presented unstable linear features, while the band-pass images (figure 4.17 (b) to (g)) produced a clear linear feature, which can be easily identified. There is an elongated blue area between green colour area (sabkha) and light green (alluvial plain), where there may be a transitional zone.

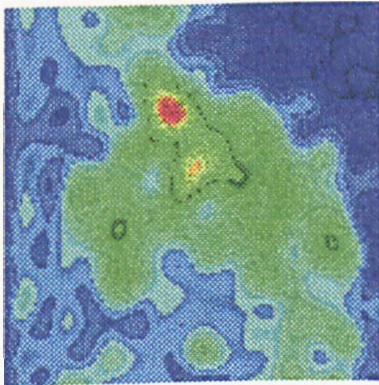
In Band 4, the resulting outputs are similar with some degree of differences in pattern and texture. Of all the soil areas in segment I enhanced using the PCT procedure, sabkha area is the only distinct one and show some differences from Band 7, which dominated by distinct green colour (Figure 4.18). Also, no major differences in the infrequency images except the alluvial plain area which is less complex than in Band 7 (Figure 4.19). In the cluster images, both Bands have similar features, with minor differences especially in the sabkha and the alluvial plain. The sand sheet is more or less similar for both bands (Figure 4.20). Overall the resulting images of Band 7 are clearer than in Band 4.

4.4.4.2 Test Segment II

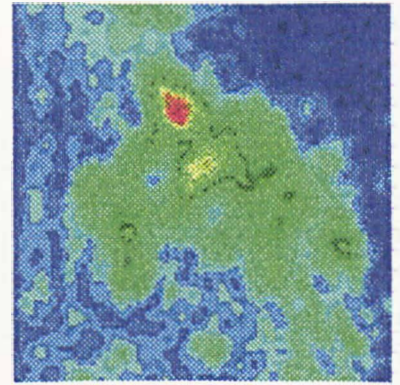
The band-pass images especially the kernel image produced coherent zones and can be identified easily across the image. In addition, there are linear features established by this procedure, one example is seen in the gypsiferous pediplain area. Two thin roughly circular linear features can be identified, shown in black. The gypsiferous pediplain landform is displayed as a green colour and is a coherent area but within it are linear features. In addition, it appears also in light green in the other location of the image



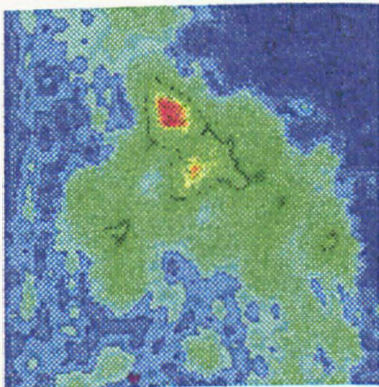
(a)



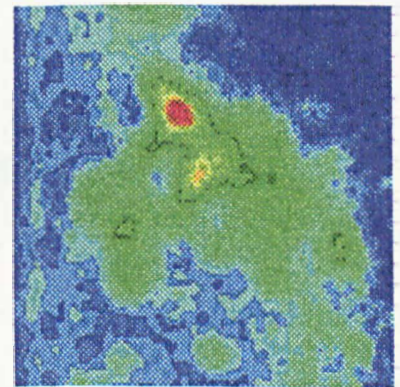
(b)



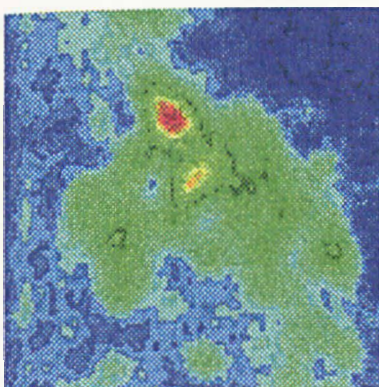
(c)



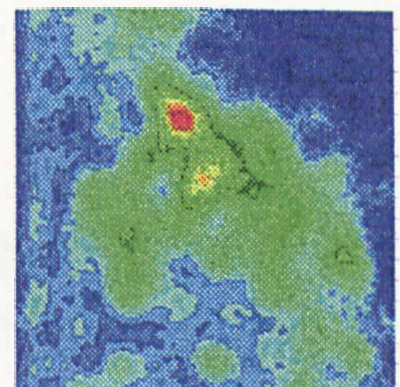
(d)



(e)



(f)



(g)

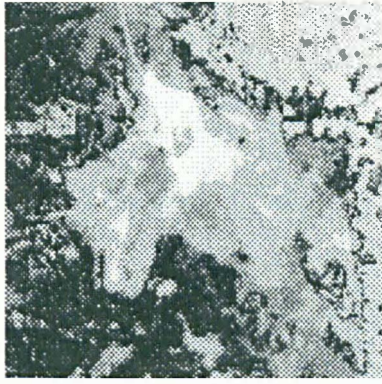
Figure 4.21: PCT images of Band 7, (a) original (b) kernel (c) First band-pass (d) second band pass (e) third band pass (f) fourth band pass (g) fifth band pass (Segment II).

such as the rounded green colour at the bottom of the image, with two elongated features in the east and northeast of the image.

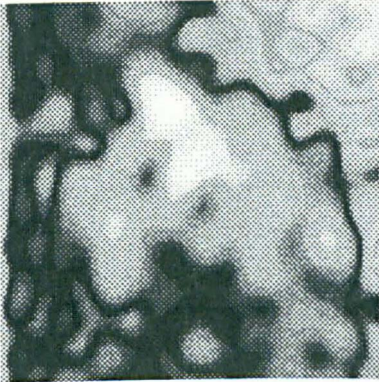
The gypsiferous pediplain area is dominated by light blue colour, with scattered green and dark blue zones (Figure 4.21). These zones are coherent and can be easily identified. The sand sheet area is displayed in dark blue colour, with a few small zones in very dark blue, which can be identified especially in the raw data (4.21 (a)). However, in the transformed images, there are only very dark blue zones. There is a clear linear feature between the sand sheet and the sabkha areas, which can be identified especially in the kernel band-pass image (Figure 4.21 (b)). This linear feature is difficult to distinguish in the raw data image.

Infrequency images exhibit some degree of coherent and robust features except the original image (Figure 4.22 (a)). In the west part of the area, which is the gypsiferous pediplain, features are not well defined in the original image where there are mixed elongated light grey zones. However, the band-pass images are well defined, and the scattering areas are not apparent especially in the kernel, first, and third band-pass filters (Figures 4.22 (b), (c) and (e)). The infrequency images also show a number of zones in the subkha area that can be separated into three (Figure 4.22 (b)).

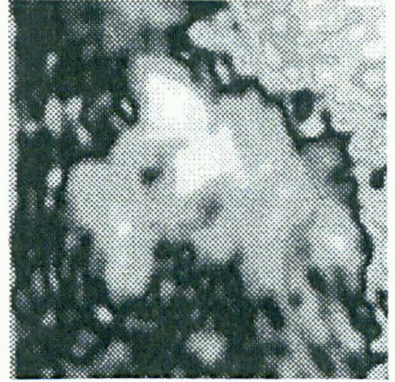
In general, there were many zones automatically drawn in the transformed band-pass images. These zones can be recognised and discriminated across the set of images. In



(a)



(b)



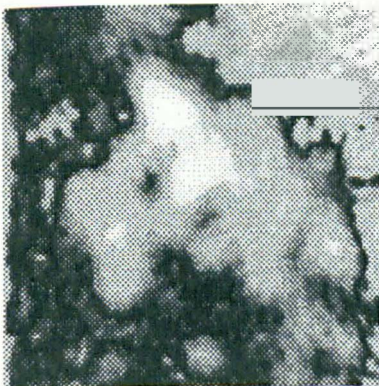
(c)



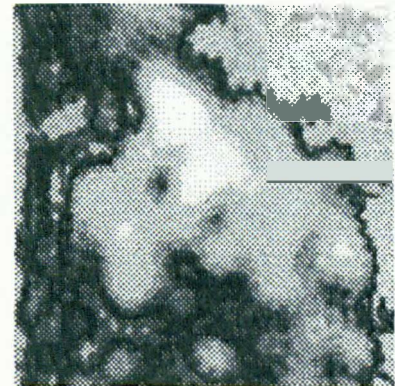
(d)



(e)



(f)



(g)

Figure 4.22: Infrequency images of Band 7, (a) original (b) kernel (c) First band-pass (d) second band pass (e) third band pass (f) fourth band pass (g) fifth band pass (Segment II).

addition, linear features in band-pass images are shown as clear and robust lines, especially in fourth and fifth band-pass images (Figure 4.22 (f) and (g)).

Comparing figure 4.23 with the soil maps (MAW, 1986, 1995) indicates little correspondence between most of the areas. Greater disagreement occurs in the middle part of the sabkha area, where there are much more complex zones, in what is classified as an individual zone. The same thing occurred in the other areas. The overall comparison between the original image to band-pass images show that the band-pass images (Figure 4.23 (b) to (g)) produced robust and coherent zones and linear features as well. Further, while the sabkha appears a little bit mixed and incoherent in the original raw data (Figure 4.23 (a)), it appears like a uniform area of two zones in the transformed images, with small zones displayed as yellow and blue, which may be interpreted as dunes. The other soil units were represented very clearly in the band-pass images, especially figure 4.23 (b).

The PCT images of Band 4 show similar features in most cases to Band 7 except there is somewhat less complexity especially in the sabkha area (Figure 4.24). Greater agreement with Band 7 is seen in the infrequency images as well as the cluster images, where not only most of main areas (sabkha, gypsiferous pediplain, and the sand sheet) are similar but also the minor areas except a few parts. But overall Band 7 produced clearer features than Band 4 (Figures 4.25 and 4.26).

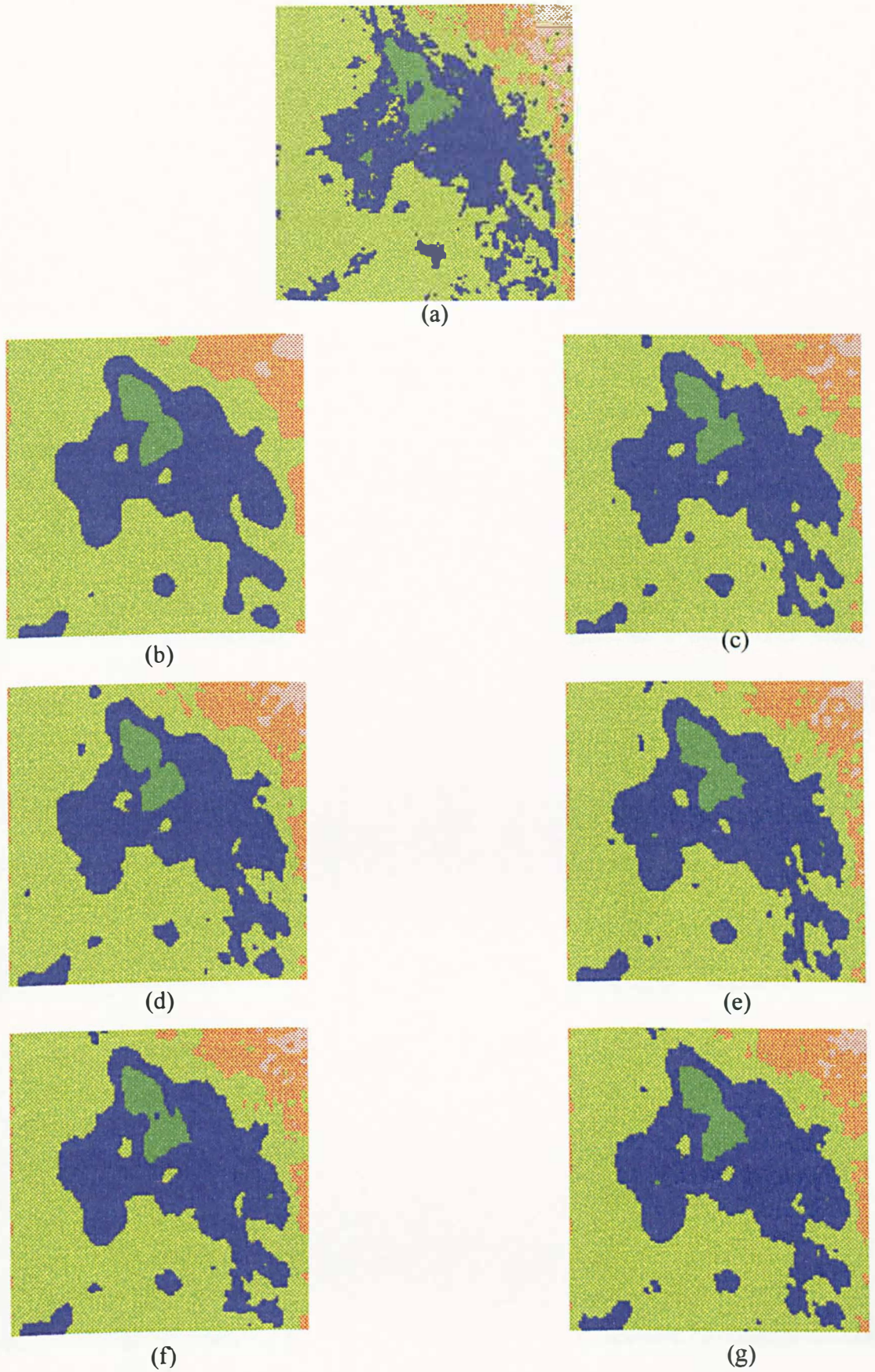
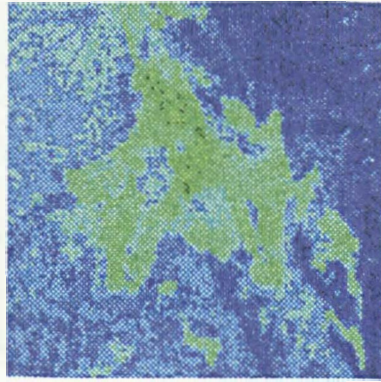
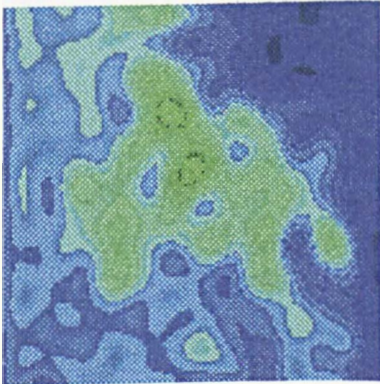


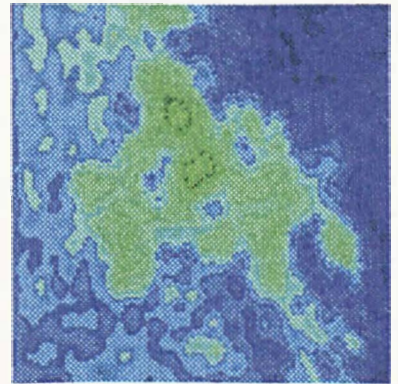
Figure 4.23: Unsupervised fuzzy k -means images of Band 7, (a) original (b) kernel (c) First band-pass (d) second band pass (e) third band pass (f) fourth band pass (g) fifth band pass (Segment II).



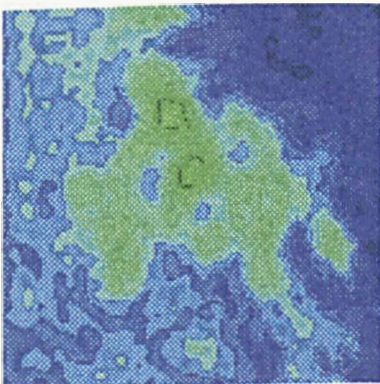
(a)



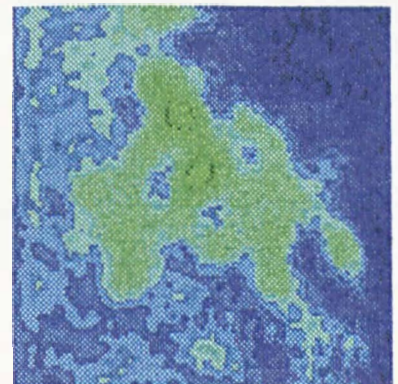
(b)



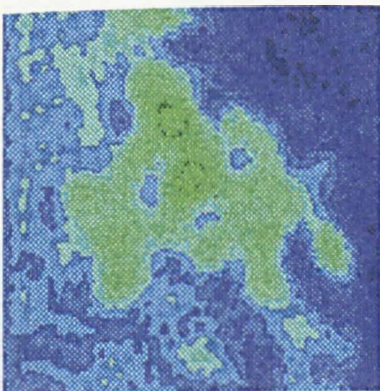
(c)



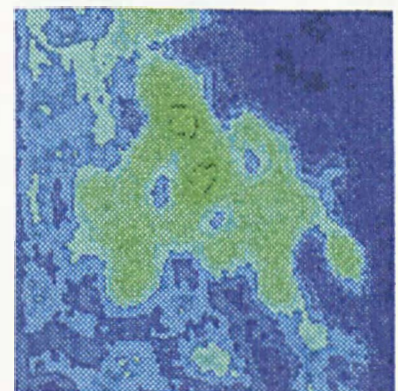
(d)



(e)

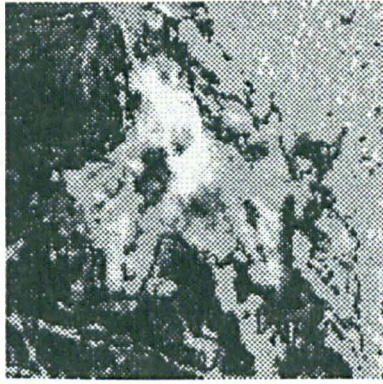


(f)



(g)

Figure 4.24: PCT images of Band 4, (a) original (b) kernel (c) First band-pass (d) second band pass (e) third band pass (f) fourth band pass (g) fifth band pass (Segment II).



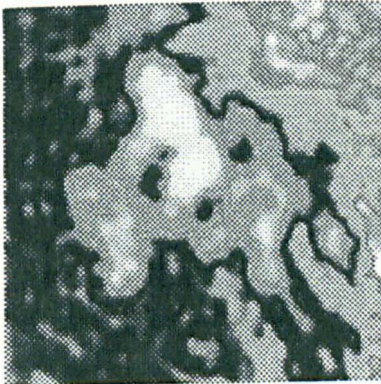
(a)



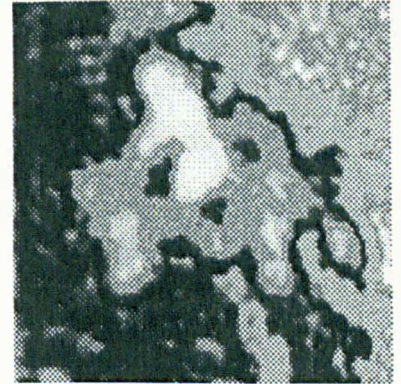
(b)



(c)



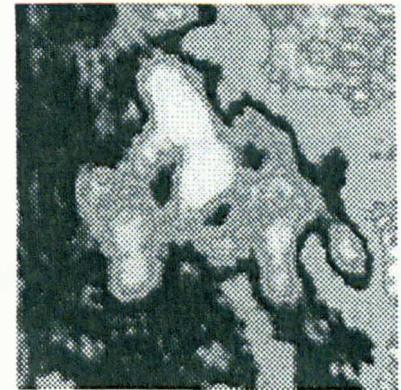
(d)



(e)



(f)



(g)

Figure 4.25: Infrequency images of Band 4, (a) original (b) kernel (c) First band-pass (d) second band pass (e) third band pass (f) fourth band pass (g) fifth band pass (Segment II).

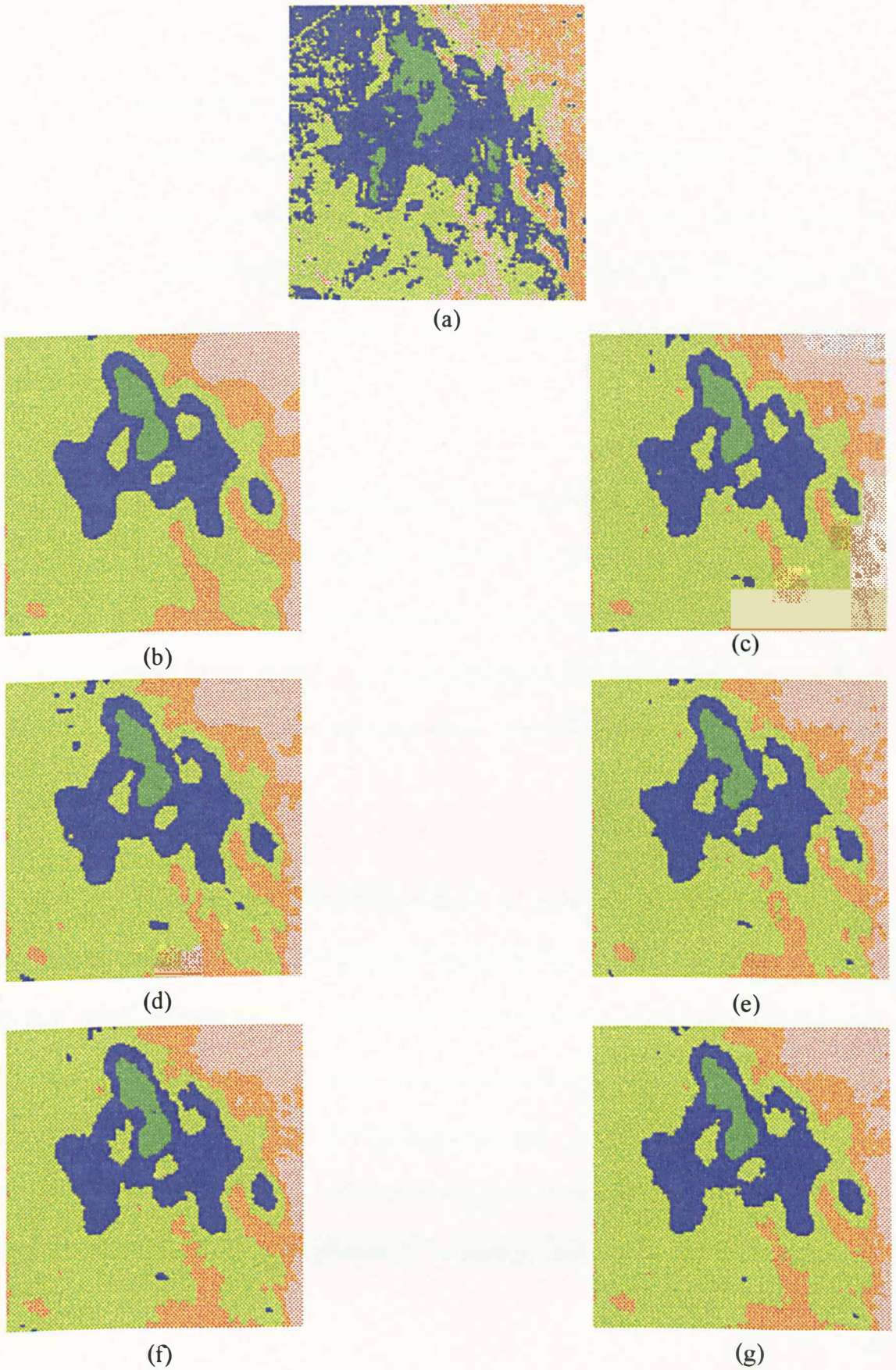


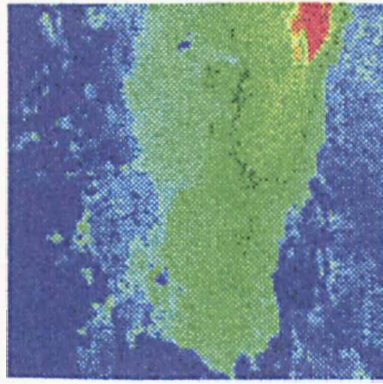
Figure 4.26: Unsupervised fuzzy k -means images of Band 4, (a) original (b) kernel (c) First band-pass (d) second band pass (e) third band pass (f) fourth band pass (g) fifth band pass (Segment II).

4.4.4.3 Test Segment III

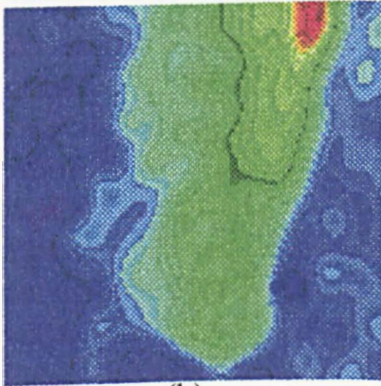
Most of the band-pass images (Figure 4.27 (b) to (g)) produced coherent zones and the most distinguishable features are in the kernel image. A clear linear feature, shown in these images, is self-evident. The sabkha unit, for instance, has a very low reflectance in the IR band- 7 region, which displayed as green, yellow, and orange colour. It also shows a clear black linear feature.

The light blue colour zone, shown in the raw data, is scattered and has complex patterns (Figure 4.27 (a)). In the filtered images especially the kernel band-pass image (Figure 4.27 (b)), there are consistent robust patterns. The green colour zone in the filtered images (Figure 4.27 (b) to (g)), was well established and can be discriminated from other areas. However, with the raw data image it is difficult to define and match the extent of the green zones

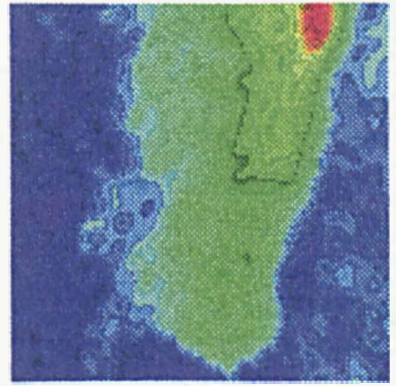
In images of figure 4.28, the improvements of coherent patterns in the spatial information are self-evident. The degree of similarity between the images and soil maps (MAW, 1986, 1995) is not fully convincing. For example the sabkha area, discriminated by its grey brightening, is displayed as two zones in the raw data (4.28 (a)). However, the surrounded zones are difficult to discriminate and it is difficult to interpret a linear feature. The established zones in the transformed band-pass images (Figure 4.28 (b) to (g)) are coherent and easily discriminated. In terms of linear features, the band-pass



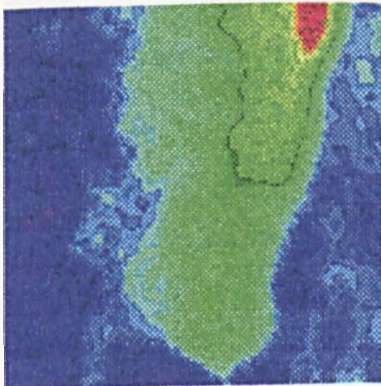
(a)



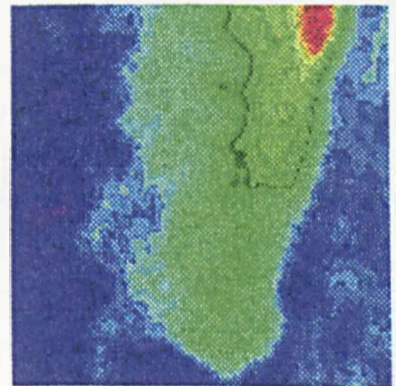
(b)



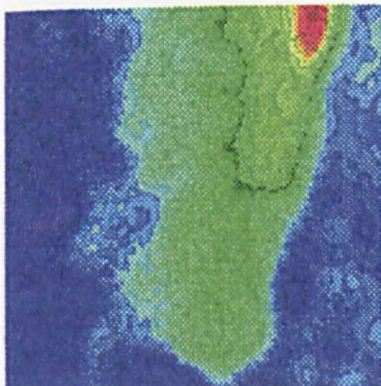
(c)



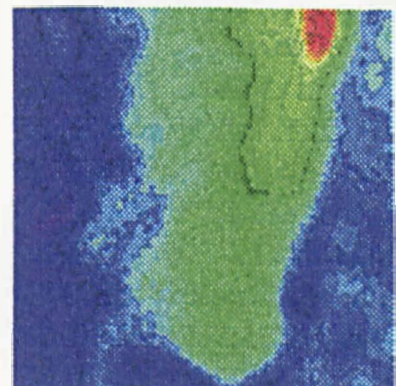
(d)



(e)



(f)

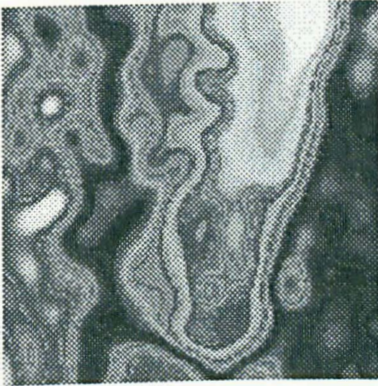


(g)

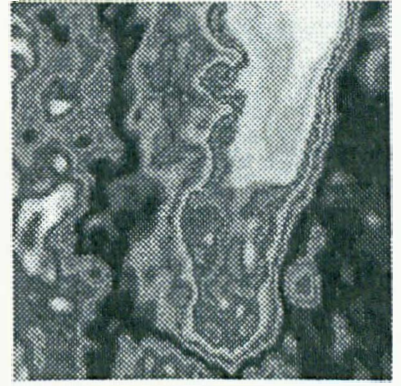
Figure 4.27: PCT images of Band 7, (a) original (b) kernel (c) First band-pass (d) second band pass (e) third band pass (f) fourth band pass (g) fifth band pass (Segment III).



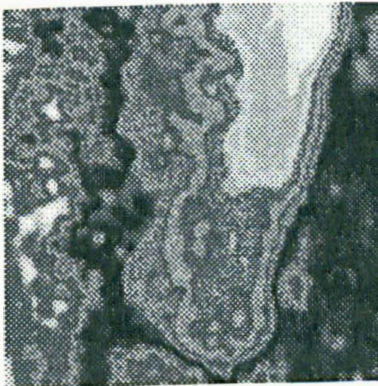
(a)



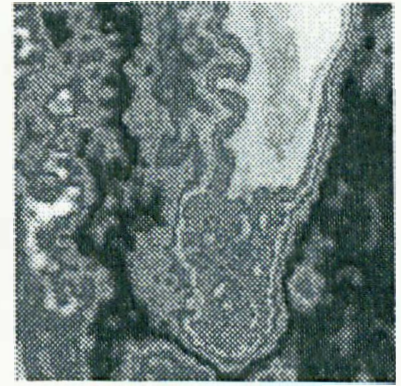
(b)



(c)



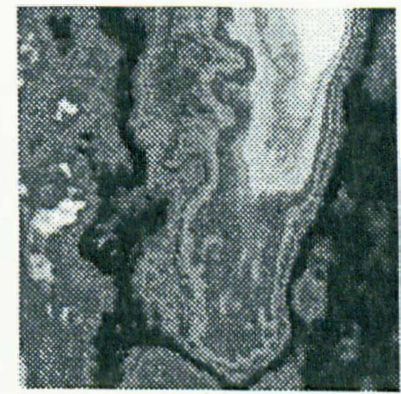
(d)



(e)

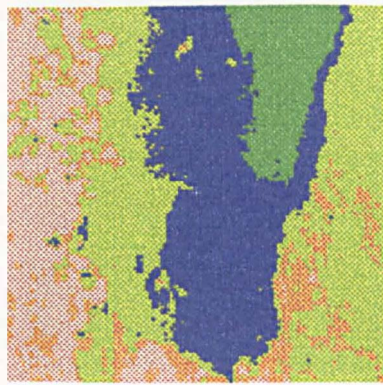


(f)



(g)

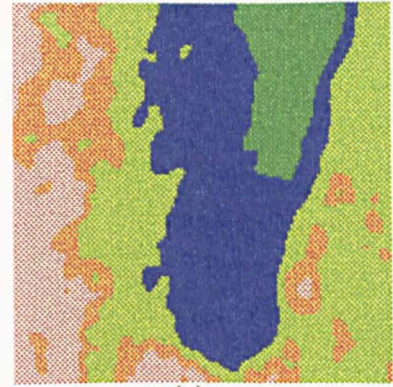
Figure 4.28: Infrequency images of Band 7, (a) original (b) kernel (c) First band-pass (d) second band pass (e) third band pass (f) fourth band pass (g) fifth band pass (Segment III).



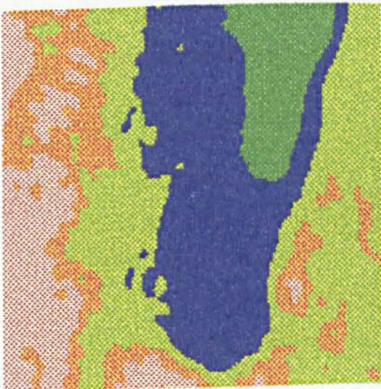
(a)



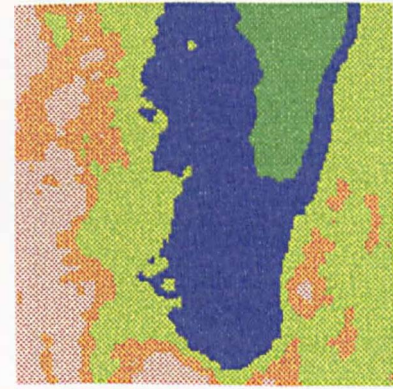
(b)



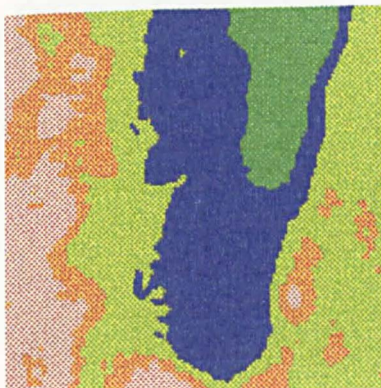
(c)



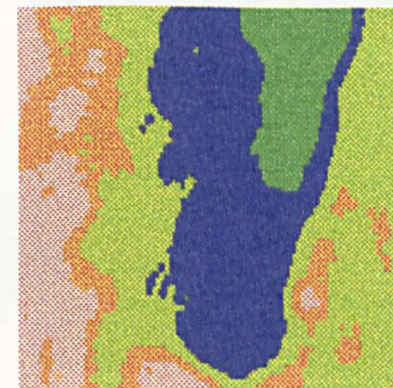
(d)



(e)

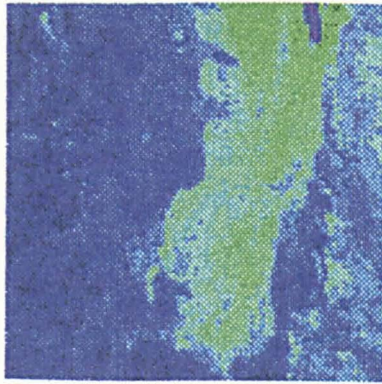


(f)

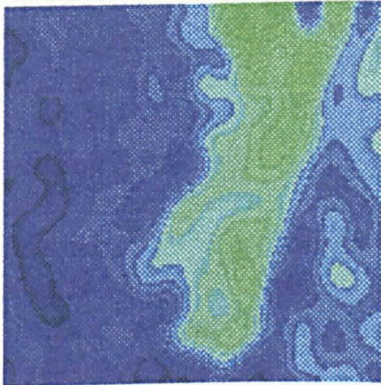


(g)

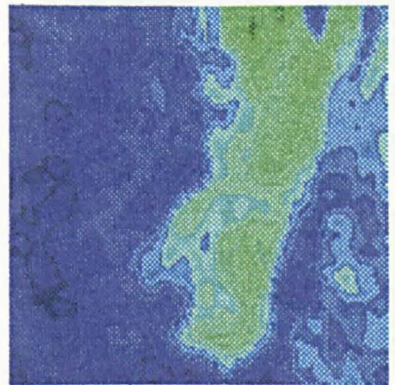
Figure 4.29: Unsupervised fuzzy k -means images of Band 7, (a) original (b) kernel (c) First band-pass (d) second band pass (e) third band pass (f) fourth band pass (g) fifth band pass (Segment III).



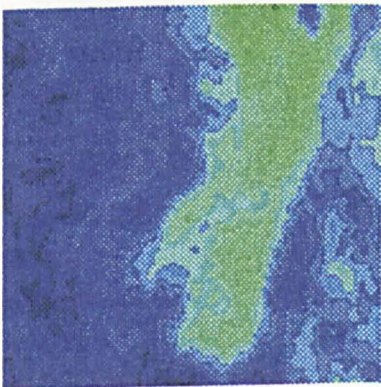
(a)



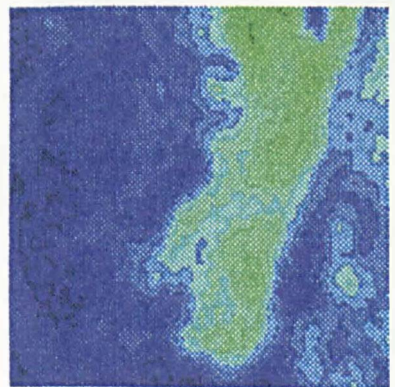
(b)



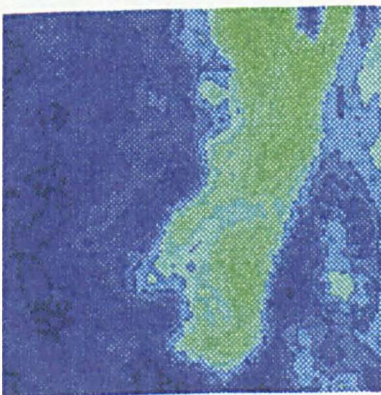
(c)



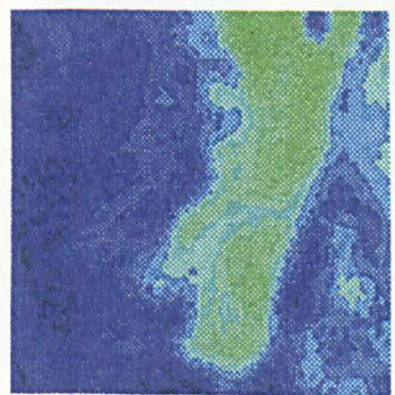
(d)



(e)

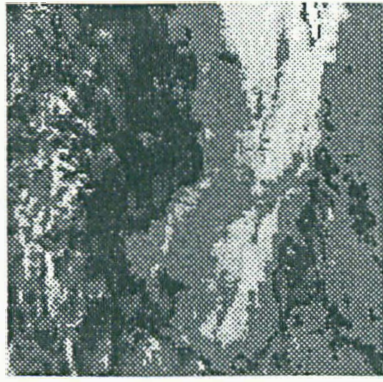


(f)



(g)

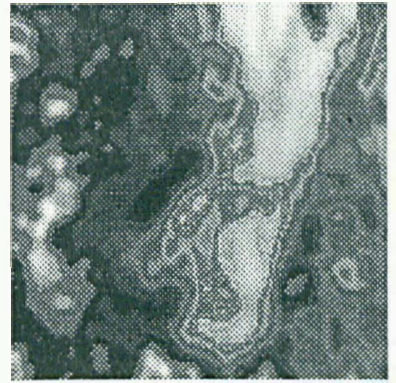
Figure 4.30:PCT images of Band 4, (a) original (b) kernel (c) First band-pass (d) second band pass (e) third band pass (f) fourth band pass (g) fifth band pass (Segment III).



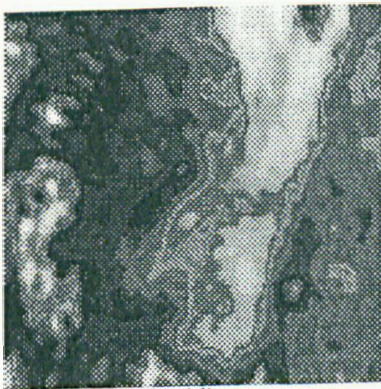
(a)



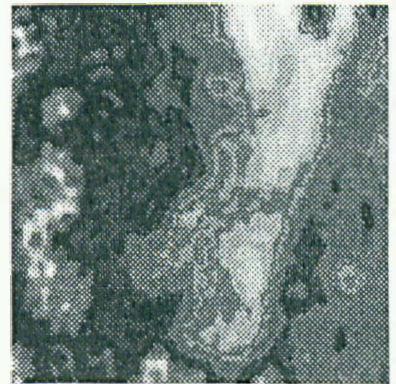
(b)



(c)



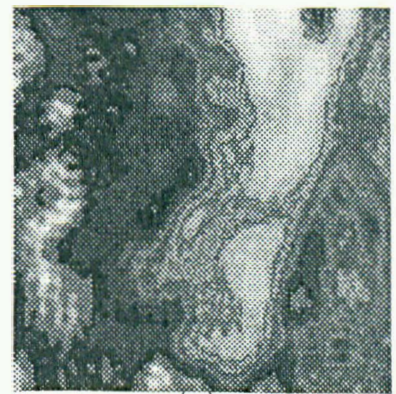
(d)



(e)

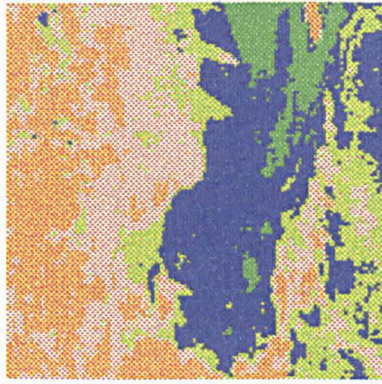


(f)

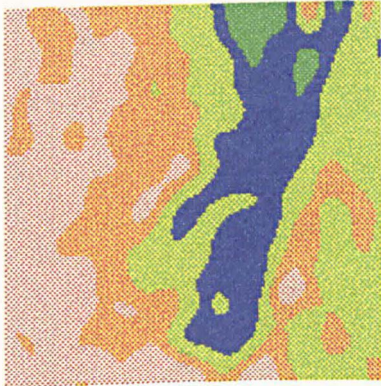


(g)

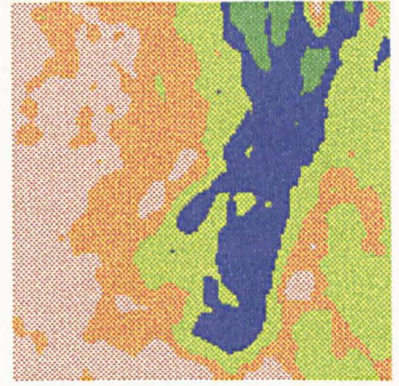
Figure 4.31: Infrequency images of Band 4, (a) original (b) kernel (c) First band-pass (d) second band pass (e) third band pass (f) fourth band pass (g) fifth band pass (Segment III).



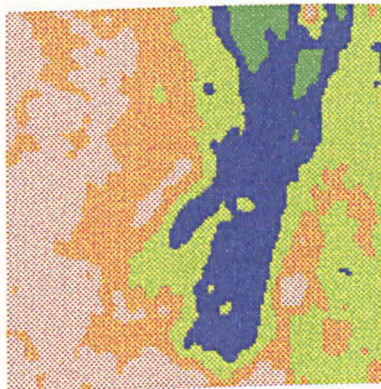
(a)



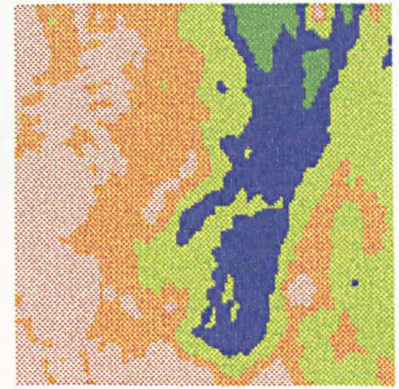
(b)



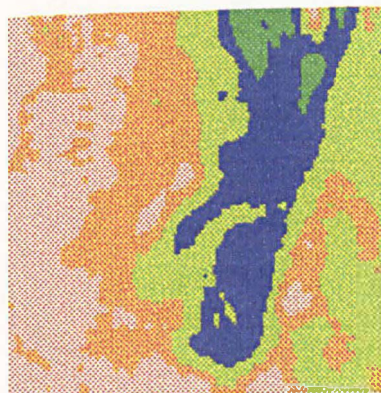
(c)



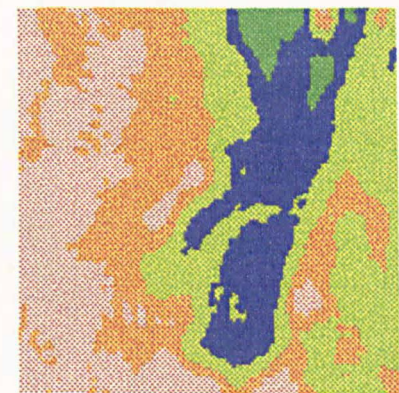
(d)



(e)



(f)



(g)

Figure 4.32: Unsupervised fuzzy k -means images of Band 4, (a) original (b) kernel (c) First band-pass (d) second band pass (e) third band pass (f) fourth band pass (g) fifth band pass (Segment III).

Table 4.4. Summary of the features identification of the inverse filtered images.

List landform	Soil type	PCT	Infrequency	Unsupervised clustering
Sabkha	Salorthid / Gypsic solochk	Simple identifiable units A thin linear areas as artefact unit	Simple identifiable units Clear thick linear feature zone	Two dominant units Clear thick border zone
Alluvial plain	Gypsiorthid / Calciorthid	Many simple identifiable zones within the landform	Clear identifiable linear features. Zones established within the landform	One dominant zone
Sand sheet and Dunes	Torripsamment	Simple identifiable zones and surrounded by linear features within the landform	Many clear zones within the landform	Simple identifiable zones within the landform
Gypsiferous pediplain	Gypsiorthid / Petric yypsisls	Somewhat complex identifiable zones and no evidence of linear features within the landform	Somewhat complex, no evidence of linear features	Approximately one dominant identifiable zone, few small zones within the landform

filter images produce clear and robust linear features especially in third and fourth band-pass images (Figure 4.28 (d) and (f)).

In cluster images, all the main soil areas are clear and there is some agreement with soil maps (MAW, 1986, 1995). In terms of linear features, the raw data presents a linear feature, but well defined in the band-pass images (figure 4.29 (b) to (g)). The elongated blue area between green colour area (sabkha) and light green area (alluvial plain) is well established where there might be a transitional soil zone.

There are few differences between features in Band 4 than in Band 7. The one feature that appeared somewhat different is the sabkha area as it is always different in other images (Figure 4.30). The features of the infrequency and the cluster images are similar in Band 7 with minor differences in other parts, but the overall results of Band 7 shows clearer features than Band 4 (Figures 4.31 and 4.32). Table 4.4 summarises the features identification of this spectral model.

4.6 Summary

In this chapter, the spectral analysis, which was based on the Fast Fourier Transform, was described. Using masking techniques in the analysis of spatial frequencies in the images, it is shown that low frequencies dominate the overall pattern. Generally complexity of image elements increases with addition of high frequencies and different parts of the image show different effects of specific frequency bands. Based on visual

interpretation, specific wavebands affect components of specific areas to different degrees. The use of spectral method, using masking techniques, together with the enhancement techniques has shown distinct features in the output images. Each enhancement has the capability of partitioning the data sets. Both PCT and infrequency enhancements show more features than the cluster method. The degree of producing coherent patterns was achieved. Both wavebands show similar results, but the overall results show that the features in band 7 are clearer than in Band 4.

The spatial spectral approach at one level confirms the portioning of test areas into the conventionally mapped units. However, it is shown that some areas are intrinsically more complex while others are well represented by the units at this scale. There is clear evidence that at this scale there are transition zones that are sufficiently extensive to be mapped as distinct units. Also there are clear linear features within zones. In addition the complexity of particular unit types is not consistent from one test segment to another.

CHAPTER 5

ARTIFICIAL NEURAL NETWORK MODELLING

5.1 Introduction

A neural network, considered as a non-linear regression model, has become a practical tool for use in many classification, pattern recognition, optimisation, and forecasting applications. An Artificial Neural network, in concept, is a connectionist model which requires processing of many inputs in parallel. In addition, in the light of memory, it is essentially content-addressable versus location-specific so that the contents of many locations contribute to the definition of values (Hewitson and Crane 1993; Atkinson and Tatnall, 1997; Bruzzone *et al.*, 1997).

Neural networks are modelled after the constructs of the human brain, wherein intelligence is stored in neural pathways as well as in memory. In artificial neural networks, knowledge is stored in the form of weights applied to node, that is, as multiplicative values to be applied to input. Instead of algorithms to determine values, a supervised network is presented with repeated examples of inputs and corresponding correct outputs and allowed self-learning (Beale and Jackson, 1991; Bischof *et al.*, 1992; Jarvis and Stuart, 1996; Poala and Schowengerdt, 1997).

5.2 Multilayer Perceptrons (MLP)

5.2.1 Introduction

The multilayer perceptrons are perhaps the most popular network architecture in use today, developed originally by Rumelhart and McClelland (1986) and discussed at length in most Neural Network text books such as Beale and Jackson (1991), Haykin (1994), and Bishop (1995). Each unit of a MLP computes a biased weighted sum of their inputs and passes this activation level through a transfer function to produce their output, and the units are arranged in a layered feed-forward topology (Aleksander and Morton, 1995; Gurney 1997). Thus, the network has a simple interpretation as a form of input-output model, with the weights and thresholds that are the free parameters of the model. Such units in each layer determine the function complexity. Important issues in MLP design include specification of the number of hidden layers and the number of units in these layers (Haykin, 1994; Bishop, 1995; Gurney, 1997; Hewitson and Crane, 1993).

The number of input and output units is defined by the problem. The number of hidden layers and units to use is far from clear. A good starting point in model design preferred by several researchers, is to use one hidden layer, with the number of units equal to half the sum of the number of input and output units (Key *et al.*, 1990; Benediktsson *et al.*, 1990a; Ripley, 1996; Benediktsson and Sveinsson , 1997).

5.2.2 Training Multilayer Perceptrons

Once the number of layers, and number of units in each layer, have been selected, the network's weights and thresholds must be set so as to minimise the prediction error made by the network. This is the role of the training algorithms. Most of the historical cases adjust the weights and thresholds in order to minimise the error. This process is equivalent to fitting the model represented by the network to the training data available (Beale and Jackson, 1991; Dreyer, 1993; Ripley, 1996). The error of particular configuration of the network can be determined by running all the training cases through the network, comparing the actual output generated with the desired or target outputs. The differences are combined together by an error function to give the network error. The most common error function is the sum-squared error, where the individual errors of output units on each case are squared and summed together (Hewitson and Crane, 1993; Aleksander and Morton, 1995; Bishop, 1995; Gurney, 1997).

In traditional modelling approaches, i. e. linear modelling, it is possible to algorithmically determine the model configuration which absolutely minimises this error. The price paid for the greater non-linear modelling power of neural networks is that, though the user can adjust a network to lower its error, they can never be sure that the error could not be lower still (Beale and Jackson, 1991; Haykin, 1994; Bishop, 1995).

Each of the N weights and thresholds of the network is taken to be a dimension in space. The $(N+1)$ th dimension is the network error. For any possible configuration of weights the error can be plotted in the $(N+1)$ th dimension, forming an error surface. The objective of network training is to find the lowest point in this multi-dimensional space. In a linear model, with sum-squared error function, the error surface is a parabola, which means that it is a smooth bowl-shape with a single minimum. Therefore, it is easy to locate the minimum (Beale and Jackson, 1991; Haykin, 1994; Bishop, 1995).

Neural network error surfaces are much more complex, and are characterised by a number of unhelpful features, such as local minima. It is not possible to analytically determine where the global minimum of the error surface is, and therefore neural network training is essentially an exploration of the error surface (Carling, 1992; Haykin, 1994; Fausett, 1994; Patterson, 1996). From an initially random configuration of weights and thresholds (i. e. a random point on the error surface), the training algorithms incrementally seek for global minimum (Fausett, 1994; Patterson, 1996). It can be achieved typically by calculating the gradient of the error surface at the current point, and then using that information to make a downhill move. Eventually, the algorithm stops in a low point, which may be a local minimum, but, on the other hand, could be the global minimum (Beale and Jackson, 1991; Bishop, 1995).

5.2.3 The Back Propagation Algorithm

The best-known example of a neural network-training algorithm is back propagation (Patterson, 1996; Haykin, 1994; Fausett, 1996). Modern second-order algorithms such as Conjugate Gradient Descent and Levenberg-Marquardt are substantially faster for many problems, but back propagation still has advantages in some circumstances, and is the easiest algorithm to understand. There are also heuristic modifications of back propagation, which work well for some problem domains, such as quick propagation and delta-bar-delta (Beale and Jackson, 1991; Aleksander and Morton, 1995; Gurney, 1997).

Most neural network methods are based on the minimisation of a cost function. The most commonly used optimisation approach applied for the minimisation is the gradient descent. Both the delta rule and the back propagation algorithm are derived by minimising the criterion function:

$$E = \sum_{p=1}^N \mathcal{E}_{p\varepsilon} = \frac{1}{2} \sum_{p=1}^N \sum_{j=1}^m (t_{pj} - o_{pj})^2$$

Where p is a pattern number, N is the sample size, t_{pj} is the desired output of the j th output neuron, o_{pj} is the actual output of the neuron and m is the number of output neuron.

In back propagation algorithm, the gradient vector of the error surface is calculated. The vector points in the direction of steepest descent from the current point, so by searching short distances, it can decrease the error. A sequence of such moves will eventually find minima of some sort. The difficult part is to decide how large the step should be (Beale and Jackson, 1991; Aleksander and Morton, 1995; Gurney, 1997). Large steps may converge more quickly, but may also overstep the solution or go off in the wrong direction. In neural network training, for example, is where the algorithm progresses very slowly along a steep, narrow, valley, bouncing from one side across to the other. In contrast, very small steps may go in the correct direction, but they also require a large number of iterations (Beale and Jackson, 1991; Aleksander and Morton, 1995; Gurney, 1997). In practice, the step size is proportional to the slope and to a special constant which is learning rate. The correct setting for the learning rate is application dependent, and is typically chosen by experiment, and it may also be time varying, and getting smaller as the algorithm progresses (Beale and Jackson, 1991; Aleksander and Morton, 1995; Gurney, 1997).

The algorithm is also usually modified by inclusion of a momentum term, and this encourages movement in a fixed direction, so that if several steps are taken in the same direction, the algorithm picks up speed. It gives the ability to escape local minima, and also to move rapidly over flat spots and plateaus (Haykin, 1994; Bishop, 1995). Therefore, the algorithm progresses iteratively through a number of epochs. On each epoch, the training cases are each submitted in turn to network, and target and actual

outputs compared and the error calculated (Haykin, 1994; Bishop, 1995). The error together with the error surface gradient is used to adjust the weights, and then the process repeats (Haykin, 1994; Bishop, 1995). The initial network configuration is random and training stops when a given number of epochs elapse, or when the error reaches an acceptable level, or when the error stops improving (Beale and Jackson, 1991; Aleksander and Morton, 1995; Gurney, 1997).

5.2.4 Over-fitting and Generalisation

The most desirable property of a network is its ability to generalise to new cases (Beale and Jackson, 1991; Aleksander and Morton, 1995; Gurney, 1997). In reality, the network is trained to minimise the error on the training set, and short of having a perfect and infinitely large training set, this is not the same thing as minimising the error on the real error surface (Haykin, 1994; Bishop, 1995).

The most important manifestation of this distinction is the problem of over-fitting (Haykin, 1994; Bishop, 1995). It is easiest to demonstrate this concept using polynomial curve fitting rather than neural networks, but the concept is precisely the same. The data is probably noisy, so that it is not necessarily expecting the best model to pass exactly through all the points (Haykin, 1994; Bishop, 1995). For instance, a low-order polynomial may not be sufficiently flexible to fit close to the points, whereas a high-order polynomial is actually too flexible, fitting the data exactly by adopting a highly eccentric shape that is actually unrelated to the underlying function (Haykin, 1994; Bishop, 1995).

Neural networks have precisely the same problem. A network with more weights models a more complex function, and therefore prone to over-fitting (Beale and Jackson, 1991; Aleksander and Morton, 1995; Gurney, 1997). However, a network with fewer weights may not be sufficiently powerful to model the underlying function. For example, networks with no hidden layers actually model a simple linear function. On the contrary, larger networks will almost invariably achieve a lower error eventually, but may indicate over-fitting rather than good modelling, so that a cross-verification should be used (Beale and Jackson, 1991; Aleksander and Morton, 1995; Gurney, 1997).

Some of the training cases are reserved, and not actually used for training in the back propagation algorithm (Beale and Jackson, 1991; Aleksander and Morton, 1995; Gurney, 1997). They are used, instead, to keep an independent check on the progress of the algorithm. It is invariably the case that the initial performance of the network on training and verification sets is the same. As training progresses, the training error naturally drops, and providing training is minimising the true error function, the verification error drops too (Beale and Jackson, 1991; Aleksander and Morton, 1995; Gurney, 1997). However, if the verification stops dropping, or indeed starts to rise, this indicates that the network is starting to over-fit the data, and training should cease (Gurney, 1997). When over-fitting occurs during the training process like this it is called over-learning (Aleksander and Morton, 1995). In this case, it is usually advisable to decrease the number of hidden units and/or hidden layers, as the network is over-

powerful for the problem at hand. In contrast, if the network is not sufficiently powerful to model the underlying function, over-learning is not likely to occur, and neither training nor verification errors will drop to a satisfactory level (Haykin, 1994; Bishop, 1995).

A problem with this approach of repeated experimentation is that the verification set does actually play a key role in selecting the model, which means that it is actually part of the training process (Haykin, 1994; Bishop, 1995). Its reliability as an independent guide to performance of the model is therefore compromised with sufficient experiments. In order to add confidence in the performance of the final model, it is therefore normal practice to reserve a third set of cases, which is known as a test set. The final model is tested with test set data, to ensure that the results on verification and training set are real, and not artefacts of the training process. Of course, to fulfil this role properly the test set should be used only once, if it is in turn used to adjust and reiterate the training process, it effectively becomes verification data (Haykin, 1994; Bishop, 1995).

5.2.5 Other Neural Networks

5.2.5.1 Radial Basis Function Networks

Weights and threshold define MLP units, which together give the equation of the defining line, and the rate of fall-off of the function from that line. Before application of the sigmoid activation function, the activation level of the unit is a hyperplane. In

contrast, its centre point and a radius define a radial unit. A point in N dimensional space is defined using N numbers, which exactly corresponds to the number of weights in a linear unit, so the centre of a radial unit is stored as weights. The radius or (deviation) value is stored as the threshold (Beale and Jackson, 1991; Aleksander and Morton, 1995; Gurney, 1997). It is worth emphasizing that the weights and thresholds in a radial unit are actually entirely different to those in a linear unit. The terminology here is critical and must be remembered that the radial weights really form a point, and a radial threshold is really a deviation (Haykin, 1994; Bishop, 1995).

A radial basis function network (RBF), therefore, has a hidden layer of radial units, each actually necessary to have more than one hidden layer to model any shape of function. And, then it turns out to be quite sufficient to use linear combination of these outputs. The RBF has an output layer containing linear units with linear activation function (Haykin, 1994; Bishop, 1995).

RBF networks have a number of advantages over MLPs. Firstly, RBFs, can model any non-linear function using a single hidden layer, which removes some design-decisions about numbers of layers. Secondly, the simple linear transformation in the output layer can be optimised fully using traditional linear modelling techniques, which are fast and do not suffer from problems such as local minima, so that RBF networks can therefore be trained extremely quickly (Beale and Jackson, 1991; Aleksander and Morton, 1995; Gurney, 1997). On the other hand, before linear optimisation can be applied to the

output layer of an RBF network, the number of radial units must be decided, and then centres and deviations must be set. Although it is much faster than MLP training, the algorithms to do this are no less prone to discovering sub-optimal combinations (Haykin, 1994; Bishop, 1995).

5.2.5.2 Kohonen Networks

Kohonen networks are used quite differently to the other networks. Whereas all other networks are designed for supervised learning tasks, Kohonen networks are designed primarily for unsupervised learning (Fausett, 1994; Haykin, 1994; Patterson, 1996). Whereas in supervised learning the training data set contains cases featuring input variables together with the associated outputs, in unsupervised learning the training data set contains only input variables (Haykin, 1994; Bishop, 1995).

One possible use is therefore in exploratory data analysis (Ito and Omatu, 1997). The Kohonen network can learn to recognize clusters of data, and can also relate similar classes to each other. The user can build up an understanding of the data, which is used to refine the network. As classes of data are recognized, they can be labeled, so that the network becomes capable of classification tasks. Kohonen networks can also be used for classification when output classes are immediately available, and the advantage in this case is the ability to highlight similarities between classes (Beale and Jackson, 1991; Haykin, 1994; Bishop, 1995).

A Kohonen network has only two layers, and they are the input layer and an output layer which known as the topological map layer. The units in the topological map layer are laid out in space typically in two dimensions. Kohonen networks are trained using an iterative algorithm. Starting with initially random set of radial centres, the algorithm gradually adjusts them to reflect the clustering of the training data (Beale and Jackson, 1991; Haykin, 1994; Bishop, 1995). Since there are no known application of ANN in image processing which deal with texture models, the discussion which follows examines the features of ANN and benefits of ANN through a consideration of its use in image processing.

5.3 ANN in Image Processing

ANN is widely used in image processing as a classification algorithm. There are many studies which have shown that the artificial neural network technique produced similar or superior classification results to those of the conventional statistical classifiers (Key *et al.*, 1989; Liu and Xiao 1991; Heermann and Khazenie 1992; Li *et al.*, 1993; Paola and Schowengerdt 1994; Yoshida and Omatu 1994). The increase in accuracy can be attributed to the using of multi-source data, i.e. when texture and ancillary data are used (Fisher *et al.*, 1994; Bruzzone *et al.*, 1997; Mather *et al.*, 1998; Lee *et al.*, 1987; Wang 1993; Zhuang *et al.*, 1991). With multi-source data the distributions tend to be less regular and for this reason the non-parametric neural network method might be a better choice for parameter estimation (Benediktsson *et al.*, 1990 and 1993).

One of the interesting findings of the feasibility of using ANN is that minimal training sets are satisfactory for neural network classifiers (Hepner *et al.*, 1990; Ritter and Hepner, 1990). According to Key *et al.* (1990), this is quite possible because a statistical classifier does not have enough data to describe the parameters of assumed distribution. However, Benediktsson *et al.* (1990a, 1990b, and 1998) and Bichof *et al.* (1992) preferred using a conventional statistical classifier to an artificial neural network when the distribution of the data is well known. On the contrary, Key *et al.* (1989, 1990) pointed out that the artificial neural network may have great flexibility in classification of pixels in the data set that differ significantly from those in the selected training sets. Furthermore, the neural network has the power for a complex data set of differentiating between classes, and this capability can be applied to very complex data sets, which have shapeless distributions (Fierens *et al.*, 1994; Paola and Schowengerdt, 1994). In general, the greater generalisation capability of the neural network allows extension to images not used in the training. For instance, Key *et al.* (1990) stated that the neural network correctly classified a much higher percentage of imagery collected on a second date than the maximum likelihood method.

These studies show clearly the power of ANN algorithms in dealing with complex non-linear relations and in allocating value with poor training data sets. ANN models are used in this study not to classify images but to model image texture. ANN models are not known to have been used to model texture of images for earth resource applications.

There are number of algorithm for measuring texture used for images in the visible and infrared wavebands and for radar images. These are, however, simple linear functions of image properties. A simple ANN model is developed here in order to address this problem (chapter 3, section 3.3).

5.4 Experimental Strategies

A simple segmentation of an image of part of Al-Ahsa region was used as a test data sets. The subsets I, II and III, which are composed of 128 lines \times 128 pixels, of Landsat Thematic Mapper (TM) data in bands 4 and 7 were used.

5.4.1 Convolution filter model

The neural network was configured as a fully interconnected back propagation linkage at three layers. The input layer was composed of i) $3 \times 3 \times 1$ (Band 7), ii) $3 \times 3 \times 1$ (Band 4) array of neurones. This provides a 3×3 pixel window to move across the TM data assuring a simultaneous consideration of texture as well as spectral decision space parameters. Using the 3×3 window of input neurones allowed the network to assimilate data of spatially adjacent pixels in both the training and classification operations.

The second layer was a single, which is known as a hidden layer, 5 neurones for both band 4 and 7. Typically the hidden layers of neurones capture low-level features, such as presence of a simple pattern in a single band, or some weighted average of several

spectral bands. Successive layers of neurones then may use the signals from neurones in the preceding layers to form more complex precepts, which may be associated more closely with desired classification in the training set. Several researchers have determined that the number of hidden layers and the number of neural units per layer greatly affect the performance of neural networks (Rumelhart *et al.*, 1986; Gorman and Sejnowski, 1988).

The output layer is composed of three neurones (Three different soil areas) and 4 neurones (Four different areas) or 5 neurones (Four areas with one duplicated) representing the target classes of landscape that were to be produced by the network.

5.4.2 Training Set Strategy

To describe the soil units with respect to complex elements as well as a linear feature in between, the training template of bitmaps were created. The area between different landforms was traced and part of it digitised on screen over the original images, and a selected training set of each land unit was derived representing different types of soil landscape units, typically from one to two blocks of around 100 pixels in size. Therefore, a training set-up that establishes sensitive clustering is optimum. The selection of four training areas (ABCD) is based on the result of unsupervised fuzzy *k*-means, and then by a selective inclusion set of training areas (i.e. AABCD, ABBCD, ABCCD, and ABCDD) and exclusion set of training areas (i.e. ABC, ABD, ACD, and BCD). These training set-ups are used to examine the effect of different areas on the

whole image texture and hence to assess if the resulting textural map represents real features or artefacts.

5.5 Results and Discussions

5.5.1 Introduction

The ANN models as described earlier in this chapter were applied to bands 4 and 7 of Al-Ahsa data sets (Test areas I, II and III). There were three test segments selected for this particular investigation, and the size of each segment is 128 rows by 128 columns.

The first results of the ANN modelling procedure are expressed as images of predicted values of each pixel based on its relation to its eight neighbour pixels. These images since they present pixel values in relation to a 3×3 area that surrounds them can be looked at as images of texture of reflectance. However, predicted pixel values will depend in the first place on the range of values in the 3×3 set. Thus, differences in texture across the image cannot be distinguished from differences of sets of values across the image. In order to eliminate this effect, the first image pixel values are divided by the original values. The resulting output image is then more a direct function of texture. Differences in values of the output image are differences in the degree to which the whole image ANN model does not fit the local situation. The assessment of texture image results is based first on a consideration of image structures such as mean and standard deviation, assuring a normal frequency distribution of Digital image

Numbers and secondly on a consideration of images subject to enhancement techniques which are determined experimentally.

5.5.2 Image Statistics

The output images were compared in terms of image statistics and histograms. The output images relate to training areas of the image A, B, C, and D. the combinations of training sets considered are: (i) ABCD for the four areas, (ii) ABC, ABD, ACD, and BCD for three areas, and (iii) AABCD, ABBCD, ABCCD, and ABCDD. The table of image statistics for both bands 4 and 7 shows wide deviations in mean and standard deviations of digital number in response to different training area set-ups. For Band 4 mean values differ between 20.4 and 40.2 and standard deviations for these means are 4.07 and 21.2. Wide fluctuations in means can perhaps be expected with an output which is computed as a division of two images (see tables 5.1, 5.2, 5.3).

Inclusion and exclusion of areas have profound effects on the frequency histogram of the output images. Excluding the training area for zones A and B produce two radically different histograms with significant differences in the numbers of peaks, their degree of separation and their Kurtosis. Excluding the training area for zones C and D have smaller effects on the histograms. Conversely, inclusion the training area for A and B produce marked changes in the histograms. Here too are differences in the number of peaks and their separation and kurtosis. Whereas inclusion of the training area for C and D does not have substantial effects in relation to the histograms of Bands 4 and 7 with

Table 5.1. Image statistics of segment I.

Test-I	Mean	St. deviation	Minimum	Maximum
ABCD-4	29.23	8.58	10.00	68.00
ABCD-7	28.67	6.83	7.00	53.00
ABC-4	34.81	6.52	15.00	79.00
ABC-7	33.74	5.96	7.00	68.00
ABD-4	29.69	8.69	13.00	77.00
ABD-7	27.78	6.87	7.00	54.00
ACD-4	36.13	7.93	13.00	79.00
ACD-7	35.91	10.01	7.00	53.00
BCD-4	40.26	21.21	2.00	98.00
BCD-7	40.26	21.21	2.00	98.00
AABCD-4	21.70	6.96	8.00	59.00
AABCD-7	20.40	4.07	4.00	41.00
ABBCD-4	27.30	9.66	8.00	66.00
ABBCD-7	24.77	7.37	5.00	53.00
ABCCD-4	28.19	10.03	8.00	77.00
ABCCD-7	26.42	8.41	5.00	49.00
ABCDD-4	29.61	9.18	10.00	77.00
ABCDD-7	28.26	7.91	7.00	53.00

Table 5.2. Image statistics of segment II.

Test-II	Mean	St. deviation	Minimum	Maximum
ABCD-4	21.28	7.31	7.00	59.00
ABCD-7	20.60	6.29	3.00	49.00
ABC-4	25.93	5.28	17.00	66.00
ABC-7	26.28	4.09	7.00	58.00
ABD-4	21.78	7.00	7.00	60.00
ABD-7	20.90	5.66	3.00	49.00
ACD-4	20.75	7.97	7.00	59.00
ACD-7	21.97	9.35	4.00	49.00
BCD-4	32.56	18.30	6.00	79.00
BCD-7	34.43	14.86	7.00	79.00
AABCD-4	18.28	4.36	10.00	66.00
AABCD-7	17.65	4.21	4.00	73.00
ABBCD-4	20.42	7.73	7.00	67.00
ABBCD-7	16.67	5.67	2.00	49.00
ABCCD-4	21.48	7.49	5.00	60.00
ABCCD-7	19.53	6.97	2.00	49.00
ABCDD-4	21.72	6.07	7.00	59.00
ABCDD-7	18.70	6.08	3.00	49.00

Table 5.3. Image statistics of segment III.

Test-III	Mean	St. deviation	Minimum	Maximum
ABCD-4	33.14	16.58	10.00	98.00
ABCD-7	29.09	13.02	6.00	67.00
ABC-4	41.44	11.53	19.00	98.00
ABC-7	37.48	10.39	6.00	81.00
ABD-4	37.05	14.69	12.00	95.00
ABD-7	27.54	13.99	6.00	68.00
ACD-4	35.39	13.59	12.00	98.00
ACD-7	30.31	9.02	6.00	62.00
BCD-4	39.46	23.90	11.00	105.00
BCD-7	39.19	29.65	2.00	102.00
AABCD-4	32.08	12.17	8.00	84.00
AABCD-7	24.82	8.52	6.00	59.00
ABB CD-4	28.31	17.55	8.00	98.00
ABB CD-7	24.75	13.42	6.00	64.00
ABCCD-4	37.24	15.95	9.00	98.00
ABCCD-7	26.79	14.26	6.00	61.00
ABCDD-4	32.12	15.99	9.00	95.00
ABCDD-7	27.85	12.84	6.00	67.00

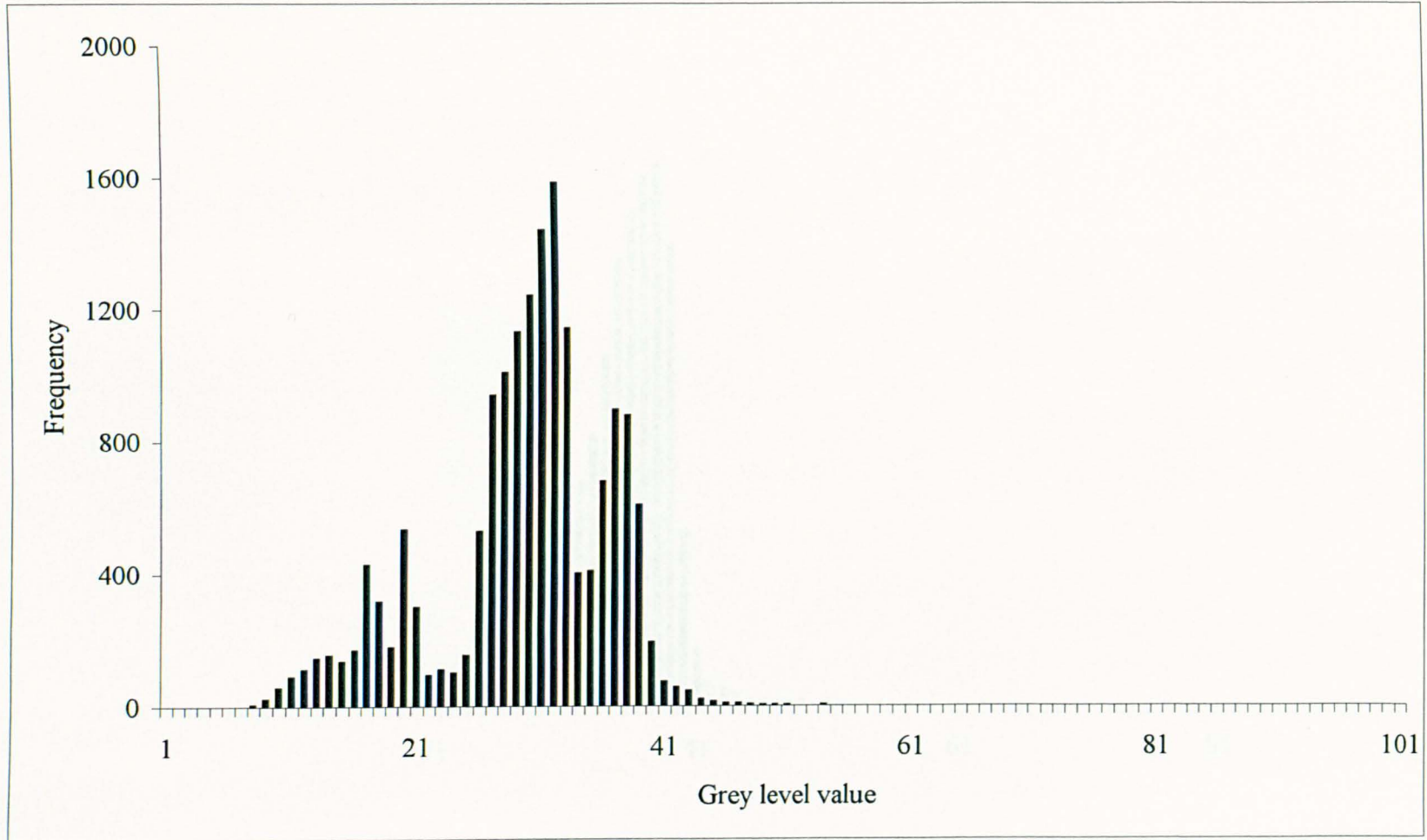


Figure 5.1: Histogram of the second output of the ABCD image (Band 7, Segment I).

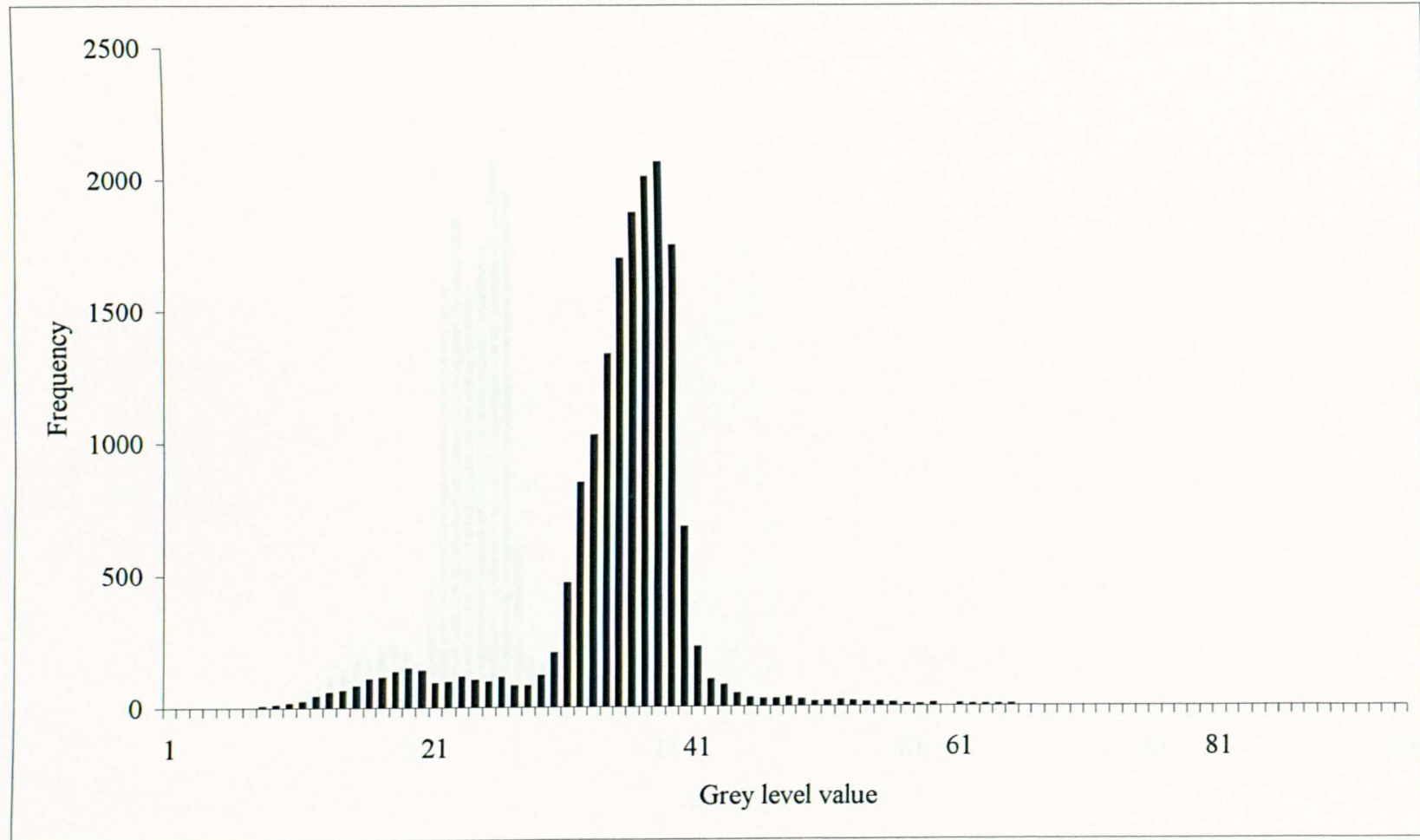


Figure 5.2: Histogram of the second output of the ABC image (Band7, segment I).

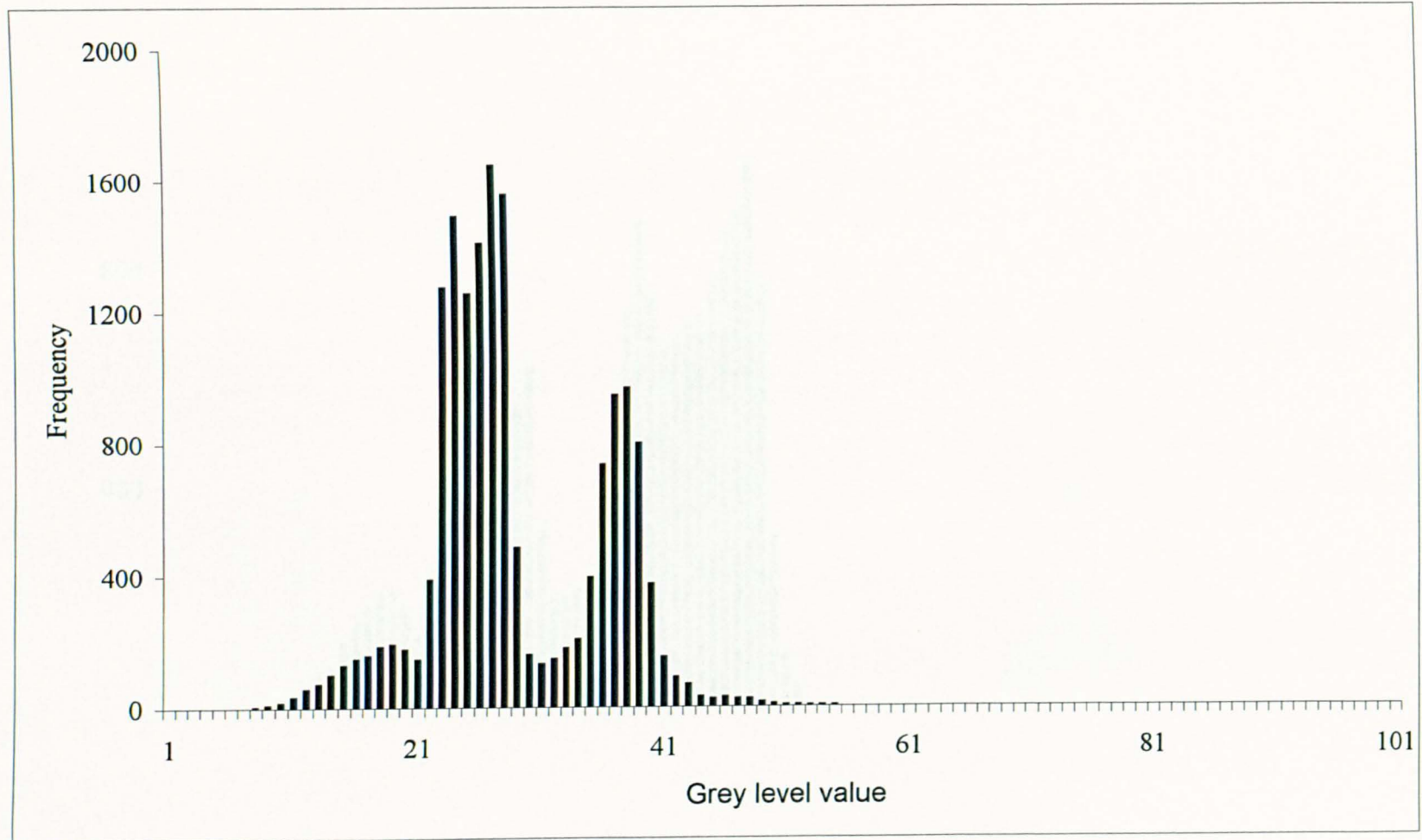


Figure 5.3: Histogram of the second output of the ABD image (Band 7, segment I).

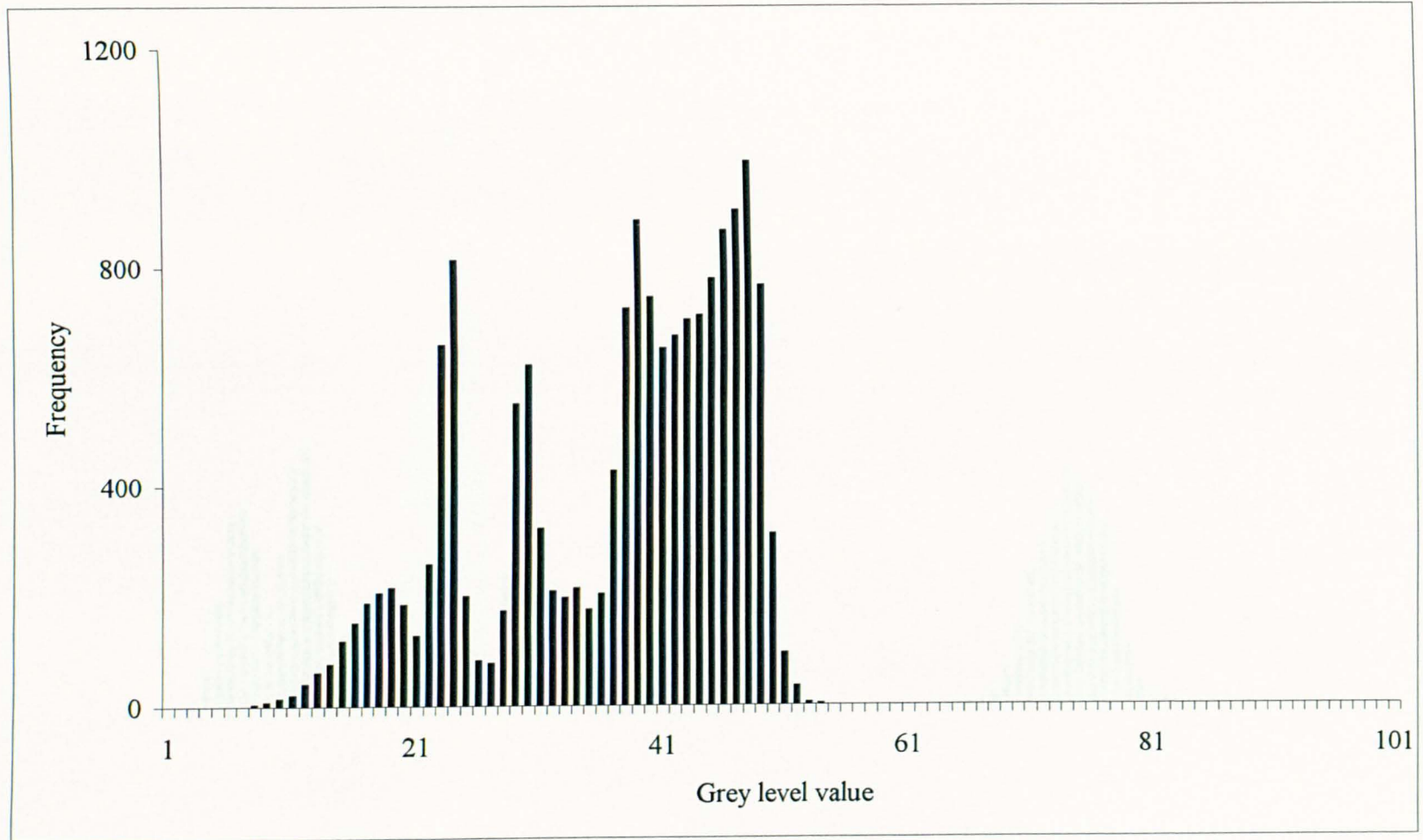


Figure 5.4: Histogram of the second output of the ACD image (Band 7, segment I).

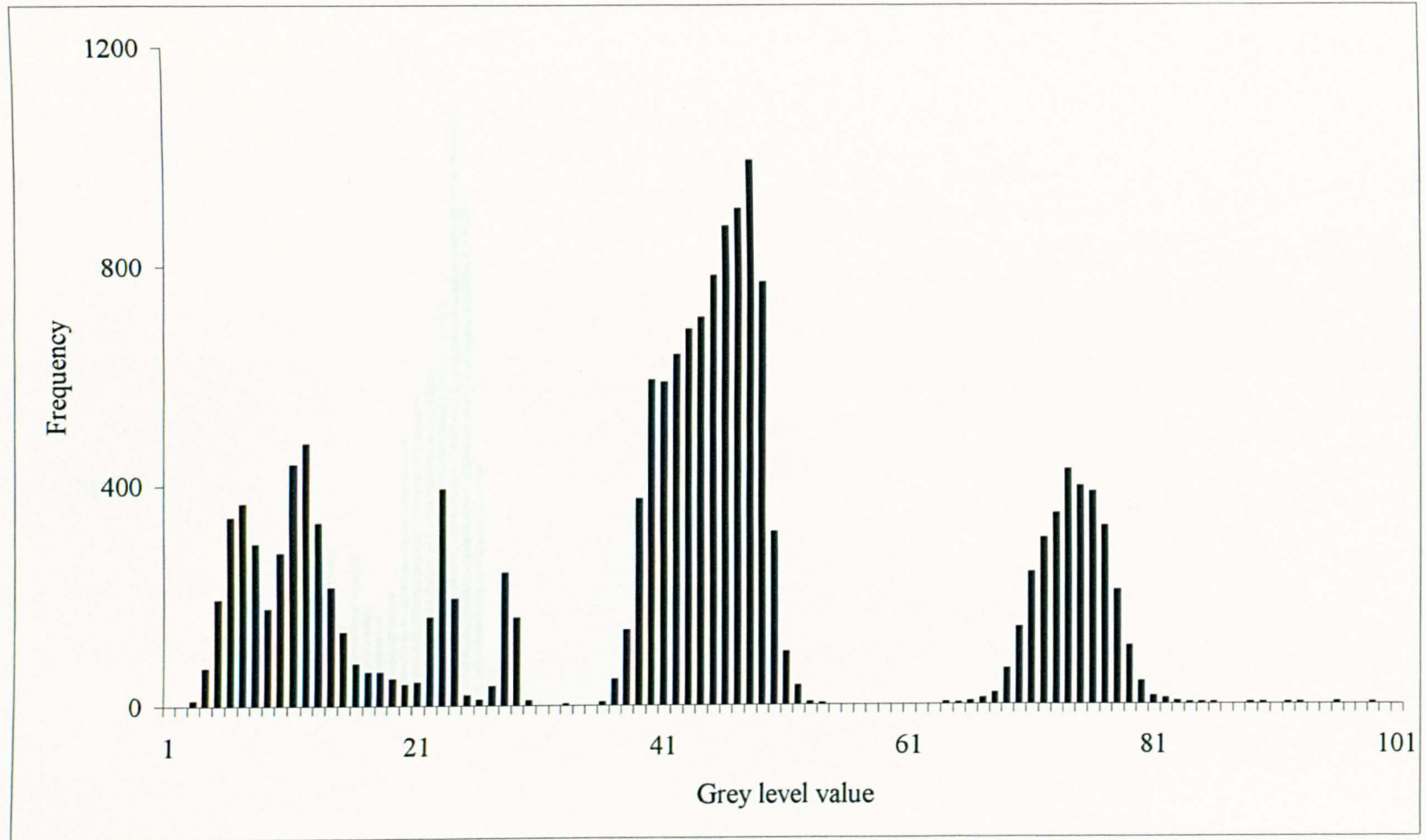


Figure 5.5: Histogram of the second output of the BCD image (Band 7, segment I).

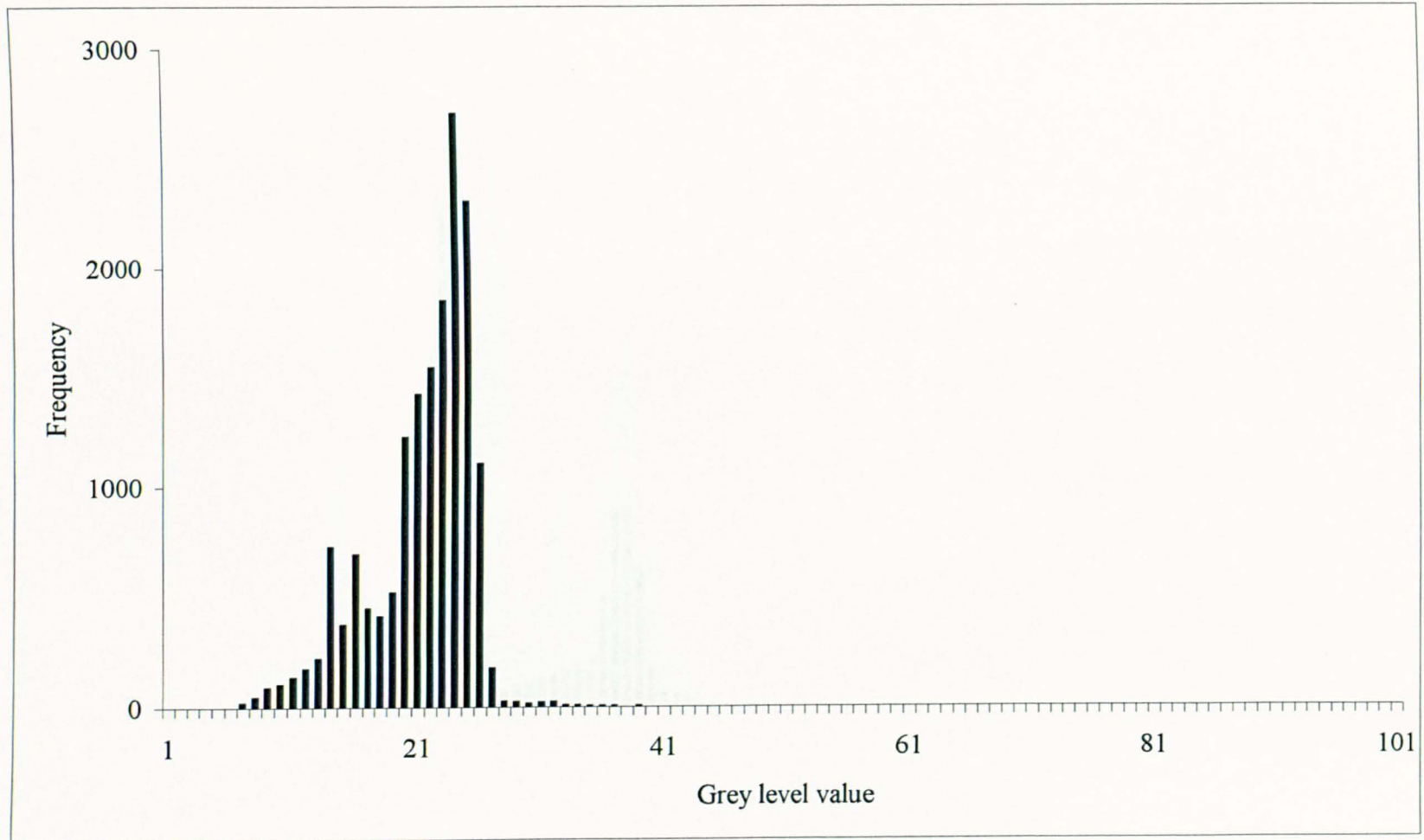


Figure 5.6: Histogram of the second output of the AABCD image (Band 7, segment I).

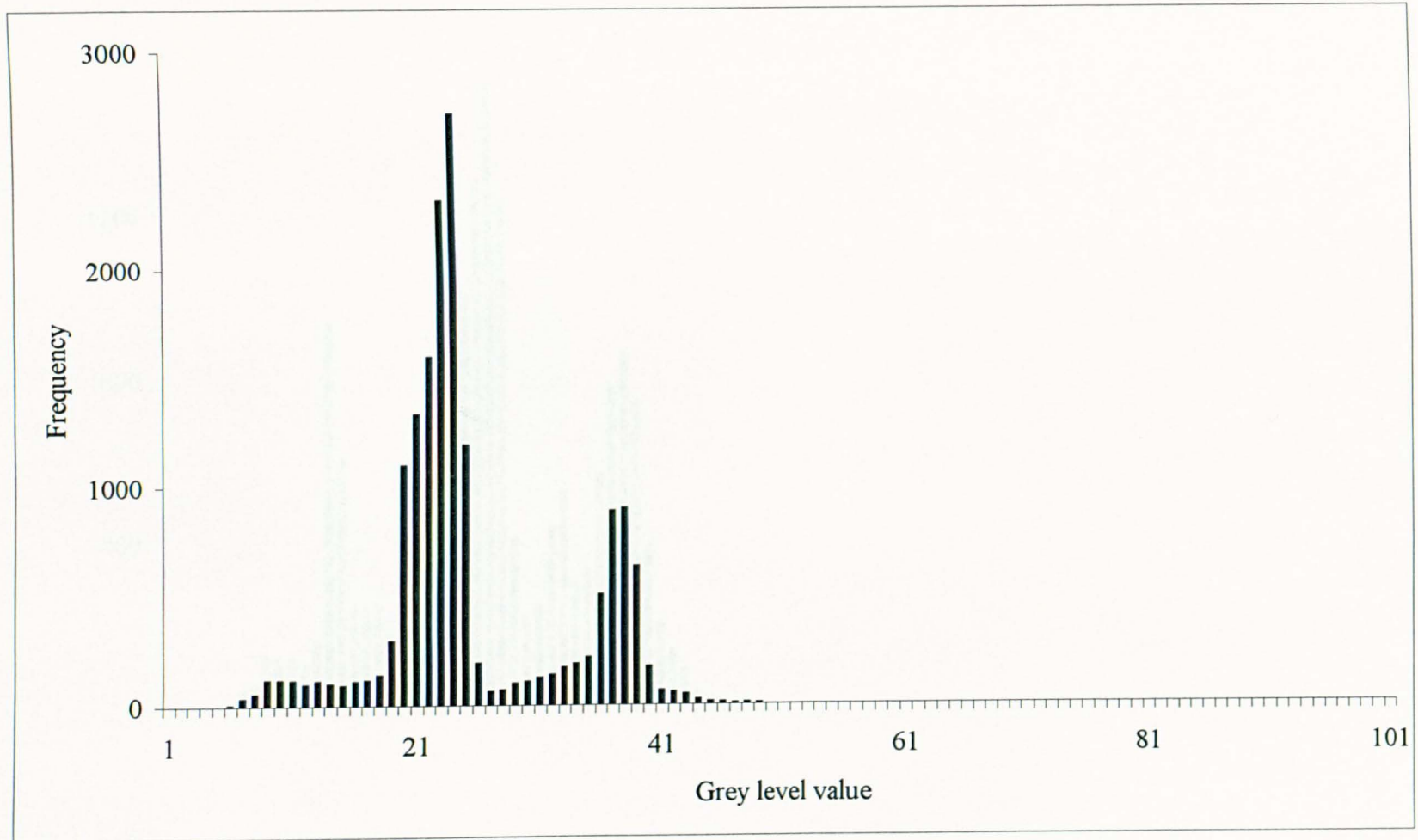


Figure 5.7: Histogram of the second output of the ABBCD image (Band 7, segment I).

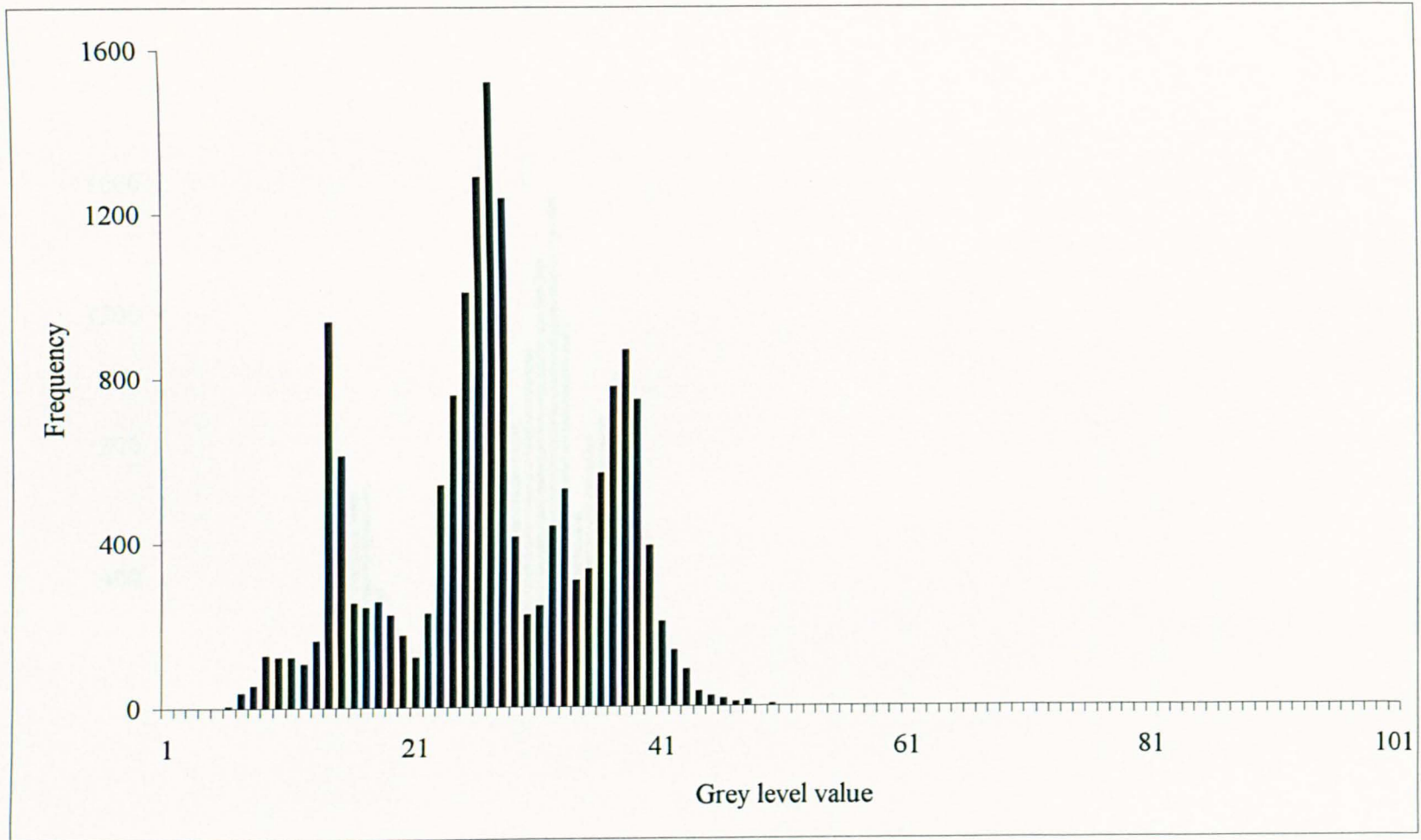


Figure 5.8: Histogram of the second output of the ABCCD image (Band 7, segment I).

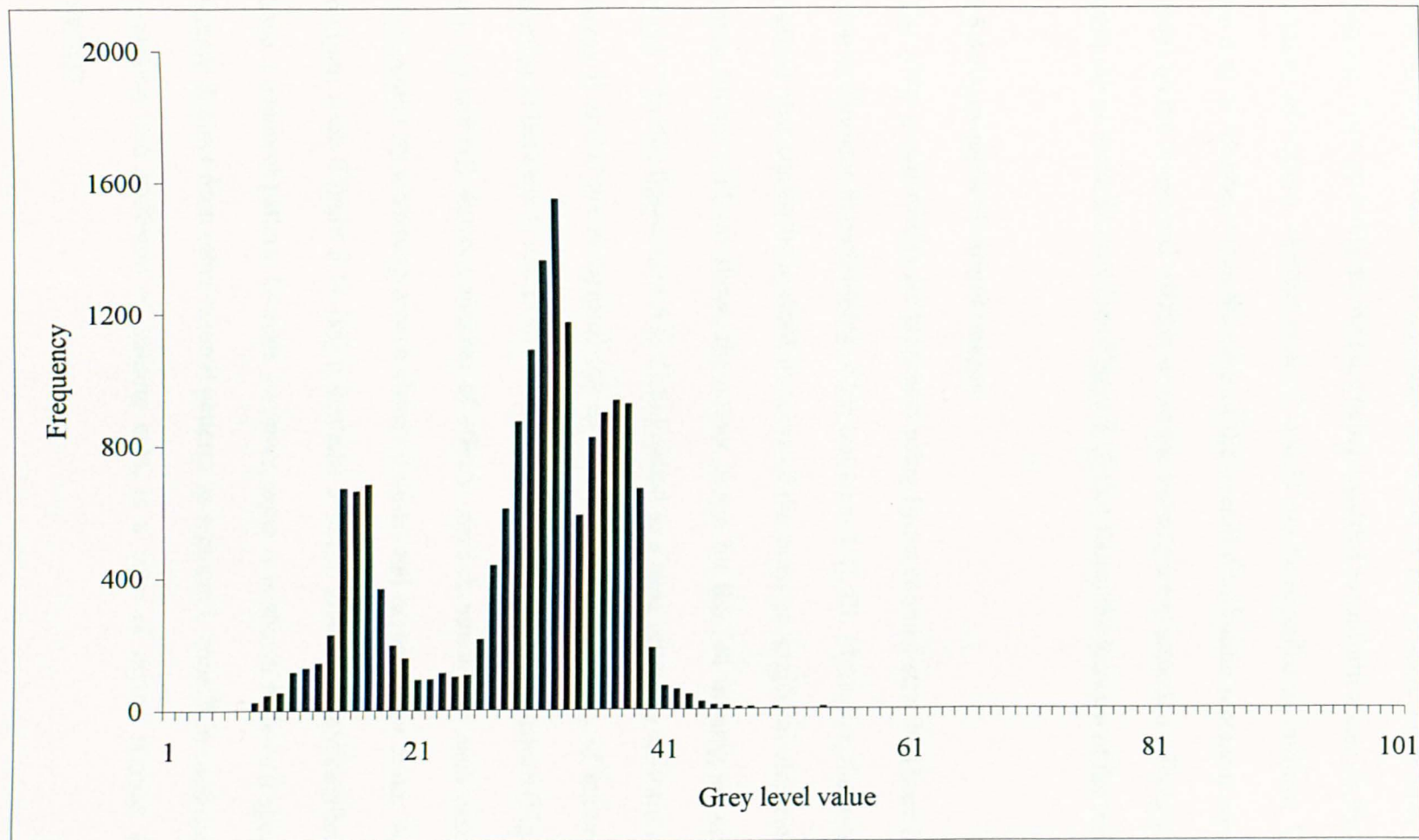
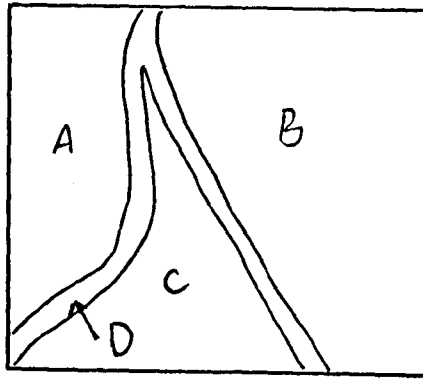


Figure 5.9: Histogram of the second output of the ABCDD image (Band 7, segment I).

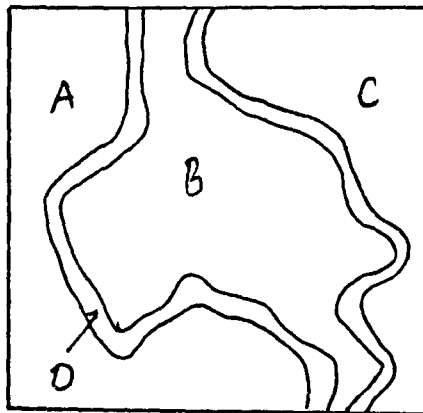
training areas ABCD. This indicates that areas A and B have more than one textural element. They probably are best not being regarded as uniform zones on the basis of this measure of texture, whereas zones C and D can be regarded as uniform. The question remains of whether or not the parts of the overall distribution represent coherent spatial zones on the image and whether or not the training areas selection affects the mapping of textural zones (see Figure 5.10 that shows the location of the training areas).

5.5.3 Assessment of output images

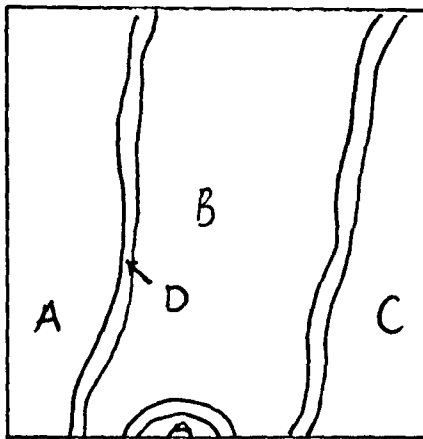
The ANN image results are presented using linear contrast stretch. These images show clear differences in partitioning of the test areas I, II, III. Moreover, the images produce patterns that can be interpreted in terms of the main geographical elements of the test areas. Figure 5.11 (a) shows the output image for the full training set-up ABCD for Band 7. In this figure, area A is distinguished as a clear relatively uniform texture zone. Areas B and C are recognised but there is considerable mixing of texture zones and confusion between C and D and B and D. Exclusion of training zones (Figure 5.11 (c), (e), (g) and (i)) shows a number of effects. Area A remains in each case where it is represented by a training area, a clearly defined and homogenous zone. With a double training zone (Figure 5.11 (k)) it contains a larger number of unclassified pixels that have a coherent pattern. Overall, however, zone A is shown to have a specific textural pattern distinct from other textural patterns in segment I. zone B in each case, with both exclusion and inclusion of training area, is a zone of mixed texture. One textural element



I



II



III

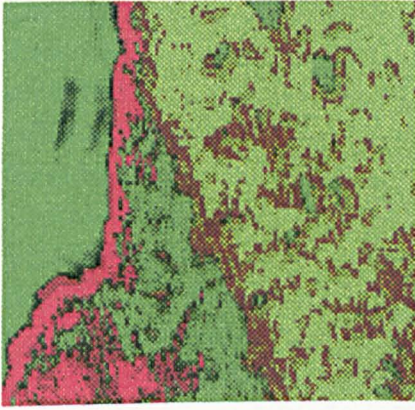
Figure 5.10: Illustration diagram of the three segments showing the four zones A, B, C, and D.

is shown in figure 5.11 (a), (g), (i), (k), (m), and (q) to form a boundary of transition zone between B and C. Zone C is also one of mixed texture with a boundary or transition zone apparent in figure 5.10 (a), (e), (k), (m), and (q). Double training areas in zone D confirms (Figure 5.11 (q)) the distinct nature of boundary zones. Confusion between zones arising from exclusion of training areas indicates that the excluded training set represents a real distinct textural zone with specific textural properties. Overall, the images show that the texture zones correspond to the spectral band pass zones shown in chapter 4. The zones do not all have simple distinct textures. Zones A and D are simple distinct but the other zones are mixed and these zones are characterised by the mixture and spatial arrangement of textural features. In zone B and C these textural elements include similar textures to those of the boundary or transitional zone,

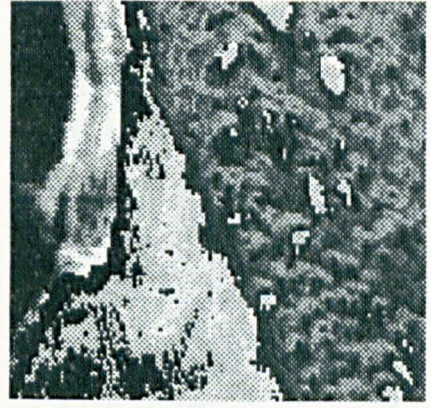
Output images of Band 4 in segment I reveal eventually the same points about the degree of distributions and homogeneity of the four zones ABC and D. however, what is clear for each zone is that the spatial extent and patterns of textural elements is different from Band 7. The zones are approximately in the same locations in that the boundary or transition zones are more or less in the same positions and have the same extent. But, there are differences and it remains to be investigated whether these differences are real or artefacts of the image processing.

Output images of the segment II are presented in figure 5.13. Although area A is recognised, there is considerable mixing of texture zones. Other areas are also appeared as mixing of texture zone except area C that is distinguished as a clear texture (Figure 5.13 (a)). Not only area A remains in each case, with both exclusion and inclusion, a mixed texture, but also area B is a mixed texture as well with a transition zone to apparent in most of the images of figure 5.13. However, homogeneous exclusion of training zones shows areas A and B. Band 4 shows somewhat similar points about the degree of distributions and homogeneity of the four zones. But there are distinct differences for each zone in terms of the spatial extent and pattern of textural elements from Band 7.

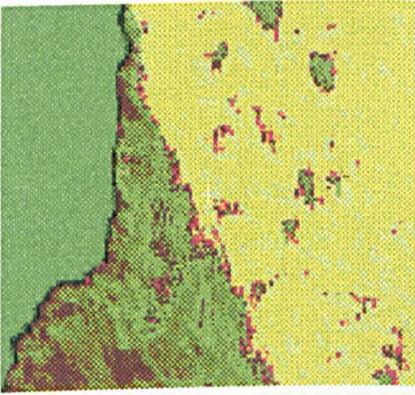
In segment III, there are similarities to segment I because they have similar landform (i.e. sabkha, alluvial plain, and sand sheet & dunes). Of all the four zones, area A is less complex than areas B, C, D. There are, however, mixed texture zones in area A, for instance figure 5.15 (k) and (m). While area B shows mixed and clear textural zones, area C is the most complex of mixing texture zones and difficult to distinguish except the image of figure 5.15 (c) and (m). In Band 4, there are some similarities of the main textural zones to band 7, although the mixing textural zones are somewhat different. Most of the distinguished linear features and zones in band 7 are clearer than in Band 4.



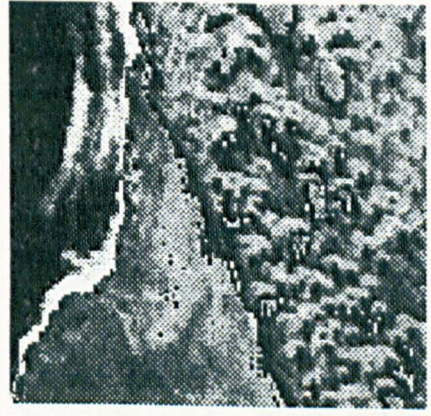
(a) ABCD



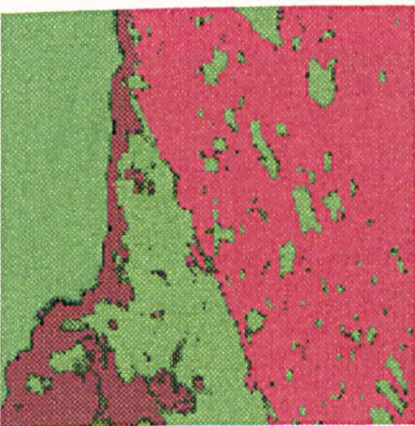
(b) ABCD



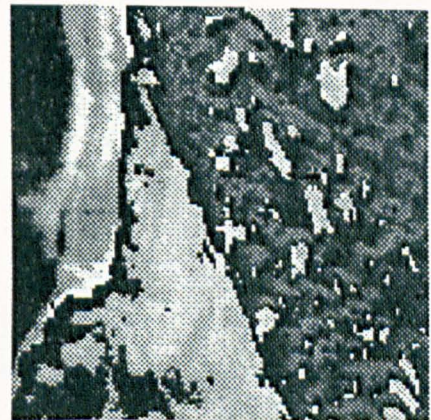
(c) ABC



(d) ABC

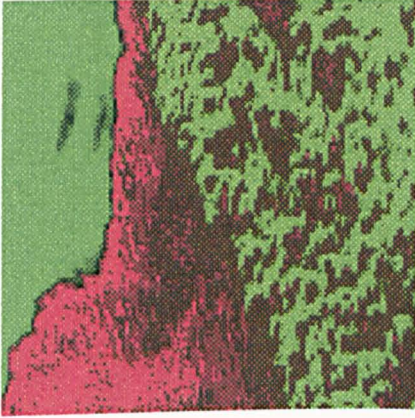


(e) ABD

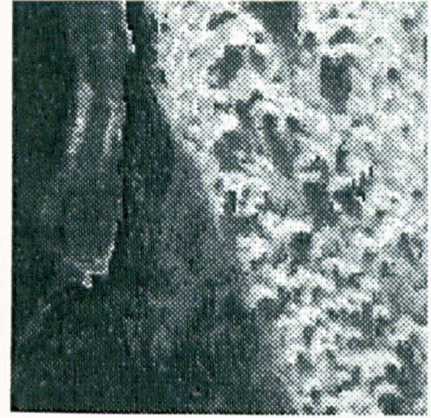


(f) ABD

Figure 5.11: Images (a) to (r) represent the ANN outputs of the training scheme for Band 7.



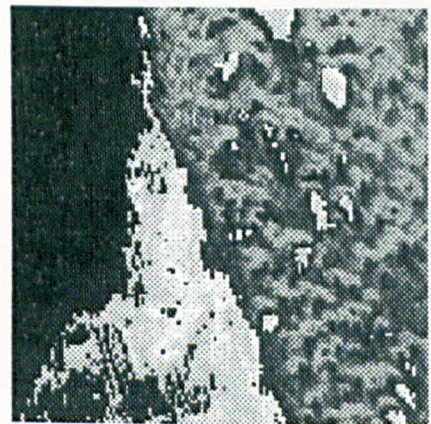
(g) ACD



(h) ACD



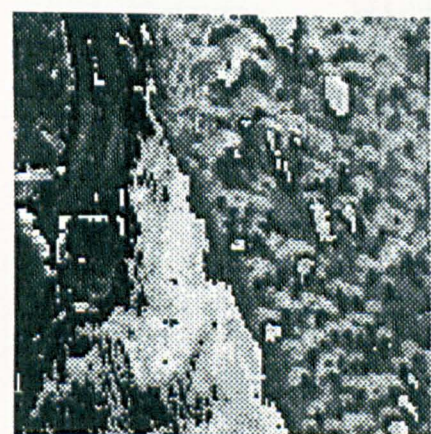
(i) BCD



(j) BCD

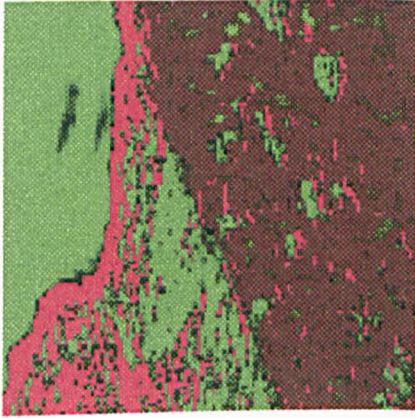


(k) AABD



(l) AABD

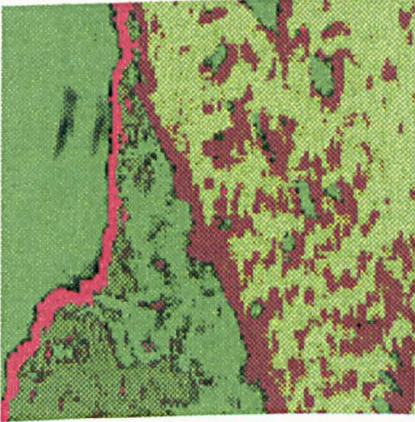
Figure 5.11 (Continued).



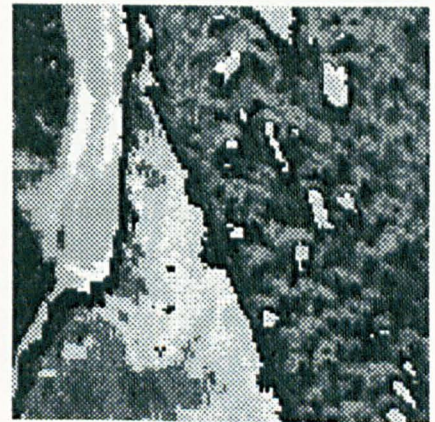
(m) ABBCD



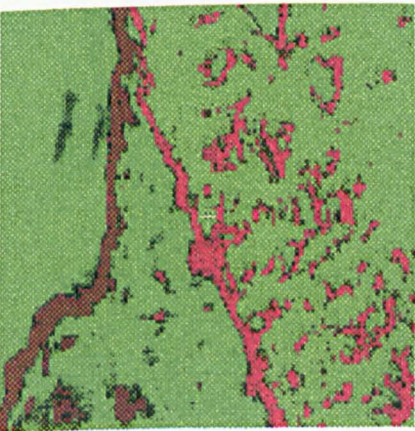
(n) ABBCD



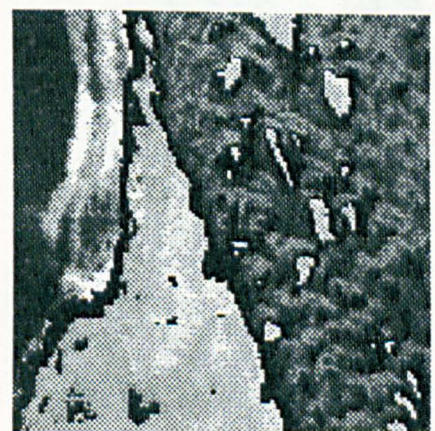
(o) ABCCD



(p) ABCCD

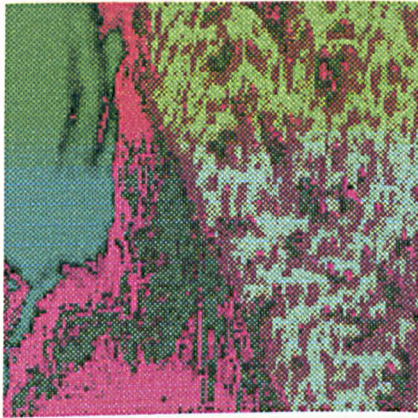


(q) ABCDD

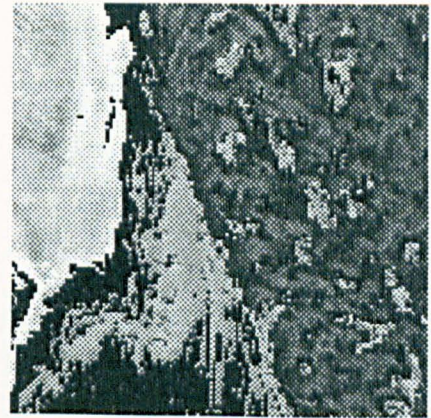


(r) ABCDD

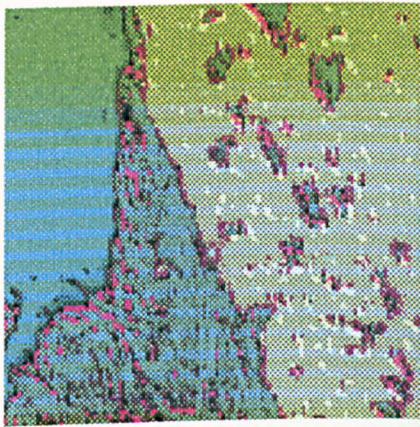
Figure 5.11 (Continued).



(a) ABCD



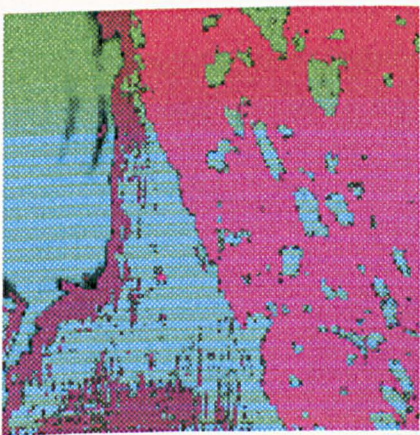
(b) ABCD



(c) ABC



(d) ABC

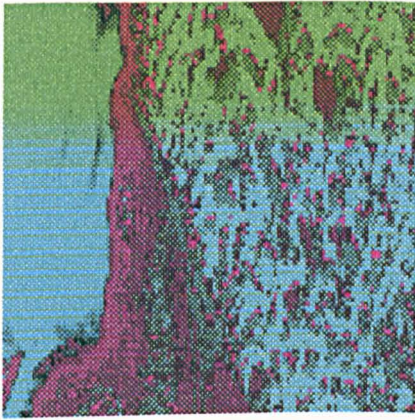


(e) ABD

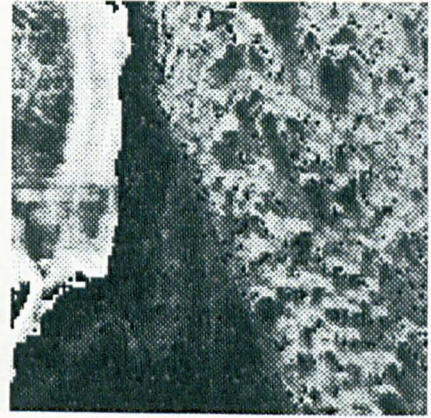


(f) ABD

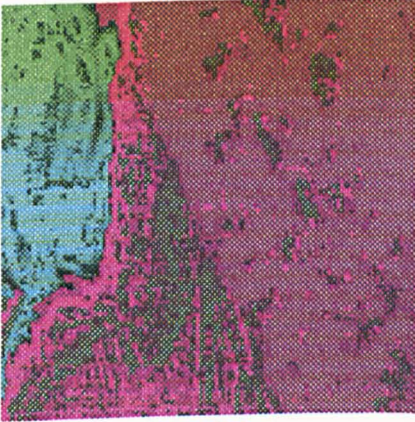
Figure 5.12 Images (a) to (r) represent the ANN outputs of the training scheme for Band 4.



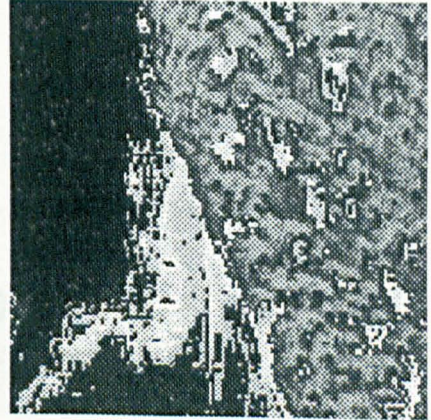
(g) ACD



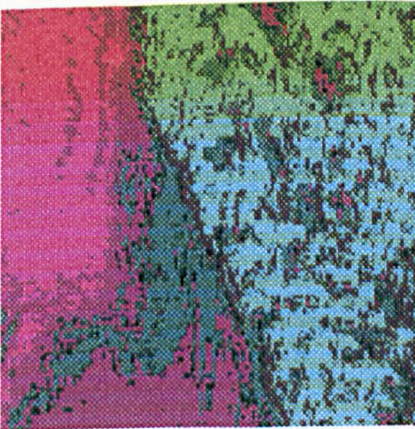
(h) ACD



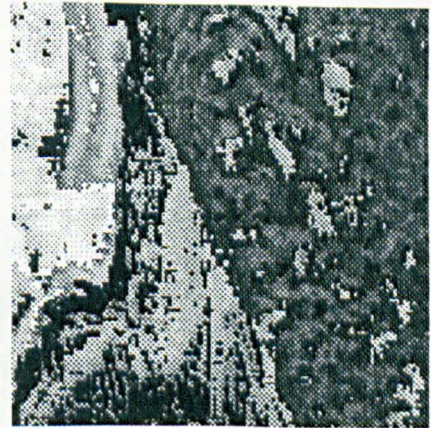
(i) BCD



(j) BCD

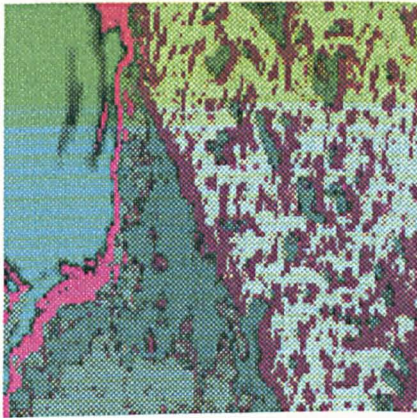


(k) AABD

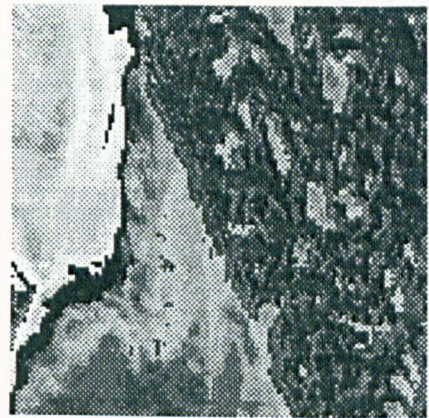


(l) AABD

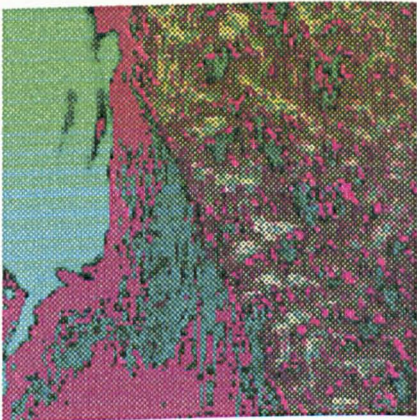
Figure 5.12 (Continued).



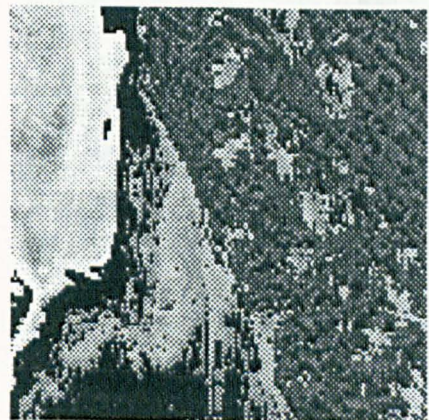
(m) ABBCD



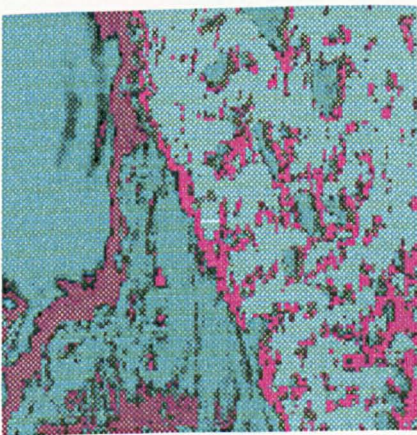
(n) ABBCD



(o) ABCCD



(p) ABCCD

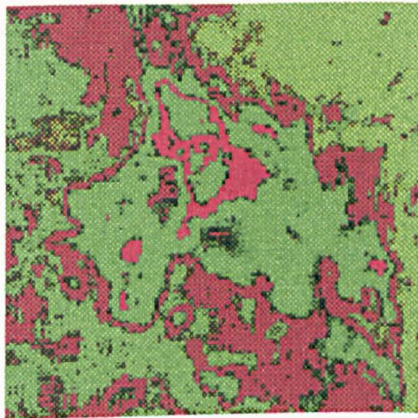


(q) ABCDD

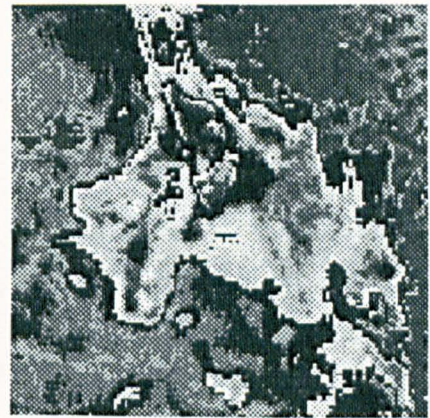


(r) ABCDD

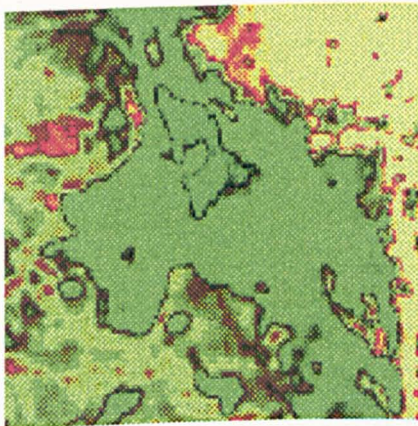
Figure 5.12 (Continued).



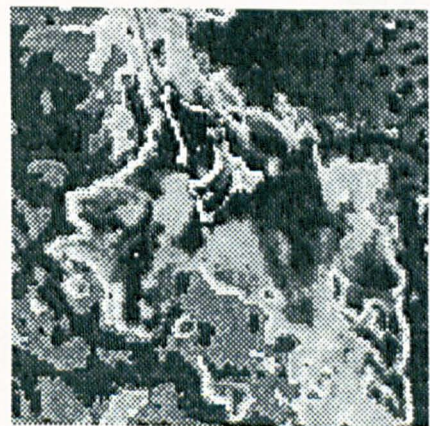
(a) ABCD



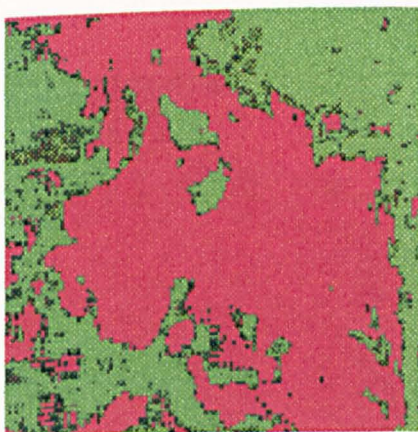
(b) ABCD



(c) ABC



(d) ABC

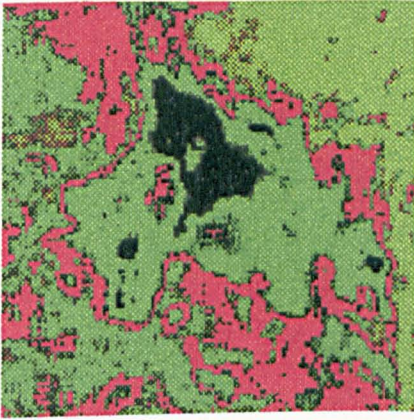


(e) ABD

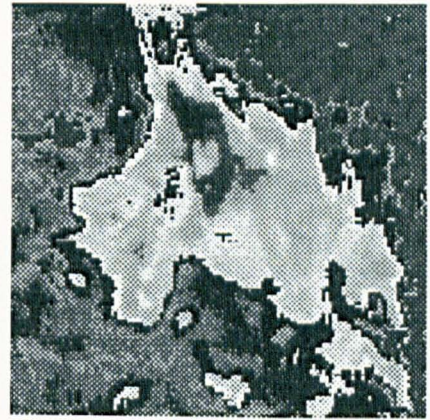


(f) ABD

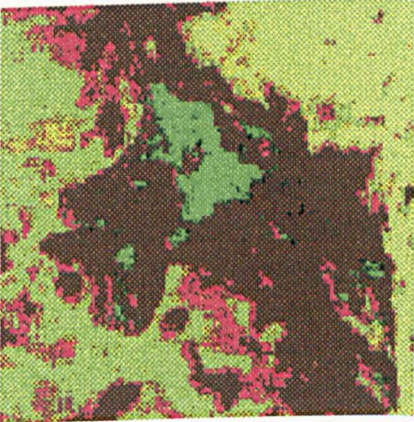
Figure 5.13 Images (a) to (r) represent the ANN outputs of the training scheme for Band 7.



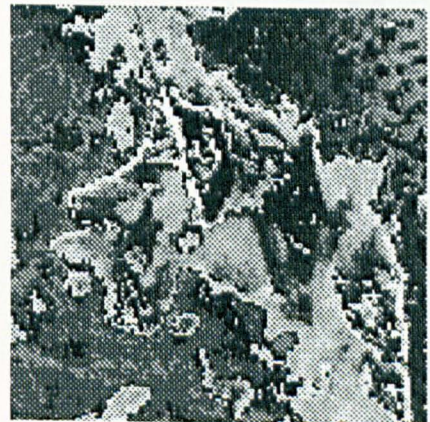
(g) ACD



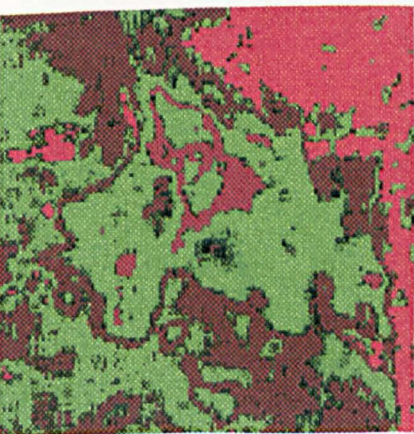
(h) ACD



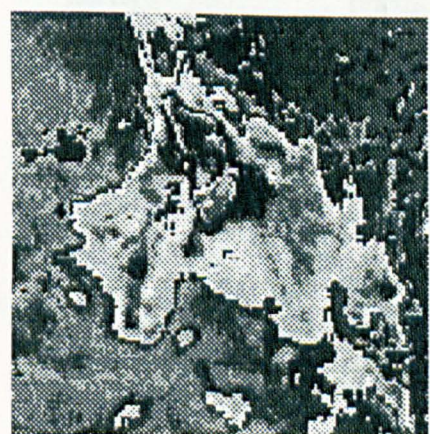
(i) BCD



(j) BCD

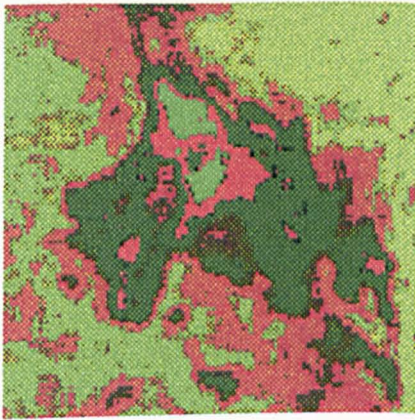


(k) AABD

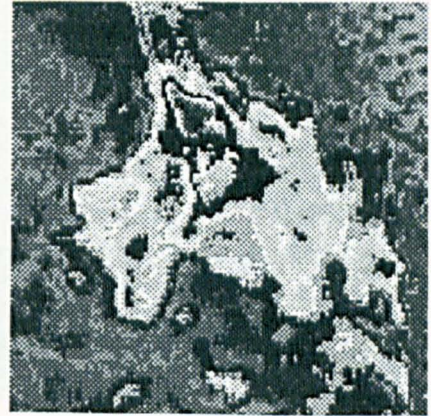


(l) AABD

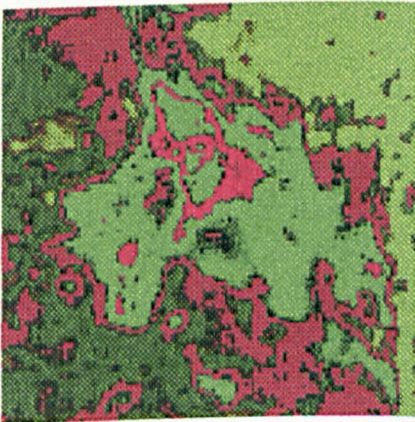
Figure 5.13 (Continued).



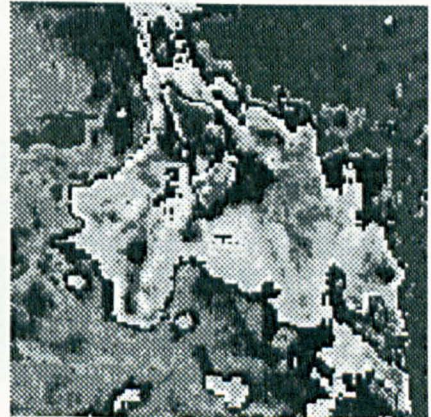
(m) ABBCD



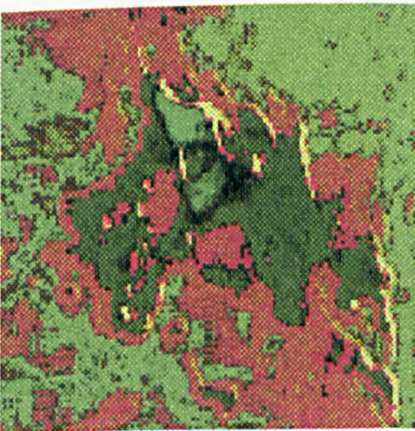
(n) ABBCD



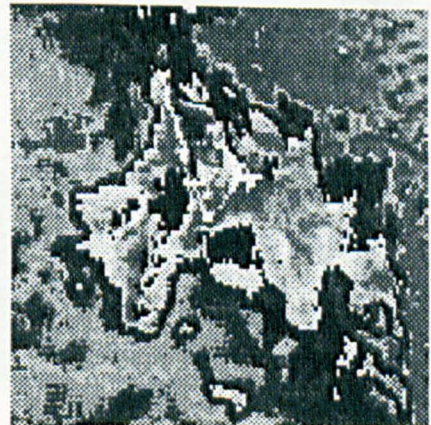
(o) ABCCD



(p) ABCCD

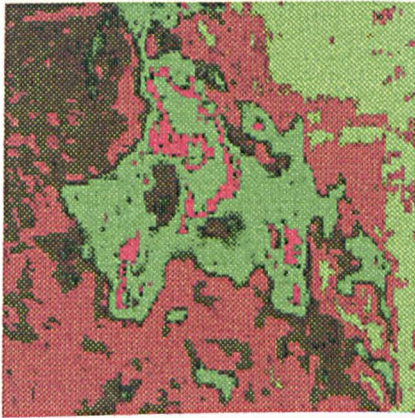


(q) ABCDD

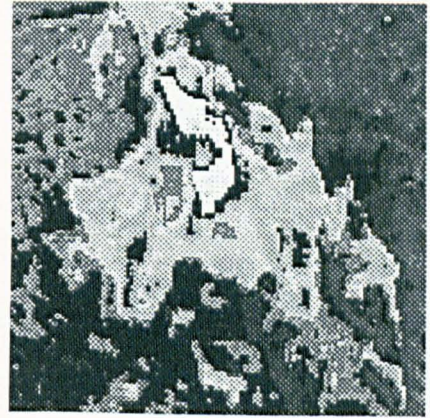


(r) ABCDD

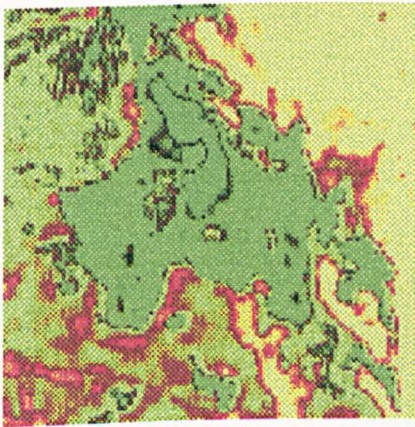
Figure 5.13 (Continued).



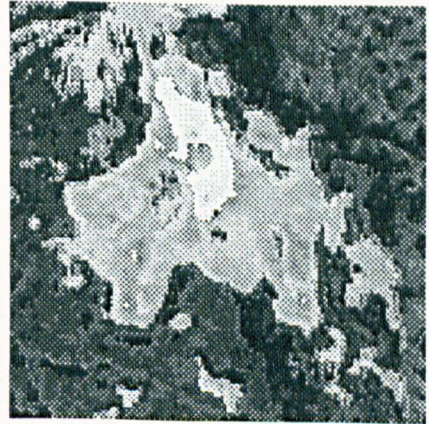
(a) ABCD



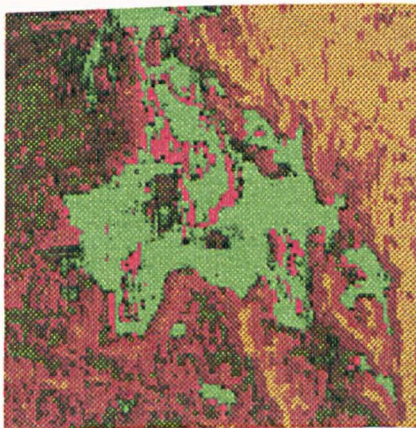
(b) ABCD



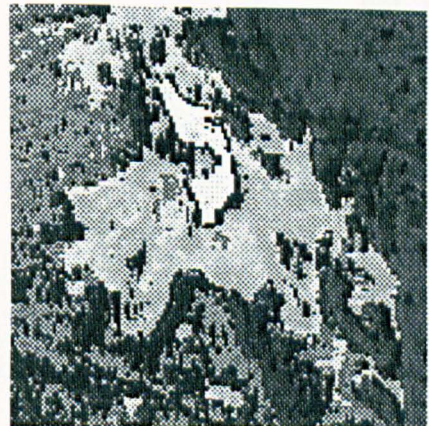
(c) ABC



(d) ABC

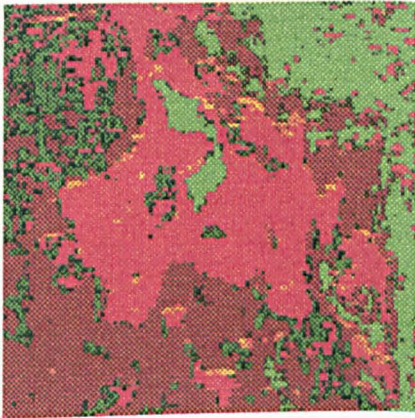


(e) ABD

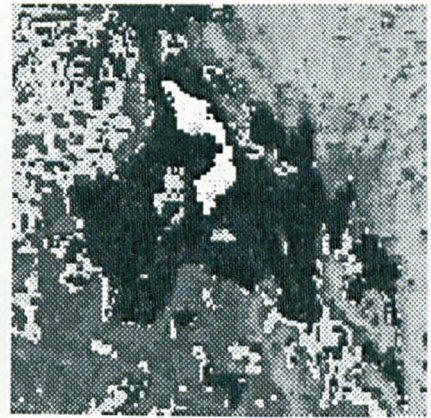


(f) ABD

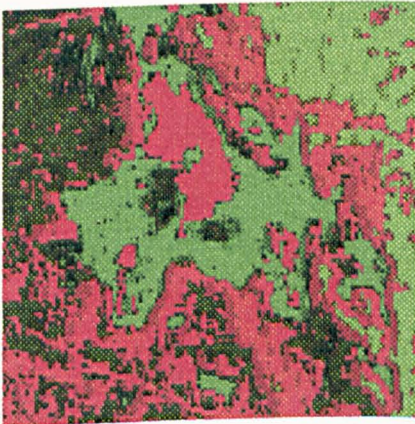
Figure 5.14 Images (a) to (r) represent the ANN outputs of the training scheme for Band 4.



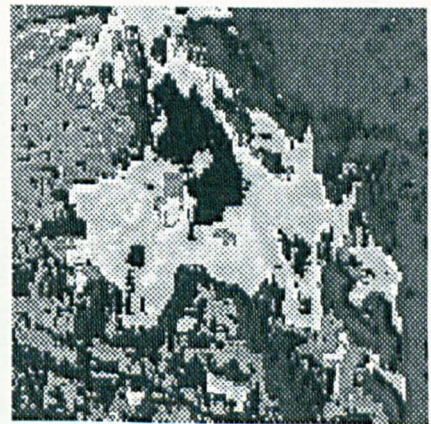
(g) ACD



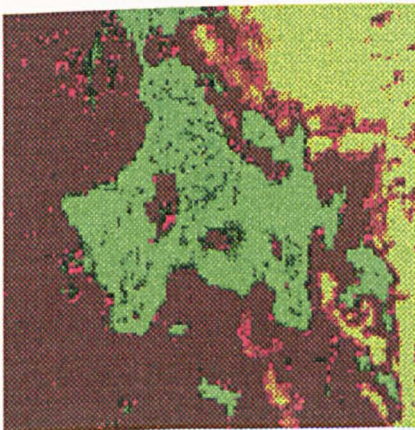
(h) ACD



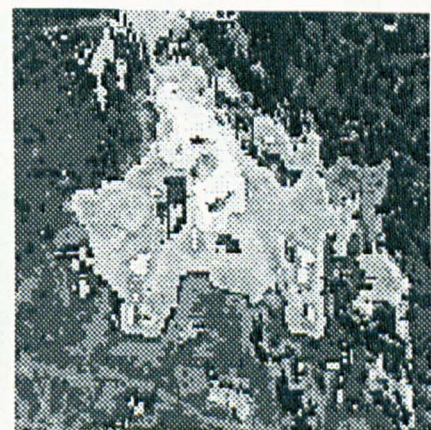
(i) BCD



(j) BCD

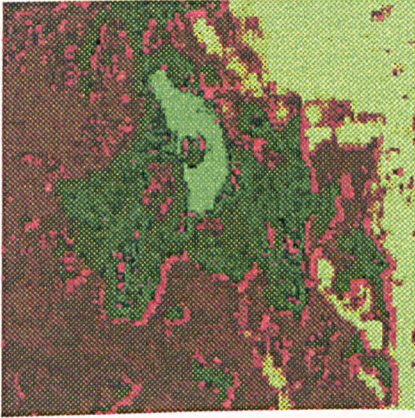


(k) AABD

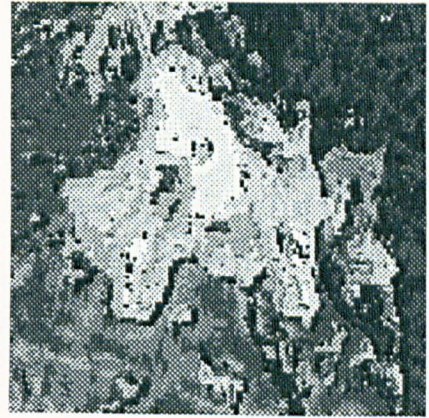


(l) AABD

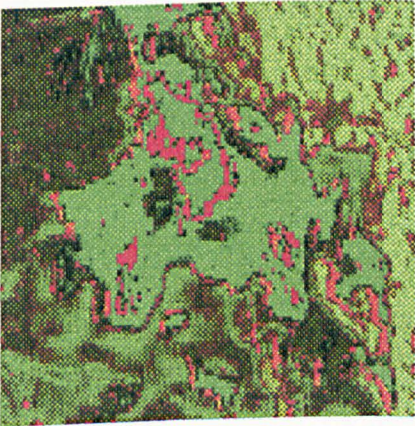
Figure 5.14 (Continued).



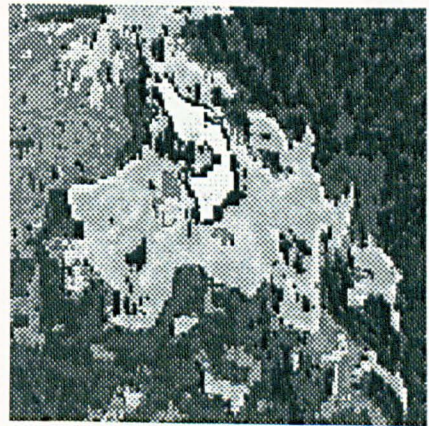
(m) ABBCD



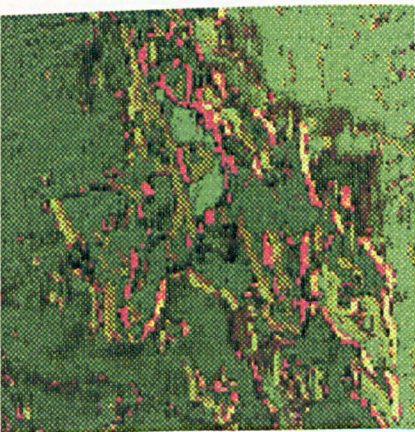
(n) ABBCD



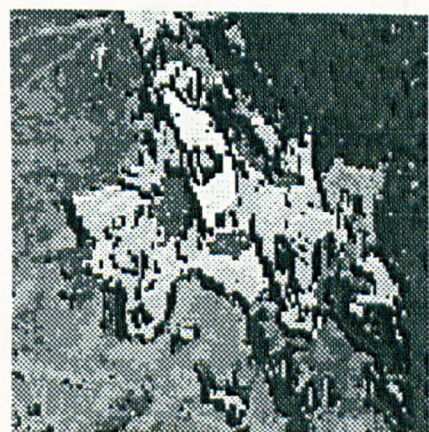
(o) ABCCD



(p) ABCCD

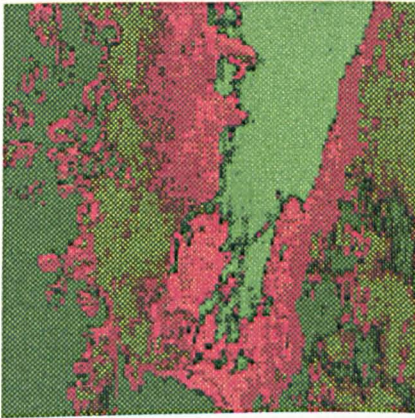


(q) ABCDD

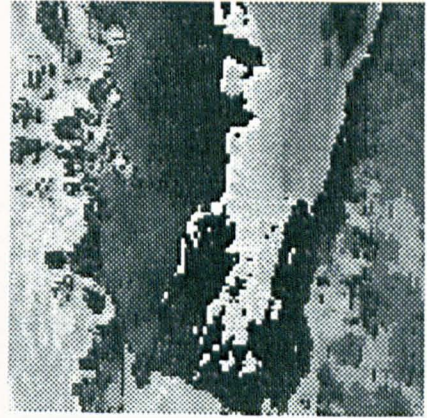


(r) ABCDD

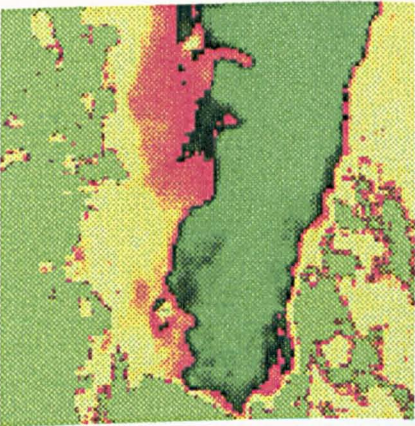
Figure 5.14 (Continued).



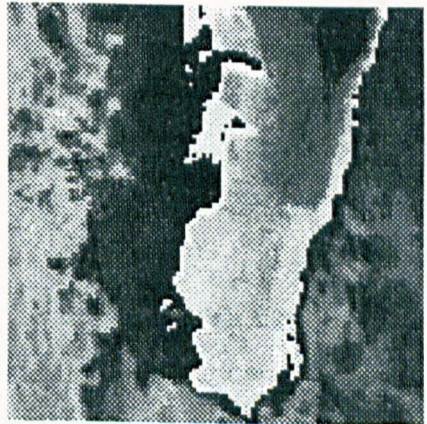
(a) ABCD



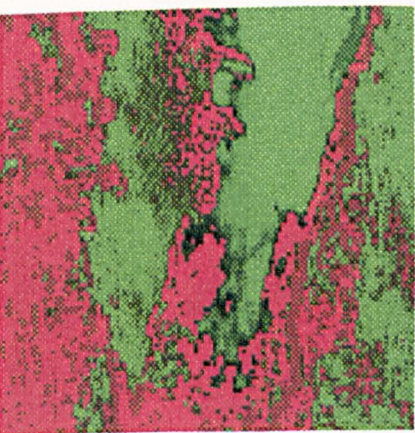
(b) ABCD



(c) ABC



(d) ABC

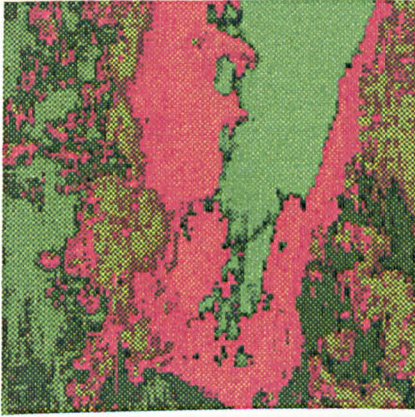


(e) ABD

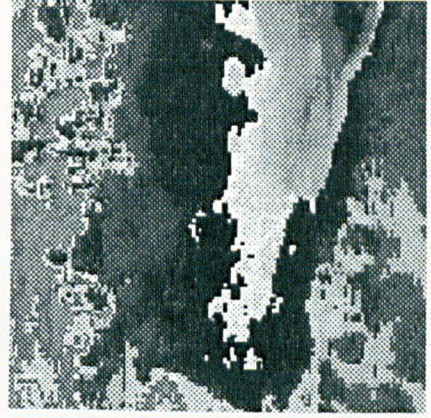


(f) ABD

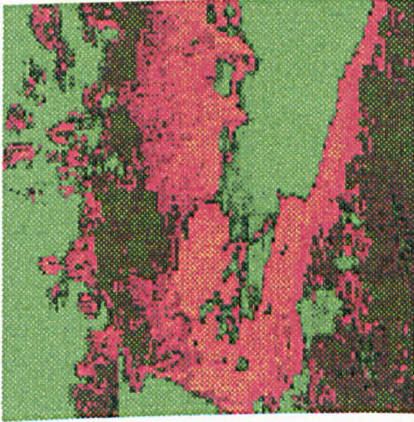
Figure 5.15 Images (a) to (r) represent the ANN outputs of the training scheme for Band 7.



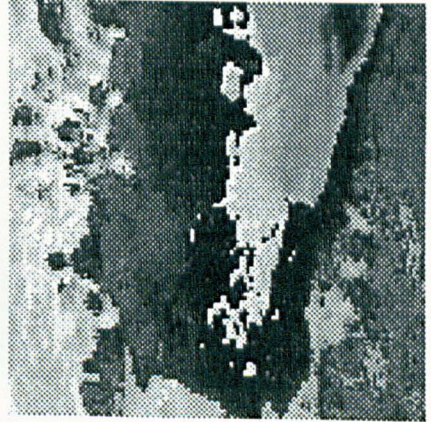
(g) ACD



(h) ACD



(i) BCD



(j) BCD

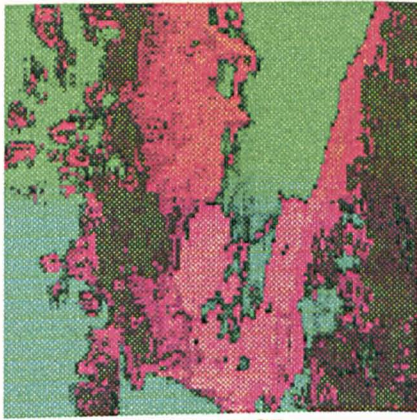


(k) AABD

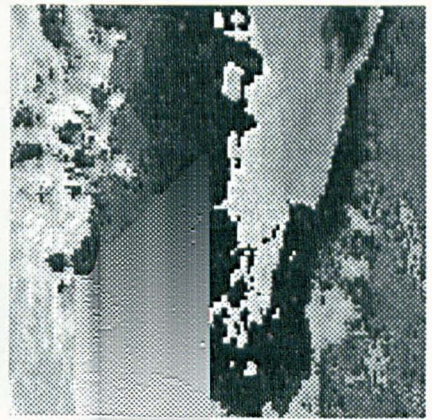


(l) AABD

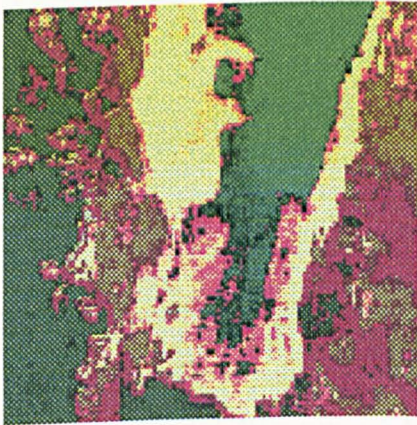
Figure 5.15 (Continued).



(m) ABBCD



(n) ABBCD



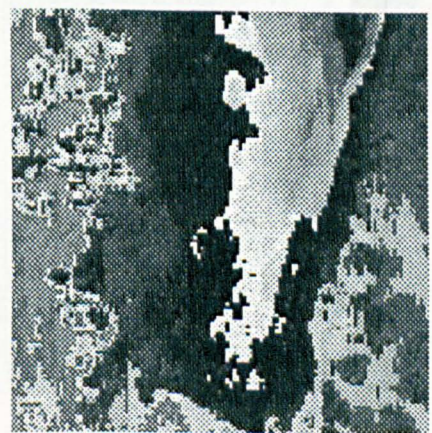
(o) ABCCD



(p) ABCCD

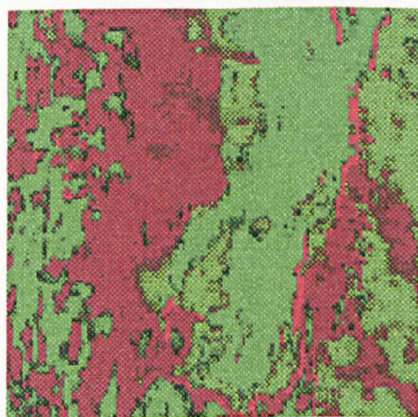


(q) ABCDD

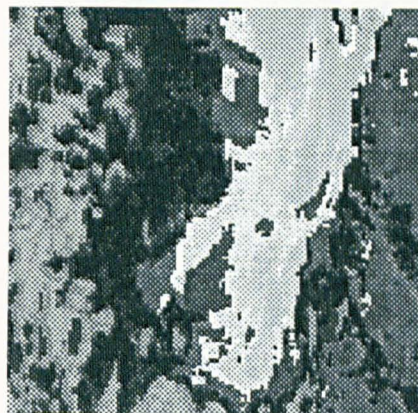


(r) ABCDD

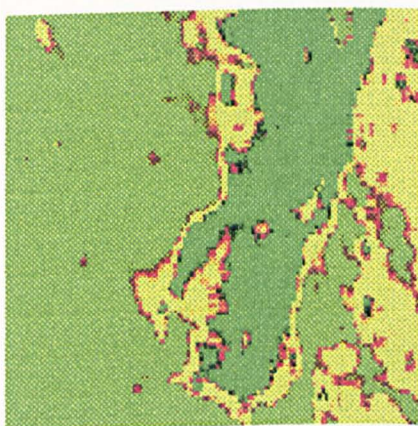
Figure 5.15 (Continued).



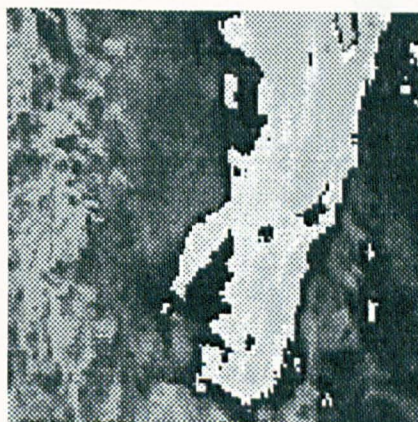
(a) ABCD



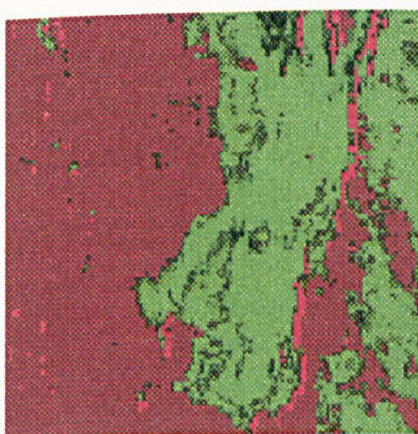
(b) ABCD



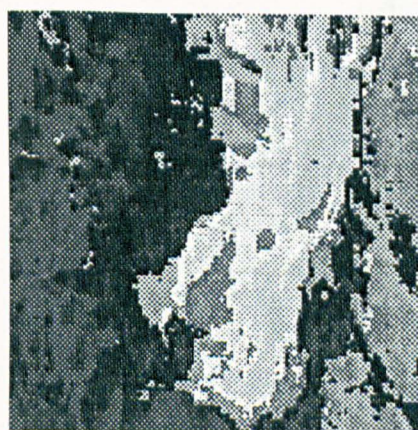
(c) ABC



(d) ABC

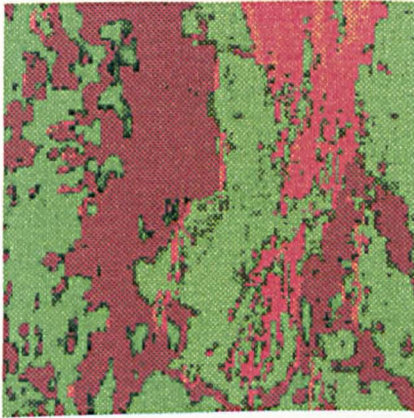


(e) ABD

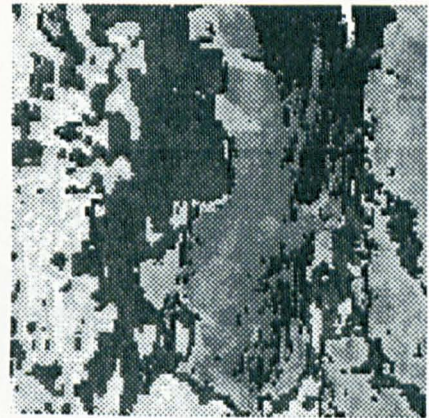


(f) ABD

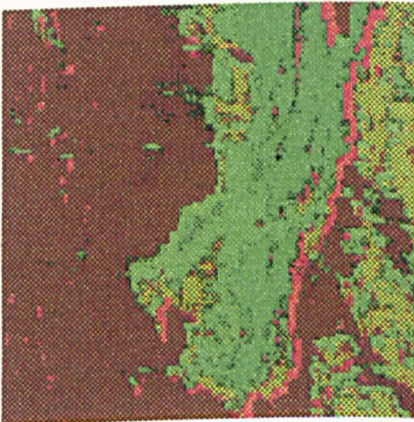
Figure 5.16 Images (a) to (r) represent the ANN outputs of the training scheme for Band 4.



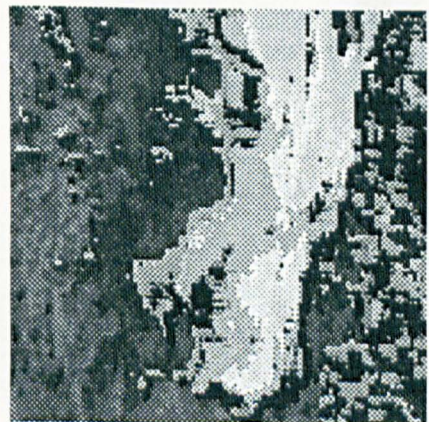
(g) ACD



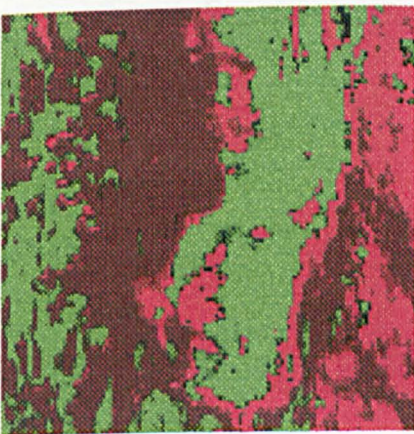
(h) ACD



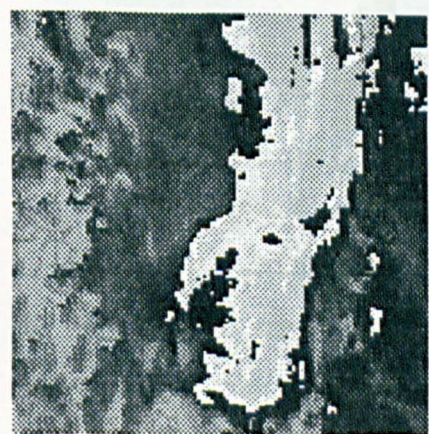
(i) BCD



(j) BCD

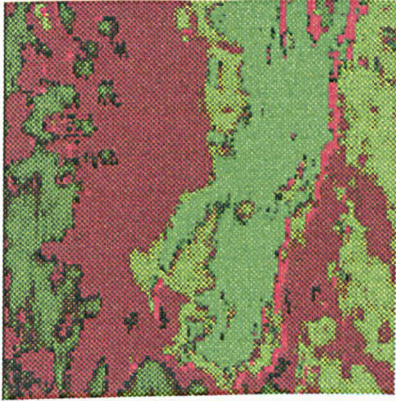


(k) AABD

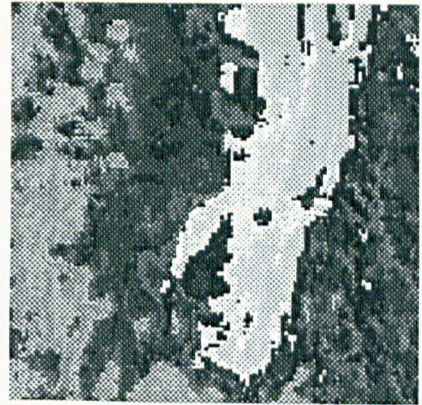


(l) AABD

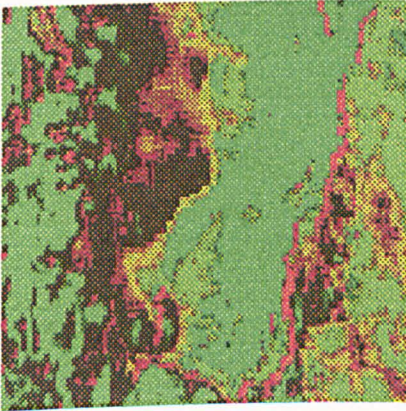
Figure 5.16 (Continued).



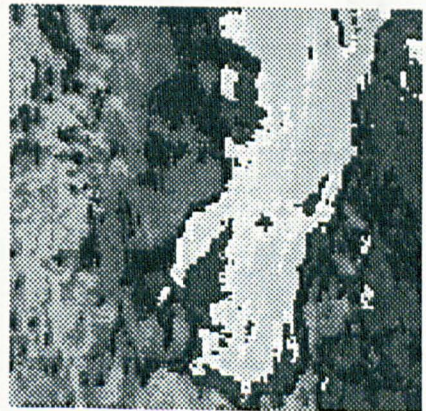
(m) ABBCD



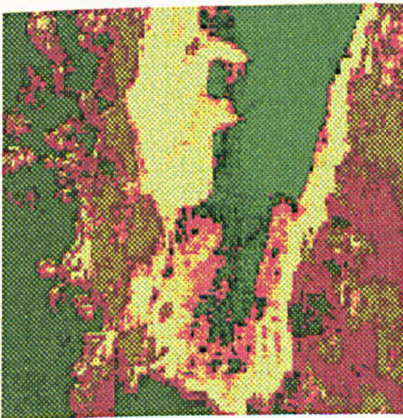
(n) ABBCD



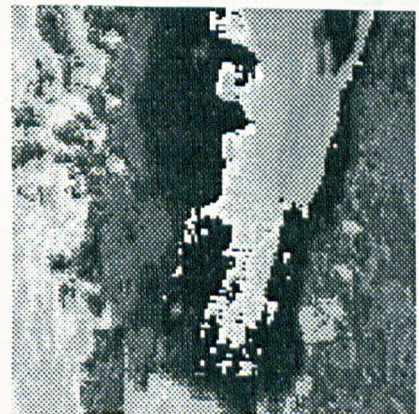
(o) ABCCD



(p) ABCCD



(q) ABCDD



(r) ABCDD

Figure 5.16 (Continued).

5.5.4 Analysis of images for soil landscape identification

Because of the way the training areas were selected, that is, on the basis of the interpreted inverse filtered FFT images, it is not possible to infer anything about the evidence for soil zones. By using training areas in areas A, B, C, and D we of necessity assume that such areas exist.

It is possible to argue that the training areas with their combinations of excluded and included members represent a set of training areas from the images, which are not severely biased. The indication that this is so is given by the fact that all the images show more or less the same number and spatial arrangement of sub-areas.

This is hardly surprising in one sense since the whole argument about the interpretation of the complex elements is based on the fact that image reflectance is controlled by real soil, and rock reflectance properties. Thus, there are bound to be persistent patterns of reflectance related to the main physical features of the study areas. However, what are not set by the selection of the training areas are the positions and nature of boundary zones and the patterns of texture within parts of the image. This means, we can usefully examine the relation between image segmentation using ANN and soil/landform units (MAW, 1986, 1995) in terms of boundary properties and within zone variability.

5.5.4.1 Test segment I

The end product of the main soil/landform units of this segment is given in figure 5.11, which consists of sabkha, sand sheet & dunes, and alluvial plain. The sabkha area is well defined and appears as a distinct zone from other areas. It corresponds closely with the mapped soil and landform units in this test segment. In Band 7 the boundary with both the sand sheet & dunes and alluvial plain is clear and sharp and in many image represented by a thin line of unclassified pixels. In Band 4 the boundary is much less distinct and more irregular. The boundary zone is also narrower in Band 7.

The sand sheet & dunes unit in Band 7 appears as a distinct zone but its boundary with alluvial plain consists of a zone that is sharply defined on the alluvial plain side but not on the sand sheet side in both Bands 7 and 4. The boundary zone is narrower in Band 4. Two texture types with complex patterns consistently represent the sand sheet area.

The alluvial plain area is a complex, poorly defined area, with main textural elements similar to the boundary zones with sabkha and the sand sheet & dunes areas. There are distinct alluvial plain textures but they are not present as a coherent distinct zone.

5.5.4.2 Test segment II

Test segment II consists of sabkha, sand sheet, and gypsiferous pediplain. The result of pattern of these units is much less clear than in test segment I or segment III. The area that is consistently well defined and appears as a distinct relatively homogenous

Table 5.4. Summary of the features identification of the ANN images.

List landform	Soil type	ANN images
Sabkha	Salorthid / Gypsic solochk	One dominant identifiable zone, unclassified thin linear feature, few images show somewhat complex features
Alluvial plain	Gypssiorthid / Calciorthid	Somewhat complex zones, few images show simple zones, few identifiable broader linear features
Sand sheet and Dunes	Torripsamment	More or less complex identifiable zones, very complex in few images, no evidence of linear features
Gypsiferous pediplain	Gypsiorthid / Petric yypsisls	In most cases very complex features, very few cases show identifiable zones

unit is the sand sheet area, whereas the sabkha areas are extremely complex in terms of texture components and patterns. There is considerable ambiguity about the location and extent of the boundary zone between sabkha and the gypsiferous pediplain. The gypsiferous pediplain also is extremely complex. Band 4 shows greater complexity in the units and more ambiguity in the boundary zones than Band 7.

5.5.4.3 Test segment III

In this segment, the sand sheet is a very complex area, shown as a very broad, poorly defined boundary to the sabkha. Appearances are much more complex in Band 7 than Band 4. The sabkha unit is a persistent and well-defined area but complex. There is ambiguity in boundary areas with sand sheet but not with alluvial plain. The boundary with alluvial plain is consistently narrower and sharper than with sand sheet. The alluvial plain is clear, in consistent location and made up two or more textural elements with complex patterns. Table 5.4 summarises the feature identification of the ANN model.

5.6 Summary

This study has explored the ANN method of maximising and utilising the soil mapping of digital imagery. The texture approach together with training strategy show different output images in terms of identifying linear features and zones. Of all the resulting images of the training scheme, the images of the ABC training parameters was the most simple and coherent in terms of identifying the main soil zones. Although this ANN

method is under prior assumption of selecting the training areas, the training strategy has shown that the outputs of the data sets sometimes are simple and sometimes are complex. This means that this method can be used, as a measure of complex elements in the feature space scales.

CHAPTER 6

MULTIFRACTAL ANALYSIS

6.1 Introduction

In the interpretation and analysis of digital images of remotely sensed data, the scale of observation and measurement is critical in determining image properties and features. Many environmental processes and patterns are scale dependent in the sense that the way they appear is homogeneous at one spatial scale and heterogeneous at another (Davis *et al.*, 1991; Ehleringer and Field, 1993). Since spatial heterogeneity constrains the ability to transform information from one scale to another, an important issue in the integration and analysis of remote sensing data is the resolution scales of different data sets. Several studies have shown that landscape pattern has a significant influence on the response of measurements to changes in spatial scale (Turner *et al.*, 1989a and 1989b; Lam and Quattrochi 1992). Scale in a remote sensing perspective can be characterised as the integral of space and time over which a measurement is made. Thus, the element of scale is presented as a metric used to measure the space and time elements for a phenomenon or process under observation (Davis *et al.*, 1991; Quattrochi, 1993).

In this chapter, the fractal and multifractal analyses are presented as a means of examining the multi-scale properties of images. This is one of a set of such analyses but

has been widely used by mathematicians and is available in standard software products (Fraclab with Matlab). Most of the simulated fractals features are homogeneous since the fractals consist of a geometrical figure repeated on an ever-reduced scale. As a result the fractal dimension of any feature will remain the same on all scales. In the real world fractals are not homogeneous features. This means there is rarely an identical stimulus repeated on all scales. Two features might have the same fractal dimension and yet look completely different. Therefore, the real world fractals are heterogeneous features in which there is non- uniformity possessing rich scaling and self-similarity properties that can change from point to point. Since there is always some kind of scaling restriction with physical fractals for obvious reason, the development of multifractal analysis may resolve such complexity.

6.2 Fractal analysis

6.2.1 Background

Fractal analysis has become a familiar term in the worlds research in the last 10 years especially in geoscience research following the pioneering work of Benoit Mandelbrot and others (Culling, 1984; Townshend and Justice, 1988; De Cola, 1989; Turner *et al.*, 1989a, 1989b; Lam and Quattrochi, 1992; Kineman, 1993; Steyaert, 1993). In addition, fractals and fractal analysis have been suggested as an innovative technique for characterising remote sensing images as well as identifying the effects of scale changes on the properties of images (De Cola, 1989; Lam and Quattrochi, 1992). Fractal dimension is key parameter of fractal analysis that is used to represent the spatial

complexity of point patterns, lines, and surfaces. This means the higher the fractal dimension, the more complex the form. Recent studies of fractal analysis, such as the concept of self-affinity, random fractal, and multifractals, have expanded fractal applications to many phenomena where pure fractals with strict self-similarity do not exist (Lovejoy and Schertzer, 1990; Levy-Vehel and Berroir, 1991; Evertsz and Mandelbrot, 1992; Lavalley *et al.*, 1993; Levy-Vehel and Berroir, 1993; Davis *et al.*, 1994; Levy-Vehel, 1998; Levy-Vehel and Vojak, 1998)

Moreover, fractals are seen as a potentially robust method for understanding landscape complexity in which landscape features become fragmented depending upon the scale of observation and measurement (Qiu *et al.*, 1999; Emerson *et al.*, 1999). Consequently, heterogeneity controls our perception of the landscape being composed of a patchwork of different elements that make the landscape complex in appearance, structure, and function. The complexity, therefore, results from fundamental interactions that generate patterns composed of (i) physical processes that alter landscape structure and (ii) cultural and human-induced activities (Lovejoy and Schertzer, 1990; Lavalley *et al.*, 1993; Qiu *et al.*, 1999; Emerson *et al.*, 1999). Understanding how of the geometric shape and size of the land cover patterns, for instance, in terms of complexity are related to natural and human processes in order to determine the appropriate spatial scales and the type of remote sensing data to use in analysis of landscape dynamics (Qiu *et al.*, 1999; Emerson *et al.*, 1999). Therefore, fractals can be applied to a variety of landscape problems because they have the opportunity to describe many of the irregular,

fragmented patterns found in nature (Mandelbrot, 1983). Since the applications of fractals are varied, there are some limitations describing the degree to which the area of a landscape patch is related to its edge, and how this measure can be modified to address diversity. In order to measure the heterogeneity of the landscape and the complexity of patch interaction within it, the fractal relation to patch area to patch edge of this landscape must be determined (Olsen, *et al.*, 1993). However, there is another factor that affects the extant biophysical processes across a landscape. The juxtaposition of a patch to other patches, therefore, in terms of spatial arrangement can have significant effects, as can the number of different patches in one area and the equal distribution of patches across the landscape (Rex and Malanson, 1990; Olsen, *et al.*, 1993). Olsen *et al.* (1993) used fractals as a method for determining patch complexity and addressed their effectiveness when combined with measures to determine richness and evenness of patches within a landscape.

The reason that fractal has been adopted in research is the fact that many patterns in the natural world are not measured as well as they should be. These patterns have underlying spatial structure of considerable complexity based on self-similarity (Lovejoy and Schertzer, 1990; Lavalley *et al.*, 1993; Qiu *et al.*, 1999; Emerson *et al.*, 1999).

Remote sensing is a discipline that concerns itself with the observation and monitoring of the state of the planet. The observation is basically consisting of natural patterns in the spatial and temporal domains (Campbell, 1996; Jensen, 1996). Further, the patterns

are often observed at a variety of different space scales. As a result, it is extensively valuable that fractals could have much relevance for remote sensing.(Qiu *et al.*, 1999; Emerson *et al.*, 1999).

Unfortunately, the number of practitioners in remote sensing who have tried to apply fractal analysis techniques to the data sets is extremely small, this is attributed to the lack of mathematical background especially fractal geometry as well as the lack of availability of software packages.

6.2.2 Fractal Theory

Starting with the theory of a line, Euclidean geometry explains that it is a figure of one dimension, which is basically the length. If the line is extending many times around and around, back and forth without crossing itself until it fills a sheet of paper, Euclidean geometry defines, it still as a line, a figure of one dimension. However, our intuitions strongly tell us that if the line fills the entire plane, it must be two-dimensional.

In classical geometry, the dimension of a curve is defined as 1, a plane as 2, and cube as 3. This is called topological dimension and is characterised by real value between 1 and 2, according to the curve's degree of complexity. Similarly, a plan may have a dimension whose value lies between 2 and 3. This concept of fractional dimension was formulated by mathematicians Hausdorff and Besicovitch (Mandelbrot, 1983). Mandelbrot (1983) later called it fractal dimension and defined fractals as a set for

which the topological Hausdorff-Besicovitch dimension strictly exceeds the topological dimension. Since then, the definition of fractals has been modified and a complete definition is still lacking.

The derivation of fractals arises from the fact that most spatial pattern of nature, including curves and surfaces, are so irregular and fragmented that classical geometry finds difficult to provide tools for analysis of their forms. For instance, the coastline of an island is neither straight nor circular, and no other classical curve can serve in describing and explaining its form without extra artificiality and complexity.

The key concept of fractals is the use of self-similarity to define D . Many curves and surfaces are statistically self-similar meaning that each portion can be considered as a reduced scale image of the whole. Thus, D can be defined as

$$D = \log N / \log(1/r)$$

Where $1/r$ is a similarity ratio, and N is the number of steps needed to traverse the curve. Practically, the D value of a curve (e.g. coastline) is estimated by measuring the length of the curve using various step sizes. The more irregular the curve, the greater increase in length as step size decreases. And D can be estimated by the following regression equation:

$$\text{Log}L = C + B \log G$$

$$D = 1 - B$$

Where L is the length of the curve, G is the step size, B is the slope of the regression, and C is a constant. The D value of a surface can be estimated in a similar fashion and is discussed in detail in the methods section. Another aspect of fractal concepts is the generation of fractal curves and surfaces. Based on the model of Brownian motion in physics, together with the concept of self-similarity.

6.2.3 Fractal Surface Measurement Methods

Several approaches to estimate the fractal dimension of real textures have been proposed in the literature, but the most widely used methods that have been used by geoscientists are described briefly in next subsections.

6.2.3.1 Isarithm Method

The isarithm method, sometimes called the walking-divider method, utilises the isarithms of the surface as a means in determining the fractal dimension D of the surface where the equation is written as:

$$D_{\text{surface}} = D_{\text{isarithmetic}} + 1$$

The algorithm was evolved from Goodchild (1980), Shelberg, *et al.* (1983), and Jaggi, *et al.* (1993). In addition to the data matrix with numbers of rows and columns specified.

6.2.3.2 Variogram Method

In this method, the variogram function, which describes how variance in surface height varies with distance, is used for estimating the fractal dimension. The only difference between the traditional variogram and the variogram used in fractal estimation is that distance and variance are portrayed in double-log form. The slope of linear regression performed between these two variables is then used to determine the fractal dimension, where the equation is written as:

$$D = 3 - (b / 2)$$

The algorithm was pioneered and evolved from Mark and Aronson (1984), and being developed by Jaggi, *et al.* (1993).

6.2.3.3 Triangular Prism Method

The triangular prism method compares the surface areas of the triangular prisms with the pixel area (step size squared) in log-log form (Clarks, 1986; Jaggi, *et al.*, 1993). For each step size, the triangular prisms are constructed by connecting the heights of the four corners of the pixel to its centre, with the centre height being the average of its

corners. The areas of these surfaces can be calculated by using trigonometric formulae. The fractal dimension is calculated by performing regression on the surface areas and pixel areas, where the equation is written as

$$D = 2 - b$$

This algorithm was evolved by Clarks (1986) and developed by Jaggi *et al.* (1993).

6.3 Applications of Monofractal

In geosciences, fractals have been used mainly for measuring and simulating spatial forms and processes, and are considered an attractive spatial analytical tool (Goodchild and Mark, 1987; Jaggi *et al.*, 1993). Despite the numerous applications in the last two decades, there are very few direct references to the application of fractals in remote sensing (De Cola, 1989; Lam, 1990). An expanded employment of fractals in remote sensing research is considered useful to a better understanding of the relation between surface variation and spatial properties of remotely sensed data. This is especially true when one considers that remote sensing is the main source of data that we can use for analysing the spatial dependence of surface and atmospheric phenomena at relatively large scales and over large areas (Lovejoy and Schertzer, 1988; Davis *et al.*, 1991).

The measurement of the fractal dimension, D of a spatial phenomenon is the first step toward an understanding of spatial complexity. The higher the D , the more spatial

complexity is present. The fractal dimension of a point pattern can be any value between 0 and 1; a curve, between 1 and 2; and a surface, between 2 and 3. For instance, coastlines have dimension values typically approximately 1.2-1.3, and topographic surfaces around 2.2-2.3 (De Cola, 1989; Lam, 1990). However, in spectral reflectance surfaces, such as those reflected by Landsat-TM, the fractal dimensions are much higher, approximately 2.7-2.9 (Lam, 1990; Jaggi *et al.*, 1993; Lam *et al.*, 1998; Emerson *et al.*, 1999; Qiu *et al.*, 1999).

The fractal dimension has been used as a spatial measure for describing the complexity of spatial data, including remote sensing imagery (Lam 1990). The fractal dimension of a linear feature such as a coastline can be any value between 1 and 2, depending on its complexity. Similarly, for a surface, the fractal dimension lies between 2 and 3. This dimension value is derived from the entire surface, and it reflects the overall characteristics of the surface. When applied to remote sensing data, an image will be represented as a surface and the fractal dimension value of the surface represents the complexity of the image. In addition, it has been shown that fractal dimension changes across the spectral bands of Landsat TM imagery (De Cola, 1989; Lam, 1990).

6.4 Multifractal Approach

The definition of generalised fractal dimension described in the previous section 6.2 supplies a method for estimation based on the concept of the three methods. However, as demonstrated by Dubuc *et al.* (1989), although very simple to use, the monofractal

methods have many limitations and drawbacks that make it not so attractive for discrete image processing. In particular, the results are strongly dependent on the origin of the partitioning grid.

Since the mathematical definition of the multifractal approach is beyond the scope of this research, a brief definition of fundamental facts about the multifractal theory is presented. Complete and rigorous definitions of multifractal theory can be found in (Falconer,1990; Levy Vehel and Vojak, 1998; Dekking. *et al.*, 1999).

The following is the Local Singularity Coefficient:

$$\alpha (x) = \lim_{\delta \rightarrow 0} \frac{\log \mu (\beta_{\delta} (x))}{\log \delta}$$

Where $\beta_{\delta} (x)$ is an open-ball of diameter δ centred on the point x and when the limit exists,

$\alpha(x)$ is often called the *Hölder* coefficient.

$$\dim E = \inf \{ s : \lim_{\delta \rightarrow 0} \inf \sum_{i=0}^{\infty} | E_i |^s = 0 \}$$

$$= \sup\{ s : \lim_{\delta \rightarrow 0} \inf \sum_{i=0}^{\infty} |E_i|^s = \infty \}$$

Where $\{E_i\} 1 \leq i \leq \infty$ is a δ -cover of E

It is quite straightforward that to apply multifractal tools to image analysis. Following the previous equations, points are naturally associated to pixels of the image, open-balls to windows centered on each pixel, measures to functions of grey level intensities.

A first natural choice is to define the measure μ as the *SUM* of the grey level intensities of pixels (i, j) contained in a window centered on pixel (x, y) . Other functions of grey level intensities of the image can be defined in which we can distinguish three types of functions of grey level intensities according to their respective properties. The first one is the *SUM* capacity. The following is the *MAX* capacity leading to local singularity coefficients reflecting the sharpness of the image in the neighborhood of the pixel (x, y) , which is altimetric. The *ISO* capacity is planimetric since it is sensitive to the spatial distribution of the measure. The *SUM* is considered as a mixed capacity since it responds to both sharpness and spatial distribution of the measure.

6.5 Application to image analysis

Fractal and multifractal analysis was introduced in image processing, but it is not yet used extensively. Several studies have used the fractal dimension to perform texture

classification and image segmentation (Lam, 1990; Jaggi *et al.*, 1993; Lam *et al.*, 1998; Emerson *et al.*, 1999; Qiu *et al.*, 1999). However, few studies have been devoted to the use of multifractals in image analysis (Falconer, 1994; Levey-Vehel and Vojak, 1996). The multifractal approach assumes that the 2D grey level image can be considered as a 3D surface in which the grey levels can be assimilated to a spatial coordinate on the z-dimensional. However Levy-Vehel (1998) pointed out that this assumption has no theoretical basis, since the scaling properties of the grey levels are generally different from those of the space coordinates. Therefore, the grey levels should be considered only as a relative measure of fractal dimension.

6.6 Image processing

The fractal and multifractal modelling procedures which are used in this investigation consist of the following stages:

- Computing the pointwise Hoelder exponent capacities (*MAX*, *ISO* and *SUM*) based on the kernel window sizes of 1×1 to 5×5 and applied to the data sets. This produces image of the Hoelder exponents for the three image segments I, II, and III.
- Computing the multifractal segmentation based on difference between the raw data and the exponents capacity using a set of segmentation parameters (table 6.1). This procedure produces a set of images which present sequentially the detection of edge elements defines major edge features and zones within an image.

Table 6.1: Multifractal segmentation parameters.

	Point	Spread
Segment-1	1	0.1
Segment-2	1	0.3
Segment-3	1	0.5
Segment-4	1	0.7
Segment-5	1	0.9
Segment-6	2	0.1

- The final stage is to compute the regularisation dimension, which is based on measuring the fractal dimensions across the data set. Visualisation of the regularization dimension using multiple passes (voices) of the data set (4, 8, 16, 32, and 64), which allows visual exploration of the fractal patterns. Images of regularization dimension show isolines of equal fractal dimensions. Isolines enclose areas of fractal dimensions. Concentrations of isolines indicate transition areas of fractal dimensions within the image. Areas free of isolines indicate relatively homogenous areas in terms of fractal dimensions.

6.7 Results and Discussions

6.7.1 Introduction

Fractal and multifractal analysis models were applied to Bands 4 and Band 7 of the Al-Ahsa data sets. The same subsets of test segments I, II and III that have been used for the previous models (FFT and ANN) were also used for this technique. In this section, the discussion covers the resulting images of fractal and multifractal processing, which include the following:

- Statistics that are determined by the pointwise Hoelder exponents images.
- Enhanced images derived from the pointwise Hoelder exponents for image processing with *MAX*, *ISO* and *SUM* values.
- Multifractal segmentation images derived from a sequence of segmentation parameters.
- Regularisation dimensions derived using a sequence of regularisation parameters in order to produce a contour zonation based on local fractal dimension.

The results of the fractal and multifractal modelling procedure are expressed as images of enhanced pointwise Hoelder exponent capacities (*MAX*, *ISO* and *SUM*). Each capacity of the Hoelder exponents has different properties as follows:

- *MAX* is a multifractal measure of the local peakedness of fractal dimension.
- *ISO* is a multifractal measure of the local uniformity of fractal dimension.

- *SUM* incorporates both sharpness and spatial distribution of fractal values and is the sum of *ISO* and *MAX*.

The segmentation image is an extracted image of detected change between the original raw data and the Hoelder exponent images of *MAX*, *ISO* and *SUM*. Images of segmentation show edge elements in the original images. The contour image is based on the measuring of the regularisation dimension that computes the fractal dimension. Thus, the end product appears as a different colour contouring zonation of specific fractal dimension.

6.7.2 Image statistics

The resulting data structure of multifractal modelling of the enhancement procedures (pointwise Hoelder exponents, *MAX*, *ISO* and *SUM*) were compared in terms of image statistics and histograms. The statistics of mean values and standard deviation of Hoelder exponents differed considerably. The image of the *MAX* capacity presents, for instance, the lowest values of its image mean value, whereas the *SUM* capacity presents the highest of statistics values. The mean value of the *ISO* capacity is in between the mean value of the previous capacities (see table 6.2).

The histograms of these exponents' capacity images were totally different from each other (see figures 6.1, 6.2, 6.3). For instance, the histogram of the *MAX* image shows one dominant peak across the dynamic range of values from 0 to 100 out of the normal

0 to 255 range. This peak is somewhat concentrated at the first hundred of the dynamic range, but the rest of the dynamic range appears as a very small pin. However, the appearance of the *ISO* histogram is stretched through the full dynamic range and it shows two dominant peaks. The first peak is very thin and very high at the first two of the dynamic range, while the second peaks is very broad and appears in range of 40-250 DN. The *SUM* histogram shows two dominant peaks but they are different from the previous exponent image because both peaks are thin; even-though the peak at approximately the 210-240 DN appeared somewhat broader.

On the basis of the image statistics there are no clear structures in terms of local peakedness of fractal dimension. However, for local homogeneity of fractal dimension there are two distinct types of feature with very high and very low levels of homogeneity in fractal dimensions. The *SUM* histogram simply reflects the joint distributions.

Table 6.2: Image statistics of Hoelder exponent images for the three segments.

Segment I	Min. value	Max. value	Median	Mean	S. deviation
MAX-4	0.00	255.00	90.00	93.41	63.42
MAX-7	0.00	255.00	121.00	115.94	81.45
ISO-4	0.00	255.00	170.00	154.39	60.66
ISO-7	0.00	255.00	178.00	162.98	63.32
SUM-4	0.00	255.00	235.00	218.12	59.06
SUM-7	0.00	255.00	210.00	193.83	57.81

Segment II	Min. value	Max. value	Median	Mean	S. deviation
MAX-4	0.00	255.00	20.00	30.45	35.43
MAX-7	0.00	255.00	8.00	18.43	26.29
ISO-4	0.00	255.00	170.00	155.36	64.23
ISO-7	0.00	255.00	178.00	161.33	67.00
SUM-4	0.00	255.00	227.00	208.23	60.45
SUM-7	0.00	255.00	210.00	192.56	58.62

Segment III	Min. value	Max. value	Median	Mean	S. deviation
MAX-4	0.00	255.00	12.00	20.13	25.71
MAX-7	0.00	255.00	12.00	20.47	27.44
ISO-4	0.00	255.00	178.00	160.44	62.49
ISO-7	0.00	255.00	186.00	165.33	67.70
SUM-4	0.00	255.00	231.00	213.69	57.85
SUM-7	0.00	255.00	219.00	199.25	60.73

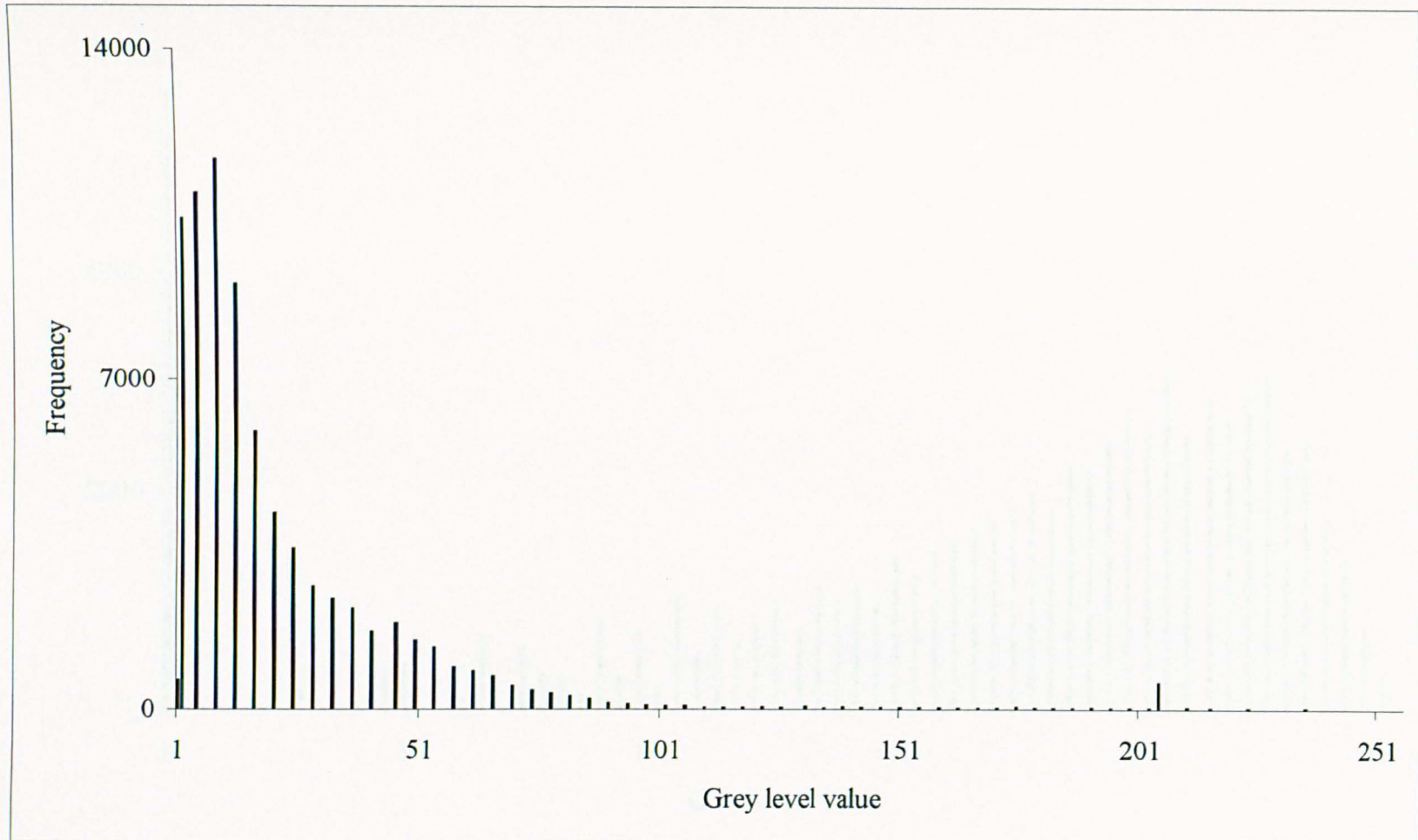


Figure 6.1: Histogram of the MAX pointwise Hoelder exponent image (Band 7, segment I).

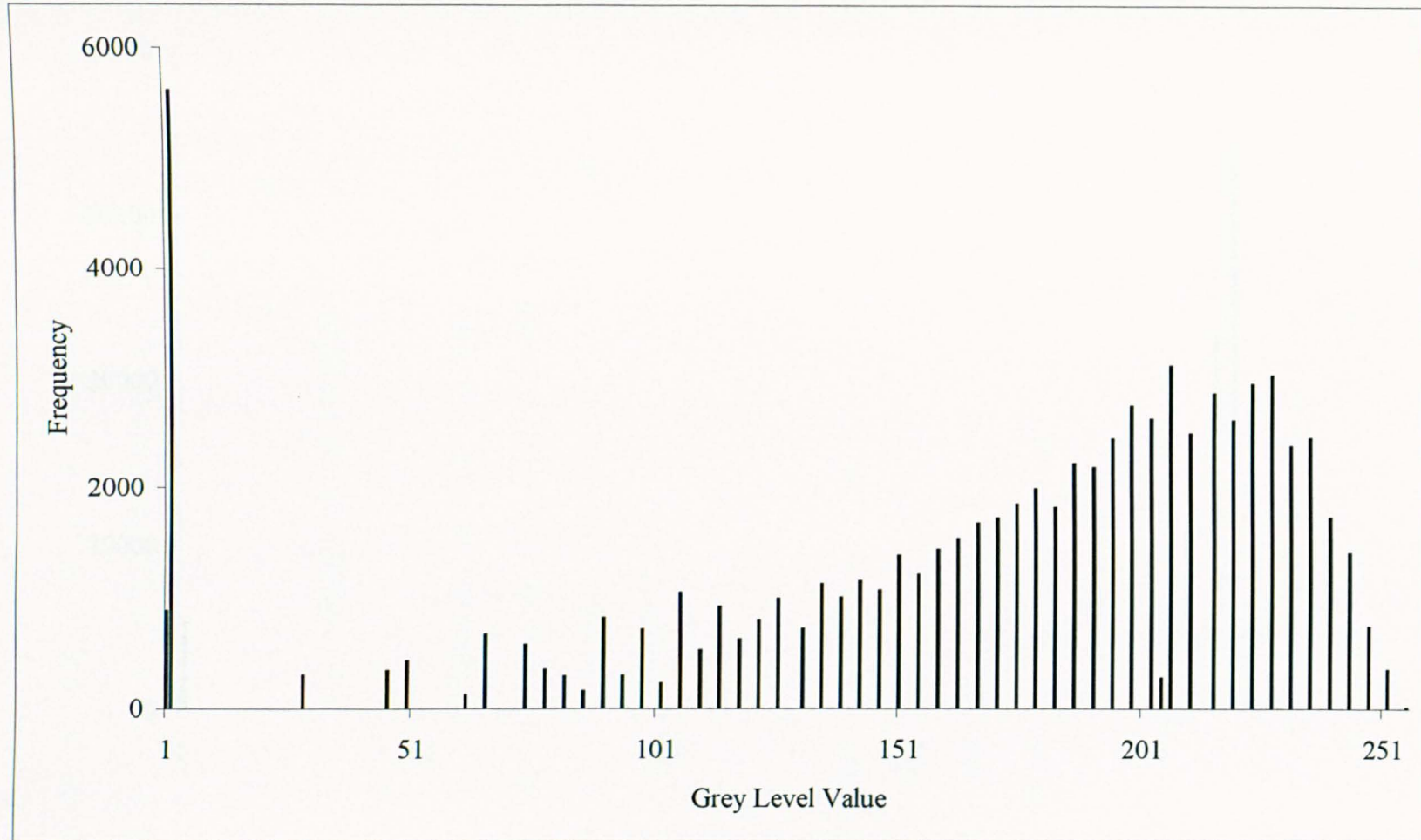


Figure 6.2: Histogram of the ISO pointwise Hoelder exponent image (Band 7, segment I).

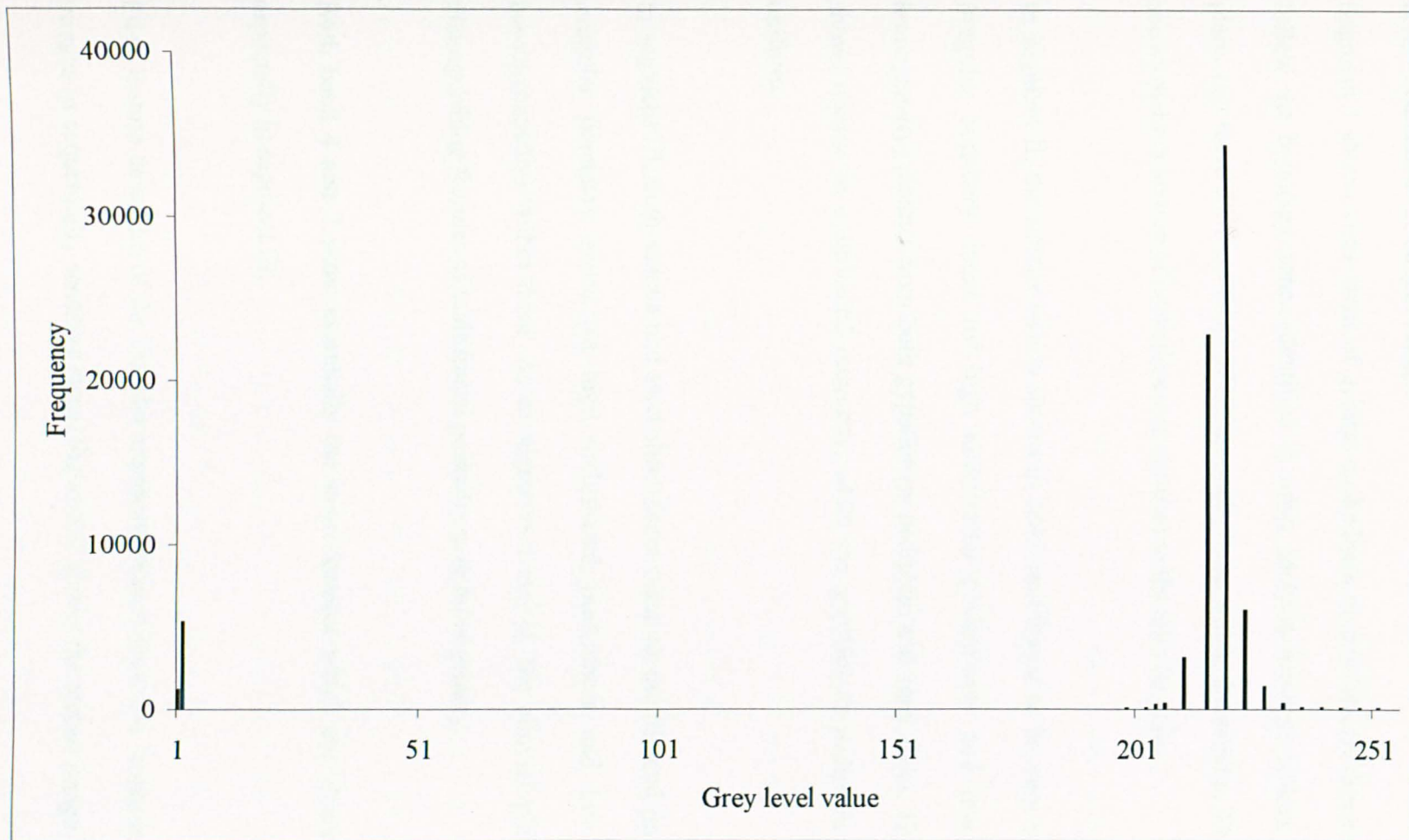


Figure 6.3: Histogram of the SUM pointwise Hoelder exponent image (Band 7, segment I).

6.7.3 Assessment of output images

Segment I shows clear areas of greater peakedness in multifractal dimensions. These follow the boundary zones identified in other analysis between sabkha and alluvial plain. But there are clear areas of higher peakedness within the sabkha. The sand sheet shows distinct texture of peaked-ness in contrast to the alluvial plain.

In segment II, the sabkha area is shown in *MAX* multifractal to be very complex with irregular boundary zones (of high multifractal peaked-ness and low multifractal homogeneity) distinct from both gypsiferous pediplain and sand sheet. The sand sheet shows texture in multifractal measures, while the gypsiferous pediplain is relatively uniform.

In segment III, both sabkha and sand sheet show complex multifractal properties with irregular boundary zones (of high multifractal peakedness and low multifractal homogeneously) within them. As in segments I and II, the alluvial plain shows no distinguishing features of multifractal peakedness or homogeneity.

Both band 4 and 7 show essentially the same features which are clearer in Band 7 especially in segment III.

Edge feature detection of the Hoelder exponent images show the 'contours' within the images in sequentially sensitive steps. Figure 6.7 shows the output image for the *MAX*

exponent images. The edge of the sabkha unit is distinguished as two patterns. No edges of alluvial plain appeared. Very few edges points appeared in the sand sheet area. Figure 6.8, Sabkha and Sand sheet are detected, while a very few edges appeared in the alluvial plain. In figure 6.9 is more or less similar in points because this exponent is the combined of *MAX* and *ISO* values. In Band 4, there are not many edge features except in the sand sheet area, which can be distinguished but with no significant edges as it appeared in the sabkha area.

In segment II, the sabkha area is very complex for all Hoelder exponents images (Figures 6.13, 6.14, 6.15), whereas the sand sheet area is distinct but less complex. In the gypsiferous pediplain unit, there is no evidence of edge patterns and it is displayed as a homogenous area except figure 6.14 (e), which shows few scattered edges. The results of Band 4 and 7 are more or less similar, where sabkha and sand sheet areas are complex, but the gypsiferous pediplain is homogenous.

The edge of the sabkha area is also detected in segment III in addition to another edges patterns appeared within the area, this means this area is heterogeneous (Figure 6.19). There is no evidence of edges patterns in other areas, and since these areas are showing to be uniform, that means they are homogeneous. In other exponents (Figure 6.20, 6.21), although the edge of sabkha area is detected, it is more complex than the *MAX* exponent images. Band 4 shows more complexity of edges patterns, and it is difficult to draw interpretation of any features except in the images of figure 6.22. The edges

patterns are only self-evident in the sabkha area, while other areas are simple and homogenous.

In the regularisation dimension images, both Bands 7 and 4 show somewhat similar complexities of patterns. They show that sabkka and sand sheet areas in each case are very complex in terms of spatial differences in fractal dimensions, while the alluvial plain is very simple. In all segments, the heterogeneity of patterns within the sabkha and sand sheet areas are self-evident (Figures 6.25 to 6.30). Overall both bands (7 and 4) show the same main areas, but different features within them especially in segment III (e. g. sabkha area is more complex in Band 4 than in Band 7).

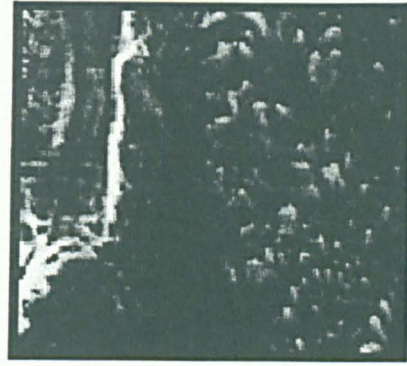
6.7.4 Analysis of multifractal images for soil landscape identification

6.7.4.1 Test Segment I

In this segment, the sabkha unit appeared as complex features. Many complex linear patterns of fractal properties are identified within and at the edges of this area. There is no evidence of dominant zones. The alluvial plain area is very simple in each case and does not have any linear features or dominant zones. It can be considered as a homogenous area. The sand sheet area is somewhat more complex than the alluvial plain because in most cases it appears as complex features (Figures 6.8 to 6.12). However, there is no evidence of linear features or zones. There are few differences between Band 4 and 7, but Band 7 is somewhat less complex than Band 4.



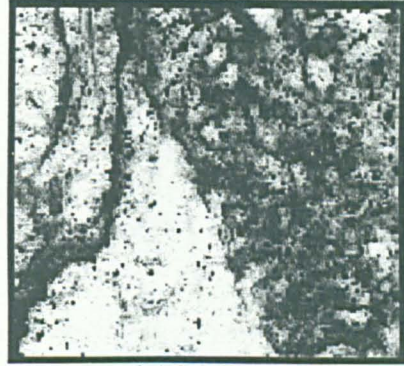
a (MAX Band 4)



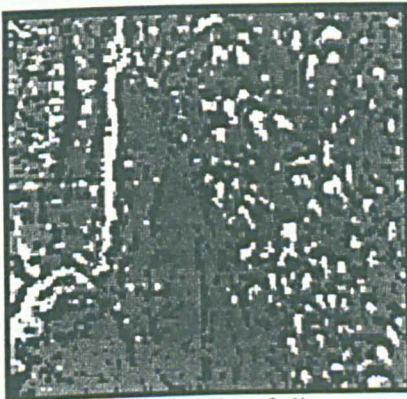
b (MAX Band 7)



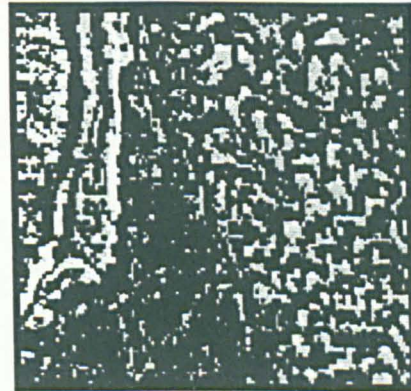
c (ISO Band 4)



d (ISO Band 7)

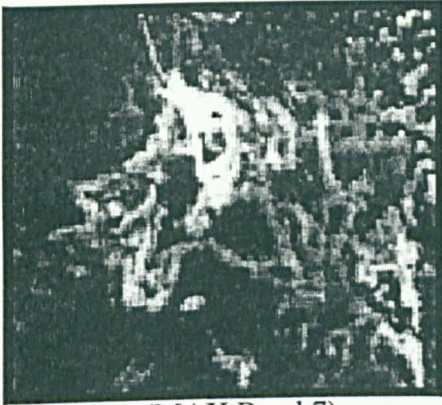


e (SUM Band 4)

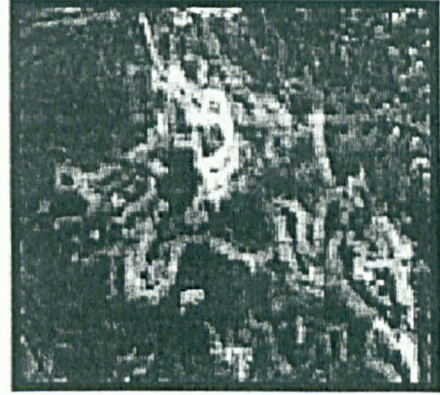


f (SUM Band 7)

Figure 6.4 Images a to f represent different Hoelder exponent images for Band 4 and 7 (Test area 1).



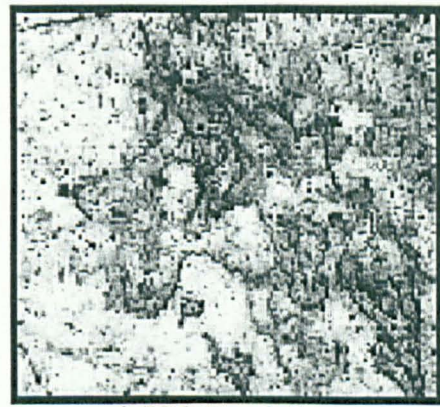
a (MAX Band 7)



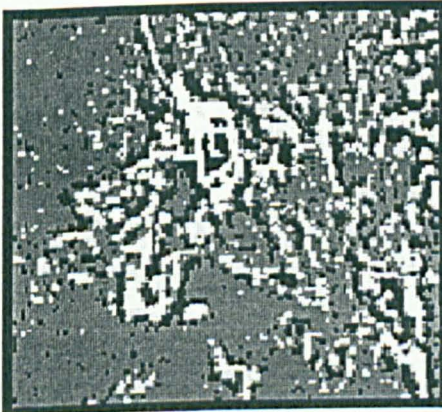
b (MAX Band 4)



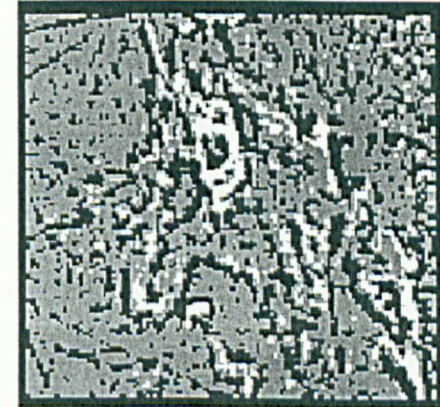
c (ISO Band 7)



d (ISO Band 4)

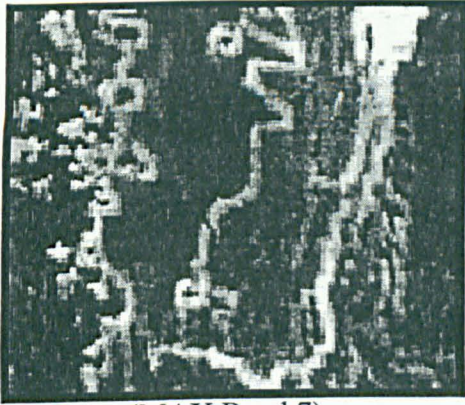


e (SUM Band 7)

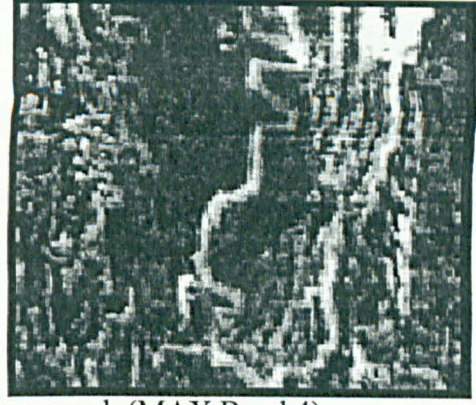


f (SUM Band 4)

Figure 6.5: Images a to f represent different Hoelder exponent images for Band 4 and 7 (Segment II).



a (MAX Band 7)



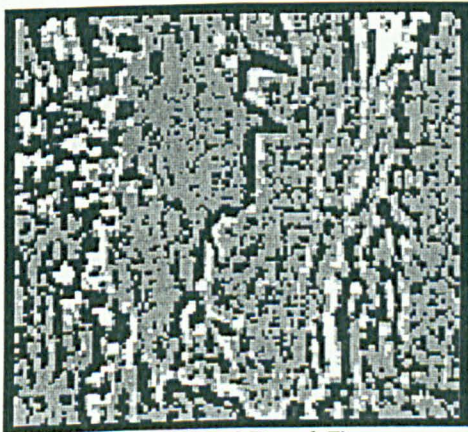
b (MAX Band 4)



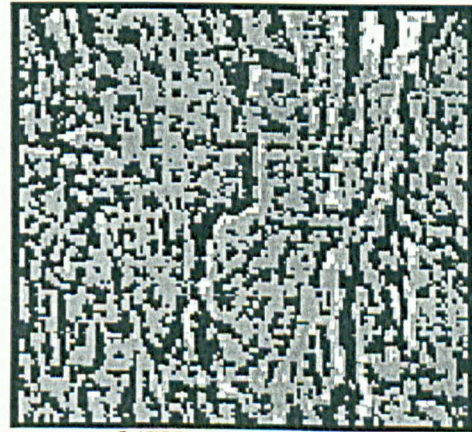
c (ISO Band 7)



d (ISO Band 4)

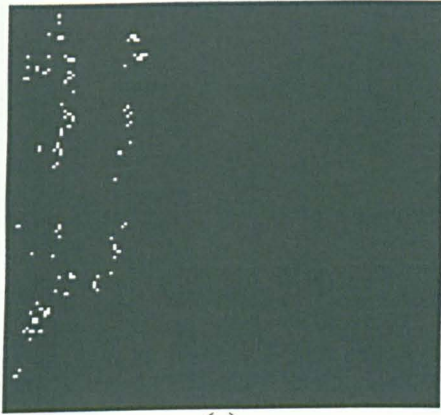


e (SUM Band 7)

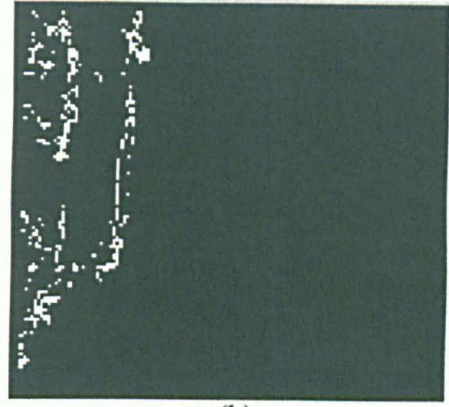


f (SUM Band 4)

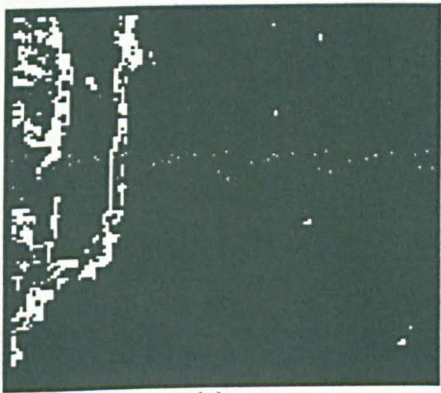
Figure 6.6: Images a to f represent different Hoelder exponent images for Band 4 and 7 (Segment III).



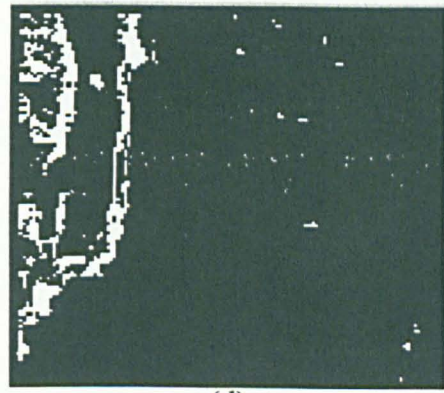
(a)



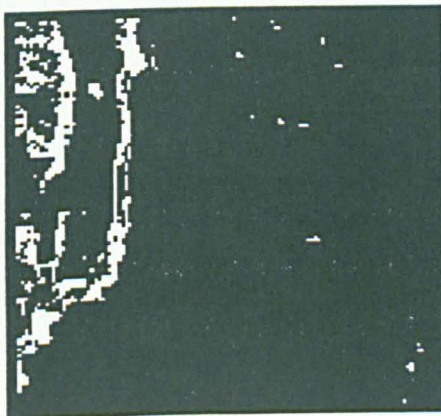
(b)



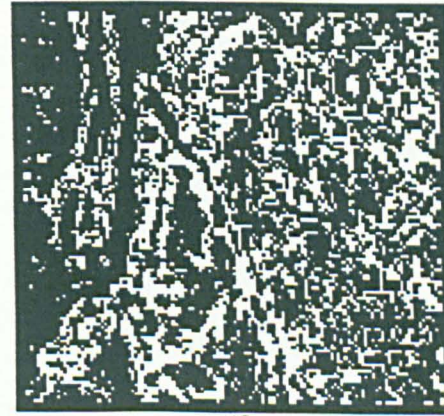
(c)



(d)

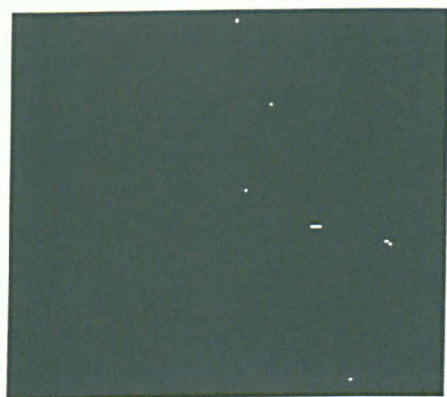


(e)

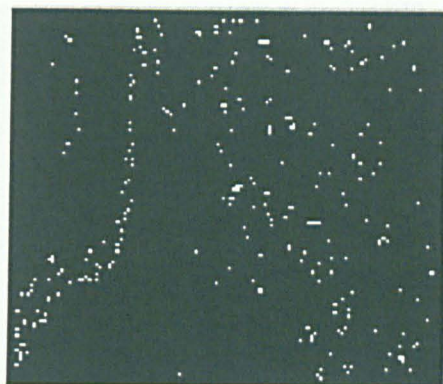


(f)

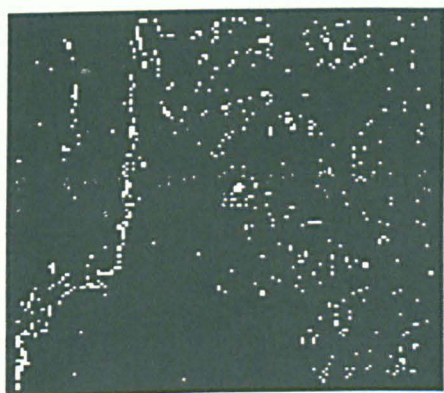
Figure 6.7: Images (a) to (f) represent MAX Hoelder exponent of multifractal segmentation of different parameters setup for Band 7 (Segment I).



(a)



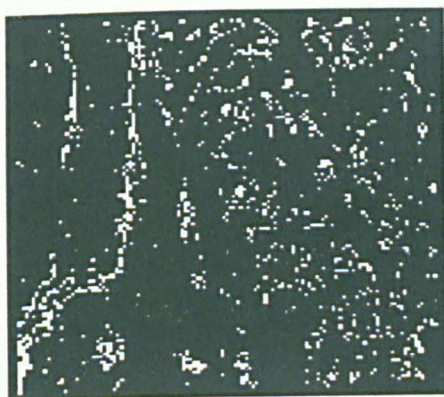
(b)



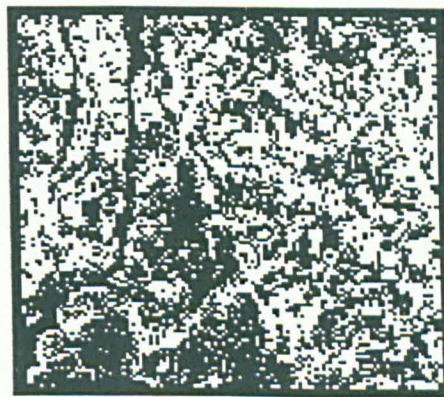
(c)



(d)

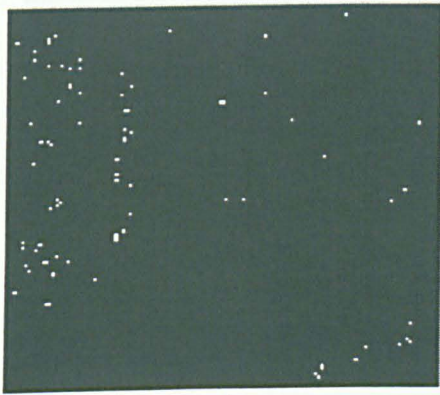


(e)

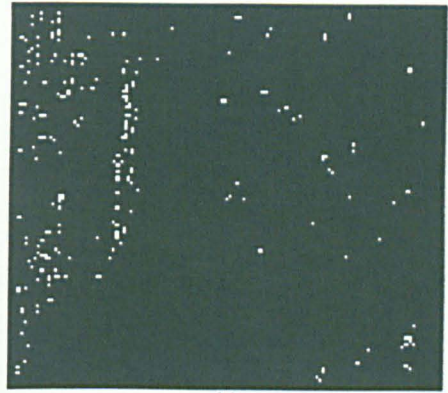


(f)

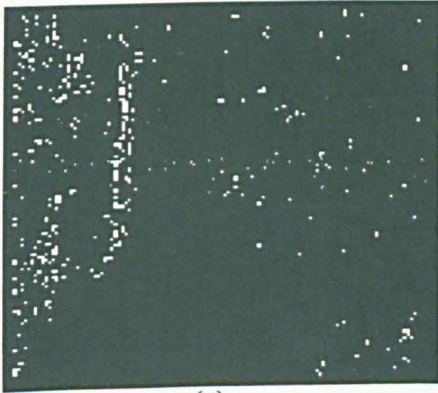
Figure 6.8: Images a to f represent ISO Hoelder exponent of multifractal segmentation images of different parameters setup for Band 7 (Segment I).



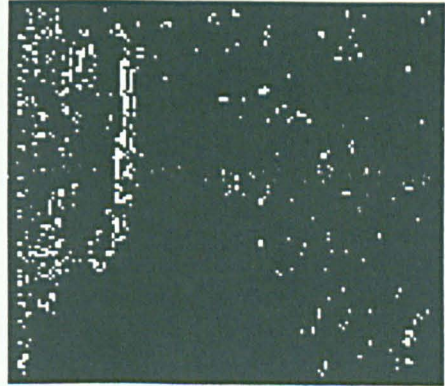
(a)



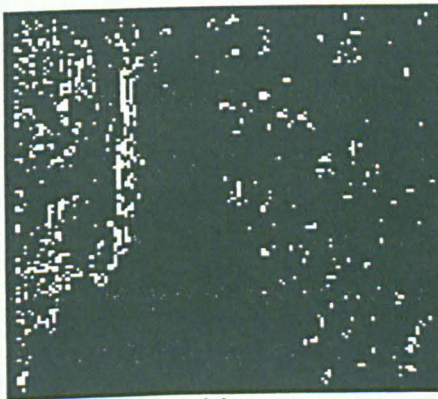
(b)



(c)



(d)

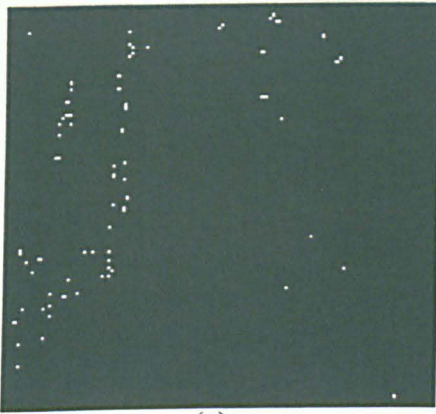


(e)



(f)

Figure 6.9: Images (a) to (f) represent SUM Hoelder exponent of multifractal segmentation images of different parameters setup for Band 7 (Segment I).



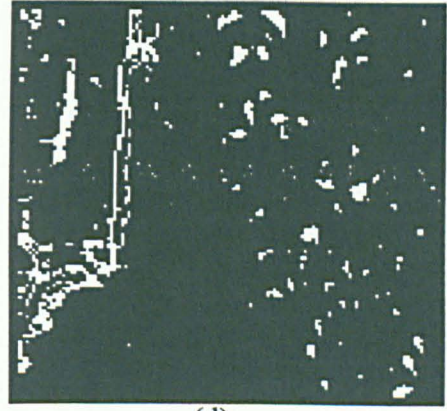
(a)



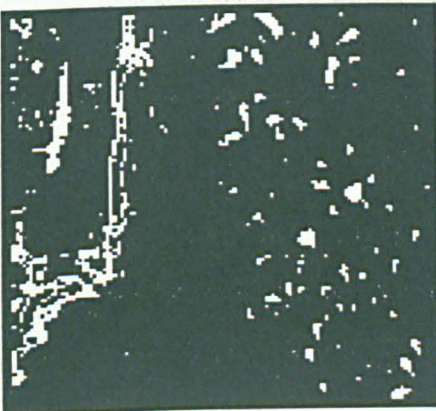
(b)



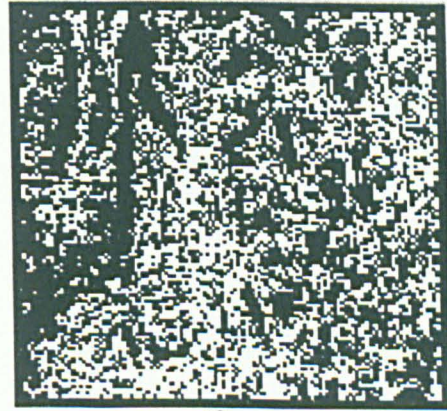
(c)



(d)

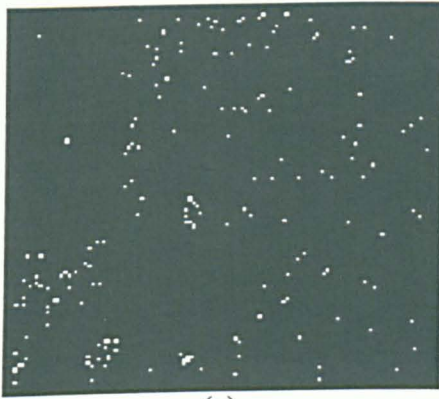


(e)

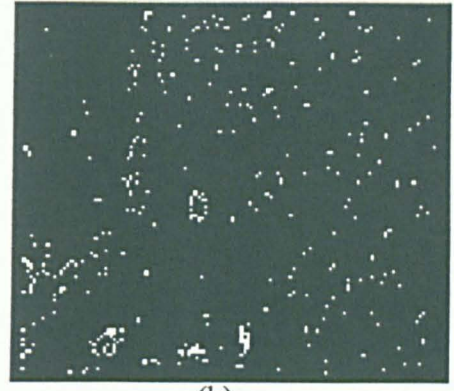


(f)

Figure 6.10: Images (a) to (f) represent MAX Hoelder exponent of multifractal segmentation images of different parameters setup for Band 4 (Segment I).



(a)



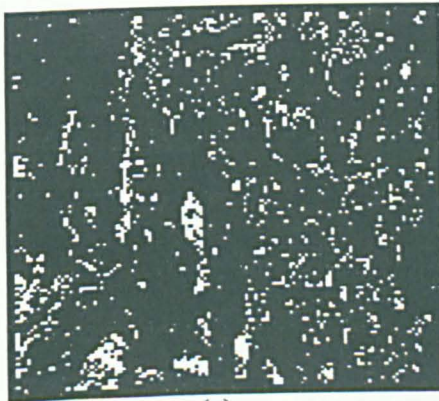
(b)



(c)



(d)

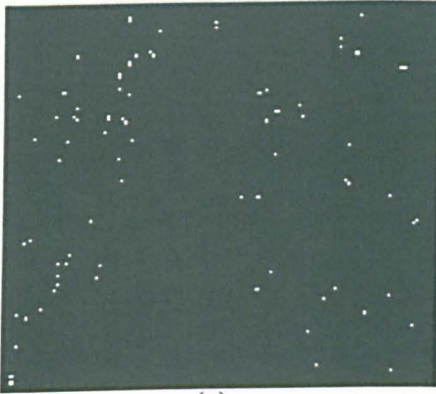


(e)

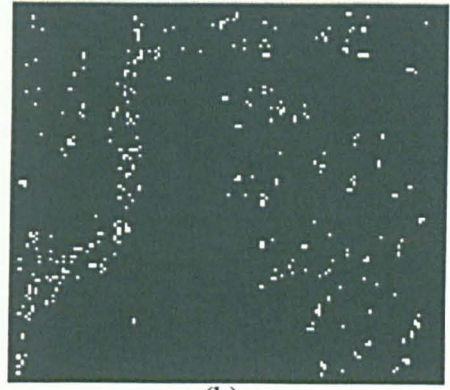


(f)

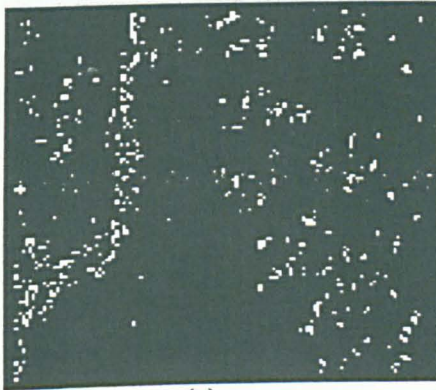
Figure 6.11: Images (a) to (f) represent ISO Hoelder exponent of multifractal segmentation images of different parameters setup for Band 4 (Segment I).



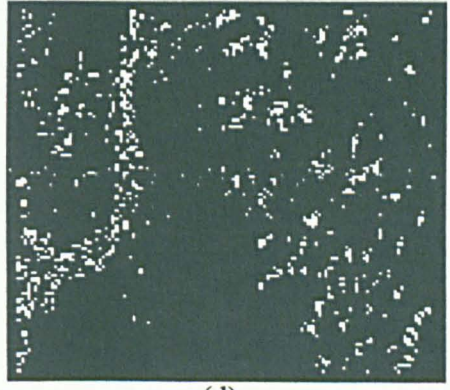
(a)



(b)



(c)



(d)

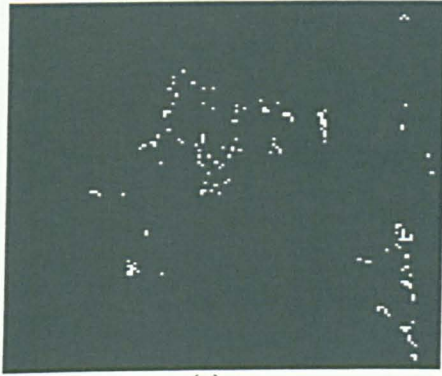


(e)

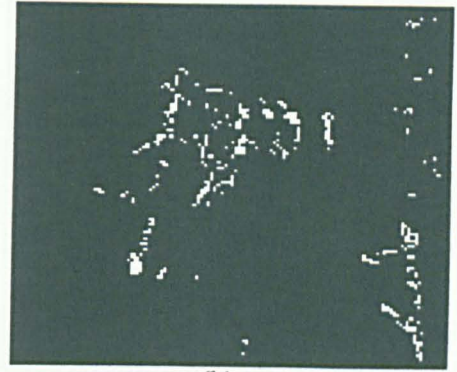


(f)

Figure 6.12: Images (a) to (f) represent SUM Hoelder exponent of multifractal segmentation images of different parameters setup for Band 4 (Segment I).



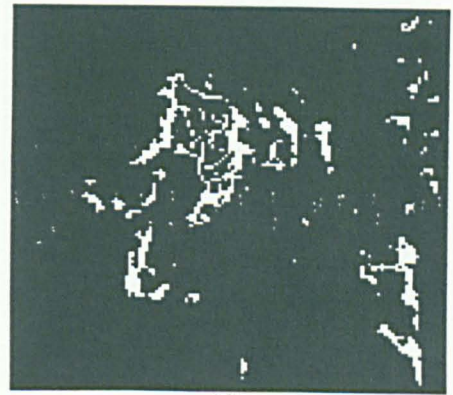
(a)



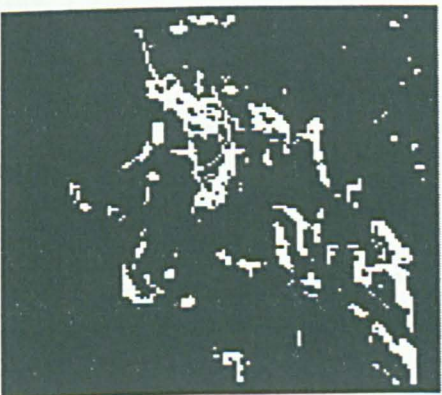
(b)



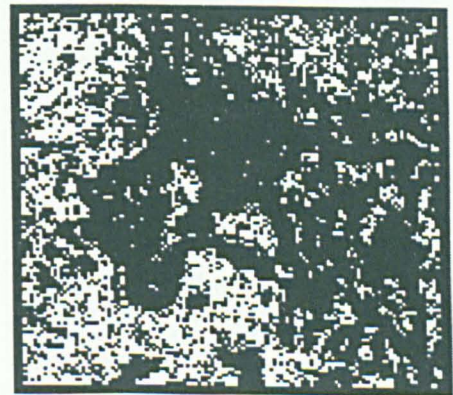
(c)



(d)

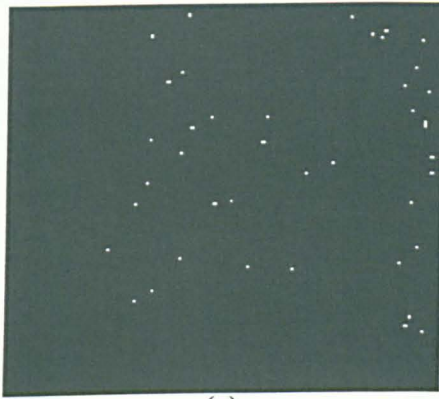


(e)

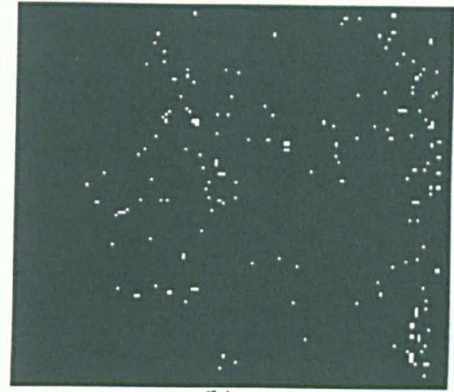


(f)

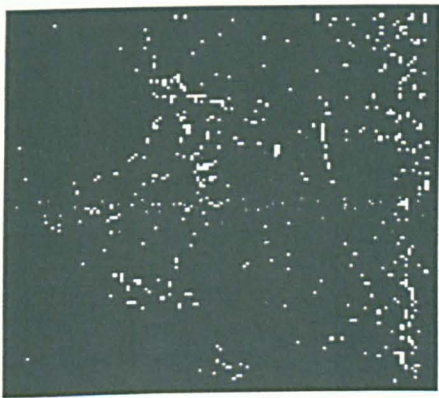
Figure 6.13: Images (a) to (f) represent MAX Hoelder exponent of multifractal segmentation images of different parameters setup for Band 7 (Segment II).



(a)



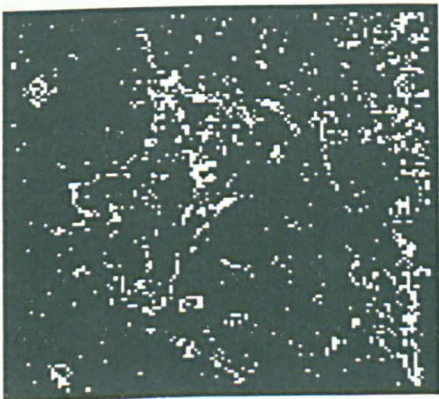
(b)



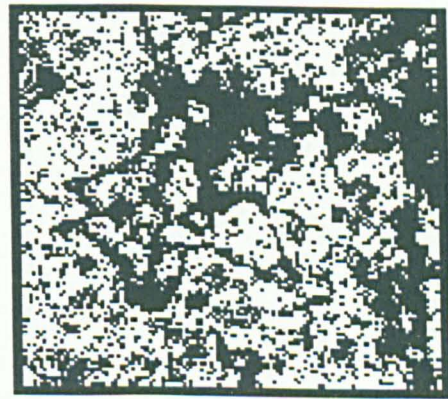
(c)



(d)

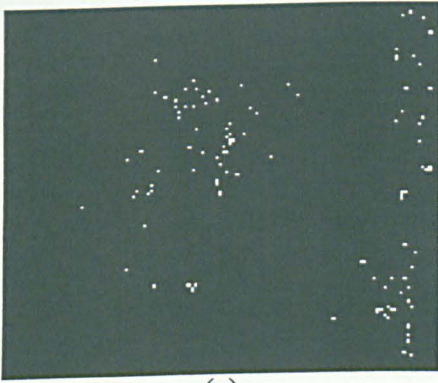


(e)



(f)

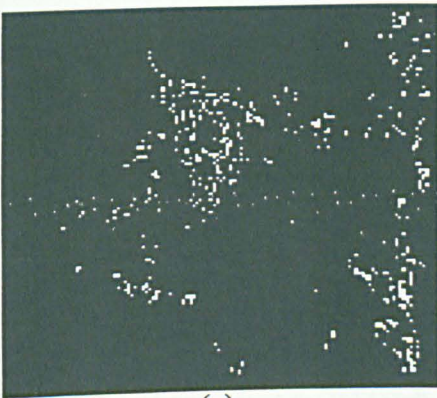
Figure 6.14: Images (a) to (f) represent ISO Hoelder exponent of multifractal segmentation images of different parameters setup for Band 7 (Segment II).



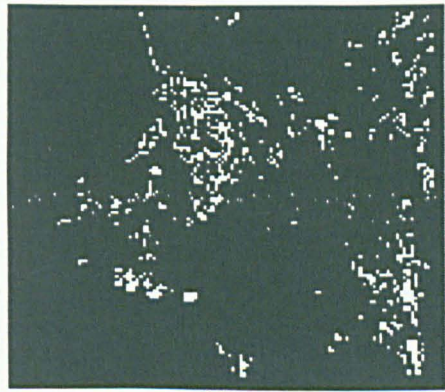
(a)



(b)



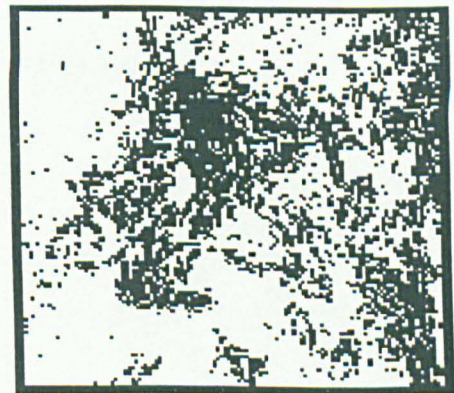
(c)



(d)



(e)

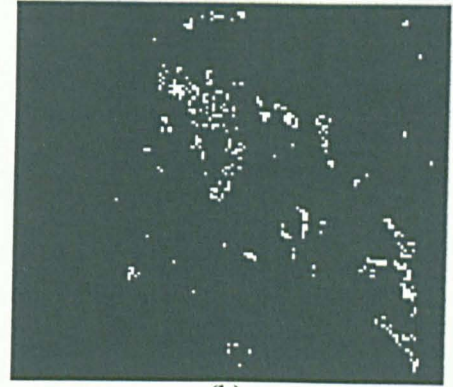


(f)

Figure 6.15: Images (a) to (f) represent SUM Hoelder exponent of multifractal segmentation images of different parameters setup for Band 7 (Segment II).



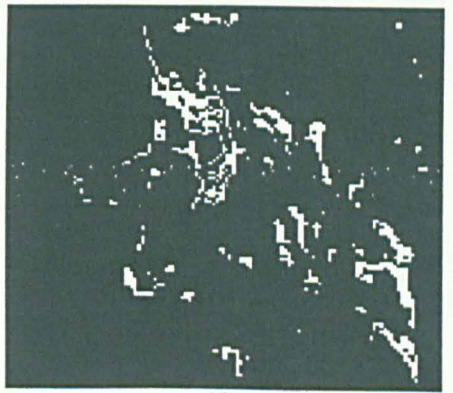
(a)



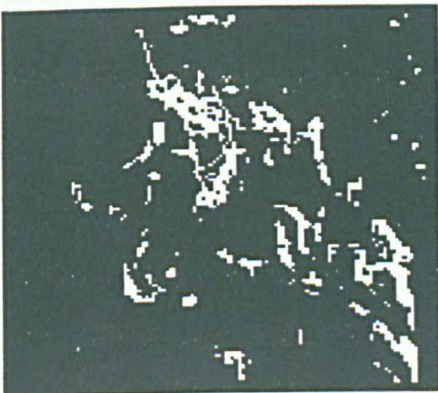
(b)



(c)



(d)

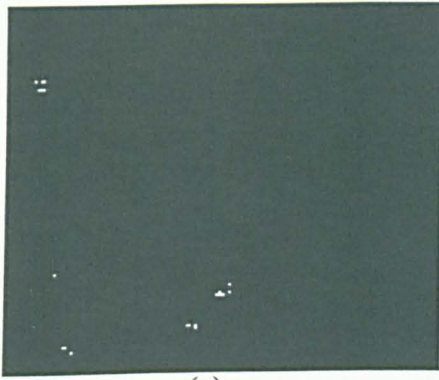


(e)

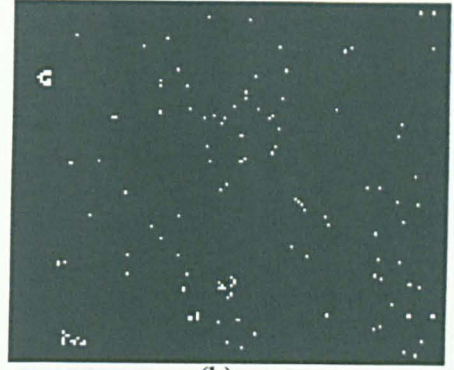


(f)

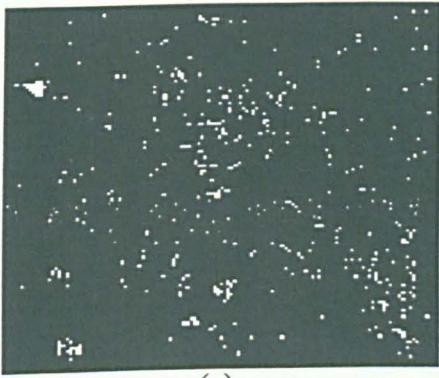
Figure 6.16: Images (a) to (f) represent MAX Hoelder exponent of multifractal segmentation images of different parameters setup for Band 4 (Segment I).



(a)



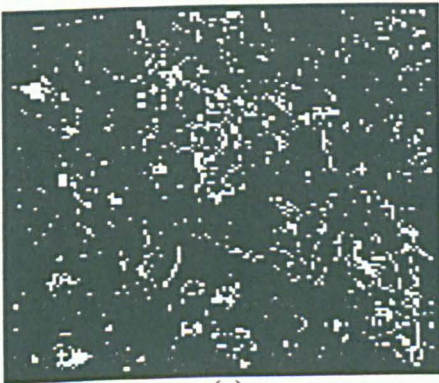
(b)



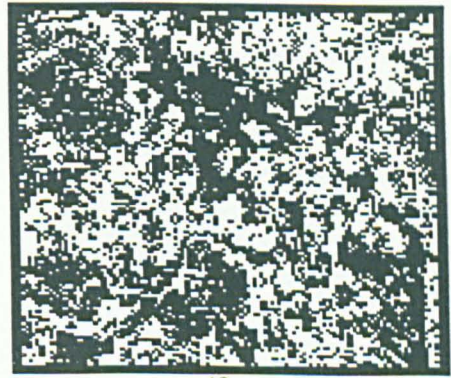
(c)



(d)

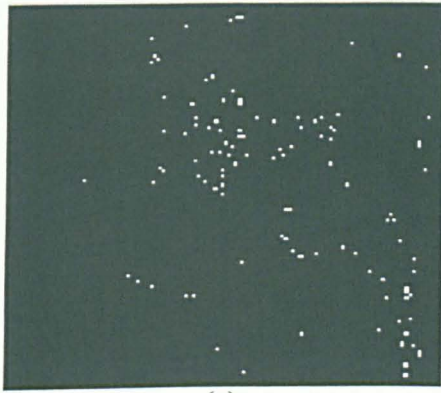


(e)



(f)

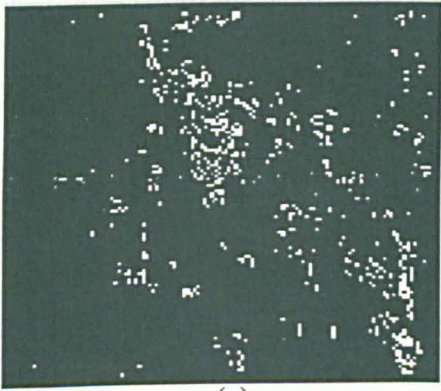
Figure 6.17: Images (a) to (f) represent ISO Hoelder exponent of multifractal segmentation images of different parameters setup for Band 4 (Segment II).



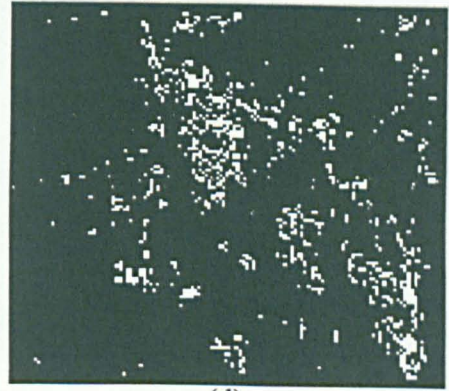
(a)



(b)



(c)



(d)

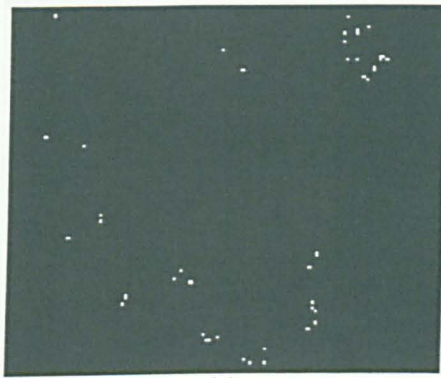


(e)

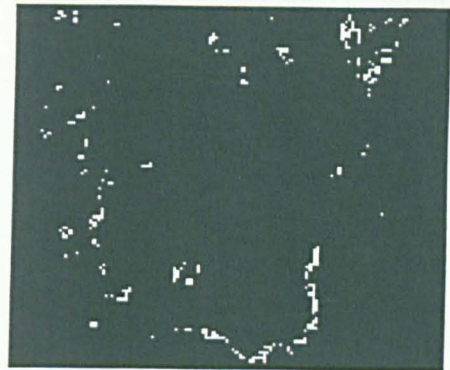


(f)

Figure 6.18: Images (a) to (f) represent SUM Hoelder exponent of multifractal segmentation images of different parameters setup for band 4 (Segment II).



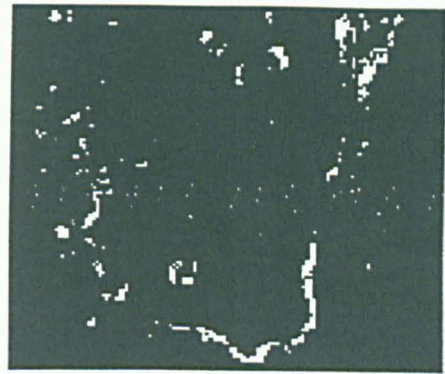
(a)



(b)



(c)



(d)

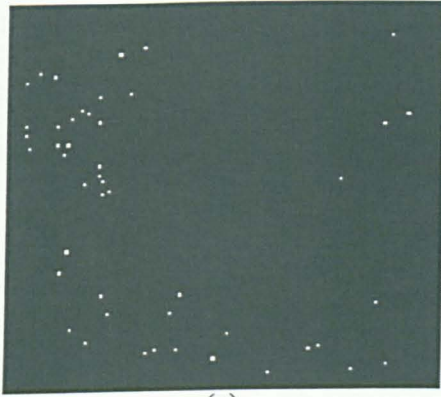


(e)

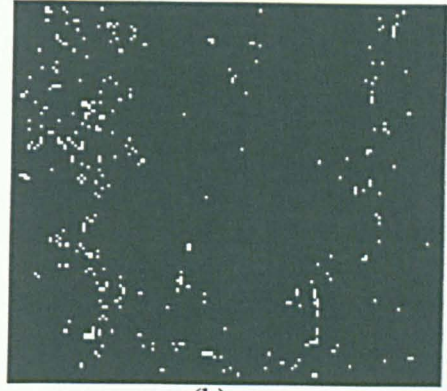


(f)

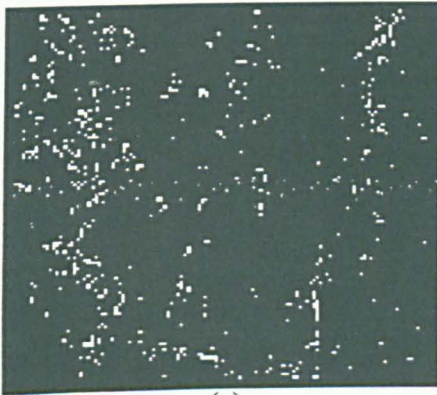
Figure 6.19: Images (a) to (f) represent MAX Hoelder exponent of multifractal segmentation images of different parameters setup for Band 7 (Segment III).



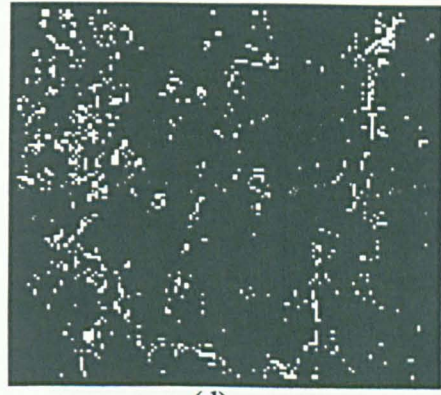
(a)



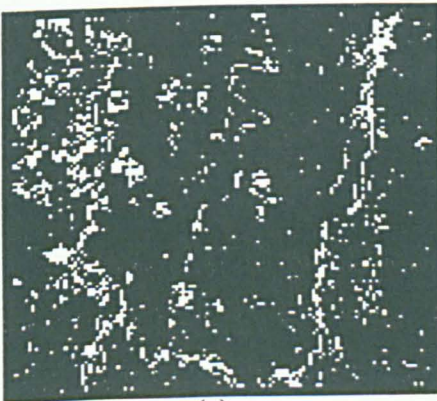
(b)



(c)



(d)

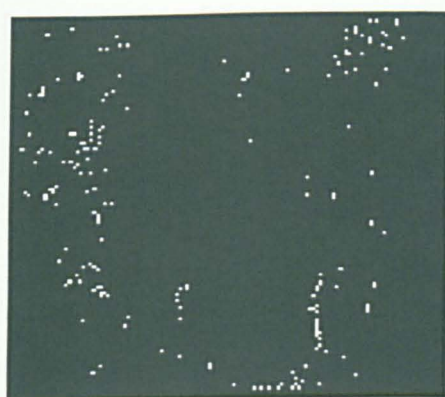


(e)

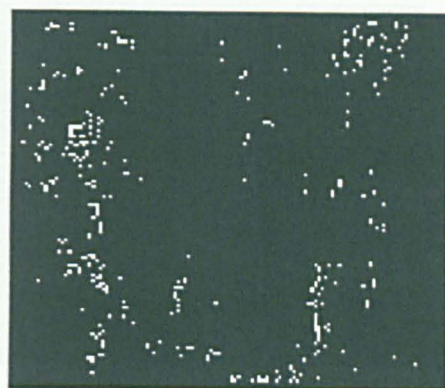


(f)

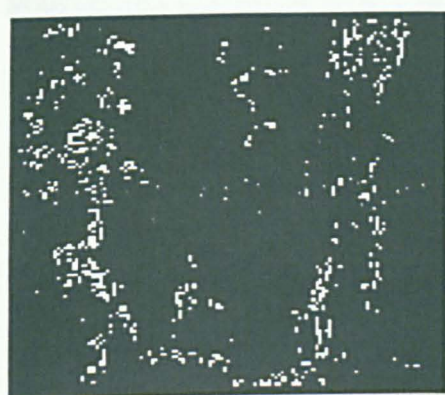
Figure 6.20: Images (a) to (f) represent ISO Hoelder exponent of multifractal segmentation images of different parameters setup for Band 7 (Segment III).



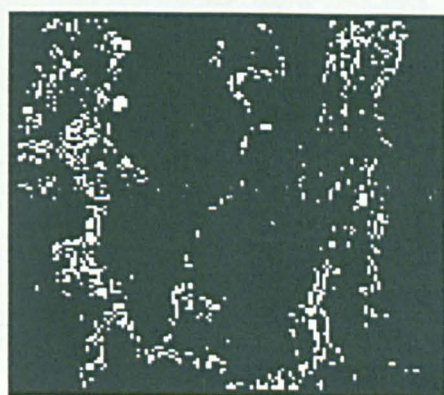
(a)



(b)



(c)



(d)



(e)



(f)

Figure 6.21: Images (a) to (f) represent SUM Hoelder exponent of multifractal segmentation images of different parameters for Band 7 (Segment III).

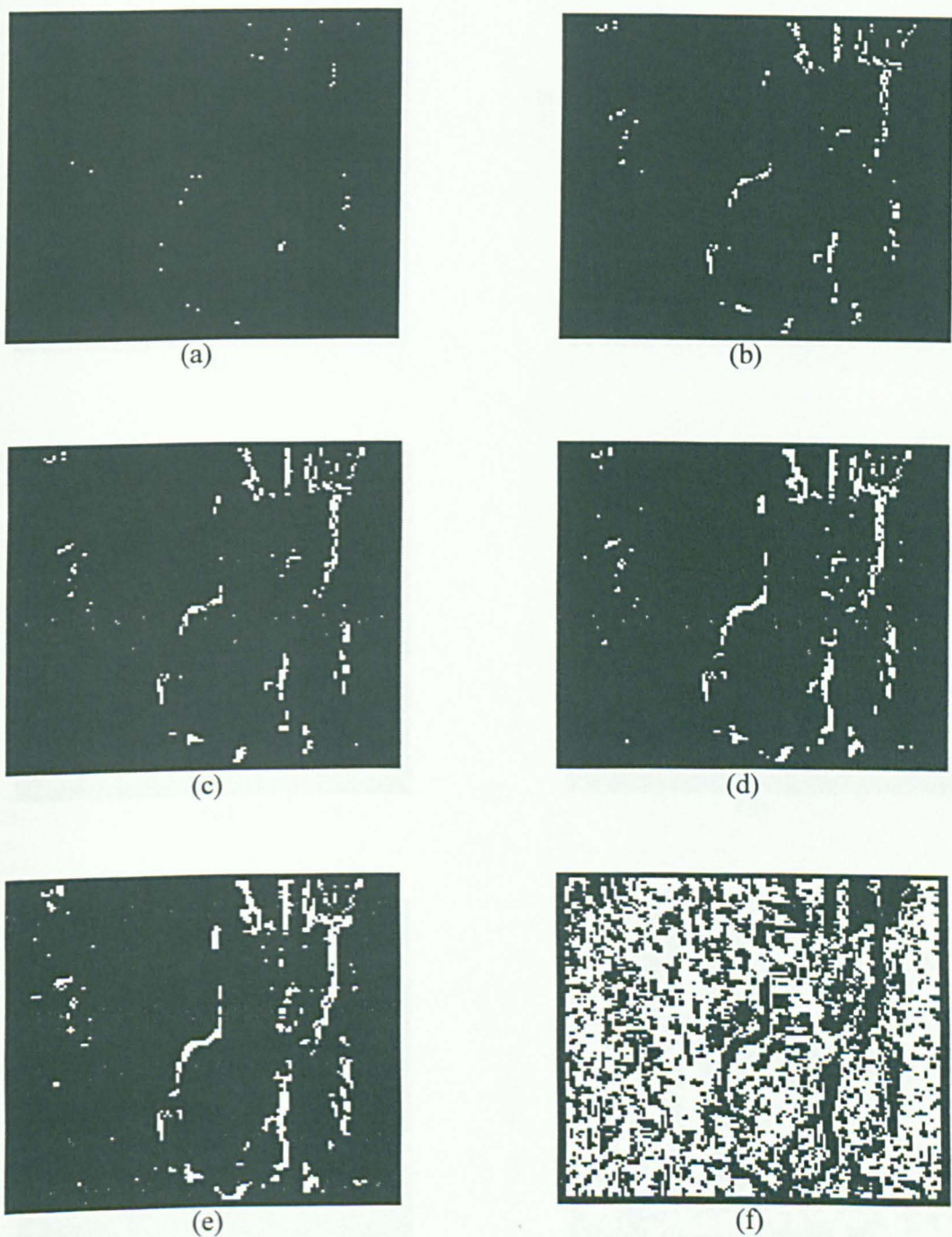
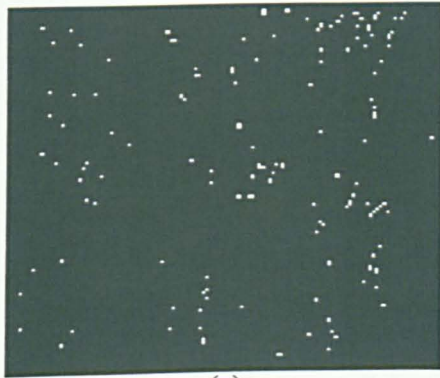


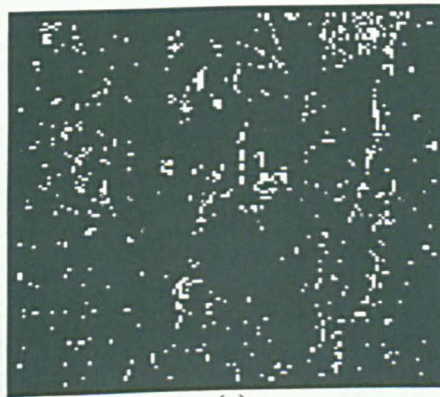
Figure 6.22: Images (a) to (f) represent MAX Hoelder exponent of multifractal segmentation images of different parameters setup for Band 4 (Segment III).



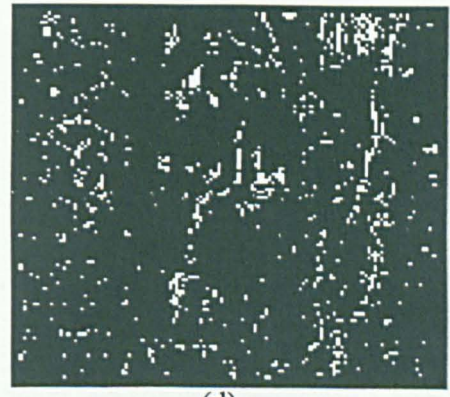
(a)



(b)



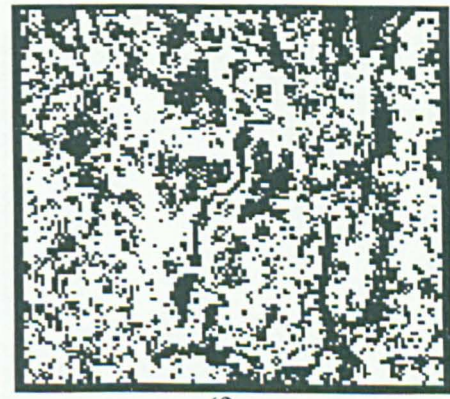
(c)



(d)

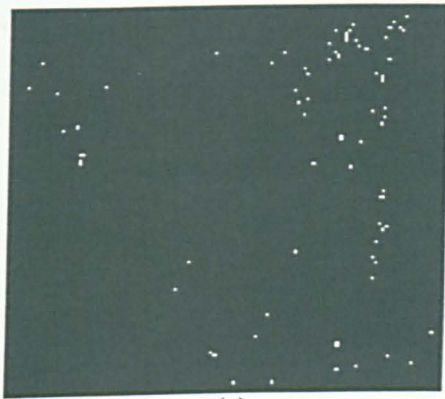


(e)

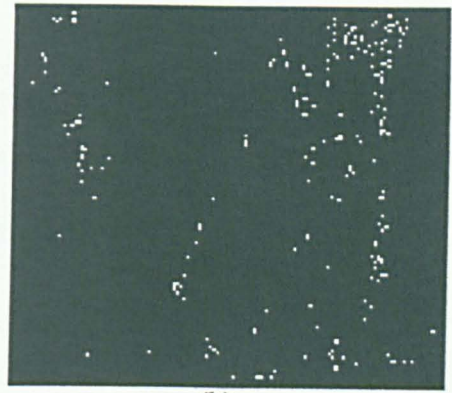


(f)

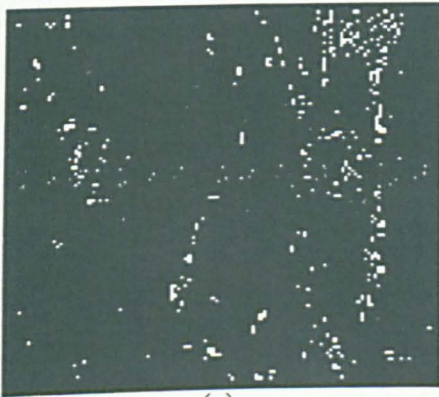
Figure 6.23: Images (a) to (f) represent ISO Hoelder exponent of multifractal segmentation images of different parameters setup for Band 4 (Segment III).



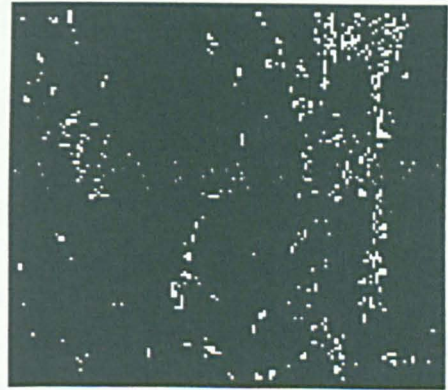
(a)



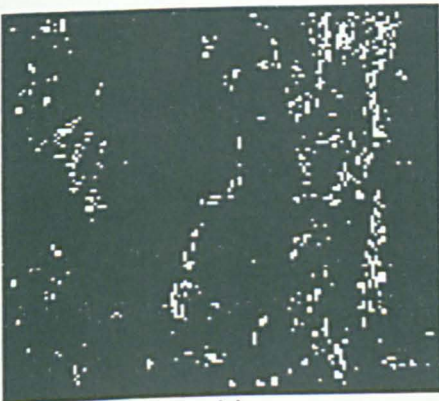
(b)



(c)



(d)



(e)



(f)

Figure 6.24: Images (a) to (f) represent SUM Hoelder exponent of multifractal segmentation images of different parameters setup for Band 4 (Segment III).

6.7.4.2 Test Segment II

The sabkha area is very complex in each output. Linear features are self-evident and can be easily distinguished throughout the sabkha area. Other linear features are also detected within the sabkha area, but are very complex. There is no evidence of zones. In most cases, the gypsiferous pediplain is simple except images in figures 6.14(e) and 6.17(e), which show some kind of complexity. Neither linear features nor zones are evident in the gypsiferous pediplain area. The sand sheet area, in each case, is very complex and it is difficult to distinguish either linear feature or zones that might be considered as a heterogeneous plain. Bands 4 and 7 show essentially the same features but they are somewhat clearer in Band 7.

6.7.4.3 Test Segment III

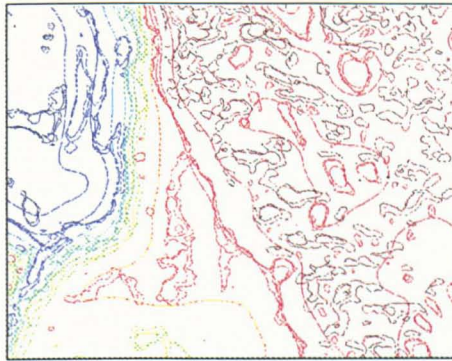
The edges detection of sabkha area are pronounced, and not only many linear features almost surround the area, but also many linear features appeared within the whole sabkha area, which show that this area is a very complex heterogeneous area. In most analysis, the sand sheet shows complex elements, while the alluvial plain is a simple and generally homogenous area. No linear features or zones are distinct in these areas. There are no major differences between Bands 4 and 7 (Figures 6.19 to 6.24).

6.7.5 Analysis of fractal images for soil landscape identification

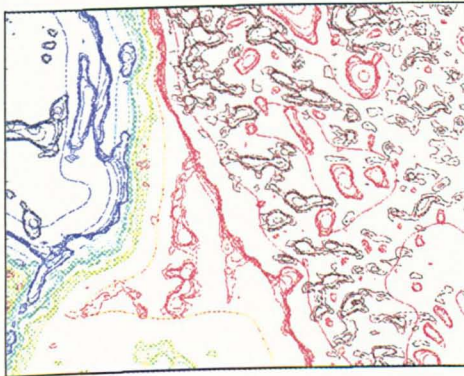
Figures 6.25 and 6.26 show the regularisation dimension images for segment I. In these images the sabkha area is complex and shows very clear spatial transitions to the

alluvial plain area, which might represent transition zone. The alluvial plain is simple and generally homogenous though a transition zone is evident across it a N-S direction. The sand sheet area is a very complex showing very complex patterns across the area. Overall Bands 7 and 4 show similar features with somewhat clearer features in Band 7.

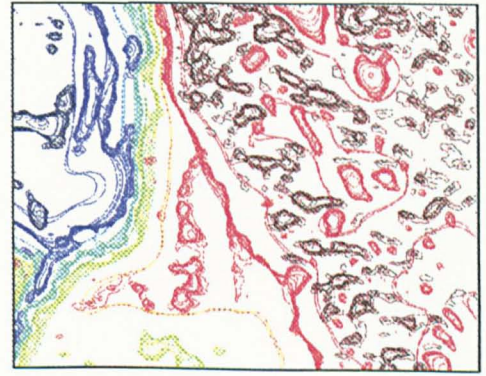
Segments II and III show that sabkha areas are complex (Figures 6.27 to 6.30), but complexities of features are greater in segment II (Figures 6.27 and 6.28). Also, the sand sheet areas are very complex, which show many patterns across the area in these segments. The gypsiferous pediplain, which only appears in segment II, is somewhat complex. Similar features are self-evident in both bands (7 and 4), but clearer in Band 7. However, the gypsiferous pediplain area is simpler in band 4 than in Band 7. Table 6.3 summarises the features identification of the fractal and multifractal model.



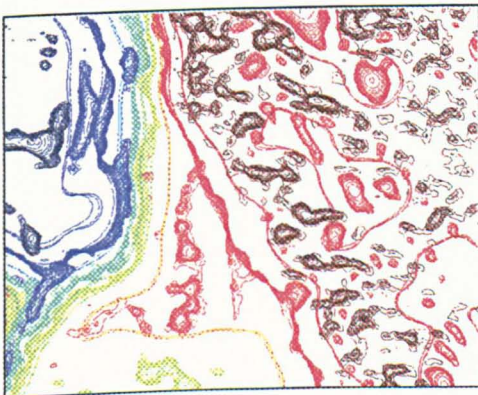
(a)



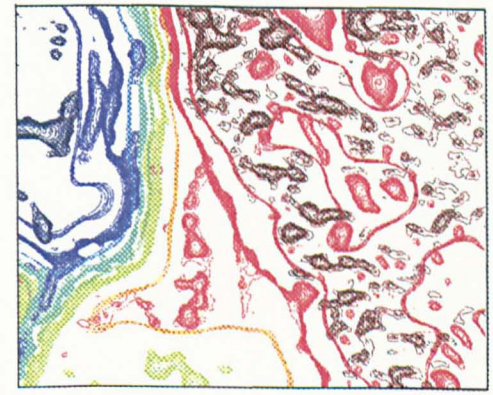
(b)



(c)

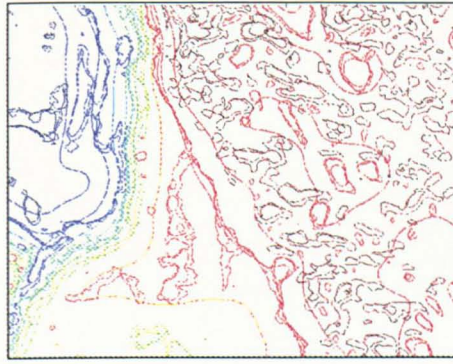


(d)

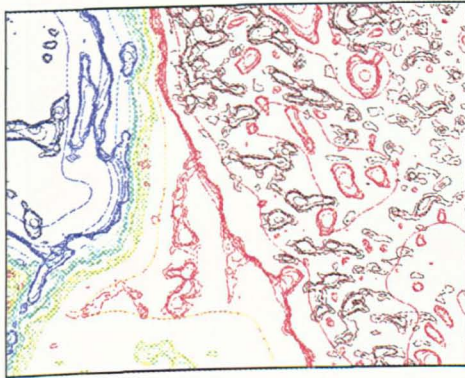


(e)

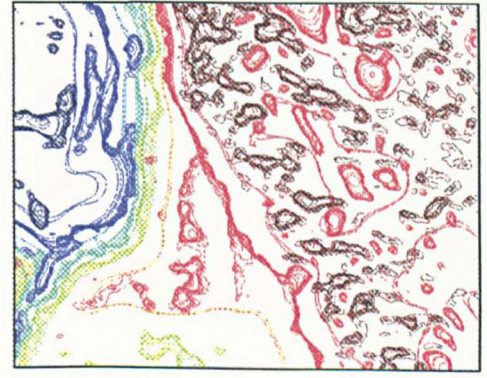
Figure 6.26: Images (a) to (e) represent the Fractal dimensions images of different parameters setup for Band 4 (Segment I).



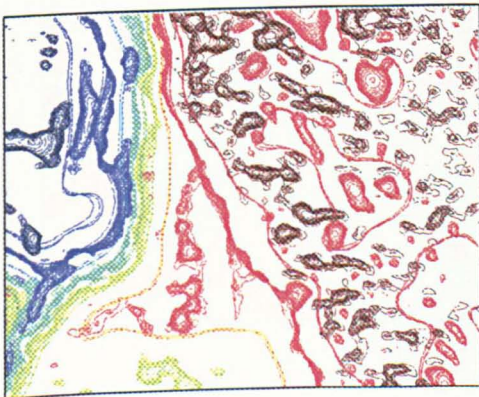
(a)



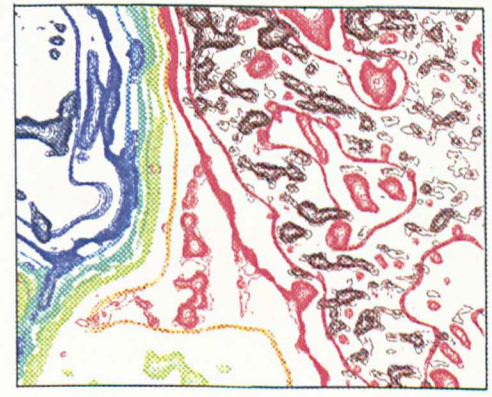
(b)



(c)

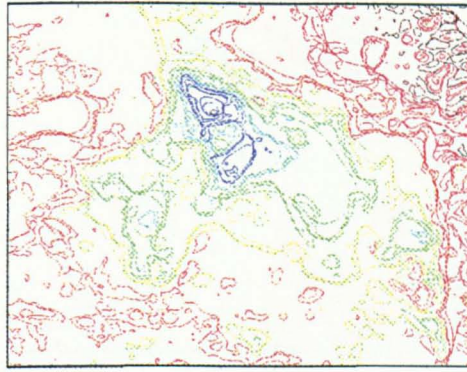


(d)

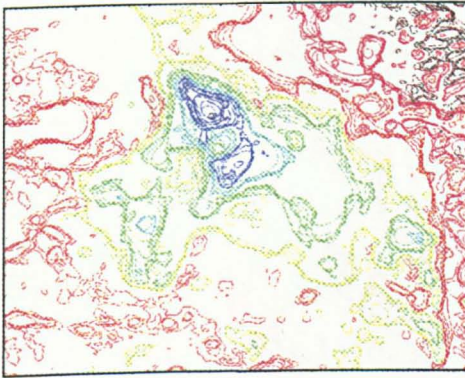


(e)

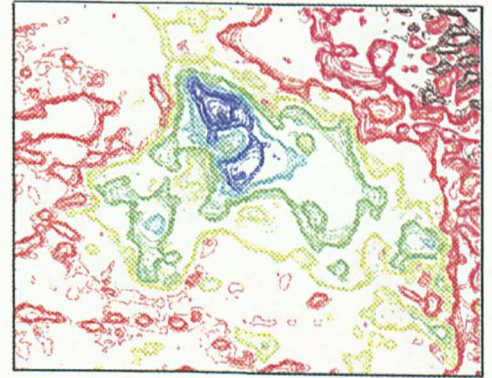
Figure 6.26: Images (a) to (e) represent the Fractal dimensions images of different parameters setup for Band 4 (Segment I).



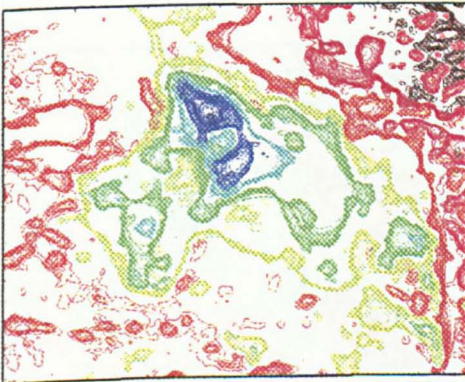
(a)



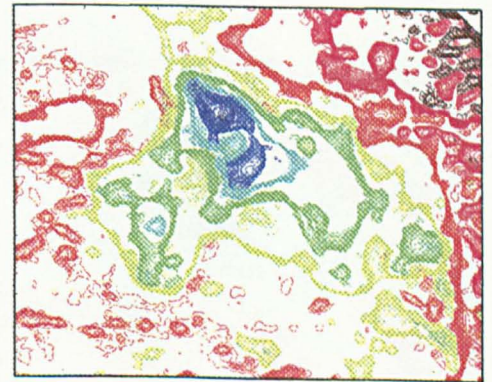
(b)



(c)

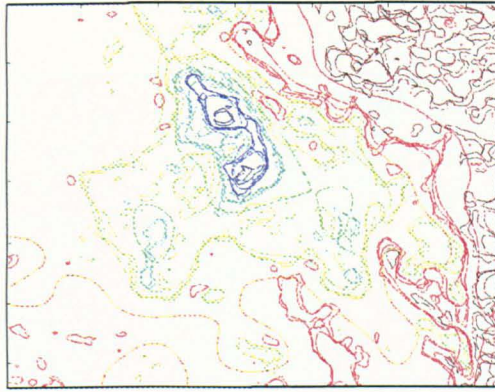


(d)

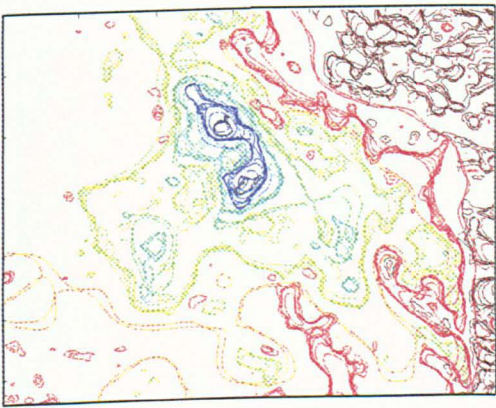


(e)

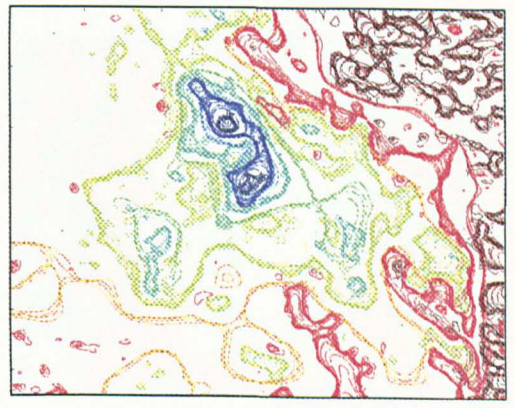
Figure 6.27: Images (a) to (e) represent the Fractal dimensions images of different parameters setup for Band 7 (Segment II).



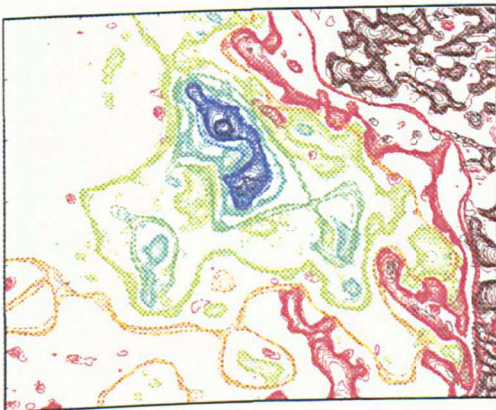
(a)



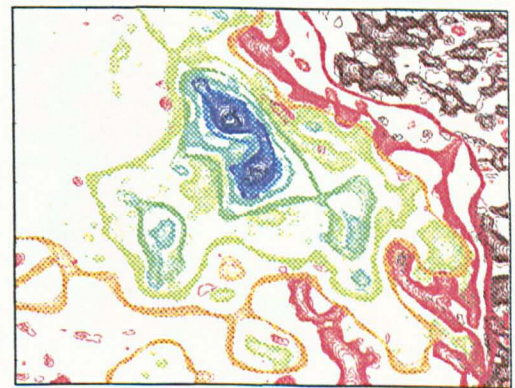
(b)



(c)

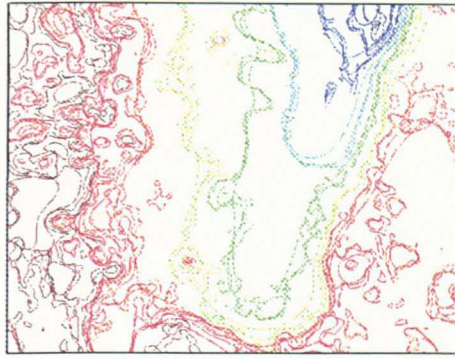


(d)

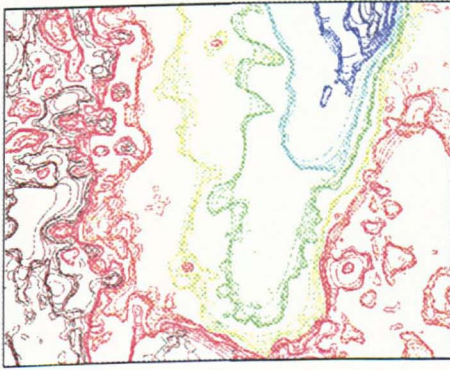


(e)

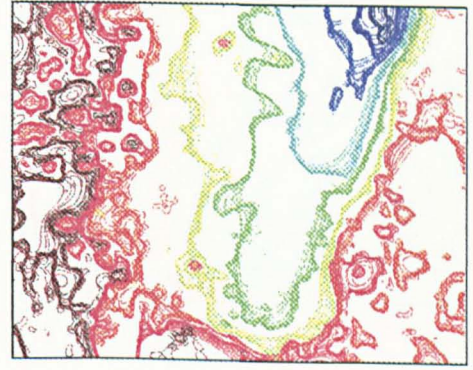
Figure 6.28 Images (a) to (e) represent the Fractal dimension images of different parameters setup for Band 4 (Segment II).



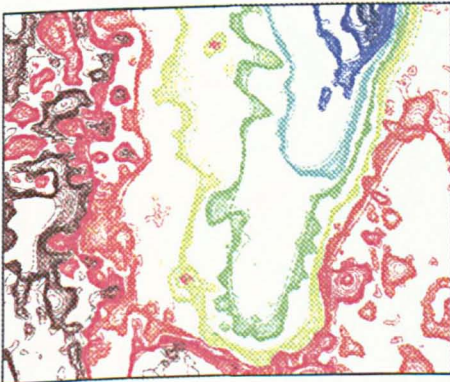
(a)



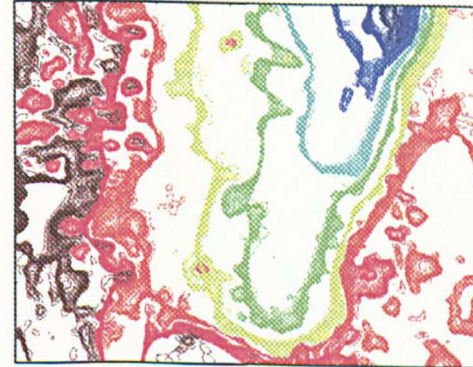
(b)



(c)

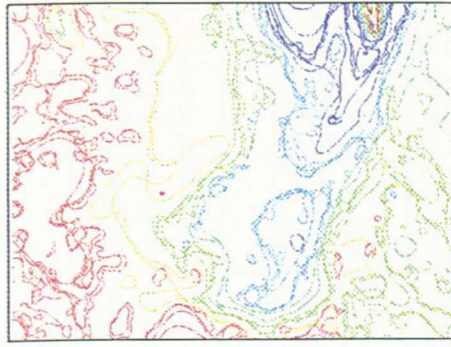


(d)

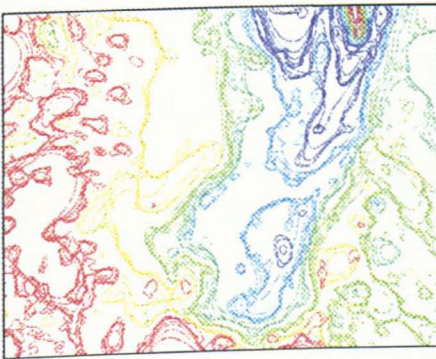


(e)

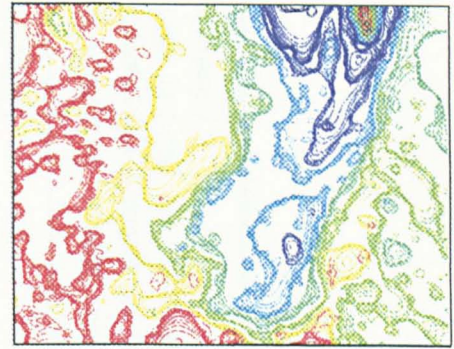
Figure 6.29: Images (a) to (e) represent the Fractal dimensions images of different parameters setup for Band 7 (Segment III).



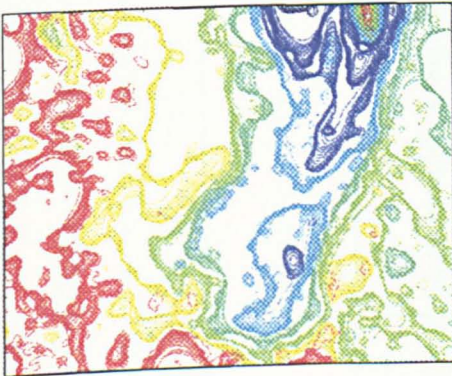
(a)



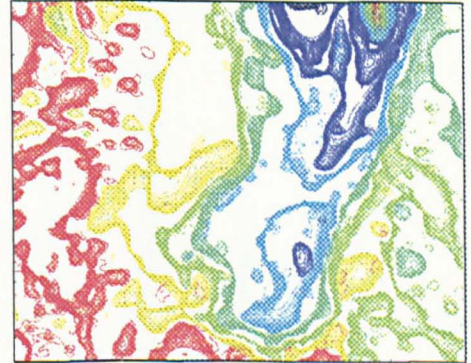
(b)



(c)



(d)



(e)

Figure 6.30: Images (a) to (e) represent the Fractal dimensions images of different parameters for Band 4 (Segment III).

Table 6.3. Summary of the features identification of the fractal images.

List landform	Soil type	Hoelder exponent images	Segmentation images	Regularisation dimension images
Sabkha	Salorthid / Gypsic solochk	Very complex features, clear identifiable transition zones, broad linear features	Very complex features, Broad identifiable linear features	Many complex features, broad transition zones
Alluvial plain	Gypssiorthid / Calciorthid	Clear and simple identifiable landform, no linear features	Very simple feature, neither evidence of zones nor linear features	Simple features, few linear features, no evidence of dominant zones
Sand sheet and Dunes	Torripsamment	Very complex features, no evidence of linear features	Very simple feature in some cases, and very complex in another, no linear features	Very complex features in each segments, many linear features
Gypsiferous pediplain	Gypsiorthid / Petric yypsisls	Very simple feature, no appearance of features or patterns diversity in this landform	Very simple in most cases except somewhat complex in ISO images, no linear features	Approximately simple features, except somewhat complex in Band 7, no evidence of dominant zones

6.8 Summary

In this chapter we have described fractal and multifractal methods for analysing data in relation to remote sensing imagery. This chapter has explored these methods of measuring the fractal and multifractal properties of the data sets. It was shown that the Hoelder exponents capacities show discernible results in terms of complex elements. Also, these exponents have shown the diversity of output in the segmentation images. Of all these exponents, *MAX* segmentation images were the most partitioned in terms of showing linear features. In the regularisation images, not only the main soil units has been identified but also many linear features within and between these units were self-evident such as the transition zone between sabkha and alluvial plain areas in segment I. Both wavebands 4 and 7 show the same features with minor differences.

CHAPTER 7

DISCUSSION AND CONCLUSIONS

7.1 Introduction

The purpose of this chapter is to assess the potential of the complex mapping techniques described in this thesis for mapping soil landscapes. Additionally, it is to investigate the relations between elements identified by the three techniques in order to (i) distinguish artefacts from real, complex features, and (ii) identify how spatial phenomena are represented by the various metrics. The first issue in this assessment is whether or not the resulting maps are interpretable in terms of individual complex elements. The second is about the relationship between complex elements viz. spatial frequency components, ANN model behaviour, and fractal structure. A third issue following from these is whether or not the complex mapped elements have any relation to traditional soil map units. A further issue not examined here is the field evidence for the complex elements.

For all techniques, in order to interpret output images, it is necessary to have at least two spectrally different image features when using complex elements over a data set. For this reason, but to avoid unnecessary complexity in images, three situations were selected for image segments where the same sets of image features could be expected.

In addition, not only different types of units but also two wavebands of Landsat TM are considered in order to help assess what features are real and what are artefacts.

7.2 The Interpretation of maps in terms of complex elements

7.2.1 Theoretical Considerations

The FFT method developed in this thesis isolates spatial frequency components in specific wavebands. The filtered inverse FFT produces an image, which shows the radiation in specific spatial frequency bands.

In other areas of image analysis, specific wavebands are used for feature identification. For example, low frequencies are removed to extract the high frequencies in images, which show features such as building in photographs (Rosenfeld and Kak, 1976; Pratt, 1978; Green, 1983; Ekstrom, 1984; Niblack, 1986; Gonzalez and Wintz, 1987). In this work, however, it was shown that if low frequencies are blacked out, the resulting images could not be interpreted. Each image considered here, therefore, retains low frequencies. That is, the major large features of the image are always present. The differences between images are only due to differences in medium to high frequencies.

Four broad types of area can be distinguished in the three study segments in terms of traditional theory of soil formation. These are sand sheet, sabkha, gypsiferous pediplain, and alluvial plains. Three types are present in each segment. There is no assumption, however, that the frequency components of the images are directly related to

geomorphological/soil units. We can expect that there will be, across the area of the image, differences in the size, extent and pattern of surface features that will produce differences in spatial spectra. The question is then whether these results are coherent and interpretable. The set of images from the filtered inverse FFT procedure shows the set of spatial frequency components of the image in two wavebands. The images are enhanced to (i) display optimised (forced) zoning of the image, and (ii) to display specific elements based on infrequency. If there are real zones of spatial frequency properties related to soil properties, then we would expect a strong correspondence between the spatial patterns of the first two displays and the display of infrequent components would highlight transition or boundary areas between zones.

The ANN method developed in this investigation is a non linear measure of image texture. However, the measure is relative to the image as a whole and is, in this sense, arbitrary. Difference within an image shows relative differences in texture. For this reason, training areas are changed systematically. By changing the measure of image texture the stability of texture patterns can be tested. Display of these texture images is by simple linear contrast stretch. Thus, there is no process of selection of image elements. The set of output images, as opposed to single images, shows the textural zones.

There is a subjective element in the selection of training sets since initially four are chosen which correspond to the main zones identified in the FFT analysis and which are

at least in part based on classical soil units mapped by MAW (1986, 1995). However, by using additional training areas in each of the four units and considering every combination of training areas against units, it should be possible to judge if the inclusion or exclusion and duplication of training areas has an effect on output images. If the classical soil units are real, then the addition of training areas in individual units should have little effect and the exclusion of units should have a marked effect. If no real units exist then there should be little effect either of addition or subtraction of training areas. If there are real units and they differ from the classical ones then the addition and subtraction processes should both have a marked effect on the output image elements.

The fractal properties are a quantitative measure of the irregular features in terms of measuring, for instance, soil landscape properties of patterns and texture. That is based on the local fractal dimensions that are used as a texture measure. Because a local fractal represents more than a point, its estimates should be realised by moving a pre-set size filter over the entire image. This is a crucial issue because there is an effect of selection of the filter size, which relates to heterogeneity and homogeneity within the image. If the size is too large, the boundaries are somewhat blurred, while the local fractal dimensionality estimates will be erratic if it is too small.

It is reasonable to assume that different kinds of soil landscape features might have characteristically different texture, pattern, or roughness at different scales that in turn

could be expressed in terms of a set local fractal properties. Consequently, multifractal analysis of remotely sensed data may reveal information on patterns of soil and rock outcrops much better than single local procedures. The multifractal analysis of images should provide for a more accurate representation of the nature of the complexity both of boundaries and surfaces.

Further, if there are real physical patterns of complexity, the three techniques should confirm this in the output images with consistent patterns or features. We can expect, however, that there are differences in the images between the techniques because the complex spatial properties of soils are manifest in different ways. We can expect differences between images also because of artefacts. Additionally, there will be differences between images for TM bands 4 and 7 simply because these bands show different properties of soils. The types of features, which are expected with each of, the techniques, coupled with the image enhancement technique, are summarised below:

Table 7.1: Summary of major identifying features for the three techniques.

Techniques	Types of features
FFT	Zones, linear features, transition zones
ANN	Zones, transition zones
Multifractal	Transition zones, edges of patterns, contours

7.2.2 Empirical Results

Analysis of spatial frequencies allows us to partition images into major zones. In each of the areas there are 3 mapped soil /landform units (MAW, 1986, 1995). Partitioning of the filtered images gives 5 zones in each case. These filtered images show the following:

- The dominant spatial frequencies are the low frequencies.
- Specific spatial frequencies are associated with patterns in specific zones, but these are not a dominant element of images.
- Existence of boundary zones in each area
- Some units are represented by two or more zones.
- Soil units are not everywhere the same in the study segments in terms of spatial frequencies.
- Band 7 and 4 are essentially the same, but show different degrees of complexity in different segments.
- There are linear features, narrower zones of specific spatial frequencies.

ANN models of texture also show 5 mapped zones in each segment based on 3 or 4 different training zones and with a variety of training areas set-ups. The results achieved may be summarised as follow:

- Some soil units are represented by two or more zones.
- These are boundary zones which are similar to zones in the soil units with two zones.
- Individual soil unit types are different in complexity between areas.
- Broad patterns of texture are not the same in each segment for the same soil units.
- The output images are similar to those of spatial frequencies, but show clearly differences in the patterns and features of specific parts of the image segments.
- Patterns of mixed zones are different between soil unit types.
- Bands 7 and 4 are essentially the same, but show different degrees of complexity in different zones and in different segments. There is no consistent relation to mapped units.

Multifractal analysis does not give zones but shows in the Hoelder exponents and the segmentation images that there are clear patterns of complexity (e. g. spatial transition), which have some correspondence to the soil units. The results achieved may be summarised as follow:

- Sabkha areas are everywhere the most complex and the area within sabkha to be is made up of linear transition zones in each of the segments.

- Only parts of the sand sheets show similar levels of complexity but the patterns are patchy.
- Other areas are homogenous or show local transitions within transitions in patterns rather than between zones.
- Segmentation of edges confirms these patterns and also shows that Bands 7 and 4 are markedly different in contributing to the local spatial transition properties of soils.
- Regularisation dimension images allow a broad partitioning of the images. They show that transitions across the image are not related to specific boundaries. The dimension of the image segments is related to the patterns and density of transitions. However, there are no consistent patterns and densities that correspond to soil units or the soil zones identified by FFT or ANN analysis.

Table 7.2 summarises the mapping of soil units and zones by the three techniques.

Table 7.2: The relation of the three complex metrics to mapped units.

	Units	FFT	ANN	Multifractal
Mapped units	Sabkha	Clear and simple	Clear and simple	Clearly differentiated, complex linear transitions
	Sand sheet	Moderately complex zones	Clearly differentiated, Complex patch transitions	Ambiguous borders, complex patch transitions
	Alluvial plain	Simple	Ambiguous, complex	Simple
	Gypsiferous pediplain	Complex	Complex	Complex, linear transitions
Zones identified from image analysis	Boundary areas	Well simple defined	Simple well defined or ambiguous with sand sheet and between alluvial plain	Complex

7.3 Discussion

It is not surprising that patterns of mapped soil units (MAW, 1986, 1995) are perceivable in almost every output image. Although the units are mapped at 1: 50, 000 and produced at 1: 250,000 scale and the images are displayed at approximately 1: 50,000 scale, the position of the unit boundaries are clear and well defined to the Landsat-5 Thematic Mapper image features. These boundaries fit well, in the sense, that the positions of the boundaries correspond to positions of the image features.

What has to be perceived is that the process of the “fitting” is a complex process of searching and interpreting image elements because the correspondence between the soil unit boundaries and image elements is not a simple one-to-one correspondence with linear features in reflectance images. Unlike locations along the positions of unit boundaries the degree of clarity of a boundary varies, the nature of the boundary changes and in some places disappears, whereas differences are perceived on the basis of colour tone and texture in any combination. In traditional mapping using remotely sensed data, it is combination of evidence with contextual information on geology and topography that is used to map soils. However, to look at images more objectively would lead to different results. In this study the objectivity is attempted by applying metrics of complex elements of images.

A simple fuzzy k -means cluster applied to raw data and to spatial spectral components gives different zones from the soil maps. In the study segments, each of which has three mapped units, the automatic classification algorithm perceives five zones. This indicates that more units are identified than by the traditional method at this scale, which is the scale at which the maps are produced and used. The key here is that in the analysis, there is no zone that has more status than the others. Only if we presume that the soil units are real then it is perceptive to explain the “additional” zones as sub-members of the units. With this presumption, at this scale we must accept five units in each segment of the whole image. The credibility of the areas mapped by the complex measures is then established, in advance of any field evidence, although conglomeration of evidence

from different measures of complex elements of image will produce different results. Then it is possible to assess the difference between the areas derived from complex measures and the traditional mapping units.

Unsupervised classification of raw data in Band 4 and 7, spatial spectral segmentation and the ANN texture analysis all confirm that the study segments are made up of 5 types of area. These five areas can be considered to correspond to the soil units (Sabkha, sand sheet, alluvial plain, and gypsiferous pediplain) added to areas that represent part of these units and are also found in the transitional zones between the units. With this description, it could be based on a presumption of the reality of soil units. Alternatively, the pattern can be described as distributions of soil properties (reflectance) with the study segments, which show:

1. areas of more or less uniform and distinct properties.
2. areas of mixed properties with specific patterns of two (or more members).
3. areas of more or less uniform properties of which are not distinct but are similar to properties of one of the members of mixed areas.

The third types of area are between areas of distinct uniform properties and of mixed properties. In patterns of mixed properties, they can be (amongst other possible theoretical patterns not observed in this study) linear or patchy within a mosaic. The distribution of the third type of area can be as the adjacent area with the common property as part of its mixture on one side only of perceivably linear patterns as in

segment I in which it gives a sharp boundary on one side and a broken or irregular boundary on the other. Once accepting these types of area as being of similar environments and the reality broad environmental conditions of the study segments, then the analysis of spatial spectra and texture (ANN model) also show that the properties of types of units are not consistent across all areas. This leads us to assume the existence of units. Another alternative, perhaps more objective, description would be that there is a variety or if it is demonstrable (which with only three study segments it is not) a spectrum of patterns of properties. It is possible to envisage, for instance, a range of patchiness of soil properties within a mixture from small widely spaced patches to large closely spaced patches.

Results of the fractal and multifractal analysis give a clear, objective picture of distribution of variability of areas in the study segments. The concept that emerges from these analyses is of continuous spatial distributions of complexity rather than zonation texture or other properties. These analyses confirm the idea, developed with the spatial spectral and ANN models of broad areas of the study segments or soil units being associated with particular levels and patterns of complexity. However, this description also leads us to assume the existence of zones or units.

In the fractal and multifractal results, more objectively, an impression is given of a surface of complexity. It has particular parts of the surface, which have broadly similar

degrees and patterns of complexity. Other parts are characterised by gradients of complexity with some of them gradual and some of them steep.

Consequently, there are implications of these results for soil mapping at the theoretical and practical levels. In the theoretical level the implications are about the existence of soil units defined following the classical approach. The existence of coherent reiterative and robust spatial patterns of complex metrics gives confidence to the idea that such patterns are real. The fact that they do not conform to soil units suggests that the units are not appropriate of the soil landscape. In the practical level, it is unlikely that the classical approach would be abandoned. There are good reasons why it should not be abandoned. Most important of these is that the units are based on substantial bodies of theory on fieldwork and on sampling. There is at present nowhere near the same support of the ideas of mapping complex elements. It seems, therefore, that the place of these ideas is to complement the traditional mapping approach and raise awareness that soils are inherently complex.

7.4 Conclusion

The aims and objectives of this thesis were (Chapter 1, page 9):

- The first aim was to apply each technique to the classification and segmentation of a satellite image, which represented a set of soil landscapes relatively unaffected by vegetation.

In the application of each technique, the objectives were:

- To develop the procedures by which a soil map could be obtained,
- To explore the controls on the procedures and the relations of image outputs to these controls,
- To develop an appropriate means of visualisation.

A further aim was to evaluate the usefulness of the three techniques for soil mapping. In this evaluation there were two objectives:

- Comparison of the performance of the three techniques in mapping soil landscapes.
- Comparison of the three techniques singly and in combination with conventional soil mapping.

In conclusion, this study has shown:

- Procedures were established for techniques which resulted in robust and coherent images of soil landscapes which could be simply interpreted in the light of knowledge of soil properties and soil forming factors in the study area.
- FFT and fractal and multifractal analysis provided unsupervised mapping outputs.
- Visualisation procedures of the outputs of each technique were established by trial and error.

- Techniques showed different properties. Some similarities in segmentation of images but more significantly major differences. Demonstrates that there are several types of complexity which reveal different spatial soil properties.
- Comparison of each technique with conventional soil maps showed that at the scale of mapping the conventional maps neglect many spatial properties of soil and conflict with zones and boundaries revealed through objective techniques (FFT, Fractal/Multifractal).
- Even on the basis of supervised classification (ANN) based on conventional maps, the images showed much more complex segmentation than the conventional maps.

7.5 Further Work

More detailed investigations are required in various regions with different geological and geomorphological conditions as well as different land-cover/land-use type (i.e. vegetation, urbanisation, agricultural). The FFT method has shown its utility in being able to show and partition the data sets into zones. It would be useful if this method more used for vegetation problems such as (i) forest disease (i.e. in terms of dry and healthy trees), (ii) deciduous and coniferous forest, (iii) grassland and cropland. Because the ANN method used in this study is based on a prior assumption about zones, it needs to be used in unsupervised manner in order better to assess the textural division of soil landscapes. Also, since the fractal method seemed to be superior to the other methods, further investigations are recommended especially measuring other complex

phenomena. There are some particular aspects of the investigation that may prove advantageous in further investigations as they were given brief considerations.

It would also be useful if sample sets within the test segments under investigation could be extensively studied regarding the soil properties and soil reflectance (i.e. field spectroscopy measurements in order to establish an empirical field base for the ideas expressed here). Since the higher spectral resolution will ensure more spectral sensitivity to the different landforms and the greater number of bands will increase the number of complex components, and this gives the complex metrics the ability to show deeper investigations in terms of measuring complex phenomena, particularly fractal properties.

REFERENCES AND BIBLIOGRAPHY

The following list includes both cited references and other sources consulted during this project.

Abram, M. and Kale, A. B. (1984), "Recent Developments in Lithological Mapping Using Remote Sensing Data," In *Remote Sensing for geological Mapping*, (Eds). P. Teleki and C. Weber, Proceedings of the Seminar in Orleans, France: 177-189.

Adams, J. B., Sabol, D. E., Kapos, V., Filho, R. A., Roberts, D. A., Smith, M. O., Gillespie, A. R. (1995), "Classification of multispectral images based on fractions of endmembers: application to land-cover change in the Brazilian Amazon," *Remote Sensing of Environment*, 52: 137-154.

Al-Barrak, S. A. (1993), *Agricultural Land Properties of Al-Ahsa*, Saudi Arabia: Al-Husseiny press.

Aldakheel, Y. Y. (1998), Remote Sensing of Crop Water Stress: Measurements and Modelling, *Ph.D. Thesis*, University of Salford, U.K.

Aleksander, I., Morton, H. (1995), *An Introduction to Neural Computing*, 2nd edition, London: International Thomson Computer Press.

Al-Hinai, K. G. (1988), Quaternary Aeolian Sand Mapping in Saudi Arabia using Remote Sensing Imagery, *Ph.D. Thesis*, University of London, U.K.

Al-Hinai, K. G., Khan, M. A., and Canas, A. A. (1991), "Enhancement of Sand Dune Texture From Landsat Imagery Using Difference of Gaussian Filter," *International Journal of Remote Sensing*, 12(5): 1063-1069.

Al-Jaber, M.A. (1989), The Structural Instability of Soils of the Old and New Lands of Al-Hassa Oasis, Saudi Arabia, *Ph.D. Thesis*, University of Salford, U.K.

Al-Saifi, M. M. and Qari, M. Y. H. T. (1996), "Application of Landsat Thematic Mapper data in Sabkha Studies at the Red Sea Coast," *International Journal of Remote Sensing*, 17(3): 527-536.

Al-Sari, A. M. (1989), The Geological Investigation of Multispectral Remote Sensing Data for Mahd Adh Dhahab and Jabal Said Districts, Western Saudi Arabia, *Ph.D. thesis*, University of Durham, U.K.

Al-Sayari, S. S. and Zotl, J. G. (1978), *Quaternary Period in Saudi Arabia*, New York: Springer-Verlag.

Andres, L., Salas, W. A., and Skole, D. (1994), "Fourier Analysis of Multi-Temporal AVHRR Data Applied to a Land Cover Classification," *International Journal of Remote sensing*, 15(5): 1115-1121.

Asrar, G. (1989), *Theory and Applications of Optical Remote Sensing*, New York: John Wiley & Sons.

Atkinson, P. M., Tatnall, A. R. L. (1997), "Introduction: Neural Networks in Remote Sensing," *International Journal of Remote sensing*, 18(4): 699-709.

Avery, T. E. and Berlin, G. L. (1985), *Interpretation of Aerial Photographs*, 4th edition, Minneapolis: Burgess.

Bagnold, R. A. (1965), *The Physics of Blown Sand and Desert Dunes*, London: Methuen & CO. LTD.

Ballard, D. H., and Brown, C. M. (1982), *Computer Vision*, Englewood Cliffs, New Jersey: Prentice-Hall Inc.

Bartolucci, L. A. (1979), "Digital Processing of Remotely Sensed Multispectral Data," *LARS Technical Report 07047*, West Lafayette, IN: Purdue University, The Laboratory for Applications of Remote Sensing.

Barkeshli, S., Radecki, D. J., and Sabbagh, H. A. (1992), "On a Linearized Inverse Scattering Model for a Three-Dimensional Flow Embedded in Anisotropic Advanced Composite Materials, *IEEE Transaction on Geoscience and Remote Sensing*, 30(1): 71-80.

Barrett, E. C., and Curtis, L. (1992), *Introduction to Environmental Remote Sensing*, 3rd edition, Chapman and Hall, London.

Bastin, L. (1997), "Comparison of fuzzy c-means classification, linear mixture modelling and MLC probabilities as tools for unmixing coarse pixels," *International Journal of Remote sensing* 18(17): 3629-3648.

Batty, M., and Xie, Y., (1996), Preliminary Evidence for a Theory of the fractal City, *Environment and Planning A*, 28(10): 1745-1763.

Beale, R., Jackson, T. (1990), *Neural Computing: An Introduction*, Bristol: Institute of Physics Publishing.

Belward, A. S. and Valenzuela, C. R. (1991), *Remote Sensing and Geographical Information Systems for Resources Management in Developing Countries*, Dordrecht: Kluwer Academic Publishers.

Benediktsson, J. A., and Sveinsson, J. R. (1997), "Feature Extraction for Multisource Data Classification with Neural Networks," *International Journal of Remote sensing*, 18(4): 727-740.

Benediktsson, J. A., Swain, P. H. (1990), "Statistical Methods and Neural Network Approach for Classification of Data from Multiple Sources, Technical Report TR-EE 90-64, Laboratory for Applications of Remote Sensing and School of Electrical Engineering, Purdue University, West Lafayette.

Benediktsson, J. A., Swain, P. H., Erosy, O. K., Hong, D., (1990a), "Classification of Very High Dimensional Data Using Neural Networks" *Proceedings IGARSS '90*, New York: I.E.E.E. Press, 2: 1269-1272.

Benediktsson, J. A., Swain, P. H., Erosy, O. K. (1990b), "Neural Network Approaches Versus Statistical Methods in Classification of Multisource Remote Sensing Data, *IEEE Transactions of Geoscience and Remote Sensing*, 28: 540-552.

Benediktsson, J. A., Swain, P. H., Erosy, O. K. (1993), "Conjugate-gradient Neural Networks in Classification of Multisource and Very-high-dimensional Remote Sensing Data" *International Journal of Remote Sensing*, 14(15): 2883-2903.

Bernstein, R. (1976), "Digital Image Processing of Earth Observation Sensor Data," *IBM Journal of Research and Development*, 20:40-57.

Bezdek, J. C. (1981), *Pattern Recognition with Fuzzy Objective Function Algorithms*, Plenum Press, New York

Bischof, H., Schneider, W., Pinz, A. J. (1992), "Multispectral Classification of Landsat-Images Using Neural Networks, *IEEE Transactions on Geoscience and Remote Sensing* 30(3): 482-490.

Bishop, C. (1995), *Neural Networks for Pattern Recognition*. Oxford: University Press.

Blonda, P., LA Forgia, A. (1994), "Multispectral Classification of Landsat Images by a modular neural network architecture," *Proceedings of the International Geoscience and Remote Sensing Symposium (IGARSS '94)*, Pasadena, CA, (Piscataway, NJ: I.E.E.E.): 1873-1876.

Bodechtel, J. and Frei, M. (1992), "Geoscientific Achievements," *International Journal of Remote sensing*, 13(6 and 7): 305-1318.

Bonham-Carter, G. F. (1994), *Geographic Information Systems for Geoscientists: Modelling with GIS*, Canada: Pergamon.

Booth, D. J., and Frei, M. (1989), "A comparison of Classification Algorithms in Terms of Speed and Accuracy after the Application of a Post-Classification Model Filter," *International Journal of Remote Sensing*, 10(7): 1271-1276.

Bracewell, R. (1986), *The Fourier Transform and its Applications*, New York: McGraw-Hill.

Brady, N. C., and Weil, R. R. (1999), *The Nature and Properties of Soils*, 12th edition New Jersey: Prentice Hall.

Bruzzone, L., Coneese, F., Maselli, F., Roll, F. (1997), "Multisource Classification of Complex Rural Areas by Statistical and Neural-Network Approaches," *Photogrammetric Engineering and Remote Sensing*, 63(5): 523-533.

Burgess, T. M. and Webster, R. (1980), “Optimal interpolation and isarithmic mapping of soil properties: I The semi-variogram and punctual kriging, *Journal of Soil Science*, 31: 315-331.

Burrough, P.A. (1981), “ Fractal Dimensions of Landscapes and Other Environmental Data,” *Nature*, 294(19): 240-242.

Burrough, P. A. (1986), *Principles of Geographical Information Systems for Land Resources Assessment*, New York: Oxford University Press.

Burrough, P. A. (1989), “Fuzzy Mathematical Methods for Survey and Land Evaluation,” *Journal of Soil Science*, 40:477-492.

Burrough, P. A., and McDonnell, R, A. (1998), *Principles of Geographical Information Systems*, New York: Oxford University Press Inc.

Burrough, P. A. van Gaans, P. F. M. and Hootsmans, R. (1997), “Continuous Classification in Soil Survey: Spatial Correlation, Confusion and Boundaries,” *Geoderma*, 77: 115-135.

Campbell, J. (1996), *Introduction to Remote Sensing*, 2nd edition, London: Taylor and Francis.

Canus, C., and Levy Vehel, J. (1996), “Change Detection in Sequences of Images by Multifractal Analysis,” *In INRIA Internal Report*.

Carling, A. (1992), *Introducing Neural Networks*, Wilmslow, UK: Sigma Press.

Carnahan, W. H., and Zhou, G. (1986), “Fourier Transform Techniques for the Evaluation of the Thematic Mapper Line Spread Function,” *Photogrammetric Engineering and Remote Sensing*, 52(5): 639-648.

Carroll, D. M. Evans, R. and Bendelow, V. C. (1976), *Air Photo-Interpretation for Soil Mapping*, England: Adlard and Son limited.

Chavez, P. Jr., and Bauer, B. (1982), “An Automatic Optimum Kernel-Size Selection Technique for Edge Enhancement”, *Remote Sensing of Environment*, 12: 23-38.

Chen, K. S., Yen, S. K., and Tsay, D. W. (1997), “Neural Classification of SPOT Imagery Through Intergration of Intesity and Fractal In Information,” *International Journal of Remote sensing*, 18(4): 763-783.

Clarks, K. C. (1986), Computation of The Fractal Dimension of Topographic Surfaces Using The Triangular Prism Surface Area Method, *Computers & Geosciences*, 12(5): 713-722.

Clark, C. and Boyce, J. (1999), “The detection of ship trail clouds by artificial neural network,” *International Journal of Remote Sensing*, 20(4): 711-726.

Civco, D. L. (1993), “Artificial Neural Networks for Land-Cover Classification and Mapping,” *International Journal of Geographic Information Systems*, 7: 173-186.

Colwell, R. N., ed. (1983), *Manual of Remote Sensing*, 2nd edition, Falls Church, Virginia: American Society of Photogrammetry.

Courtney, F. M. and Trudgill, S. T. (1984), *The Soil: An Introduction to Soil Study*, 2nd edition, London: Hodder and Stoughton.

Cracknell, A., and Hayes, L. (1991), *Introduction to Remote Sensing*, London: Taylor and Francis.

Crosta, A. P., and Moor, J. M. (1989), "Geological Mapping Using Landsat Thematic Mapper Imagery in Almeria Province, Southeast Spain," *International Journal of Remote Sensing*, 10(3): 505-514.

Culling, W. E. H. (1986), "Highly Erratic Spatial Variability of Soil-pH on Iping Common, West Sussex," *CATENA*, 13(1): 81-98.

Curran, P. J., (1985), *Principles of Remote Sensing*, New York: Longman Inc.

Davis, F. W., Quattrochi, D. A., Ridd, M. K., Lam, S. -N., Walsh, S. J., Michaelsen, J.C., Franklin, J., Stow, D. A., Johannsen, C. J., Johnston, C. A. (1991), "Environmental analysis using integrated GIS and remotely sensed data: some research needs and priorities," *Photogrammetric Engineering and Remote Sensing*, 57(6): 689-697.

Davis, A., Marshak, A., Wiscombe, W., Cahalan, R., (1994), "Multifractal characterisation of nonstationarity and intermittancy in geophysical fields: observed, retrieved, or simulated," *Journal of Geophysical Research*, 99(D4): 8055-8072.

Decature, S. E. (1989), "Applications of neural networks to terrain classification," in *proceeding IJNN'89 Washington DC*, Vol. I, pp 283-288.

De Cola, L. (1989), " Fractal Analysis of a Classified Landsat Scene," *Photogrammetric Engineering and Remote Sensing*, 55(5): 601-610.

De Gruijter, J. J. Walvoort, D. J. J. and van Gaans, P. F. M. (1997), “Continuous Soil Maps a Fuzzy set Approach to Bridge the Gap between Aggregation Levels of Process and Distribution Models,” *Geoderma* 77: 169-195.

De Jong, S.M. and Burrough, P.A. (1995), “ A Fractal Approach to the Classification of Mediterranean Vegetation Types in Remotely Sensed Images,” *Photogrammetric Engineering and Remote Sensing*, 61(8): 1041-1053.

Dekking, M., Levy Vehel, J., Lutton, E., Tricot, C. (1999), *Fractals: Theory and Applications in Engineering*, London: Springer-Verlag.

Dong-Chen, H., and Wang, L. (1990), “Texture Unit, Texture Spectrum, and Texture Analysis”, *IEEE Transaction on Geoscience and Remote Sensing*, 28(4): 509-512.

Dreyer, P. (1993), “Classification of Land Cover Using Optimized Neural Nets on Spots Data,” *Photogrammetric Engineering and Remote Sensing*, 59(5): 617-621.

Drury, S. A., (1990), *A Guide to Remote Sensing Interpreting Images of the Earth*, Oxford: Oxford University Press.

Drury, S. A., and Hunt, G. A. (1989), “Geological Uses of Remotely-Sensed Reflected and Emitted Data of Lateritized Archaean Terrain in Western Australia,” *International Journal of Remote Sensing*, 10(3): 475-497.

Dubuc, B., Quiniou, J. F., Roques-Carmes, C., Tricot, C., Zuker, S. W. (1989), “Evaluation the fractal dimension of profiles,” *PHYSICAL REVIEW A*, 39(3): 1500-1512.

Dymond, J. R., (1992), “How Accurately Do Image Classifiers Estimate Area?” *International Journal of Remote Sensing*, 13(9): 1735-1742.

Edwards, G. and Lowell, K. E. (1996), "Modelling Uncertainty in Photointerpreted Boundaries," *Photogrammetric Engineering and Remote Sensing*, 62(4): 337-391.

Ehleringer, J. R., Field, C. B. (1993), *Scaling Physiological Processes: Leaf to Globe*, San Diego: Academic Press.

Ehrhard, D. G., Easton, R. L. Jr., Schott, J. R., and Comeau, M. J. (1993), "Frequency-Domain Texture Features for Classifying SAR Images", *Proceeding of SPIES OE/Aerospace and Remote Sensing*, 1960(3): 21-32.

Ekstrom, M. P., ed. (1984), *Digital Image Processing*, Orlando: Academic Press.

Elachi, C. (1987), *Introduction to the Physics and Techniques of Remote Sensing*, New York: John Wiley and Sons.

El-Baz, F. (1984), *Deserts and Arid Lands*, Netherlands: Martinus Nijhoff Publishers.

El-khatib, A. (1980), *Seven Green Spikes*, M. A. W., Saudi Arabia, 2nd edition, Jeddah, Saudi Arabia: Dar al-Asfahani.

Emerson, C. W., Lam, N.S.N., Quattrochi, D. A. (1999), Multi-Scale Fractal Analysis of Image Texture and Pattern, *Photogrammetric Engineering and Remote Sensing*, 65(1): 51-61.

Estats, J. E., Hajic, E. J., and Tinney, L. R. (1983), "Fundamentals of Image Analysis: Analysis of Visible and Thermal Infrared Data," In *Manual of Remote Sensing*, 2nd edition, (ed) Colwell, R. N. Falls Church, Virginia: American Society of Photogrammetry, Vol. (1): 987-1124.

Evertsz, C. J. G., Mandelbrot, B. B., (1992), "Multifractal measures, in *Chaos and Fractals: New Frontiers in Science*, Peitgen, H. –O, Jurgens, H., and Saupe, D., Eds., New York: Springer-Verlag, 921-969.

Falconer, K. (1990), *Fractal Geometry*, New York: John Wiley and Sons.

Fausett, L. (1994), *Fundamentals of Neural Networks*. New York: Prentice Hall.

Feder, J. (1988), *Fractals*, New York: Plenum Press.

Fierens, F., Kanellopoulos, I., Wilkinson, G. G., and Megier, J., (1994), "Comparison and Visualisation of Feature Space Behaviour of Statistical and Neural Classifiers of Satellite Imagery," *Proceedings of the International Geoscience and Remote Sensing Symposium (IGARSS '94)*, Pasadena, CA, (Piscataway, NJ: IEEE): 1880-1882.

Fisher, P. F. (1987), "The nature of soil data in GIS—Error or uncertainty," International Geographic Information Systems (IGIS) Symposium: The research agenda, VIII- Application and Implementation, Arlington Virginia, pp 307-318.

Fisher, P. F. and Pathirana, S. (1990), "The Evaluation of Fuzzy Membership of Land Cover Classes in the Suburban Zone," *Remote Sensing of Environment*, 34:121-132.

Fisher, P. F. and Pathirana, S. (1993), "The Ordering of Multitemporal Fuzzy Land-Cover Information Derived from Landsat MSS Data," *Geocarto International*, 8(4): 5-14.

Fisher, M. M., Stauffer, P., Gopal, S., Steinnocher, K. (1994), "Evaluation of neural pattern classifiers for a remote sensing application," *IEEE Transactions on Geoscience and Remote Sensing*, to be appear.

Fitzpatrick, E. A. (1986), *An Introduction to Soil Science*, 2nd edition, London: Longman Scientific and Technical.

Fleming, M. D., Berkebile, J. S., and Hoffer, R. M. (1975), "Computer Aided Analysis of Landsat-1 MSS Data: A Comparison of Three Approaches, Including a Modified Clustering Approach," *LARS Information Note 072475*, Laboratory for Applications of Remote Sensing, Purdue University, West Lafayette, IN.

Foody, G. M. (1996), "Relating the Land-Cover Composition of Mixed Pixels to Artificial Neural Network Classification Output," *Photogrammetric Engineering and Remote Sensing*, 62(5): 491-499.

Foody, G. M. (1999), "The significance of border training patterns in classification by a feedforward neural network using back propagation learning," *International Journal of Remote sensing*, 20(18): 3549-3562.

Foody, G. M. and Trodd, N. M. (1993), Non-Classificatory Analysis and Representation of Heathland Vegetation from Remotely Sensed Imagery," *GeoJournal*, 29(4): 343-350.

Fryberger, S.G., Al-Sari, A., and Clisham, T.J. (1983), "Eolian Dune, Interdune, Sand Sheet, and Siliciclastic Sabkha Sediments of an Offshore Prograding Sand Sea, Dhahran Area, Saudi Arabia", *The American Association of Petroleum Geologists bulletin*, 67(2): 280-312.

Fryberger, S.G., Al-Sari, A., Clisham, T.J., Rizvi, S-A. R., and Al-Hinai, K.G. (1984), "Wind Sedimentation in the Jafurah Sand Sea, Saudi Arabia", *Sedimentology*, 31: 413-431.

Gillespie, A.R. (1980), "Digital Techniques of Image enhancement," In *Remote Sensing in Geology*, (Eds) Siegal, B.S. and Gillespie, A.R., New York: John Wiley and Sons, 139-226.

Gillespie, A.R., Kahle, A.B., and Walker, R.E. (1980), "Color Enhancement of Highly Correlated Images, I: Decorrelation and HSI Contrast Stretches," *Remote Sensing of Environment*, 20: 209-235.

Goetz, A.F.H. and Rowan, L.C. (1981), "Geologic Remote Sensing," *Science*, 211:781-791.

Goetz, A.F.H., Solomon, G.V.J.E. and Rock, B.N. (1985), "Imaging Spectrometry for Earth Remote Sensing," *Science*, 228(4704): 1147-1153.

Gong, P. (1996), "Integrated Analysis of Spatial Data from Multiple sources: Using Evidential Reasoning and Artificial Neural Network Techniques for Geological Mapping," *Photogrammetric Engineering and Remote Sensing*, 65(5): 513-523.

Gonzalez, R. C., and Wintz, P. (1987), *Digital Image Processing*, 2nd edition, Reading, Massachusetts: Addison-Wesley.

Goodchild, M.F. (1980), "Fractals and the Accuracy of Geographical Measures," *Mathematical Geology*, 12(2): 85-98.

Goodchild, M.F. (1992), "Description of Terrain as a Fractal Surface, and Application to Digital Elevation Model Quality Assessment," *Photogrammetric Engineering and Remote Sensing*, 58(11): 1568-1570.

Goodchild, M. F., and Mark. D. M. (1987), "The Fractal Nature of Geographic Phenomena," *Annals of the Association of American Geographers*, 77(2): 265-278.

Gorman, P., and Sejnowski, T. (1988), "Learned classifications of sonar targets using a massively parallel network," *IEEE Transactions Acoustic Speech Signal Processing*, 36: 1135-1140.

Green, W. B. (1983), *Digital Image Processing: A Systems Approach*, New York, NY: Van Nostrand Reinhold Company.

Gupta, R.P. (1991), *Remote Sensing Geology*, Berlin: Springer-Verlag.

Gurney, K. (1997), *An Introduction to Neural Networks*, London: UCL Press Limited.

Hardy, J.R. (1983), "Data Collection by Remote Sensing for Land Resources Survey," *Terrain Analysis and Remote Sensing*, ed. J.R.G. Townshend, London: George Allen and Unwin, 16-36.

Hassan, M.M. (1988), "Filtering Digital Profile Observations," *Photogrammetric Engineering and Remote Sensing*, 54(10): 1391-1394.

Haykin, S. (1994), *Neural Networks: A Comprehensive Foundation*, New York: Macmillan Publishing.

Hearnshaw, H.M. and Unwin, D.J. eds. (1994), *Visualization in Geographical Information Systems*, Chichester: John Wiley and Sons.

Heermann, P. D., Kazenie, N. (1992), "Classification of Multispectral Remote Sensing Data Using a Back-Propagation Neural Network," *IEEE Transactions on Geoscience and Remote Sensing*, 30: 81-88.

Hepner, G. F., Logan, T., Ritter, N., and Bryant, N. (1990), "Artificial Neural Network Classification Using a Minimal Training Set: Comparison to Conventional Supervised Classification," *Photogrammetric Engineering and Remote Sensing*, 56(4): 469-473.

Heuvelink, G.B.M., and Burrough, P.A. (1993), "Error Propagation in Cartographic Modelling Using Boolean Logic and Continuous Classification," *International Journal of Geographical Systems*, 7(3): 231-246.

Hewitson, B.C. and Crane, R.G. eds. (1994), *Neural Nets: Applications in Geography*, Dordrecht: Kluwer Academic Publishers.

Heddi, M. and Petch, J. (1998), "Using artificial neural network models for detecting linear features in Landsat images," preprint.

Heddi, M., Vehel, J. L., Petch, J. (1998), "Linear features mapping from satellite images using multifractal analysis," preprint.

Hoffer, R. H. (1978), Biological and physical considerations in applying computer aided analysis techniques to remote sensing data, in *Remote Sensing: The Quantitative Approach* (eds) Swain, P. H. and Davis, S. M., New York: Mc Graw-Hill.

Hord, R.M. (1982), *Digital Image Processing of Remotely Sensed Data*, New York: Academic Press.

Huang, J. and Torcotte, D. L. (1989) Fractal Mapping of Digitised Images: Application to the Topography of Arizona and Comparisons With Synthetic Images, *Journal of Geophysical Research*, 94(B6): 7491-7495.

Hunt, G. R., Salisbury, J. W. (1970), Visible and Near-Infrared Spectra of Minerals and Rocks: I Silicate Minerals, *Modern Geology*, 1: 283-300.

Hunt, G. R., Salisbury, J. W. (1971a), Visible and Near-Infrared Spectra of Minerals and Rocks: II Carbonates, *Modern Geology*, 2: 23-30.

Hunt, G. R., Salisbury, J. W. (1971b), Visible and Near-Infrared Spectra of Minerals and Rocks: XI Sedimentary Rocks, *Modern Geology*, 5: 211-217.

Hunt, G. R., Salisbury, J. W. (1971c), Visible and Near-Infrared Spectra of Minerals and Rocks: XII Carbonates, *Modern Geology*, 5: 221-228.

Irons, R. D., Weismiler, R. A., Peterson, G. W. (1989), Soil reflectance. In G. Asrar (ed). *Theory and Application of Optical Remote Sensing*, John Wiley & Sons, New York. 66-106.

Irvin, B.J. Ventura, S.J. and Slater, B.K. (1997), "Fuzzy and Isodata Classification of Landform Elements from Digital Terrian Data in Pleasant Valley, Wesconsin," *Geoderma*, 77: 137-154.

Ito, Y., and Omatu, S. (1997), "Category Classification Method Using Self-Organizing Neural Network," *International Journal of Remote sensing*, 18(4): 829-845.

Jackson, M. L., Lim, S. H., Zlanzy, L. W. (1986) Oxides, hydroxides, and aluminosilicate. In K. Klute (ed). *Methods of Soil Analysis, Part 1*, 2nd edition. American Society of Agronomy, Madison, WI, USA. 101-150.

Jaggi, S., Quattrochi, D.A., and Lam, N.S-N. (1993), " Implementation and Operation of Three Fractal Measurement Algorithms for Analysis of Remote-Sensing Data," *Computers and Geosciences*, 19(6): 745-767.

- Jahne, B.** (1991), *Digital Image Processing*, New York: Springer-Verlag.
- Jain, A.K.** (1989), *Fundamental of Digital Image Processing*, Englewood Cliffs, New Jersey: Prentice Hall.
- Jarvis, C. H., Stuart, N.** (1996), "The Sensitivity of A Neural Network for Classifying Remotely Sensed Imagery" *Computers and Geosciences*, 22(9): 959-967.
- Jensen, J.R.** (1997), *Introductory Digital Image Processing: A Remote Sensing Perspective*, 2nd edition, Upper Saddle River, New Jersey: Prentice Hall.
- Jenson, S.K. and Waltz, F.A.** (1979), " Principal Component Analysis and Canonical Analysis in Remote Sensing," *Proceedings of the American Photogrammetric Society, 45th Annual Meeting* , Falls Church, Virginia, 337-347.
- Johannsen, C.J. and Sanders, J.L.** (Eds) (1982), *Remote Sensing for Resource Management*, Ankeny, Iowa: Soil Conservation Society of America.
- Jones, C.** (1997), *Geographical Information Systems and Computer Cartography*, England: Longman.
- Julian, J.H., Orford, D., and Whalley, W.B.** (1989), " Three Implementations of Fractal Analysis of Particle Outlines," *Computers and Geosciences*, 15(2): 199-207.
- Kahle, A. B.** (1984), Measuring Spectra of Arid Lands, In *Deserts and Arid Lands*, El-Baz, F (Ed), Martinus Nijhoff Publishers, Netherlands. 195-217
- Kamata, S., and Kawaguchi, E.** (1993), "Application of Neural Network Approach to Classify Multi-Temporal Landsat Images," *Proceedings of the International Geoscience*

and Remote Sensing Symposium (IGARSS '93), Tokyo, Japan, (Piscataway, NJ: I.E.E.E.): 716-718.

Kavzoglu, T. and Mather, P. M. (1999), "Pruning artificial neural networks: an example using land cover classification of multi-sensor images," *International Journal of Remote sensing*, 20(14): 2787-2803.

Key, J., Maslanik, J. A., and Schweiger, A. J. (1990), "Neural Network vs. Maximum Likelihood Classification of spectral and Textural Features in Visible, thermal, and Passive Microwave Data," *Proceedings of the International Geoscience and Remote Sensing Symposium (IGARSS '90)*, Collage Park, MD, (Piscataway, NJ: I.E.E.E.): 1277-1280.

Kineman, J. J. (1993), "What is a science database? Design considerations for global characterization in the NOAA-EPA global ecosystems database project," *In Environmental Modelling with GIS*, Goodchild, M. F., Parks, B. O., Steyaert, L. T., eds, New York: Oxford University Press, pp 372-378.

Klinkenberg, B. and Goodchild, M.F. (1992), "The Fractal Properties of Topography: A Comparison Methods," *Earth Surface Processes and Landforms*, 17: 217-234.

Kruse, F.A. (1988), "Use of Airborn Imaging Spectrometry Data to Map Minerals Associated with Hydrothermally Altered Rocks in the Northern Grapevine Mountains Nevada and California," *Remote Sensing of environment*, 24(1): 31-51.

Lagacherie, P., Legros, J.P., and Burrough, P.A. (1995), "A Soil Survey Procedure Using the Knowledge of Soil Patterns Established on a Previously Mapped Reference Area," *Geoderma*, 65:283-301.

- Lagacherie, P., Cazemier, D.R., van Gaans, P.F.M., and Burrough, P.A. (1997),** “Fuzzy *k*-means Clustering of fields in an Elementary Catchment and Extrapolation to a Larger Area,” *Geoderma*, 77:197-216.
- Lam, N. S. N. (1990),** “Description and Measurement of Landsat TM Images Using Fractals,” *Photogrammetric Engineering and Remote Sensing*, 56(2): 187-195.
- Lam, N.S.N., and Quattrochi, D. A. (1992),** On the Issues of Scale, Resolution, and Fractal analysis in the Mapping Sciences, *Professional Geographer*, 44(1): 88-97.
- Lam, N.S.N., Quattrochi, D. A., Qiu, H. L., Zhao, W., (1998),** “Environmental assessment and monitoring with image characterization and modelling system using multiscale remote sensing data, *Applied Geographic studies*, 2(2): 77-93.
- Lam, S. (1993),** “Fuzzy Sets Advance Spatial Decision Analysis,” *GIS World*, 6(12): 58-59.
- Lauwerier, H. (1987),** *Fractals Images of Chaos*, England: Penguin Group.
- Lavallee, D., Jourdan, D., Guatier, C. (1993),** “Universal multifractal properties of microwave satellite data,” *ACSM/ASPPRS Annual Convention*, 171-181.
- Lee, B. G. (1996),** “Neural Networks Applications in The Geosciences: An Introduction” *Computers and Geosciences*, 22(9): 955-957.
- Lee, T., Richards, J. A., Swain P. H. (1987),** “Probabilistic and evidential approaches for multisource data analysis,” *IEEE Transactions on Geosciences and Remote Sensing*, 25: 283-293.

Legg, C.A. (1992), *Remote Sensing and Geographic Information Systems: Geological Mapping, Mineral Exploration and Mining*, New York: Ellis Hordwood.

Levy Vehel, J. (1998), "Introduction to the multifractal analysis of images," *In INRIA Internal report*.

Levy Vehel, J. and Berroir, J. (1991), "Application to multifractal theory to image analysis," *In INRIA Internal report*.

Levy Vehel, J. and Berroir, J. (1993), "Image analysis through multifractal description," *In INRIA Internal report*.

Levy Vehel, J. and Mignot, P. (1998), "Multifractal Segmentation of Images," *In INRIA Internal Report*.

Levy Vehel, J. and Vojak, R. (1998), "Multifractal analysis of choquet capacities: Preliminary Results," *Advances in Applied Mathematics*, 20(1): 1-43.

Li, H., Liu, Z., and Sun, W. (1993), "A New Approach to Pattern Recognition of Remote Sensing Image Using Artificial Neural Network," *Proceedings of the International Geoscience and Remote Sensing Symposium (IGARSS '93)*, Tokyo, Japan, (Piscataway, NJ: I.E.E.E.): 713-715.

Lillisand, T.M. and Kiefer, R.W. (1994), *Remote Sensing and Image Interpretation*, 3rd edition, New York: John Wiley and Sons.

Liu, Z. K., and Xiao, J. Y. (1991), "Classification of Remotely-Sensed Image Data Using Artificial Neural Networks," *International Journal of Remote Sensing*, 12: 2433-2438.

- Lo, C. P.** (1986), *Applied Remote Sensing*, London: Longman Scientific and Technical.
- Lovejoy, S., and Schertzer, D.** (1990), "Multifractals, university classes and satellite and radar measurements of cloud and rain fields," *Journal of Geophysical Research*, 95(D3): 2021-2034.
- Low, A.** (1991), *Introductory Computer Vision and Image Processing*, London: The McGraw-Hill Companies.
- Magee, R.W., Moor, J.McM. and Coates, D.** (1986), "Thematic Mapper Data Applied to Mapping Hydrothermal Alteration in Southwest Mexico," *5th Thematic Conference on Remote Sensing for Exploration Geology*, Reno, Nevada, 373-382.
- Mandelbrot, B. B.** (1983), *The Fractal Geometry of Nature*, San Francisco: W.H. Freeman Co.
- Mannan, B. Roy, J. and Ray, A. K.** (1998), "Fuzzy ARTMAP Supervised Classification of Multi-spectral Remote-Sensing Images," *International Journal of Remote Sensing*, 19(4): 767-774.
- Marion, A.** (1991), *An Introduction to Image Processing*, London: Chapman and Hall.
- Mark, F.M. and Aronson, P.B.** (1984), "Scale-Dependent Fractal Dimensions of Topographic Surfaces: An Empirical Investigation, with Applications in Geomorphology and Computer Mapping," *Mathematical Geology*, 16(7): 671-683.
- Maselli, F. Rodolfi, A. and Conese, C.** ((1996), "Fuzzy Classification of Spatially Degraded Thematic Mapper Data for the Estimation of Sub-Pixel Components," *International Journal of Remote sensing*, 17(3): 537-551.

Mather, P.M. (1987), *Computer Processing of Remotely Sensed Images: An Introduction*, New York: John Wiley and Sons.

Mather, P.M. (1999), *Computer Processing of Remotely Sensed Images: An Introduction*, 2nd edition, New York: John Wiley and Sons.

Mather, P. M. Tso, B. and Koch, M. (1998), "An Evaluation of Landsat Spectral Data and SAR-Derived Textural Information for Lithological Discrimination in the Red Sea Hills, Sudan," *International Journal of Remote Sensing*, 19(4): 587-604.

MAW (1986), *General Soil Map of the Kingdom of Saudi Arabia*, Ministry of Agriculture and water, Riyadh.

MAW (1995), *The Land Resources*, Ministry of Agriculture and water, Riyadh.

Mays, M. D. Bogardi, I. And Bardossy, A. (1997), "Fuzzt logic and Risk-Based Soil Interpretations," *Geoderma* 77: 299-315.

McBratney, A. B., and De Gruijter, J. J. (1992), "A Continuum Approach to Soil Classification by Modified Fuzzy *k*-means with Extragrades," *Journal of Soil Science*, 43:159-175.

McBratney, A. B. and Odeh, I. O. A. (1997), "Application of Fuzzy Sets in Soil Science: Fuzzy Logic, Fuzzy Measurements and Fuzzy Decisions," *Geoderma*, 77: 85-113.

Mulders, M. A. (1987), *Remote Sensing in Soil Science*, Amsterdam: Elsevier.

Muller, J.P. (1988), *Digital Image Processing in Remote Sensing*, London and Philadelphia: Taylor and Francis.

Newton, A.R. and Boyle, T.P. (1993), "Discriminating Rock and Surface Types with Multispectral Satellite Data in the Richtersveld, NW Cape Province, South Africa," *International Journal of Remote Sensing*, 14(5): 943-959.

Niblack, W. (1986), *An Introduction to Digital Image Processing*, Englewood Cliffs, New Jersey: Prentice Hall.

Odeh, I. O. A., McBratney, A. B., and Chittleborough, D. J. (1990), "Design of Optimal Sample Spacings for Mapping Soil Using Fuzzy *k*-means and Regionalized Variable Theory," *Geoderma*, 47:93-122.

Olsen, E.R., Ramsey, D.R., and Winn, D.S. (1993), "A Modified Dimension as a Measure of Landscape Diversity," *Photogrammetric Engineering and Remote Sensing*, 59(10): 1517-1520.

Olsson, L., and Eklundh, L. (1994), "Fourier Series for Analysis of Temporal Sequences of Satellite Sensor Imagery," *International Journal of Remote Sensing*, 15(18): 3735-3741.

Paola, J. D., Schowengerdt, R. A. (1997), "The Effect of Neural-Network Structure on a Multispectral Land-Use/Land-Cover Classification," *Photogrammetric Engineering and Remote Sensing*, 63(5): 535-544.

Paola, J. D., Schowengerdt, R. A. (1995), "A Review and Analysis of Backpropagation Neural Networks for Classification of Remotely-Sensed Multi-spectral Imagery," *International Journal of Remote Sensing*, 16(16): 3033-3058.

Papo, H.B. (1984), "Digital Terrain Models for Slopes and Curvatures," *Photogrammetric Engineering and Remote Sensing*, 50(6): 695-701.

Patterson, D. B. (1996), *Artificial Neural Networks*, Singapore: Prentice Hall.

Polidori, L. (1991), "Description of Terrain as a Fractal Surface, and Application to Digital Elevation Model Quality Assessment," *Photogrammetric Engineering and Remote Sensing*, 57(10): 1329-1332.

Polis, D.F. (1975), "Fourier Spectra for Non-Homogeneous Patterns," *Photogrammetric Engineering and Remote Sensing*, 321-323.

Pratt, D.A., Foster, S.J., and Ellyett, C.D. (1980), "A Calibration Procedure for Fourier Series Thermal Inertia Models," *Photogrammetric Engineering and Remote Sensing*, 46(4): 529-538.

Pratt, W.K. (1978), *Digital Image Processing*, New York: John Wiley and Sons.

Qari, M.Y. (1990), Geological Analysis of Parts of the Southern Arabian Shield Based on Landsat TM Imagery, *Ph.D. Thesis*, Department of Geological Sciences, University College London, UK.

Qiu, H.L., Lam, N.S.N., Quattrochi, D. A., and Gamon, J. A. (1999), Fractal Characterisation of Hyperspectral Imagery, *Photogrammetric Engineering and Remote Sensing*, 65(1): 63-71.

Quattrochi, D. A. (1993), "The need for lexicon of scale terms in integrating remote sensing data with geographic information systems," *Journal of Geography*, 92(5): 206-212.

Rau, Y. C., and Lure, Y. M. F. (1993), "Classification of remote sensing data using partially trained neural network, In proceeding IEEE International Geoscience and Remote Sensing Symposium, pp 728-730.

Rees, W.G. (1990), *Physical Principles of Remote Sensing*, Cambridge: Cambridge University Press.

Rex, K. D., and Malanson, G. P. (1990), "The fractal shape of riparian forest patches," *Landscape Ecology*, 4(4): 249-258.

Richards, J.A. (1994), *Remote Sensing Digital Image Analysis*, 2nd edition, New York: Springer-Verlag.

Ripley, B. D. (1996), *Pattern Recognition and Neural Networks*, Cambridge: Cambridge University Press.

Ritter, N. D. and Hepner, G. F. (1990), "Application of an artificial neural network to land-cover classification of Thematic Mapper imagery, *Computers and Geosciences*, 16: 873-880.

Roach, D.E. and Fowler, A.D. (1993), "Dimensionality Analysis of Patterns: Fractal Measurements," *Computers and Geosciences*, 19(6): 849-869.

Rose, J. (1989), "Spatial Interference in the AVIRIS Imaging Spectrometer," *Photogrammetric Engineering and Remote Sensing*, 55(9): 1339-1346.

Rosenfeld, A. and Kak, A.C. (1976), *Digital Picture Processing*, New York: Academic Press.

- Rosenholm, D., and Torlegard, K.** (1988), "Three-Dimensional Absolute Orientation of Stereo Models using Digital Elevation Models," *Photogrammetric Engineering and Remote Sensing*, 54(10): 1385-1389.
- Rowan, R.L.** (1975), " Application of Satellites to Geological Exploration, *American Scientist*, 63:393-403.
- Rowell, D.L.** (1994), *Soil Science Methods and Applications*, England: Addison Wesley Longman Limited.
- Rumelhart, D. E., Hinton, G. E., Williams, R. J.** (1986), "Learning internal representations by error propagation, In *Parallel Distributed Processing Explorations in the Multistructure of Cognition*, Vol, I: Foundations, edited by D. E. Rumelhart and J. L. McClelland, Cambridge, MA: The MIT press, pp 318-362.
- Sabins, F.F. Jr.** (1987), *Remote Sensing: Principles and Application*, 2nd edition, New York: W.H. Freeman and Company.
- Schott, J. R.** (1997), *Remote Sensing: The Image Chain Approach*, New York: Oxford University Press.
- Schowengerdt, R. A.** (1983), *Techniques for Image Processing and Classification in Remote Sensing*, New York: Academic Press.
- Shelberg, M.C., Lam, N., and Moellering, H.** (1983), " Measuring the Fractal Dimension of Surfaces," *Proceeding 6th International Symposium on Automated Cartography*, 2: 319-328

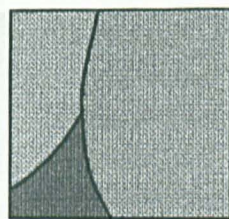
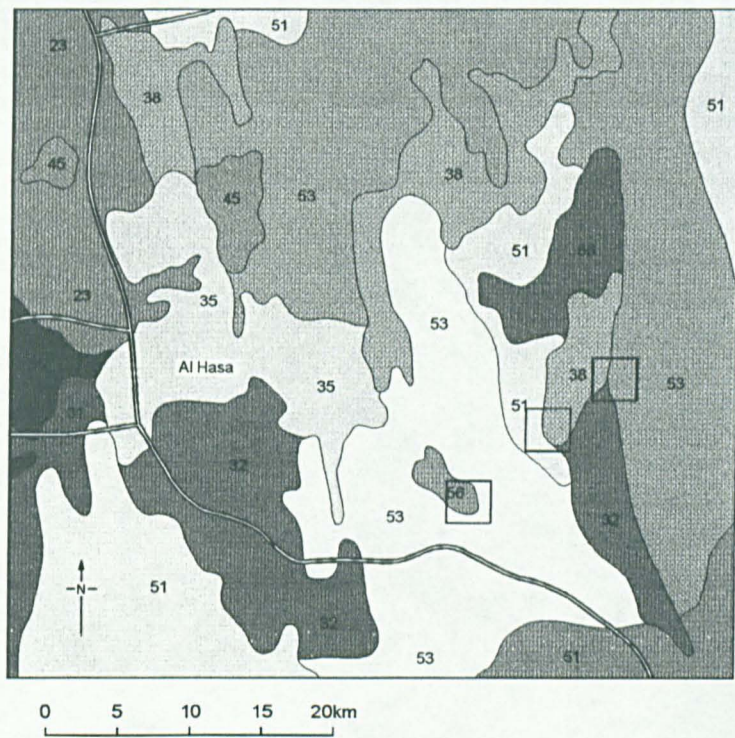
- Skidmore, A. K., Turner, B. J., Brinkhof, W., Knowles, E.** (1997), "Performance of a Neural Network: Mapping Forests Using GIS and Remotely Sensed Data," *Photogrammetric Engineering and Remote Sensing*, 63(5): 501-514.
- Spanias, A. S., Jonsson, S. B., and Stearns, S. D.** (1991), "Transform Methods for Seismic Data Compression," *IEEE Transaction on Geoscience and Remote sensing*, 29(3): 407-416.
- Steyaert, L. T.** (1993), "A perspective on the state of environmental simulation modelling," *In Environmental Modelling with GIS*, Goodchild, M. F., Parks, B. O., Steyaert, L. T., eds, New York: Oxford University Press, pp 16-30.
- Stoner, E. R. and Baumgardner, M. F.** (1981), "Characteristic variations in reflectance of soil surface," *Soil Science Society of America Journal*, 45: 1161-1165.
- Stromberg, W. D. and Farr, T. G.**(1986), "A Fourier-Based Texture Feature Extraction Procedure", *IEEE Transaction on Geoscience and Remote Sensing*, 24(5): 722-731.
- Suits, G.H.** (1983), " The Nature of Electromagnetic Radiation," *Manual of Remote Sensing*, ed. R.G. Reeve, Falls Church, Virginia: American Society of Photogrammetry.
- Swain, P. H. and Davis, S. M.** (1978), *Remote Sensing: The Quantitative Approach*, New York: McGraw-Hill.
- Tate, N.J.** (1998), " Estimating the Fractal Dimension of Synthetic Topographic Surfaces," *Computers and Geosciences*, 24(4): 325-334.
- Teran, A.R., Santisbon, C., and Roberts, M.J.** (1992), " Using Fractals to Identify Regular and Irregular Shapes into Satellite Images," *Jaina*, 3(3): 22-23.

- Townshend, J.R.G.**, ed. (1981), *Terrain Analysis and Remote Sensing*, London: George Allen and Unwin.
- Townshend, J.R.G.** (1992), "Land Cover," *International Journal of Remote Sensing*, 13(6 and 7): 1319-1328.
- Townshend, J.R.G.**, and **Justice, C. O.** (1988), "Selecting the spatial resolution of satellite sensors required for global monitoring of land transformations," *International Journal of Remote Sensing*, 9(2): 187-236.
- Turner, M. G.**, **Dale, V. H.**, **Gardner, R. H.** (1989a), "Predicting across scales: theory, development, and testing," *Landscape Ecology*, 3(3/4): 245-252.
- Turner, M. G.**, **O'Neill, R. V.**, **Gardner, R. H.**, **Milne, B. T.** (1989b), "Effects of changing spatial scale on the analysis of landscape pattern, *Landscape Ecology*, 3(3/4): 153-162.
- Unwin, D.** (1989), "Fractals and the Geosciences Introduction," *Computers and Geosciences*, 15(2): 163-165.
- Van Der Meer, F.** (1999), "Iterative spectral unmixing (ISU)," *International Journal of Remote sensing*, 20(17): 3431-3436.
- Wang, D.** (1993), "Pattern recognition: neural networks in perceptive," *IEEE Expert*, 8: 52-59.
- Wang, F.** (1990a), "Improving Remote Sensing Image Analysis through Fuzzy Information Representation," *Photogrammetric Engineering and Remote Sensing*, 56(8): 1163-1169.

- Wang, F.** (1990b), "Fuzzy Supervised Classification of Remote Sensing Images," *IEEE Transaction on Geoscience and Remote Sensing*, 28(2): 194-201.
- Wang, F.** (1991), "Integrating GIS's and Remote Sensing Image Analysis Systems by Unifying Knowledge Representation Schemes," *IEEE Transaction on Geoscience and Remote Sensing*, 29(4): 656-665.
- Watson, K.** (1993), "Processing Remote Sensing Images Using the 2-D FFT-Noise Reduction and Other Applications," *Geophysics*, 58(6): 835-852.
- Whalley, W. R., Leeds-Harrison, P. B., and Bowman, G. E.** (1991), Estimation of Soil Moisture Status Using Near Infrared Reflectance, *Hydrological Processes*, 5: 321-327
- White, L. P.** (1977), *Aerial Photography and Remote Sensing For Soil Survey*, Oxford: Clarendon Press.
- White, R. E.** (1997), *Principles and Practice of Soil Science: The Soil as a Natural Resource*, Oxford: Blackwell Science.
- Webster, R. and Oliver, M. A.** (1990), *Statistical Methods in Soil and Land Resource Survey*, New York: Oxford University Press.
- Yoshida, T., and Omatu, S.** (1994), "Neural Network Approach to Land Cover Mapping," *IEEE Transactions on Geoscience and Remote Sensing*, 32: 1103-1109.
- Zadeh, L. A.** (1965), "Fuzzy Sets," *Information and Control*, 8: 338-353.

Zeng, Y., Gantzer, C. J., Payton, R. L., Anderson, S. H. (1996), "Fractal Dimension and Lacunarity of Bulk Density Determined with X-ray Computed Tomography," *Soil Science American Journal*, 60: 1718-1724.

Zhuang, X., Engel, B. A., Baumgastner, M. F., Swain, P. H., (1991), "Improving classification of crop residues using digital land ownership data and Landsat TM imagery, *Photogrammetric Engineering and Remote Sensing*, 57(11): 1487-1492.



Segment I



Sand sheets and dunes



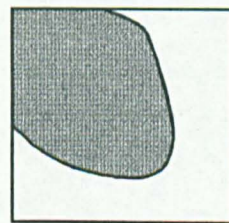
Pediplain with shallow soils



Gypseos pediplain with sand cover



Sabkhas



Segment II



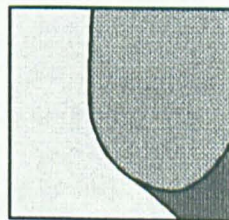
Sand sheets and sabkha



Pediplain with deep soils



Alluvial plain



Segment III



Pediplain with sandcover



Sand dunes



Gypseous pediplain

Figure 2.5 General soil map and the locations of test areas (after MAW, 1986)

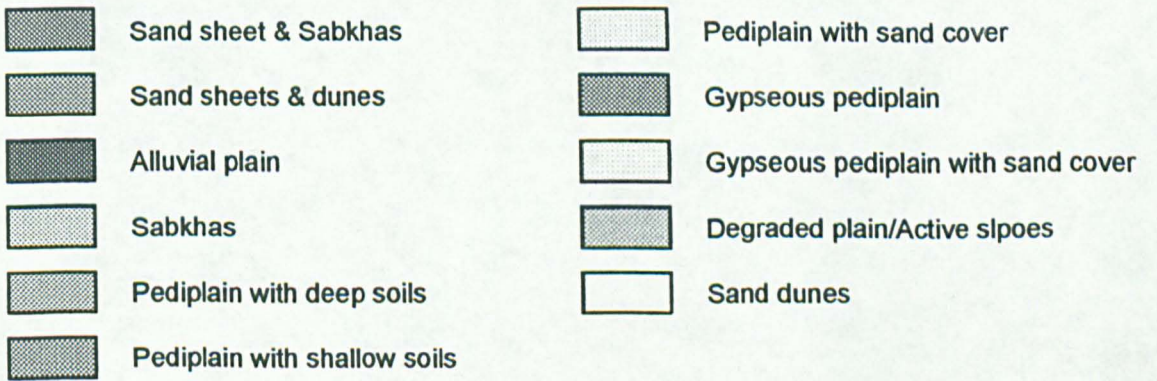
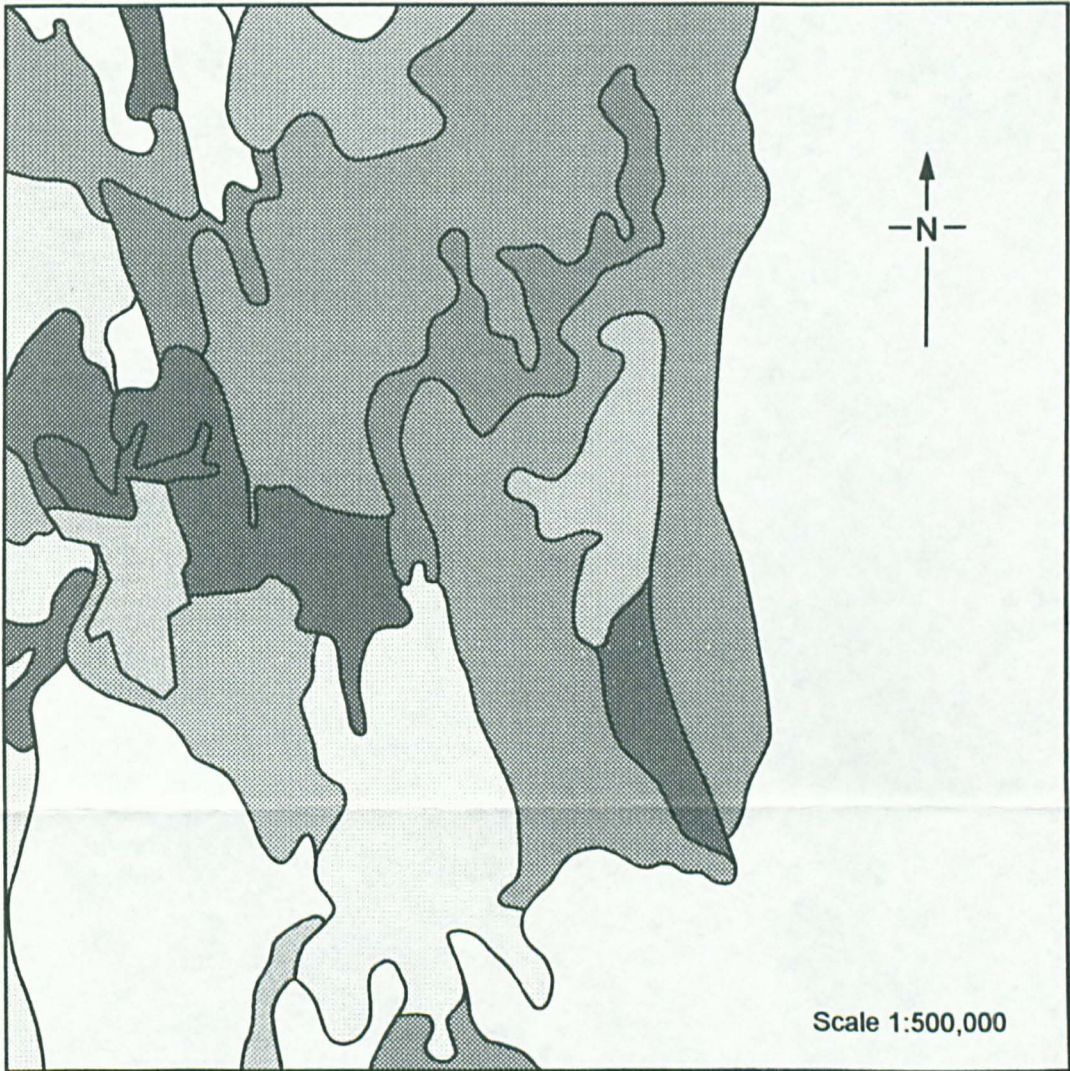
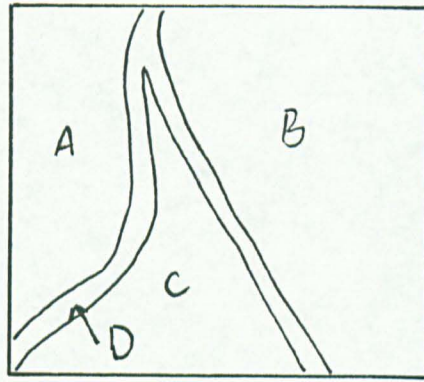
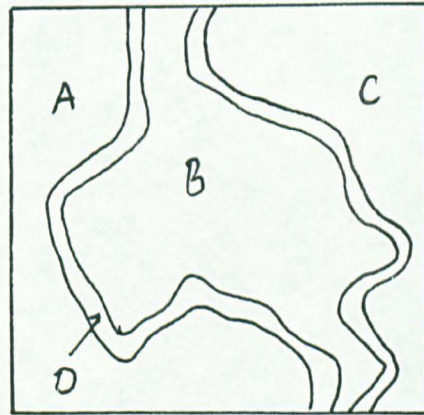


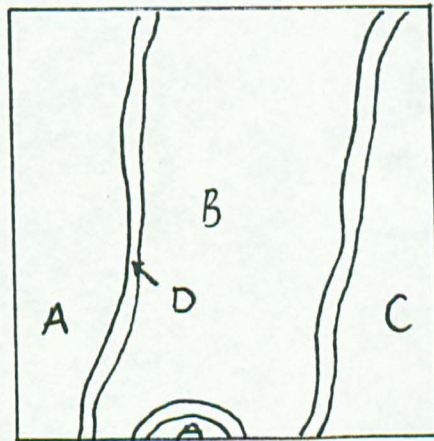
Figure 2.6 General Landform map (after MAW 1995)



I



II



III

Figure 5.10: Illustration diagram of the three segments showing the four zones A, B, C, and D.